Author:
Coe, Mary K

Title:
Hydrophobicity Across Length Scales

The Role of Surface Criticality

Hydrophobicity Across Length Scales: The Role of Surface Criticality

Mary Kathryn Coe

School of Physics

A dissertation submitted to the University of Bristol in accordance with the requirements for award of the degree of Doctor of Philosophy in the Faculty of Science.

July 2021

Word Count: 51234

Abstract

From proteins to plant leaves, hydrophobicity is ubiquitous. Despite this, the underlying physical mechanism relating hydrophobicity on the microscopic and macroscopic length scales remains undetermined. In part, this is due to the wealth of disciplines involved, from solvation to surface science, which provide unique views on hydrophobicity but whose relation to one another has rarely been considered.

Studies of hydrophobicity on both microscopic and macroscopic length scales have reported an enhancement of local density fluctuations. Within recent studies of a Lennard-Jones fluid on macroscopic length scales, similar density fluctuations have been attributed to the existence of a surface critical point called drying [1]. Within this thesis, it is postulated that this drying critical point is also responsible for hydrophobic density fluctuations on both microscopic and macroscopic length scales, and provides the relation of hydrophobicity across length scales. As this drying critical point influences Lennard-Jones fluids, it is also postulated that hydrophobicity is no more than a specific case of solvophobicity.

To explore these postulates, a mesoscopic thermodynamic analysis is performed to anticipate how hydrophobic and solvophobic systems, subject to a drying critical point, on all length scales should be expected to behave. These predictions are then tested for a Lennard-Jones fluid numerically using classical density functional theory, and for a simple water model using Grand Canonical Monte Carlo. Combined, these results provide clear evidence that the mechanism underlying hydrophobicity and solvophobicity across microscopic and macroscopic length scales is a drying surface critical point.

To Mum, Dad and Uncle Raymond.

Acknowledgements

Firstly, I would like to thank my supervisor, Prof Nigel Wilding, for his guidance through this project. His ideas, advice and patience have proven invaluable over the past four years. I would also like to thank my unofficial supervisor, Prof Bob Evans, for his support and for the frequent discussions on the large background this project entailed. His willingness to share his vast knowledge, and our lively discussions about this project have been both greatly appreciated and much enjoyed. I'd particularly like to thank Bob for his patience over the last year, as the pandemic saw us move from working on whiteboards to e-mailing scans of derivations and notes back and forth. It hasn't been easy, but we got there in the end.

I would also like to thank Prof Matthias Schmidt and his PhD students, Tobias Eckert, Florian Sammüller and Nico Stuhlmüller, for introducing me to the local thermal susceptibility and reduced density prior to their publication. Without this, chapter 8 would likely not exist. Also, thank you to Prof Roland Roth for the cDFT code he shared with us near the beginning of this project. Not only did this show me where I was going wrong initially, it also taught me numerical implementation tricks which have helped considerably.

I would like to thank Dr Tom Underwood for all his help during the early days of this project, and in particular his incredible patience and positivity when explaining computational techniques I struggled to grasp. Also, thank you to all of my office mates, both at the University of Bath and the University of Bristol, for their company on the many coffee breaks we took and for making the office such a welcoming place. Although our areas did not always align, their suggestions when I was struggling with code or maths were indispensable. I'd also like to thank the graduate team in the School of Physics at the University of Bristol for their continued help throughout the transfer process, and for humouring myself and other students when we suggested funding for pizza and quiz nights. I'm incredibly grateful for the work they do to give all of us the best possible PhD experience.

Finally, I would like to thank my Mum, Dad and Uncle Raymond for all their support over the past four years. In particular, I would like to thank them for listening patiently whenever I talked about this project, even though I am sure they had no idea what I was talking about. Also to my best friend Dr Rachael Blakey, for always being there, especially through the difficult writing process.

They say it takes a village to raise a child. Well, it certainly takes an entire university (or two) to produce a thesis. Without you all, this thesis would not have been possible.

Authour's Declaration

I declare that the work in this dissertation was carried out in accordance with the requirements of the University's Regulations and Code of Practice for Research Degree Programmes and that it has not been submitted for any other academic award. Except where indicated by specific reference in the text, the work is the candidate's own work. Work done in collaboration with, or with the assistance of, others, is indicated as such. Any views expressed in the dissertation are those of the author.

SIGNED: ..... DATE:.....

For the purpose of this thesis, a Python module for implementing classical density functional theory and a C++ program for implementing Grand Canonical Monte Carlo, as described in chapter 4, were written. These will be made publicly available in due course at https://github.com/marykcoe.

Contents

List of Figures

List of Tables

List of Abbreviations

cDFT	classical density functional theory
ff	fluid-fluid
FMT	fundamental measure theory
FS	finite size
GC	grand canonical
LJ	Lennard-Jones
LR	long-ranged
MFT	mean field theory
MC	Monte Carlo
mW	monatomic water
sf	substrate/solute-fluid
SK	sharp-kink
SR	short-ranged

List of Symbols

Bulk Properties

μ	Chemical potential
μ_{co}	Chemical potential at liquid-vapour coexistence
T	Temperature
T_D	Drying temperature
T_c	Bulk critical temperature
γ_{lv}	Liquid-vapour surface tension
ρ_l	Density of the liquid at liquid-vapour coexistence
ρ_v	Density of the vapour at liquid-vapour coexistence
ρ_b	Density of the liquid when oversaturated

Surface Properties

R_s	Radius of the solute
σ_s	Diameter of a particle within the solute/planar substrate
ρ_s	Density of the solute/planar substrate
$\rho(r)$	Density profile as measured from the centre of a solute of radius R_s
$\rho(z)$	Density profile as measured from the surface of a planar substrate
ℓ_{eq}	Equilibrium width of depleted density region
χ_μ	Local compressibility
χ_T	Local thermal susceptibility
χ_*	Reduced density
$\chi_{x,b}$	Value of χ_x, where $x = \mu, T, *$, in the bulk fluid
ε_s	Well depth of solute/substrate-fluid interaction potential
ε_{sf}	Measure of solute/substrate-fluid attraction

ε_c	Value of well-depth of solute/substrate-fluid interaction potential at the drying critical point
$\varepsilon_{sf,c}$	Value of ε_{sf} at the drying critical point

Relevant to Models Used

σ	Diameter of a LJ particle
ε	Well depth of LJ fluid interaction potential
σ_{mw}	Diameter of a mW particle
ε_{mw}	Well depth of mW interaction potential

Effective Interface Potential

$\Delta\rho$	$\rho_l - \rho_v$
$\delta\mu$	$\mu - \mu_{co}$
$\tilde{p}$	Effective pressure, defined as $\tilde{p} = \delta\mu\Delta\rho + 2\gamma_{lv}/R_s$
t'	Effective reduced temperature, defined as $t' = (\rho_v\varepsilon\sigma^6 - \rho_s\varepsilon_s\sigma_s^6)\varepsilon^{-1}\sigma^{-3}$
$\tilde{t}$	Reduced temperature defined as $\tilde{t} = (T - T_D)/T_D$
R_c	Length scale of capillary evaporation

Chapter 1

Introduction

Hydrophobicity is ubiquitous. Many aquatic and semi-aquatic plants, such as the lotus, utilise hydrophobicity in their self-cleaning mechanisms which reduce their chances of infection from harmful pathogens present in the bodies of water in which they grow [2]. Butterflies have been found to utilise hydrophobicity to ensure that rain droplets which fall on their wings roll off away from their bodies [3]. Proteins have been found to utilise localised hydrophobicity to evacuate surrounding water and enable ligand binding [4]. Detergents utilise the hydrophobicity driven self assembly of amphiphilic molecules into micelle structures to remove grease from clothes [5]. The influence of hydrophobicity is felt in every aspect of our lives.

Despite this, our understanding of hydrophobicity is limited. To some extent, this is because of the way in which it has been studied. Hydrophobicity on the length scales of proteins or micelles has often been studied from the view point of solvation [6, 7]. Great progress has been made in understanding the free energy changes involved when solvating smooth spherical solutes [6], including the influence of temperature [8] and solute-water attractions [9], though most notably significant changes in behaviour have been observed when the size of the solute is increased from that of a water molecule, to that much larger than a water molecule [6]. The influence of solutes of varying shapes and sizes on the local structure of water has also been considered in great detail [10–16], though conclusions have not always agreed. In contrast, hydrophobicity of plants and insect wings has typically been studied from the view point of surface science [17, 18], where the general focus has been on the structure of the surface, and engineering of coatings with low surface energy [19]. Perhaps unsurprisingly, few studies have sought to compare hydrophobicity on the length scales of proteins to hydrophobicity on the length scales of plant leaves [10].

Attempting to compare the manifestations of hydrophobicity across all length scales is difficult not only because of the different approaches taken to their study, but also because of the different behaviours observed. How does the behaviour of water droplets relate to solvation? One answer to this comes in the form of the local structure of water at the surface of large hydrophobic solutes and at macroscopic surfaces. In such circumstances, water molecules have been found to adopt preferential orientations [10, 11, 16, 20, 21], and to retreat from the surface or solute, forming a region of depleted density or 'gap' [6, 9, 22–27].

However, around even fairly large solutes, this region has been found to be small [10, 11], and readily reduced by the presence of solute-water attractions [9, 28]. As such, relating hydrophobicity across length scales using the local structure of water has proven difficult.

In addition to changes in the local structure of water, simulation studies of both solutes and surfaces have shown that hydrophobicity is associated with localised enhanced density fluctuations [23, 28, 29]. Importantly, these fluctuations have been found to be a more sensitive measure of hydrophobicity [23, 28] than the local structure of water, and thus more easily detectable. In fact, there is evidence that it is these density fluctuations which drive various hydrophobic processes, for example the collapse of hydrophobic polymer chains [30] or the evacuation of water near biomolecules [31].

An immediate question is then: what mechanism drives these density fluctuations? Drawing inspiration from recent solvophobic studies of Lennard-Jones fluids, it is possible that this mechanism is a surface critical point named drying. Evans et al. [1, 32] have demonstrated that large density fluctuations near solvophobic planar substrates are induced by a drying surface critical point, and furthermore that systems in the vicinity of this surface critical point exhibit a wealth of critical phenomena, for example scaling behaviour and critical exponents. Earlier studies by Stewart and Evans [33, 34] used similar methods to show that systems with very large solutes also obeyed scaling behaviour, though their studies focused on measures such as the adsorption, and did not consider density fluctuations. Considering such studies, it is plausible that an underlying drying surface critical point influences solvophobicity, and potentially relates solvophobicity on microscopic length scales to that on macroscopic length scales.

There is reason to believe a drying surface critical point may also be responsible for the large density fluctuations observed in macroscopic and microscopic studies of hydrophobicity and therefore might relate hydrophobicity across length scales. This reason stems not only from the similarities in solvophobic and hydrophobic behaviour reported in many studies [1, 23, 35, 36], but also from early evidence of a drying critical point in a study of macroscopic hydrophobicity by Evans and Wilding [23]. The existence of a drying critical point in both solvophobic and hydrophobic studies would also suggest that both interactions are governed by the same underlying mechanism, and that hydrophobicity is simply a specific case of solvophobicity, rather than a unique interaction.

Considering this, two postulates are made.

Postulate 1

The physical mechanism which underlies hydrophobicity is a surface critical point called drying, and it is this mechanism which relates hydrophobicity on the microscopic and macroscopic length scales.

Postulate 2

Hydrophobicity is simply a specific case of solvophobicity, and the mechanism underlying both is a drying critical point.

It is the purpose of this thesis to explore these. This is done as follows. In chapter 2, the thermodynamics, statistical mechanics and phase transitions theory which is necessary to understand the postulates is presented. A particular emphasis within chapter 2 is placed on understanding the similarities and differences between bulk and surface phase transitions, as the latter are far less well understood than the former. Following this, our current understanding of hydrophobicity and its relation to solvophobicity and phase transitions is reviewed in chapter 3. This provides the foundation of knowledge on which this thesis builds. In chapter 4, the numerical and simulation methods used within this thesis are presented. Notably, the present work makes use of two methods, which each provide valuable insight into solvophobicity and hydrophobicity respectively. Chapter 5 then presents a mesoscopic thermodynamic analysis of the expected behaviour of systems near to a drying critical point. Such an analysis has been utilised extensively in studies of solvophobicity, for example [1, 32–34, 37, 38], and provides insight into how results should be displayed and interpreted. In chapters 6 and 7, the two postulates are tested using results for solvophobic and hydrophobic systems respectively. The behaviour of different measures of density fluctuations near to the drying critical point is then compared in chapter 8, before final conclusions on the validity of the postulates are drawn in chapter 9.

Chapter 2

Thermodynamics and Statistical Mechanics of Phase Transitions

The purpose of this thesis is to explore the relationship between hydrophobicity and a surface phase transition termed drying. It is therefore important to understand what a surface phase transition is and, in particular, how it differs in presentation and properties from a bulk phase transition, the latter of which is fairly well understood. Achieving this understanding is only possible by first setting out the necessary thermodynamics, statistical mechanics and phase transitions theory. This chapter aims to do this, whilst also defining the measures which will be used to probe the relationship between hydrophobicity and drying.

2.1 Thermodynamics

The first law of thermodynamics defines the Fundamental Thermodynamic Relation as [39]

$$\mathrm{d}U = T\mathrm{d}S + \sum_i F_i \mathrm{d}L_i + \sum_\alpha \mu_\alpha \mathrm{d}N_\alpha \tag{2.1.1}$$

which describes how the internal energy, U, of a system changes when heat is supplied or when work is done. The supplied heat is measured by $T\mathrm{d}S$, where T is the temperature of the system and S the entropy, whilst the work done takes two forms. The first form represents the mechanical work, which is measured by $F_i\mathrm{d}L_i$, where F_i is a generalised force and L_i the associated generalised length. The second form of work is the chemical work, which is measured by $\mu_\alpha \mathrm{d}N_\alpha$, where μ_α and N_α are the chemical potential and number of particles of the α component of the system respectively. As the work presented here is concerned with one-component fluids, the α subscripts can be neglected.

For an isotropic one-component bulk fluid, equation (2.1.1) becomes [39]

$$\mathrm{d}U = T\mathrm{d}S - p\mathrm{d}V + \mu\mathrm{d}N \tag{2.1.2}$$

where p is the pressure of the fluid and V the volume it occupies. From this relation it is possible to define various free energies via Legendre transforms, which allow an understanding of how the energy of a system under adiabatic, isothermal, isobaric or isochoric conditions

changes when heat is supplied or work is done. Of relevance to solvation, defined as the process in which a solute is dissolved into a fluid, is the Gibb's free energy [39]

$$G(T,p,N) = U + pV - TS \equiv H - TS = \mu N \tag{2.1.3}$$

where $H = U + pV$ is defined as the enthalpy. The Gibbs' free energy describes a system that undergoes isothermal and isobaric processes, which are the conditions expected of solvation experiments conducted at ambient conditions.

Whilst experimental studies of solvation may occur at constant pressure and temperature conditions, simulation and theoretical studies of solvation typically use constant chemical, temperature and volume conditions. The free energy of interest in such a system is the grand potential, defined as [39]

$$\Omega(\mu,V,T) = U - TS - \mu N \equiv F - \mu N = -pV \tag{2.1.4}$$

where $F = U - TS$ is the Helmholtz free energy. The grand potential is useful in the study of phase transitions as the number of particles, N, is allowed to fluctuate.

Equations (2.1.3) and (2.1.4) represent the free energy of bulk or homogeneous fluids, for which the density is the same everywhere. If the density of the fluid is not constant, then the fluid is said to be inhomogeneous. An example of such a case is a free liquid-vapour interface, which is made by bringing the vapour and liquid phases of a fluid, which is at liquid-vapour coexistence, into contact such that an interface forms and the density of the fluid becomes spatially varying. In this case, the Fundamental Thermodynamic Relation of equation (2.1.1) becomes [40, 41]

$$\mathrm{d}U = T\mathrm{d}S - p\mathrm{d}V + \gamma\mathrm{d}A + \mu\mathrm{d}N \tag{2.1.5}$$

where $\gamma\mathrm{d}A$ represents the mechanical work done when changing the surface area, A, of the interface, which has surface tension γ. The grand potential then becomes [40]

$$\Omega(\mu,V,T) = U - TS - \mu N \equiv -pV + \gamma A \tag{2.1.6}$$

From equation (2.1.4), $-pV$ can be identified as the grand potential of the bulk fluid, $\Omega_b = -pV$. The excess grand potential, Ω_{ex}, can then be identified as $\Omega_{ex} = \Omega - \Omega_b$, which allows for the definition of the surface tension as [41]

$$\gamma = \frac{\Omega_{ex}}{A} \equiv \frac{\Omega - \Omega_b}{A} \tag{2.1.7}$$

The concept of surface excess quantities can be extended by considering the difference in the derivatives of equations (2.1.4) and (2.1.6). Denoting terms in the former by the subscript b to recognise they are bulk terms, the difference between the derivatives can be written as

$$\mathrm{d}\Omega - \mathrm{d}\Omega_b = -(S - S_b)\mathrm{d}T - (N - N_b)\mathrm{d}\mu + \gamma\mathrm{d}A \tag{2.1.8}$$

From this, the surface excess entropy can be identified as $S_{ex} = S - S_b$, and the surface

excess number of particles, known as the adsorption, as $\Gamma = N - N_b$. It should be noted that this is not the typical definition of adsorption [42], however this definition proves useful when considering surfaces of different geometries. The derivative of equation (2.1.8) can also be written as $\mathrm{d}\Omega - \mathrm{d}\Omega_b = \mathrm{d}(\Omega - \Omega_b) \equiv \mathrm{d}\Omega_{ex}$. Taking the derivative of equation (2.1.7) and setting equal to equation (2.1.8) then leads to the relation [41, 42]

$$s_{ex}\mathrm{d}T + \frac{\Gamma}{A}\mathrm{d}\mu + \mathrm{d}\gamma = 0 \tag{2.1.9}$$

where s_{ex} is the surface excess entropy per unit surface area. This is Gibbs' adsorption equation [42], from which it can be recognised that [40]

$$\frac{\Gamma}{A} = -\left(\frac{\partial\gamma}{\partial\mu}\right)_T \tag{2.1.10}$$

A free liquid-vapour interface is just one example of a system for which equation (2.1.5) is true. Another example is a fluid in contact with an impenetrable planar substrate. In this case, the fluid need not be at liquid-vapour coexistence however may still exhibit an inhomogeneous density due to its interaction with the substrate. The grand potential per unit volume of the bulk fluid, ω_b, in such a system can be found to be [40]

$$\omega_b(\mu, T) \equiv \lim_{V\to\infty}\left(\frac{\Omega}{V}\right) \equiv -p_b(\mu, T) \tag{2.1.11}$$

where $p_b(\mu, T)$ is the pressure of the bulk fluid. Using this, the excess grand potential per unit area can be identified as [40]

$$\omega_{ex}(\mu, T) = \lim_{\substack{V\to\infty \\ A\to\infty}}\left(\frac{\Omega - \omega_b V}{A}\right) \tag{2.1.12}$$

and thus the grand potential of an inhomogeneous fluid, which is not at liquid-vapour coexistence, as [40]

$$\Omega = -p_b V + \omega_{ex} A \tag{2.1.13}$$

By comparison to equation (2.1.6), ω_{ex} can be identified as a surface tension of a fluid which is not at liquid-vapour coexistence. Following the same procedure as in the case of a free liquid-vapour interface, it can then be found that equation (2.1.10) holds for fluids which are not at liquid-vapour coexistence [40].

2.2 Statistical Mechanics

Thermodynamics provides an understanding of the relationships between different macroscopic properties of a system, many of which can be observed experimentally. An area of physics closely related to thermodynamics is statistical mechanics, which provides a framework in which macroscopic thermodynamic properties of a system can be described in terms of averages of microscopic configurations of particles. Consider a system consisting of N indistinguishable particles of mass m. At any given time, the state of the system can be described by a total of $6N$ generalised coordinates: $3N$ spatial coordinates, $\mathbf{r}^N = \{\mathbf{r}_1, \ldots, \mathbf{r}_N\}$ and $3N$

momenta coordinates, $\mathbf{p}^N = \{\mathbf{p}_1, \ldots, \mathbf{p}_N\}$. These $6N$ coordinates define a phase point which exists within a $6N$-dimensional phase space [39, 42–44]. Assuming that the particles interact with one another, the Hamiltonian of the system can be defined as

$$\mathcal{H} = \Phi(\mathbf{r}^N) + K(\mathbf{p}^N) + V_{ext}(\mathbf{r}^N) \tag{2.2.1}$$

where $\Phi(\mathbf{r}^N)$ represents the potential energy due to inter-particle interactions, $K(\mathbf{p}^N)$ the kinetic energy and $V_{ext}(\mathbf{r}^N)$ the external potential energy. The latter of these acts to break the translational invariance of the fluid in which case the fluid is inhomogeneous. External potentials may arise from, for example, the presence of a surface, interface or gravity. If the external potential energy is $V_{ext}(\mathbf{r}^N) = 0$, then the fluid will be uniform, in which case the fluid is homogeneous. The kinetic energy takes the well known form [42]

$$K(\mathbf{p}^N) = \sum_{i=1}^{N} \frac{|\mathbf{p}_i|^2}{2m} \tag{2.2.2}$$

The coordinates of the phase point evolve with time according to Hamilton's equations and thus over time the phase point will move through the phase space, in a direction known as its phase trajectory [42].

During the course of the phase trajectory, the variation of microscopic configurations of the particles will lead to variations in thermodynamic properties of the system, such as the pressure. However, if the system is in thermodynamic equilibrium, referred to simply as equilibrium, these properties, referred to as observables, are expected to remain constant on average. An estimate for an observable can therefore be obtained by sampling the observable during the course of a phase trajectory and taking the average. This is a time average [42, 44].

However, because the phase trajectory is governed by Hamilton's equations, it is completely deterministic. This means phase trajectories will not intersect and therefore that phase points themselves provide a set of unique samples of an observable. An alternative to a time average is therefore an average over a set of phase points which share the same thermodynamic properties. This set is known as an ensemble and such an average is known as an ensemble average [42, 44].

Under certain conditions, the time and ensemble average are equivalent, in which case the system is said to be ergodic. Ergodicity is achieved if the system passes through every available point on its phase trajectory an equal number of times, which has the further implication that it must be possible to reach every accessible point of phase space within a finite amount of time [42, 43]. Whilst it is not possible to prove that every system at thermodynamic equilibrium is ergodic, it is the case that most are and hence the equivalence of the time and ensemble averages is known as the ergodic hypothesis [44].

The distribution of an ensemble of phase points within the phase space is termed the phase space probability density. At equilibrium, this is independent of time and is denoted as $f_o(\mathbf{r}^N, \mathbf{p}^N)$. The ensemble average can then be defined as the expectation value of the

observable, $\mathcal{O}(\mathbf{r}^N, \mathbf{p}^N)$, within the ensemble [42, 44]

$$\langle \mathcal{O} \rangle = \int \mathrm{d}\mathbf{r}^N \int \mathrm{d}\mathbf{p}^N \mathcal{O}(\mathbf{r}^N, \mathbf{p}^N) f_o(\mathbf{r}^N, \mathbf{p}^N) \tag{2.2.3}$$

where $f_o(\mathbf{r}^N, \mathbf{p}^N)$, as a probability distribution, also has the property

$$\int \mathrm{d}\mathbf{r}^N \int \mathrm{d}\mathbf{p}^N \; f_o(\mathbf{r}^N, \mathbf{p}^N) = 1 \tag{2.2.4}$$

Statistical mechanics enables the prediction of this phase space probability for a given ensemble, by relating it to the available configurations of the N constituent particles. Each possible configuration, with a given $\mathbf{r}^N$ and $\mathbf{p}^N$, is called a microstate and the fundamental postulate of statistical mechanics is that a system is equally likely to be found in any of these microstates. Microstates with the same energy, E, and number of particles, N, fall within the same macrostate, the probability distribution of which for a given ensemble is given by $f_o(\mathbf{r}^N, \mathbf{p}^N)$. If each microstate is equally likely, then the probability of the system being in a given macrostate is directly related to the number of microstates which fall within that macrostate. It should be noted that the exact number of configurations which belong to a microstate depends on whether the particles are distinguishable. For distinguishable particles, each microstate corresponds to one configuration of particles. However, if the particles are indistinguishable, then for each configuration there are $N!$ possible ways in which the particles could be labelled [39, 43].

An example of a set of properties which define an ensemble is the number of particles, N, volume, V, and temperature, T. Systems which share these properties belong to the canonical ensemble, which is alternatively referred to as the NVT ensemble. This ensemble has proven useful in the formulation of many theories based on statistical mechanics, examples of which are presented throughout this work. Within the canonical ensemble, the system is imagined to exchange only heat with a bulk reservoir and the equilibrium probability distribution is found to take the form [42]

$$f_{NVT}(\mathbf{r}^N, \mathbf{p}^N) = \frac{1}{h^{3N} N!} \frac{e^{-\beta \mathcal{H}}}{Q_N} \tag{2.2.5}$$

where $\beta = (k_\mathrm{B} T)^{-1}$ with k_B as Boltzmann's constant, h is Planck's constant and Q_N is the canonical partition function defined as

$$Q_N = \frac{1}{h^{3N} N!} \int \mathrm{d}\mathbf{p}^N \int \mathrm{d}\mathbf{r}^N e^{-\beta \mathcal{H}} \tag{2.2.6}$$

The partition function acts to normalise the probability distribution and contains complete knowledge of the system in question. The partition function also provides the connection between the microscopic view taken by statistical mechanics and the macroscopic view of thermodynamics through [42]

$$F = -k_\mathrm{B} T \ln Q_N \tag{2.2.7}$$

where F is the Helmholtz free energy as defined in section 2.1. This is the natural free energy

for a canonical system, due to the constraints of constant NVT.

The Hamiltonian given in equation (2.2.1) indicates that the momenta and spatially dependent energy contributions are separable. Substitution of the Hamiltonian into the canonical partition function leads to the simplification [42]

$$\begin{aligned} Q_N &= \frac{1}{h^{3N}N!}\int \mathrm{d}\mathbf{p}^N e^{-\beta K(\mathbf{p}^N)} \int \mathrm{d}\mathbf{r}^N e^{-\beta(\Phi(\mathbf{r}^N)+V_{ext}(\mathbf{r}^N))} \\ &= \frac{1}{h^{3N}N!}\int \mathrm{d}\mathbf{p}_1 e^{-\frac{\beta}{2m}\mathbf{p}_1^2} \dots \int \mathrm{d}\mathbf{p}_N e^{-\frac{\beta}{2m}\mathbf{p}_N^2} \int \mathrm{d}\mathbf{r}^N e^{-\beta(\Phi(\mathbf{r}^N)+V_{ext}(\mathbf{r}^N))} \\ &= \frac{1}{h^{3N}N!}\left(\sqrt{\frac{2m\pi}{\beta}}\right)^{3N} \int \mathrm{d}\mathbf{r}^N e^{-\beta(\Phi(\mathbf{r}^N)+V_{ext}(\mathbf{r}^N))} \\ &= \frac{1}{\Lambda^{3N}N!}\int \mathrm{d}\mathbf{r}^N e^{-\beta(\Phi(\mathbf{r}^N)+V_{ext}(\mathbf{r}^N))} \equiv \frac{Z_N}{\Lambda^{3N}N!} \end{aligned} \tag{2.2.8}$$

where Z_N is termed the configuration integral and $\Lambda = (2\pi\beta\hbar^2/m)^{1/2}$ is the thermal de Broglie wavelength. The thermal de Broglie wavelength provides a boundary for the applicability of classical physics. If the mean separation between particles, a, is much greater than Λ, then the system can be treated classically. All systems considered here meet this requirement [42].

For the study of phase transitions, a more convenient ensemble is the Grand Canonical (GC) ensemble, which is defined as having constant chemical potential, μ, volume, V, and temperature, T, conditions. It is therefore also referred to as the μVT ensemble. Within this ensemble, the system is able to exchange both heat and particles with a bulk reservoir. The GC equilibrium probability density can be found to be [42]

$$f_{\mu VT}(\mathbf{r}^N, \mathbf{p}^N; N) = \frac{e^{-\beta(\mathcal{H}-\mu N)}}{\Xi} \tag{2.2.9}$$

where Ξ, the grand partition function, is defined as

$$\Xi = \mathrm{Tr}_{\mathrm{cl}} e^{-\beta(\mathcal{H}-\mu N)} \tag{2.2.10}$$

and the classical trace, $\mathrm{Tr}_{\mathrm{cl}}$, is defined as [45]

$$\mathrm{Tr}_{\mathrm{cl}} = \sum_{N=0}^{\infty} \frac{1}{h^{3N}N!}\int \mathrm{d}\mathbf{p}^N \int \mathrm{d}\mathbf{r}^N \tag{2.2.11}$$

As before, the Hamiltonian can be separated into its momenta, spatially and now chemically varying components. Doing so leads to the simplified form of [42]

$$\Xi = \sum_{N=0}^{\infty} \frac{e^{\beta\mu N}}{\Lambda^{3N}N!}\int \mathrm{d}\mathbf{r}^N e^{-\beta(\Phi(\mathbf{r}^N)+V_{ext}(\mathbf{r}^N))} \equiv \sum_{N=0}^{\infty} \frac{e^{\beta\mu N}}{\Lambda^{3N}N!} Z_N \tag{2.2.12}$$

The relevant thermodynamic potential for the GC ensemble is the grand potential. As in the case of the canonical ensemble, it is the grand partition function which provides the

connection to macroscopic thermodynamics through [39, 42]

$$\Omega = -k_{\mathrm{B}}T \ln \Xi \tag{2.2.13}$$

Whilst in the canonical ensemble the ensemble average is found using equation (2.2.3), within the GC ensemble, the ensemble average is defined using $\mathrm{Tr}_{\mathrm{cl}}$ [46]

$$\langle \mathcal{O} \rangle = \mathrm{Tr}_{\mathrm{cl}} f_{\mu VT} \mathcal{O} \tag{2.2.14}$$

where $\mathcal{O}$ is an observable, as before.

Within the GC ensemble, the probability of a system having N particles can be expressed as [42]

$$P(N) = \frac{1}{h^{3N} N!} \int \mathrm{d}\mathbf{p}^N \int \mathrm{d}\mathbf{r}^N f_{\mu VT}(\mathbf{r}^N, \mathbf{p}^N; N) \tag{2.2.15}$$

Using this, the canonical and GC ensembles probability densities can be related by [42]

$$\frac{1}{h^{3N} N!} f_{\mu VT}(\mathbf{r}^N, \mathbf{p}^N; N) = P(N) f_{NVT}(\mathbf{r}^N, \mathbf{p}^N) \tag{2.2.16}$$

2.3 Microscopic Descriptions of Structure in Fluids

An example of an observable of interest in the study of fluids is the one-particle density which, for inhomogeneous fluids, is spatially variant. It is obtained by taking the ensemble average of the one-particle density operator, which is defined as [42]

$$\hat{\rho}^{(1)}(\mathbf{r}) = \sum_{j=1}^{N} \delta(\mathbf{r} - \mathbf{r}_j) \tag{2.3.1}$$

Substituting this into the definition of the ensemble average for the GC ensemble, given in equation (2.2.14), gives [42]

$$\langle \hat{\rho}^{(1)}(\mathbf{r}) \rangle = \frac{1}{\Xi} \sum_{j=1}^{\infty} \frac{e^{\beta\mu N}}{\Lambda^{3N}(N-1)!} \int \mathrm{d}\mathbf{r}^{N-1} e^{-\beta(\Phi(\mathbf{r}^N) + V_{ext}(\mathbf{r}^N))} \equiv \rho^{(1)}(\mathbf{r}) \tag{2.3.2}$$

This describes the average density as measured at $\mathbf{r}$. Typically, the superscript is dropped and $\rho^{(1)}(\mathbf{r})$ is written more simply as $\rho(\mathbf{r})$. In the case of a homogeneous fluid, where $V_{ext}(\mathbf{r}) = 0$, the spatial dependence vanishes and $\rho(\mathbf{r}) \to \rho_b$, where ρ_b is the density of the homogeneous bulk fluid [42]. Descriptions of an inhomogeneous fluid are not limited to the one-particle density. For example, the two-particle density can be defined using the operator [42]

$$\hat{\rho}^{(2)}(\mathbf{r}, \mathbf{r}') = \sum_{j=1}^{N} \sum_{k=1}^{N} \delta(\mathbf{r} - \mathbf{r}_j) \delta(\mathbf{r}' - \mathbf{r}_k) \tag{2.3.3}$$

Substitution of this, with $f_{\mu VT}$, into equation (2.2.14) defines the two-particle density as [42]

$$\langle\hat{\rho}^{(2)}(\mathbf{r},\mathbf{r}')\rangle = \frac{1}{\Xi}\sum_{j=2}^{\infty}\frac{e^{\beta\mu N}}{\Lambda^{3N}(N-2)!}\int \mathrm{d}\mathbf{r}^{N-2}e^{-\beta(\Phi(\mathbf{r}^N)+V_{ext}(\mathbf{r}^N))} \equiv \rho^{(2)}(\mathbf{r},\mathbf{r}') \tag{2.3.4}$$

These descriptions of the particle distribution in an inhomogeneous fluid can be extended to three, four, five and more particles, and together form the n-particle densities, defined generally as [42]

$$\rho^{(n)}(\mathbf{r}^n) = \frac{1}{\Xi}\sum_{N=n}^{\infty}\frac{e^{\beta\mu N}}{\Lambda^{3N}(N-n)!}\int \mathrm{d}\mathbf{r}^{(N-n)}e^{-\beta(\Phi(\mathbf{r}^N)+V_{ext}(\mathbf{r}^N))} \tag{2.3.5}$$

The n-particle densities can be interpreted physically as the probability of finding particles at given spatial locations within the fluid. For example, $\rho(\mathbf{r})\mathrm{d}\mathbf{r}$ is the probability of finding a particle at $\mathbf{r}$. Integration over all $\mathbf{r}$ gives the average number of particles within the fluid as [42]

$$\int \mathrm{d}\mathbf{r}\rho(\mathbf{r}) = \langle N\rangle \tag{2.3.6}$$

or more generally

$$\int \mathrm{d}\mathbf{r}^n\rho^{(n)}(\mathbf{r}^n) = \left\langle\frac{N!}{(N-n)!}\right\rangle \tag{2.3.7}$$

Although these have been formulated in the GC ensemble, the canonical equivalent can be found by considering equation (2.2.16). The canonical equivalent of the n-particle densities is therefore [42]

$$\rho^{(n)}_{NVT}(\mathbf{r}^n) = \frac{N!}{(N-n)!}\frac{1}{Z_N}\int \mathrm{d}\mathbf{r}^{(N-n)}e^{-\beta(\Phi(\mathbf{r}^N)+V_{ext}(\mathbf{r}^N))} \tag{2.3.8}$$

Irrespective of the ensemble, the n-particle density is related to the n-particle distribution function as [42]

$$g^{(n)}(\mathbf{r}^n) = \frac{\rho^{(n)}(\mathbf{r}_1,\ldots,\mathbf{r}_n)}{\prod_{j=1}^{n}\rho^{(1)}(\mathbf{r}_j)} \tag{2.3.9}$$

This distribution function describes the deviation of the fluid structure from a random distribution [42]. Of particular importance is the pair distribution function

$$g^{(2)}(\mathbf{r},\mathbf{r}') = \frac{\rho^{(2)}(\mathbf{r},\mathbf{r}')}{\rho(\mathbf{r})\rho(\mathbf{r}')} \tag{2.3.10}$$

In a homogeneous fluid, because of the translational invariance, this reduces to a function of the distance between particles, $g^{(2)}(\mathbf{r},\mathbf{r}') \equiv g^{(2)}(|\mathbf{r}-\mathbf{r}'|)$, which is more simply written as $g(r)$. This special case is termed the radial distribution function and has been used extensively in studies of fluids due to it accessibility in experiment. Physically, the quantity $4\pi r^2\rho_b g(r)$ represents the average number of particles between r and $r+\mathrm{d}r$ from a reference particle. The radial distribution function has the further property that, far from the reference particle where particles become uncorrelated, $g(r)\to 1$ [42].

The density, $\rho(\mathbf{r})$, can also be used to provide a microscopic definition of the adsorption. Considering the latter interface system described in section 2.1, in which the chemical potential was able to take any value, the adsorption, Γ, can be expressed as [40, 42]

$$\Gamma = \int \mathrm{d}\mathbf{r}(\rho(\mathbf{r}) - \rho_b) \tag{2.3.11}$$

where $\rho(\mathbf{r})$ is as defined in equation (2.3.2), and ρ_b is the density of the bulk fluid.

2.4 Phase Transitions

Substances can exist in multiple phases, for example, as a vapour, liquid or solid, the transitions between which are referred to as phase transitions. Such transitions are most easily understood in terms of the Gibb's free energy of the individual phases involved. At a given (T, p), the preferred or stable phase of the substance is the one with the lowest Gibb's free energy per particle. If the phases have equal free energy, then either phase is stable and a phase transition can occur. Considering the definition of the Gibb's free energy in equation (2.1.3), such a situation implies that the chemical potential of each phase is equal. A phase transition can therefore occur only when the phases involved are in thermal, mechanical and chemical equilibrium [39, 42, 47].

Depending on the behaviour of derivatives of the free energy, phase transitions can either be classified as first-order or critical. If the first derivative of the free energy with respect to temperature at the transition is discontinuous, then the transition is termed first-order. The discontinuous derivative of the free energy arises due to a difference in the specific entropy of the phases involved, where the specific entropy is defined as the entropy per particle. A first-order transition in a fluid is therefore associated with the release or absorption of heat, termed the latent heat. First-order transitions are typically accompanied by sudden and dramatic changes in behaviour of the substance [47]. For example, at the liquid-vapour phase transition of water at ambient conditions, the density of liquid water lowers by several orders of magnitude to take the vapour density.

If the first derivative of the free energy is continuous, then a singularity must lie in a higher order derivative, in which case the transition is said to be critical. In contrast to the sudden change of behaviour of a substance at a first-order transition, at a critical phase transition the phases coalesce and distinction between them is no longer possible [47]. Critical phase transitions are accompanied by a wealth of interesting phenomena and are the transition of interest within this work.

2.4.1 Critical Phase Transitions

A well studied example of a critical point is the liquid-vapour critical point of a bulk fluid. This is marked by divergences in the isothermal compressibility, κ_T, defined as [42, 47]

$$\kappa_T = -\frac{1}{V}\left(\frac{\partial V}{\partial P}\right)_T \tag{2.4.1}$$

and in the specific heat capacity, C_V, defined as

$$C_V = \left(\frac{\partial U}{\partial T}\right)_V \tag{2.4.2}$$

On the approach to a critical point, observables such as κ_T and C_V exhibit power law scaling behaviour of single variables. For example, if T_c is the temperature of the critical point and T of the fluid, then on the approach to T_c from below, $\kappa_T \sim (|T - T_c|/T_c)^{-\gamma} \sim |t|^{-\gamma}$, and $C_V \sim |t|^{-\alpha}$, where t is known as the reduced temperature and α, γ are examples of critical exponents [47]. Critical exponents exist for several other observables near to the critical point, some of which will be introduced throughout this work.

In addition to critical exponents, it has been shown that, in the vicinity of a critical point, the singular part of observables can be written as a scaling function of one variable [48]. Such scaling functions are generalised homogeneous functions, which have the property

$$g(\lambda^a u, \lambda^b v) = \lambda g(u, v) \tag{2.4.3}$$

where $g(u, v)$ is a generalised homogeneous function of variables u, v, and λ is an arbitrary function. An example of a property which can be written in such a form is the singular part of the free energy of a fluid which, in the vicinity of the critical point, takes the form [39, 47]

$$\omega_{sing}(\delta\mu, t) = \lambda^{-d}\omega_{sing}(\lambda^a\delta\mu, \lambda^b t) \tag{2.4.4}$$

where $\delta\mu = \mu - \mu_{co}$ is the difference between the chemical potential of the fluid, μ, and the chemical potential at liquid-vapour coexistence, μ_{co}, and d is the dimension of the system. As λ is arbitrary, it can be freely chosen such that $\lambda^b = t^{-1}$ and hence

$$\begin{aligned}\omega_{sing}(\delta\mu, t) &= t^{d/b}\,\omega_{sing}(t^{-a/b}\delta\mu, 1) \\ &= t^{d/b}\,\Sigma\left(\frac{\delta\mu}{t^{a/b}}\right)\end{aligned} \tag{2.4.5}$$

where Σ is called the scaling function and $\delta\mu/t^{a/b}$ the scaling variable. This form of the free energy lends itself to further understanding of the critical exponents. For example, differentiating equation (2.4.5) twice with respect to t, and noting that the derivative of a generalised homogeneous function is also a generalised homogeneous function, allows for a scaling function expression of C_V. Comparing the exponents in this form of C_V to α then gives an expression for α in terms of the exponents a, b. Similarly, the exponent γ can be written in terms of a, b by differentiating equation (2.4.5) twice with respect to μ. In fact, all critical exponents can be written as variables of a, b, and hence all critical exponents can be related to one another [39, 47].

These exponents are of particular importance to the study of critical phenomena as they give rise to the concept of universality. Early experiments showed that many fluids exhibited the same critical exponents, and furthermore that these were the same exponents as those obtained from numerical three dimensional Ising model studies of magnets [47]. This universal

dependence allows the critical behaviour all fluids and three dimensional Ising magnets to be grouped into a universality class, which is called the 3-d Ising class [47]. This is remarkable, considering the very different inter-particle interactions and thermodynamic conditions of the critical point that each fluid exhibits, as well as the significant difference in appearance of magnets and fluids. It has now been determined that the critical exponents, and therefore universality class, to which a system belongs depends on very few features, examples of which include the spatial dimension in which the system exists and the range of interaction between particles [47].

Along with singularities in higher order derivatives of the free energy, a critical phase transition is associated with the onset of long-ranged order, which can be interpreted as all particles within a fluid becoming correlated. If the distance at which two particles are correlated is defined as the correlation length, ξ, then, at a critical phase transition, $\xi \to \infty$. As ξ represents the longest length scale of correlation, all particles with separations smaller than ξ are also correlated, which means that fluctuations on all length scales become important at a critical phase transition [47]. This importance can be observed physically in fluids near to the liquid-vapour critical point, where ξ can be on the order of centimetres, and hence density fluctuations occur on all visible wavelengths of light. Light incident on the fluid is thus scattered strongly, which results in the fluid appearing a milky white colour. This phenomenon is known as critical opalescence [47].

2.4.2 Mean Field Theory

Critical phenomena are vastly interesting, however their study has been hampered by the long-ranged correlations present near the critical point. One theoretical approximation to overcome this is Mean Field Theory (MFT). MFT ignores correlations and fluctuations within a system, such that particles feel only the average interaction of all other particles. MFT is therefore only quantitatively applicable when it is reasonable to consider fluctuations unimportant. The importance of fluctuations can be determined by comparing the free energy of a thermal fluctuation to the average free energy of the system [47]. Near to the critical point, the average energy per unit volume of a thermal fluctuation can be written as [47]

$$\omega_{fluc} \sim \frac{k_B T}{\xi^d} \sim |t|^{d\nu} \tag{2.4.6}$$

where d is the dimension of the system and it has been used that the behaviour of the correlation length on the approach to the critical point can be described by the exponent, ν as $\xi \sim |t|^{-\nu}$. The average singular part of the free energy per unit volume of the system can be found by integrating the specific heat capacity twice [47]

$$\omega_{sing} \sim |t|^{2-\alpha} \tag{2.4.7}$$

where α is the specific heat capacity critical exponent. For thermal fluctuations to be considered unimportant, $\omega_{fluc} \ll \omega_{sing}$ and hence [47]

$$d > \frac{2-\alpha}{\nu} \tag{2.4.8}$$

The right hand side of this can be defined as the upper critical dimension, d^*, of the system [47]. If the dimension of the system is greater than the upper critical dimension, $d > d^*$, then fluctuations can be considered unimportant and MFT can be used to make both quantitative and qualitative predictions of the critical behaviour of the system. In contrast, if $d < d^*$, then MFT can provide only a qualitative understanding of the critical behaviour of the system [47].

2.4.3 Mean Field Theory Approximation for Fluids

It is widely agreed that the short-ranged structure of a fluid is dominated by the packing of particles, a result of their finite volume, whilst the role of attractions is largely to bind the particles into a condensed phase [42]. Under such a description, fluids can be regarded as consisting of purely repulsive particles which are subject to a purely attractive background potential. This is the same description that was originally suggested by van der Waals [42] and represents a MFT approximation for fluids.

Such a description can be realised using perturbation theory. Consider two particles located at $\mathbf{r}$ and $\mathbf{r}'$ respectively. The interaction between them, $\phi_\lambda(\mathbf{r}, \mathbf{r}')$, can be written as the sum of a purely repulsive reference potential, $\phi_o(\mathbf{r}, \mathbf{r}')$, and a weak purely attractive perturbation potential, $\phi_{att}(\mathbf{r}, \mathbf{r}')$. The strength of the perturbation is controlled by the parameter λ. When $\lambda = 0$, there is no perturbation and hence $\phi_\lambda(\mathbf{r}, \mathbf{r}') = \phi_o(\mathbf{r}, \mathbf{r}')$. Conversely, when $\lambda = 1$, $\phi_\lambda(\mathbf{r}, \mathbf{r}') = \phi_o(\mathbf{r}, \mathbf{r}') + \phi_{att}(\mathbf{r}, \mathbf{r}')$ and hence the full effect of the perturbation is felt. Assuming λ varies smoothly between 0 and 1, the perturbative potential between the particles can be written as [39, 42]

$$\phi_\lambda(\mathbf{r}, \mathbf{r}') = \phi_o(\mathbf{r}, \mathbf{r}') + \lambda\phi_{att}(\mathbf{r}, \mathbf{r}') \qquad 0 \leq \lambda \leq 1 \tag{2.4.9}$$

and the potential energy felt between all particles as

$$\Phi_\lambda = \sum_{j=1}^{N} \sum_{k>j}^{N} \phi_\lambda(\mathbf{r}_j, \mathbf{r}_k) \tag{2.4.10}$$

Working within the canonical ensemble, and assuming the fluid is not subjected to an external potential, equation (2.2.7) can be used to determine the derivative of the excess Helmholtz free energy of the fluid [39, 42]

$$\begin{aligned} \frac{\partial(\beta F_{ex})}{\partial\lambda} &= -\frac{1}{Z_N}\frac{\partial Z_N}{\partial\lambda} \\ &= \frac{\beta}{2}\int \mathrm{d}\mathbf{r} \int \mathrm{d}\mathbf{r}' \int \mathrm{d}\mathbf{r}^{N-2} \frac{N!}{(N-2)!}\frac{e^{-\beta\Phi_\lambda}}{Z_N}\phi_{att}(\mathbf{r}, \mathbf{r}') \\ &= \frac{\beta}{2}\int \mathrm{d}\mathbf{r} \int \mathrm{d}\mathbf{r}' \rho_\lambda^{(2)}(\mathbf{r}, \mathbf{r}')\phi_{att}(\mathbf{r}, \mathbf{r}') \end{aligned} \tag{2.4.11}$$

where Z_N represents the configuration integral and the λ subscript represents that $\rho_\lambda^{(2)}(\mathbf{r}, \mathbf{r}')$ is the two-particle density of the fluid subjected to the perturbed potential. Integrating this

with respect to λ gives

$$\beta F_{ex} = \beta F_o + \frac{\beta}{2}\int_0^1 \mathrm{d}\lambda \int \mathrm{d}\mathbf{r} \int \mathrm{d}\mathbf{r}' \rho_\lambda^{(2)}(\mathbf{r},\mathbf{r}')\phi_{att}(\mathbf{r},\mathbf{r}') \tag{2.4.12}$$

where the integration constant, βF_o, can be recognised as the excess Helmholtz free energy of a fluid subjected only to the reference potential, referred to here as the reference fluid.

The two-particle density can be expanded in powers of λ about $\lambda = 0$. To a first order approximation, equation (2.4.12) then reduces to [39, 42]

$$\beta F_{ex} = \beta F_o + \frac{\beta}{2} \int \mathrm{d}\mathbf{r} \int \mathrm{d}\mathbf{r}' \rho_o^{(2)}(\mathbf{r},\mathbf{r}')\phi_{att}(\mathbf{r},\mathbf{r}') \tag{2.4.13}$$

where the integration over λ has been performed and $\rho_o^{(2)}(\mathbf{r},\mathbf{r}')$ is the two-particle density of the reference fluid. Physically, this represents that the structure of the fluid is assumed to be unaltered by perturbations [42].

2.4.4 Liquid-Vapour Phase Transitions

Using equation (2.3.10), $\rho_o^{(2)}(\mathbf{r},\mathbf{r}')$ can be written as a function of the pair distribution function. In a bulk fluid, the one-particle density has no spatial dependence and hence $\rho_o^{(2)}(\mathbf{r},\mathbf{r}')$ can be further simplified to $\rho_o^{(2)}(\mathbf{r},\mathbf{r}') \to \rho_b^2 g_o(r)$ where ρ_b is the homogeneous bulk density [45]. Substituting this into equation (2.4.13) then gives [42]

$$\frac{\beta F_{ex}}{N} = \frac{\beta F_o}{N} + \frac{\beta\rho_b}{2} \int \mathrm{d}\mathbf{r}\phi_{att}(\mathbf{r}) g_o(r) \tag{2.4.14}$$

where r represents the distance between particles and N the number of particles. MFT ignores correlations, hence the pair distribution function is $g_o(r) \approx 1$. This is a valid assumption if the range of $\phi_{att}(\mathbf{r})$ is much larger than the range of inter-particle separations over which $g_o(r)$ is expected to vary significantly from the bulk value [42]. An example of such a situation is if the reference potential is taken to be the hard-sphere potential and the attraction to have the form of a long-ranged inverse power law [42]. Using this simplification, the excess Helmholtz free energy per particle, $\tilde{f}_{ex} = F_{ex}/N$, can be written as [42]

$$\beta\tilde{f}_{ex} = \beta\tilde{f}_o - \beta a\rho_b \qquad \text{where} \qquad a = -\frac{1}{2}\int \mathrm{d}\mathbf{r}\phi_{att}(\mathbf{r}) \tag{2.4.15}$$

where $\tilde{f}_o$ is the excess Helmholtz free energy per particle of the reference fluid. Differentiation of this gives the equation of state

$$p_{ex} = -\left(\frac{\partial F_{ex}}{\partial V}\right)_{T,N} = \rho_b^2 \left(\frac{\partial \tilde{f}_{ex}}{\partial \rho_b}\right)_{T,N} = p_o - a\rho_b^2 \tag{2.4.16}$$

where p_o is the pressure of the reference fluid and is a function of ρ_b. If the reference potential is taken to be that of hard-spheres, this recovers van der Waals original equation of state [42].

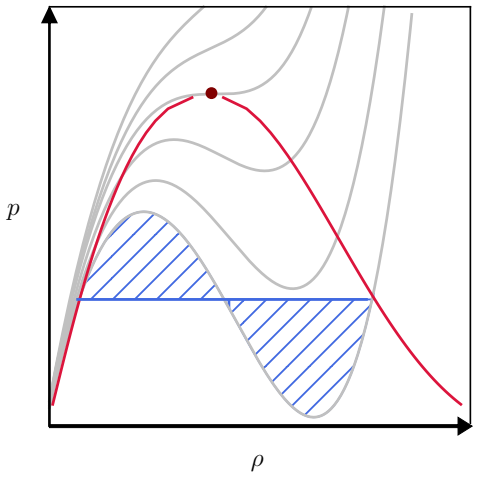

Figure 2.1: Illustration of construction of the bulk liquid-vapour phase diagram for a van der Waals fluid. The grey lines represent the pressure isotherms determined from the equation of state. Nonphysical parts of the isotherms are removed using a Maxwell construction, shown in blue. The final coexistence curve is shown in red. The critical point marks the inflection point of the critical isotherm and is represented by the red point.

Similarly, an expression for the chemical potential can be found using

$$\mu_{ex} = \left(\frac{\partial F_{ex}}{\partial N}\right)_{T,V} = \left[\rho_b \left(\frac{\partial \tilde{f}_{ex}}{\partial \rho_b}\right)_{T,V} + \tilde{f}_{ex}\right] = \mu_o - 2a\rho_b \tag{2.4.17}$$

where μ_o is the chemical potential of the reference fluid.

Plotting the pressure isotherms for equation (2.4.16) for an appropriate reference and attractive potential leads to figure 2.1 [39, 42, 47]. Three types of isotherm can be identified. When $T < T_c$, the isotherms exhibit both a peak and a trough and, for a portion of the isotherm, multiple densities exhibit the same pressure. The latter behaviour is indicative of a first-order phase transition. When $T > T_c$, the isotherms are smoothly increasing functions of the density, indicating a supercritical fluid. Finally, the isotherm which corresponds to $T = T_c$, termed the critical isotherm, exhibits a single point of inflection [39, 42, 47].

For phase stability, $\kappa_T > 0$, which can be seen to be violated between the peaks and troughs of isotherms below T_c [42]. This unstable portion is characteristic of MFT and can be removed using a Maxwell construction, which graphically represents the phase coexistence condition that the pressure and chemical potential be equal in each phase. This construction involves locating the line between the two stable phases, for which the area above, in the case of the peak, and below, in the case of the trough, are equal [39, 42, 47]. An example of such a construction is shown by the solid blue line and blue hatched areas in figure 2.1. The intersection points of the isotherm and Maxwell construction in the stable phases can then be used to define the coexistence curve of first-order phase transitions, which is indicated by the red solid line in figure 2.1.

In addition to removing the unstable portion of the isotherm, the Maxwell construction also removes a stable portion, which occurs between the intersection of the Maxwell con-

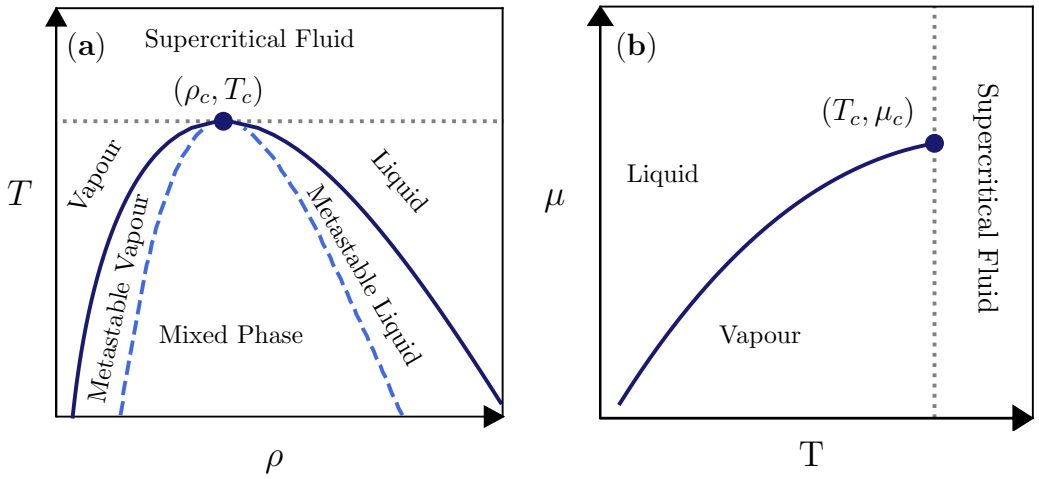

Figure 2.2: Examples of bulk phase diagrams relevant within this work. (a) Example of the density-temperature phase diagram, with phases indicated. The horizontal grey dotted line represents the critical temperature. The dark blue solid line represents the curve of first-order liquid-vapour phase transitions, whilst the light blue dashed lines represent the spinodals. The critical point is given by the dark blue point. (b) Example of the chemical potential - temperature phase diagram, with phases labelled. The vertical grey dotted line represents the critical temperature, whilst the dark blue solid line represents the first-order liquid-vapour transitions. The critical point is given by the dark blue point.

struction with the isotherm and the peak and trough. It was suggested by van der Waals that such regions represented metastable states [39]. These are states which do not represent the minimum free energy phase, but can be accessed under certain conditions. Due to their instability, any perturbation will nucleate the stable, lower free energy phase [39]. The peaks and troughs of the van der Waal loops can therefore be used to define the spinodals, which represent the boundary to which the metastable state can be accessed. However, it should be noted that these are an artefact of MFT, and do not typically exist in real fluids.

The critical point can be identified by locating the stationary point on the critical isotherm using the conditions [39, 42, 47]

$$\left(\frac{\partial p}{\partial \rho_b}\right)_{T=T_c} = 0 \qquad \left(\frac{\partial^2 p}{\partial \rho_b^2}\right)_{T=T_c} = 0 \tag{2.4.18}$$

The first condition ensures that κ_T diverges at the critical point, whilst the second ensures the gradient of the isotherm at the critical point is horizontal [42].

Using the Maxwell construction and the conditions for the critical point, the phase diagram of a MFT fluid can be obtained, the key features of which are given in figure 2.2. Phase diagrams can be constructed for any combination of parameters however, for the purpose of this work, the most pertinent are the $\rho - T$ and $T - \mu$ phase diagrams. It should be noted that, due to its simplicity, the MFT approximation for a fluid is only capable of describing the liquid and vapour phases. Real fluids can typically exist in many additional phases, such as solids, and hence phase diagrams for real fluids such as water are typically far more complex.

2.4.5 Wetting and Drying Phase Transitions

Consider a droplet of water on a surface, as shown in figure 2.3. Depending on the character of the surface, the droplet may be rounded or flat. This property can be quantified by considering the contact angle the droplet makes with the surface, denoted as θ, and an expression for θ can be derived by resolving the surface tension components of the three interfaces [49]. Doing so leads to Young's equation [41, 49, 50]

$$\cos\theta = \frac{\gamma_{sv} - \gamma_{sl}}{\gamma_{lv}} \tag{2.4.19}$$

where γ_{sv}, γ_{sl} and γ_{lv} are the surfaces tensions of the surface-vapour, surface-liquid and liquid-vapour interfaces respectively, and are as shown in figure 2.3. The contact angle a droplet of water makes with a surface provides a definition for the affinity of the surface and water. Surfaces which have low affinity with water make obtuse contact angles, such that $90° < \theta < 180°$ and are termed hydrophobic. Similarly, surfaces which have high affinity with water make acute contact angles, such that $0° < \theta < 90°$, and are termed hydrophilic.

From the definition of the contact angle, two interesting cases relating to $|\cos\theta| = 1$ arise. In the first case, where $\cos\theta = 1$ and therefore $\theta = 0°$, the droplet of water completely covers the surface and Young's equation reduces to $\gamma_{sl} = \gamma_{sv} - \gamma_{lv}$. In the second case, where $\cos\theta = -1$ and therefore $\theta = 180°$, the droplet of water forms a perfect sphere which is no longer in contact with the surface. In this case, Young's equation reduces to $\gamma_{sl} = \gamma_{sv} + \gamma_{lv}$. The approach to these cases correspond to surface phase transitions, termed wetting and drying respectively, and represent the formation of a macroscopic layer of liquid or vapour at the surface [41, 49, 50].

The reasoning behind such a phase transition was first presented by Cahn [51], whose argument was based on the scaling of these surface tensions on the approach to the critical point of the bulk fluid. Cahn noted that, as T_c is approached from below, the liquid-vapour surface tension vanishes as $\gamma_{lv} \sim (-t)^{\mu}$, where t is the reduced temperature as defined in section 2.4.1 and $\mu = (d-1)\nu$ is a critical exponent [50, 51]. For a fluid, $d = 3$ and $\nu \approx 0.63$ [47], therefore the critical exponent $\mu \approx 1.26$. In addition, Cahn argued that $\gamma_{sv} - \gamma_{sl}$ should also vanish, as the liquid and vapour cease to be distinguishable at the bulk critical point.

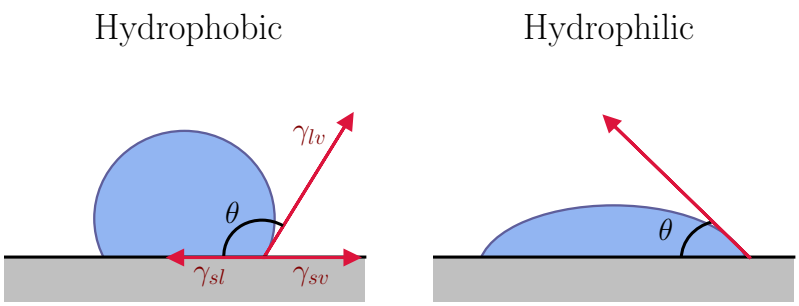

Figure 2.3: Droplet of water on a surface. If the surface is hydrophobic, the contact angle the droplet makes with the surface, θ, will be obtuse. If the surface is hydrophilic, θ will be acute. The contact angle can be found by resolving the three surface tensions within the system, indicated by the arrows and denoted as γ.

The similarity of the liquid and vapour phases in a near-critical fluid can be quantified by the order parameter $(\rho_l - \rho_v)$, which is known to vanish as $(\rho_l - \rho_v) \sim (-t)^\beta$ on the approach to T_c, where $\beta \approx 0.33$ for a bulk fluid [47]. Following Cahn's argument, the contact angle should therefore vanish as $\cos\theta \sim (-t)^{\beta-\mu} = t^{-0.93}$, which implies a divergence of $\cos\theta$ on the approach to T_c. However, the contact angle is constrained to values of $|\cos\theta| \leq 1$ and hence Cahn argued that there must exist a temperature, $T_W < T_c$, corresponding to $\cos\theta = 1$, for which the system undergoes a surface phase transition where the water fully wets the surface and after which the contact angle remains equal to 0° [51]. Similarly, in the case that $\cos\theta = -1$, a temperature $T_D < T_c$ must exist in which a vapour fully wets the surface.

Around the same time Cahn made his thermodynamic argument, Ebner and Saam [52] provided numerical evidence for a surface phase transition by considering a model of an argon gas in contact with a solid CO_2 surface. At low temperatures, a thin liquid film of argon was found to form at the CO_2 surface. Upon raising the temperature, this thin adsorbed film suddenly transformed to a thick adsorbed film, in a surface phase transition now referred to as prewetting. Their results proved controversial, with subsequent numerical and simulation studies finding no evidence of such a transition [53, 54]. It was suggested that these discrepancies were due to the parameters at which Ebner and Saam had found the transition, as a later study using a similar method that found such a transition reported it to be at a much higher temperature and far closer to liquid-vapour coexistence [55].

Subsequent studies on wetting were also subject to much debate, particularly in regards to its nature. Cahn's original thermodynamic argument suggested that wetting was a first-order transition [51], evidence for which was provided in simulation studies of lattice gas models [56, 57]. In contrast, a microscopic theory of wetting based on a MFT van der Waals model of fluids by Sullivan [58] found that wetting was instead a critical phase transition. Later studies showed both types of wetting phase transition were possible [59, 60], and that the exact nature of the transition was strongly dependent on the comparative strengths of the substrate-fluid (sf) and fluid-fluid (ff) interactions, as well as the range over which each interaction extended [59–61]. These early studies focused almost exclusively on the case of wetting, as drying was viewed as the wetting of a surface by a vapour and therefore any arguments made for wetting were believed to be generally applicable to drying too [49, 58, 62]. Lattice gas studies took this idea further, as the particle-hole symmetry directly implied that wetting and drying were equivalent provided that the bulk fluid was replaced by a liquid in the latter and that the film formed was a vapour [61].

Whilst from a phenomenological perspective, wetting and drying are similar [49], it is now appreciated that they are distinct and that their nature may differ for a given substrate and fluid [1, 38]. As this work is concerned with hydrophobicity and therefore drying, the phenomenology is presented from this perspective, however replacing the drying temperature, T_D, with the wetting temperature, T_W, the bulk liquid with a bulk vapour, a vapour film with a liquid film and an oversaturation with an undersaturation in any of the following arguments will recover wetting, as presented in texts such as [41, 49, 50].

Consider a bulk liquid, of density ρ_l, in contact with an impenetrable substrate. If the

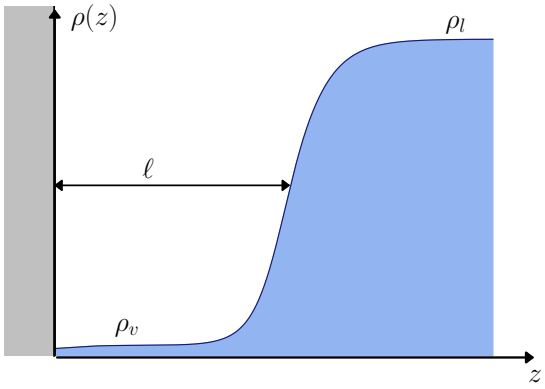

Figure 2.4: Illustration of the behaviour of a fluid, shown in blue, in contact with an impenetrable substrate, shown in grey. Near to drying, a film of vapour, of width ℓ, forms at the surface. Here, ρ_l represents the density of the fluid, at coexistence, in its liquid phase, whilst ρ_v represents the density of the fluid, at coexistence, in its vapour phase.

liquid is at coexistence with its vapour phase, of density ρ_v, a film of vapour may form at the surface of the substrate [41, 49, 50]. Such a system is shown in figure 2.4, where the width of the vapour film is denoted by ℓ. The adsorption of such a system can be found using equation (2.3.11), and will be of magnitude $\Gamma \approx -\Delta\rho\ell A_{sv}$, where $\Delta\rho = (\rho_l - \rho_v)$ and A_{sv} is the surface area of the substrate-vapour interface. The adsorption can in fact be used to define the width of the film as [49]

$$\ell \equiv \frac{-\Gamma}{A_{sv}\Delta\rho} \tag{2.4.20}$$

If the system is at equilibrium, this also provides a definition for the equilibrium film width, denoted as ℓ_{eq}.

Below T_D, the vapour film is microscopic, and hence ℓ_{eq} is finite. However, as T_D is approached from below, the equilibrium width of the film grows and exactly at T_D, drying

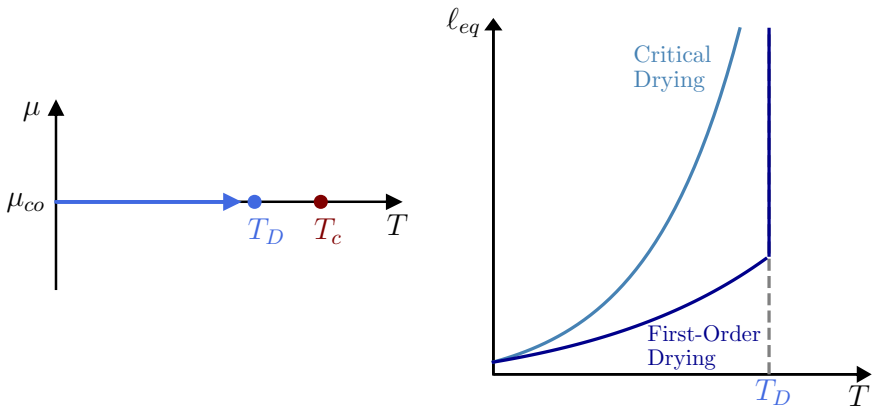

Figure 2.5: Examples of the behaviour of the equilibrium film width, ℓ_{eq}, on the approach to the drying surface phase transition. Left: Illustration of path within parameter space corresponding to the approach to critical drying. Right: If the transition is critical, as T_D is approached from below at coexistence, ℓ_{eq} will grow to a macroscopic width continuously. If the transition is first-order, then at T_D, ℓ_{eq} will jump discontinuously to a macroscopic film width. Note, the diagram on the left is purely illustrative, and does not reflect the true shape of the coexistence curve.

occurs. The vapour film then becomes macroscopic, which corresponds to the equilibrium film width becoming $\ell_{eq} = \infty$. This transition from a microscopic to macroscopic film width can either be first-order or critical. If first-order drying occurs, then ℓ_{eq} becomes macroscopic discontinuously. If the transition is instead critical, the growth of ℓ_{eq} is smooth and exactly at T_D, ℓ_{eq} diverges [41, 49, 50]. Each of these cases can be seen in figure 2.5.

If the fluid exhibits a small oversaturation, which corresponds to $\mu > \mu_{co}$, then even as T_D is approached, the vapour film will remain finite [50]. If the drying transition is first-order, then it is possible for the fluid to undergo a different but related surface phase transition, called predrying, in which the vapour film transitions from a thin to thick width. These transitions are first-order, and their magnitude depletes as the oversaturation is increased. The locus of predrying transitions allows for the definition for the predrying line on the phase diagram. This terminates in a critical point, termed the predrying critical point, at which the transition between the thin and thick film widths becomes a smooth, rounded point of inflection [49, 50, 60].

In addition to first-order, critical and predrying, there exists one other way in which the vapour film may become macroscopic, which is termed complete drying. Complete drying specifically refers the divergence of the vapour film width as μ_{co} is approached from an oversaturation, for temperatures $T_D \leq T < T_c$, and is always a continuous transition. The definition of complete drying also allows for the definition of incomplete drying. This refers to the microscopic nature of the film width, if μ_{co} is approached from an oversaturation, however for $T < T_D$ [50].

Examples of predrying, incomplete and complete drying can be seen in figures 2.6 and 2.7. Path (a) in figure 2.6 indicates predrying, as T is increased. Path (b) and (c) in figure 2.7 indicate incomplete and complete drying respectively. Path (d) in figure 2.7 indicates both predrying and complete drying, with a thin to thick film width transition occurring first, followed by a divergence in the film width as μ_{co} is approached.

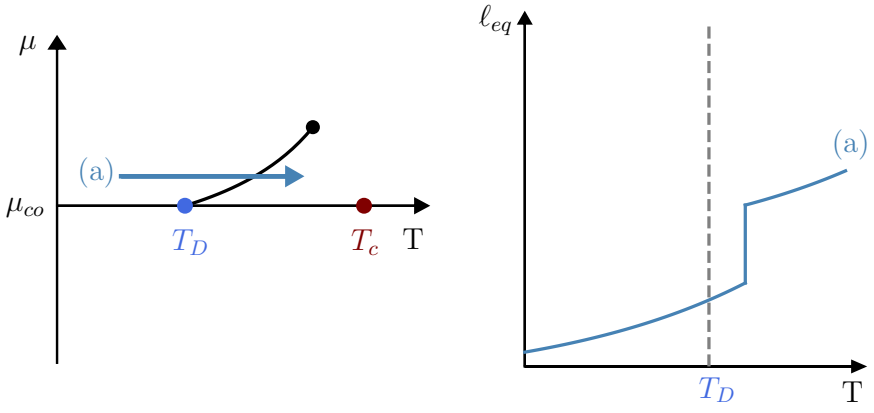

Figure 2.6: Illustration of the behaviour of ℓ_{eq} if predrying occurs. If the fluid has a small oversaturation, it is possible that, at a temperature $T > T_D$, it will undergo a phase transition from a thin to a thick film width. This is known as predrying. The predrying line extends from T_D at the coexistence line, and terminates in a critical point. Note, the diagram on the left is purely illustrative, and does not reflect the true shape of the coexistence curve.

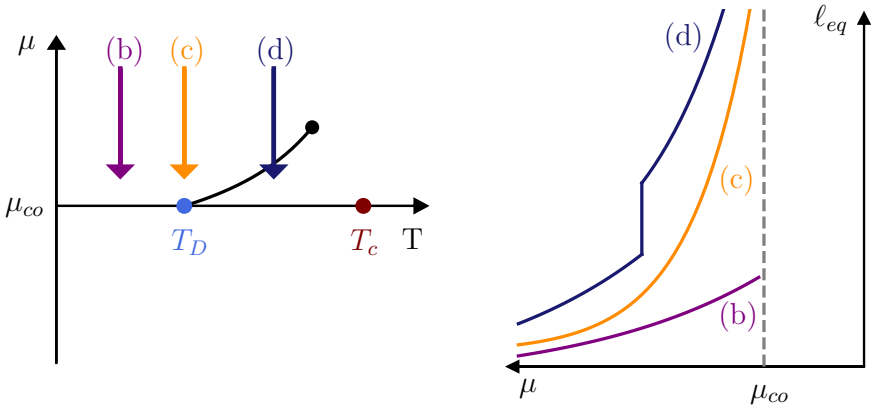

Figure 2.7: Illustration of the behaviour of ℓ_{eq} (right) along different isotherms (left), as μ_{co} is approached from above. Below T_D, indicated by (b), the vapour film grows, but remains microscopic. Exactly at T_D, indicated by (c), the equilibrium film width diverges continuously as μ_{co} is approached, in a transition termed complete drying. Above T_D, as indicated by (d), two transitions may occur. As the isotherm crosses the predrying line, the vapour film width will transition discontinuously from a thin to a thick width. Then, as μ_{co} is approached, the equilibrium film width will diverge continuously. Note, the diagram on the left is purely illustrative, and does not reflect the true shape of the coexistence curve.

As was appreciated early in the study of wetting and drying, the order of the drying transition is determined by factors such as the relative strengths of the sf interaction, denoted ε_{sf}, and ff interaction, denoted by ε, and the range of such interactions [59–61]. The latter can be classified broadly as short-ranged (SR), which are typically exponential or finite ranged in nature, or long-ranged (LR), which are typically inverse power law in nature. Only recently have the orders of wetting and drying for various combinations of these been mapped out fully [38]. Figure 2.8 presents the current understanding of the nature of each combination. Notably, in many cases, drying is a critical surface phase transition, whilst wetting is first-order. This is specifically true for the typical interactions found in simulation (SR ff LR sf) and in experiment (LR ff LR sf). As predrying can only occur in systems which undergo first-order drying, this has the consequence that predrying is not normally possible.

The order of the wetting and drying transitions can be determined from the behaviour of $\cos\theta$ on the approach to the transition, as $\varepsilon_{sf}/\varepsilon$ is varied. Figure 2.9 shows this for the case of SR ff LR sf interactions. $\cos\theta = -1$ is approached tangentially, indicating a smooth divergence and therefore a critical drying transition. In contrast, $\cos\theta = 1$ is met with a discontinuous slope, indicating a discontinuous change in film width and therefore a first-order wetting transition [38].

Our current understanding of wetting and drying has mostly come about through MFT theoretical [51, 52, 60, 61], numerical [38] and simulation [56, 57] studies, and to date there is little experimental evidence confirming the orders and behaviours of these transitions. Of the studies which exist, most have utilised hydrocarbons in contact with a liquid surface, and have explored wetting transitions [63–67]. Despite the different type of surface, the physics remains the same and such studies have reported evidence of first-order wetting [64, 65], critical wetting [63, 65–67] and prewetting [66, 67].

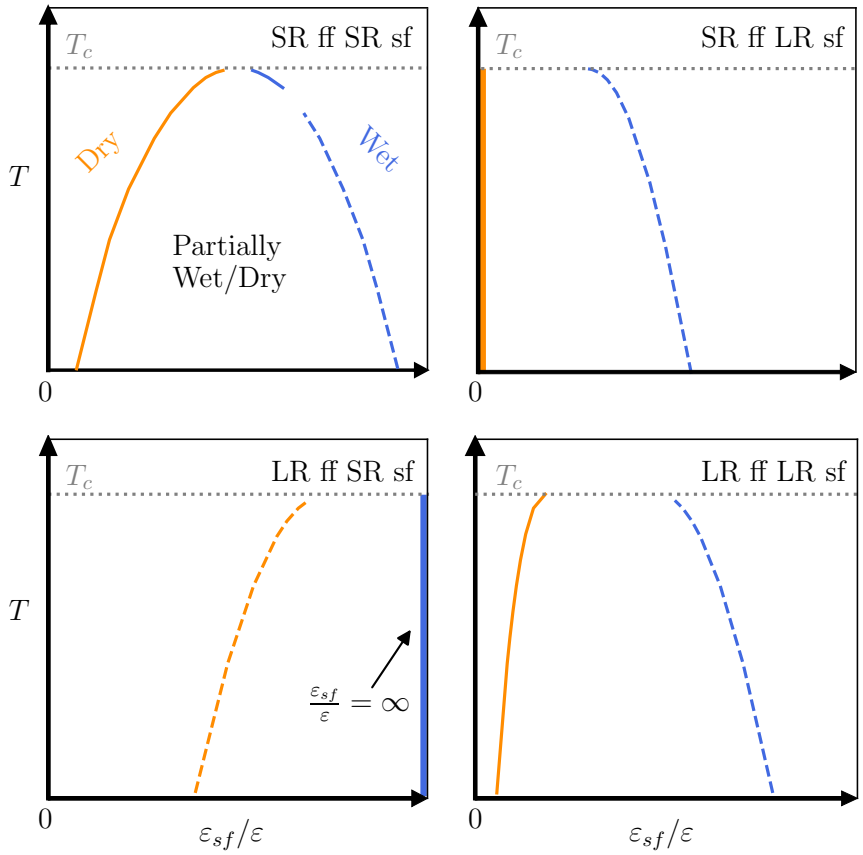

Figure 2.8: Surface phase diagrams for systems with different combinations of short-ranged (SR) and long-ranged (LR) fluid-fluid (ff) and substrate-fluid (sf) interactions. In each case, the horizontal dotted grey line represents the critical temperature. Drying transitions are indicated in dark orange, whilst wetting transitions are indicated in light blue. Solid transition lines represent critical transitions, whilst dashed transition lines represent first-order transitions. In the case of SR ff SR sf interactions, the possible states of the system are labelled.

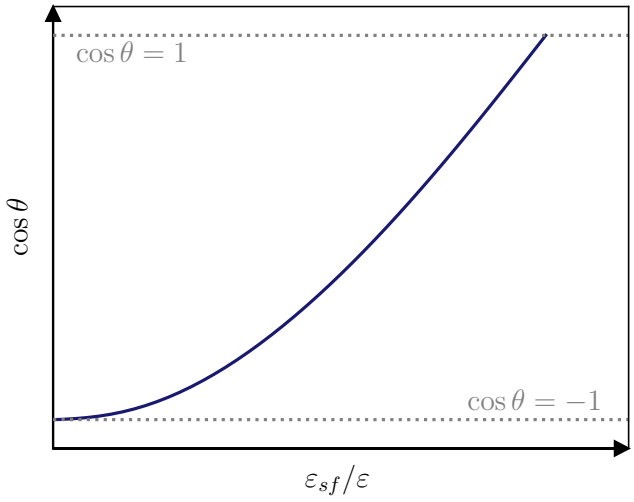

Figure 2.9: Examples of the variation of $\cos\theta$ with $\varepsilon_{sf}/\varepsilon$ for a system with SR ff LR sf interactions. The critical drying transition is indicated by the tangential approach to $\cos\theta = -1$. In contrast, the first-order wetting transition is indicated by the discontinuous slope on the approach to $\cos\theta = 1$.

2.4.6 Beyond Mean Field Theory

Whilst MFT has proven highly successful for understanding qualitatively the physics underlying critical phenomena, it is limited in its quantitative predictions due to its failure to account for fluctuations which become important when $d < d^*$. For a bulk fluid, $d^* = 4 > d$, and hence MFT has limited applicability in understanding critical phenomena in bulk fluids [47].

If fluctuations are considered important, alternative methods of study must be applied. One such method used within this work is molecular simulation. Simulations of fluids are able to account for fluctuations, as they consider the individual microscopic interactions between particles as opposed to a general underlying averaged potential. However, simulations also struggle to provide accurate quantitative results for the study of phase transitions. Large free energy barriers present between phases at a first-order phase transition can prevent transitions between phases [68]. Near critical phase transitions, the diverging correlation length becomes constrained by the size of the simulation box and properties such as κ_T fail to diverge, instead exhibiting rounded peaks. These latter behaviours are called finite size (FS) effects and further lead to phenomena such as the apparent simulation box size dependence of the critical temperature [39, 68].

FS effects can also influence simulations of surface critical behaviour however, in contrast to the bulk case, it is the component of the correlation length parallel to the surface, $\xi_{||}$, which drives these [69]. This diverges far faster than the perpendicular component, and has been shown in studies of drying to lead to the formation of a 'bubble' which covers the entire surface [1]. This may then detach from the surface and cause the system to fill with vapour, essentially becoming dry, before the critical drying transition is reached. Such a phenomenon has been termed premature drying [1]. Considering these behaviours, it is evident that great care must be taken when interpreting results involving critical phase transitions obtained from simulations.

A second alternative method which does not suffer from such effects is Renormalization Group (RG) Theory. This method utilises the scale invariance of the critical point to identify, among other properties, the critical exponents of a system. A RG treatment involves the repeated application of a renormalization transformation to the Hamiltonian, which successively removes degrees of freedom of the system, whilst leaving the underlying partition function unchanged. Only at the critical point where fluctuations are present on all length scales will such a transformation have no effect, and hence it is possible to identify the critical point and its properties, by finding such a case. In addition to its applications for finding the critical point and critical exponents, RG theory also gives a theoretical basis for the scaling function forms presented in section 2.4.2. RG theory has proven an invaluable tool for the study of critical points where $d < d^*$ [47]. A particularly important example of an RG theory for the bulk fluid is Hierarchical Reference Theory [70].

2.5 Measures of Local Density Fluctuations

As discussed in section 2.4.1, a critical point is accompanied by large fluctuations which, for a bulk fluid, can be quantified using κ_T. A surface critical point is also expected to exhibit enhanced density fluctuations however, in contrast to the bulk fluid critical point, these fluctuations are expected to be localised to the surface. As such, it is necessary to have a well defined measure of these local density fluctuations.

One such measure, which is of particular use in the GC ensemble, is the local compressibility as proposed by Evans and Stewart [37], which is defined as

$$\chi_\mu(\mathbf{r}) = \left(\frac{\partial\rho(\mathbf{r})}{\partial\mu}\right)_{T,V} \tag{2.5.1}$$

Compared to κ_T, $\chi_\mu(\mathbf{r})$ gives an indication of the spatial variation of density fluctuations. It also maintains the nice property that, in the bulk limit, $\chi_{\mu,b} \to \rho_b^2\kappa_T$ [1]. $\chi_\mu(\mathbf{r})$ has been utilised in several previous studies of wetting and drying [1, 23, 32], where it has been found to be a highly sensitive measure of fluctuations induced by a critical drying transition.

Recently, it was shown that the local compressibility is in fact just one of three possible measures of fluctuations which are present in GC systems [71]. The two other measures are the local thermal susceptibility, $\chi_T(\mathbf{r})$, and the reduced density $\chi_*(\mathbf{r})$, which are defined as

$$\chi_T(\mathbf{r}) = \left(\frac{\partial\rho(\mathbf{r})}{\partial T}\right)_{\mu,V} \tag{2.5.2}$$

$$\chi_*(\mathbf{r}) = \rho(\mathbf{r}) - T\chi_T(\mathbf{r}) - \mu\chi_\mu(\mathbf{r}) \tag{2.5.3}$$

Together, these three measures can be interpreted as describing the chemical ($\chi_\mu(\mathbf{r})$), entropic ($\chi_T(\mathbf{r})$) and energetic ($\chi_*(\mathbf{r})$) fluctuations within a system [71]. In addition, these measures can each be rewritten as a covariance, which can be convenient for simulation studies [1, 71].

Chapter 3

Views of Hydrophobicity

Hydrophobicity plays a crucial role in a variety of biological, chemical and physical processes. For example, protein folding is facilitated by the unfavourable interactions between water molecules and hydrophobic areas on the surface of the protein [72, 73]. Aggregation of amphiphilic molecules into mesoscopic structures, an essential property for detergents, is enabled by the molecule's hydrophobic components [5]. Self-cleaning mechanisms of leaves, which efficiently remove harmful spores and bacteria from plants, rely on water forming rounded droplets with low surface adhesion, which is possible only because of the hydrophobicity of the surface [2, 74].

Despite the ubiquity of hydrophobicity, its exact definition and signatures are vague. On the macroscopic scale, hydrophobicity is understood in terms of the behaviour of water droplets [19, 75], whilst on microscopic length scales, in terms of solvation [5]. Simulation studies have reported enhanced water density around some hydrophobic solutes and a reduced density around others [22]. Hydrophobic solutes also appear to influence the orientation of nearby water molecules, however exactly how seems to depend on the nature of the solute [10, 15, 16]. Terminology to describe hydrophobicity also varies, with descriptions such as force [72], effect [7, 9, 76], and hydration [31, 77] used interchangeably. Terms such as hydrophobic interaction are also used, but are typically reserved for the context of aggregation of hydrophobic solutes [5, 6].

Hydrophobicity clearly operates on a variety of length scales and varies in form between them. However, the connection between the manifestations present on each of these length scales has remained elusive. One commonality between hydrophobicity on all length scales greater than 1 nm is the observation of enhanced density fluctuations, not present at equivalent hydrophilic surfaces [23, 28, 29, 31, 73]. Similar density fluctuations reported at macroscopic hydrophobic surfaces have been speculated to arise due to a critical drying surface phase transition [23], the nature of which was described in section 2.4.5. It is therefore pertinent to ask whether such a surface critical point could influence microscopic hydrophobicity and perhaps whether the density fluctuations observed around microscopic hydrophobic solutes are remnants of those observed around macroscopic hydrophobic surfaces, believed to arise due to critical drying.

Whilst the precise nature and underlying physics of hydrophobicity remains to be determined, great progress has been made in identifying factors which influence the behaviour of water molecules around hydrophobic substrates and solutes. Variation in thermodynamic conditions [78, 79], surface chemistry and topology [19, 80], and solute size [6, 7, 77] have been found to alter water's hydrophobic response. Such factors have also been found to influence the solvophobic response of a variety of fluids, including the Lennard-Jones [1, 8, 81, 82], Jagla [35] and n-Octane [36] fluids. Furthermore, similar thermodynamic behaviour has been observed in hydrophobic and solvophobic systems, for example, in the dependence of the free energy of solvation on size of solute [35, 83]. Such correspondence between hydrophobicity and solvophobicity casts doubt as to whether the former should be regarded as a unique interaction, or whether it should be treated as simply a special case of solvophobicity.

The purpose of this chapter is to present an overview of the current understanding of hydrophobicity, solvophobicity, and their potential relation to critical drying. This understanding takes a length scale dependent view and hence in section 3.1, hydrophobicity is explored in terms of three regimes most evident in the literature. In section 3.2, the similarities and differences between hydrophobicity and the more general solvophobicity are discussed and compared, whilst in section 3.3 the possible relation between hydrophobicity on all length scales and an underlying critical surface phase transition is examined. The understanding presented here is not exhaustive and the interested reader is directed to the many reviews on the subject, for example [5, 19, 73–76, 84–86].

3.1 Hydrophobicity: A Length-Scale Dependent View

Hydrophobic solutes and substrates solvate differently depending on their size [6, 7, 87]. Experimental and simulation studies of hydrophobic molecules of comparable size to water, such as methane and xenon, have found these to typically invoke few observable changes to the surrounding water [10, 12], whilst simulation studies of larger molecules, such as neopentane and cyclopentadiene, have suggested these influence the orientation of water molecules local to their surface [10, 11]. Experiments involving macroscopic surfaces of paraffin and glass have found evidence of regions of depleted water density local to the surfaces [24, 88]. In contrast, the tendency of water droplets to form rounded shapes on hydrophobic surfaces such as rose petals or lotus leaves is well documented [2, 19, 74]. As hydrophobicity varies in form depending on the length scale, an understanding of hydrophobicity also requires a length scale dependent perspective. Considering the behaviour of water in each of the cases listed, three regimes of hydrophobicity naturally arise: a small length scale solvation regime, which describes hydration of solutes of order the size of a water molecule; a large length scale solvation regime, which describes hydration of solutes substantially larger than a water molecule, such as proteins and alkanes; and a macroscopic regime, which describes hydrophobic behaviour of planar surfaces.

3.1.1 Small Length Scale Solvation Regime

Much of our current understanding of hydrophobicity in the small length scale solvation regime is derived from the behaviour of bulk water. Bulk water has a distinct, slightly

disordered, tetrahedral structure, the formation of which is attributed to its hydrogen bonding abilities [89]. These hydrogen bonds are incredibly energetically favourable, and water will go to great lengths to preserve them. Therefore, when met with an apolar solute with which they cannot form hydrogen bonds, it is argued that water molecules will reorient themselves in such a way as to straddle the solute, as shown in figure 3.1(a) [7, 89]. This allows for water to maintain its hydrogen bonds, and amounts to hydrophobic solutes in this regime being incorporated into water's bulk structure. The density of water proximal to the hydrophobic solute would therefore be expected to be enhanced, as shown in figure 3.1(b). This expectation has been confirmed by both theoretical models of hydrophobic solvation [6] and simulations [22].

Incorporation of a hydrophobic solute into water's tetrahedral structure reduces the volume available for water molecules to occupy, whilst the necessity to maintain hydrogen bonds limits the water molecule's available orientations. Combined, this leads to a large negative hydration entropy [7, 35, 89]. Such a penalty was first rationalised by Frank and Evans [90] by the suggestion that water's structure in the first solvation shell became more ice-like around a hydrophobic solute. This suggestion has gathered popularity since its inception and has become known as the iceberg model. Whilst the iceberg model has generated great interest, agreement on its accuracy is conflicted, particularly on the definition of 'ice-like' structure [7, 12, 13, 15]. Studies which interpret this in terms of a change in the radial distribution function of water show no evidence for enhanced ice-like structure [14], with some going so far as to indicate a diminished structure [13]. If enhanced structure is instead interpreted in terms of hydrogen bond strength, evidence has been found in favour of the iceberg model [12]. Studies based on the angular distribution of water molecules have also found in favour of an enhancement of structure, however have noted that this is not necessarily ice-like [15].

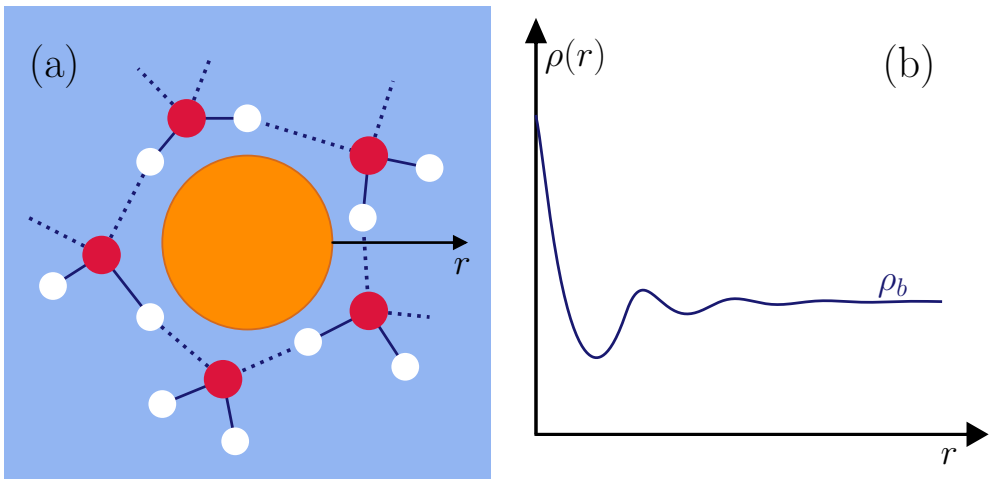

Figure 3.1: (a) Illustration of the structure water is believed to adopt around hydrophobic solutes of similar size to water molecules. A hydrophobic solute, represented by the large orange circle, is solvated in water, shown in blue. The nearby water molecules orient themselves in order to straddle the solute, and maintain their hydrogen bonds. Oxygen and hydrogen atoms are represented by the red and white circles respectively. Covalent bonds are represented by the solid lines, whilst hydrogen bonds by the dotted lines. (b) The corresponding oxygen-oxygen density profile which would be expected for such a structure of water. ρ_b here represents the density of water in the bulk liquid.

Alternative reasoning has suggested that it is instead the dynamics of water molecules about these hydrophobic solutes which are ice-like [14], however again, evidence for this is conflicted [14, 85, 91].

Although a precise understanding of the influence of small hydrophobic solutes on the structure of water has remained elusive, it has become apparent that such knowledge is unnecessary for understanding many of the thermodynamic properties of their solvation. Instead, estimates for the free energy of solvation, $\Delta\mu$, the hydration entropy, ΔS, and their temperature dependence can be obtained purely from statistical mechanics [5, 92, 93]. Within statistical mechanics, the Widom insertion method expresses the change in excess chemical potential, or free energy of solvation in this case, upon insertion of one solute particle as [42]

$$\Delta\mu = -k_{\mathrm{B}}T \ln < e^{-\beta\Delta E} > \tag{3.1.1}$$

where ΔE represents the inter-particle and external energy contributions of the solute to the Hamiltonian, and the term within the logarithm can be recognised as the canonical probability of insertion of the solute. If the hydrophobic solute can be treated as a hard-sphere, then $\Delta E = 0$ if a randomly chosen volume, large enough to accommodate the solute, is void of water molecules, and $\Delta E = \infty$ if the volume is partially occupied. The probability of insertion is therefore related to the probability of finding a volume large enough to accommodate the hydrophobic solute which is also void of water molecules. This implies equation (3.1.1) for a hard-sphere solute can be rewritten as [5, 42, 92]

$$\Delta\mu = -k_{\mathrm{B}}T \ln P(N = 0) \tag{3.1.2}$$

where $P(N)$ is the probability of finding N water molecules in a volume the size of the hydrophobic solute. Equation (3.1.2) therefore implies that the free energy of solvation for a small hydrophobic solute should scale with the volume of the solute, which has indeed been found to be the case in several theoretical and simulation studies [6, 8, 83].

For water, $P(N)$ has been found to be Gaussian for small volumes [93]. This observation has been used to rationalise the temperature dependence of hydrophobic solvation in the small length scale solvation regime [92]. $P(N)$ can be defined as [92]

$$P(N) = \frac{1}{(2\pi\sigma^2)^{1/2}} e^{-\frac{(N-<N>)^2}{2\sigma^2}} \tag{3.1.3}$$

where $< N >$ is the mean number of water molecules in the volume, and σ the variance. Substituting $P(N = 0)$ into equation (3.1.2) then gives

$$\Delta\mu \approx \frac{k_{\mathrm{B}}T\rho_b^2V^2}{2\sigma^2} + \frac{k_{\mathrm{B}}T}{2} \ln 2\pi\sigma^2 \tag{3.1.4}$$

where ρ_b is the bulk water density and V the volume of the system. For water, σ has been found to have a very weak temperature dependence [92]. Considering this, and that as a logarithm, the second term is expected to vary far slower than the first, it can be concluded that the temperature dependence of $\Delta\mu$ is dominated by the term $T\rho_b^2$ [92]. At

ambient temperature, $T = 298$ K, $\rho_b \approx 0.997$ gcm^{-3} [94] and hence $T\rho_b^2 \approx 296$ (gcm^{-3})^{2}K. However, at $T = 400$ K, where $\rho_b \approx 0.9375$ gcm^{-3} [94], $T\rho_b^2 \approx 352$ (gcm^{-3})^{2}K. Thus, the free energy of solvation is predicted to be larger at 400 K than at ambient temperature and the hydrophobicity of a solute should therefore increase upon increasing temperature. Such behaviour has been confirmed in both theoretical and simulation studies [8, 92]. These studies have found that the free energy of solvation in fact peaks near 400 K for hydrophobic solutes of order the size of a water molecule, before reducing. This latter observation can be rationalised by the rapidly decreasing density of water at higher temperatures, as the bulk liquid-vapour critical point is approached.

As well as providing a qualitative understanding of small length scale solvation behaviour, the simple statistical mechanics arguments surveyed here have also been found to provide good quantitative estimates for the hydration entropy of small hydrophobic solutes [5], which is related to equation (3.1.4) via $\Delta\mu N = \Delta G = \Delta H - T\Delta S$ [5], where ΔG is the Gibb's free energy defined in equation (2.1.3) and all other terms take their meanings of section 2.1. This is remarkable considering that the hydrophobic solute has been treated purely as a hard-sphere, with no attempt made to account for the effects of attraction between the solute and water molecules. These arguments, and their great successes, justify that small length scale solvation be understood in terms of the behaviour of bulk water.

3.1.2 Large Length Scale Solvation Regime

As the size of the hydrophobic solute grows, it becomes progressively more difficult for water molecules to reorient themselves in such a way as to retain all of their hydrogen bonds. If all hydrogen bonds cannot be retained, then the next most favourable orientation for the water molecules to adopt is to point one hydrogen bond directly at the hydrophobic solute, allowing the remaining three to be maintained with the bulk water [89]. An example of this orientation is shown in figure 3.2(a). Water molecules at the surface of the hydrophobic solute can be expected to feel a stronger attraction to the bulk water than to the solute itself, and hence it can be argued that such molecules should retreat from the surface of the solute. In this case, a region of depleted density is expected to form around the hydrophobic solute, which is represented by the lighter blue region in figure 3.2(a) and colloquially referred to as a vapour film. An example of the density profile expected for such a system is shown in figure 3.2(b). A reduction in the density of water at the surface of large hydrophobic solutes was perhaps first suggested by Stillinger [87]. Since his seminal work, many other theoretical and simulation studies have reported vapour films at the surfaces of large hydrophobic solutes [6, 9, 22, 95], whilst the preferential orientation of water molecules described above has been reported in both simulation and experimental studies of the solvation of hydrocarbons [10, 11, 16].

Water at ambient conditions is not at liquid-vapour coexistence, and instead exhibits a small oversaturation [96]. As such, any vapour film which is formed is expected to be metastable with respect to the bulk liquid and thus highly susceptible to small changes in the local thermodynamic conditions [30]. For example, increasing the temperature of water from ambient conditions towards the boiling point moves water closer to liquid-vapour coexistence.

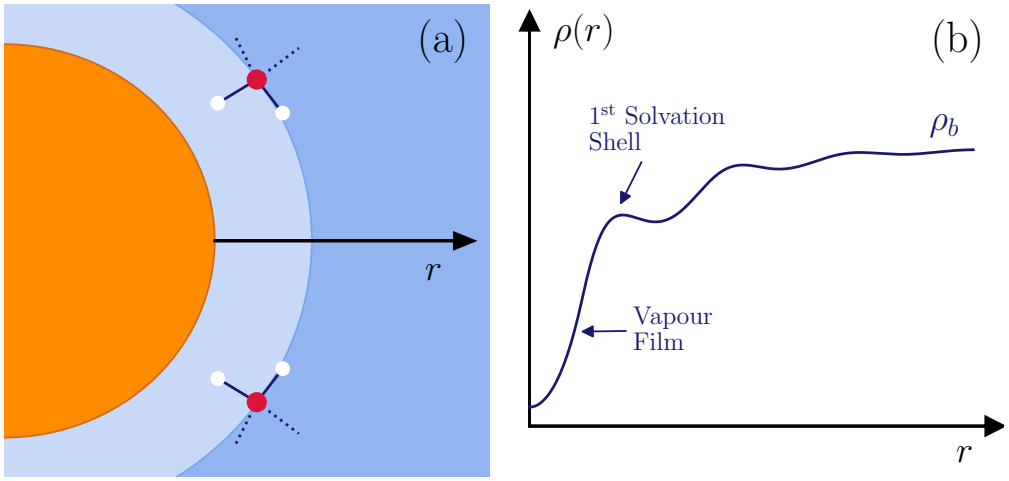

Figure 3.2: (a) Illustration of the orientation water molecules are expected to adopt around a hydrophobic solute in the large length scale solvation regime. A large hydrophobic solute, shown in orange, is solvated in water, shown in blue. Water molecules proximal to the surface of the solute orient themselves such that one of their two hydrogen atoms (white circles) points directly towards the surface of the solute. The more favourable attraction from the bulk water causes these molecules to retreat from the surface of the solute, resulting in a vapour film, which is represented by the light blue region. The oxygen atoms (red circles) sit in the first solvation shell at the edge of the vapour film. The solid lines between atoms represent covalent bonds, whilst the dotted lines represent hydrogen bonds. (b) Example of the oxygen-oxygen density profile which corresponds to such a system. ρ_b represents the bulk liquid density of the water.

This should improve the stability of the vapour film, which in turn should allow it to grow in width. In addition, as the bulk fluid nears coexistence, liquid packing effects are expected to become less pronounced. Hence, as the temperature is increased, the peak in the first and subsequent solvation shells should reduce. This has indeed been found to be the case in simulation studies of purely repulsive solutes in water [22]. In contrast, increasing the pressure above ambient conditions should act to move water away from liquid-vapour coexistence and thus deplete the vapour film whilst increasing the peak of the first solvation shell. This has been confirmed in simulation studies of both purely repulsive [22] and weakly attractive [79] solutes. Introducing a weak solute-water attraction, which acts to compete with the attraction of the bulk water, has also been found to deplete the width of the vapour film in theoretical and simulation studies [9, 28]. Evidence of slight density depletion around realistic hydrocarbon molecules has been reported in simulation studies [10, 11], though it should be highlighted that this depletion is very limited, and does not extend far from the molecule.

Density depletion itself is difficult to observe due to the short distances over which it is expected to occur. Its effects are therefore better observed in the behaviour of the free energy of solvation. Any vapour film must be accompanied by both a solute-vapour interface and a liquid-vapour like interface with the bulk fluid. If hydrophobicity in the large length scale solvation regime is characterised by the formation of these interfaces, then the surface terms in the free energy of solvation should become important. In this case, the appropriate free energy is the grand potential, defined in equation (2.1.6) as $\Omega = -pV + \gamma A$, which can be rearranged for the free energy of solvation as $\Delta\mu N = \Delta G - \gamma \Delta A$. If surface terms are important, then $\Delta\mu$ would be expected to scale with the surface area of the interface, A, as

opposed to the volume of the solute as seen in the small length scale solvation regime. Several theoretical and simulation studies have reported this to be the case [6, 8, 35, 83].

Whilst the interface between the vapour film and bulk liquid is suspected to be liquid-vapour like, it should be noted that it differs substantially in form and behaviour from a free liquid-vapour interface. For example, the liquid-vapour like interface induced by hydrophobicity is bound to the surface of the hydrophobic solute and hence small variations in its position will result in variations in the free energy of the system. In contrast, a free liquid-vapour interface incurs no free energy cost by translation. Furthermore, long wave-length thermal (capillary wave) fluctuations present at free liquid-vapour interfaces are suppressed for the curved liquid-vapour like interfaces bound to hydrophobic solutes [86]. Similarities between the free and bound liquid-vapour interfaces do remain, notably in the presence of single hydrogen bonds, known as dangling bonds, pointing towards the vapour region in both [16, 20], however these are found in much greater numbers at a free interface.

Both the density behaviour of water molecules and the free energy of solvation in the large length scale solvation regime are clearly related to the formation of interfaces however, understanding how these relate to one another is difficult. For example, previous studies have reported that $\Delta\mu$ decreases upon increasing temperature [8], which would imply that the hydrophobicity of a solute in the large length scale solvation regime decreases with increasing temperature. It is difficult to conflate this reported behaviour with the reported increasing width of the vapour film with increasing temperature [22], as the latter behaviour would perhaps imply that the solute were more hydrophobic at higher temperatures. This is but one example of a situation within the large length scale solvation regime where conclusions drawn from the local density profile of water differ from those drawn from other measures, and emphasizes the difficulty in defining hydrophobicity within this regime.

Considering this, it has been argued that the local density profile of water near a large hydrophobic solute is a poor indicator of hydrophobicity [29, 73]. Instead, it has been suggested that fluctuations in the density of water molecules local to the surface of a hydrophobic solute are a more distinct signature of hydrophobicity in the large length scale regime [28]. Whilst there have been several attempts to quantify these fluctuations [29, 79, 95], perhaps the most popular measure is the probability distribution of the occupation of a volume immediately adjacent to the surface of the hydrophobic solute [28, 31, 97]. Whilst in bulk water this follows a Gaussian distribution, next to a hydrophobic solute the probability of fewer water molecules than the mean occupying the volume has been found to increase [28]. This large probability of a low occupancy has become colloquially known as a 'fat tail' to the Gaussian distribution and is demonstrated in figure 3.3(b). Increasing the attraction between the hydrophobic solute and water molecules has been found to reduce this fat tail, moving it closer towards a Gaussian distribution [28, 97]. Occupation probability distributions around hydrophilic solutes therefore do not exhibit any notable difference from the bulk distribution, and thus this probability distribution allows hydrophobic solutes to be identified easily [28]. The enhancement of lower occupation probability increases the variance of the distribution and implies the existence of large density fluctuations local to hydrophobic solutes, which are

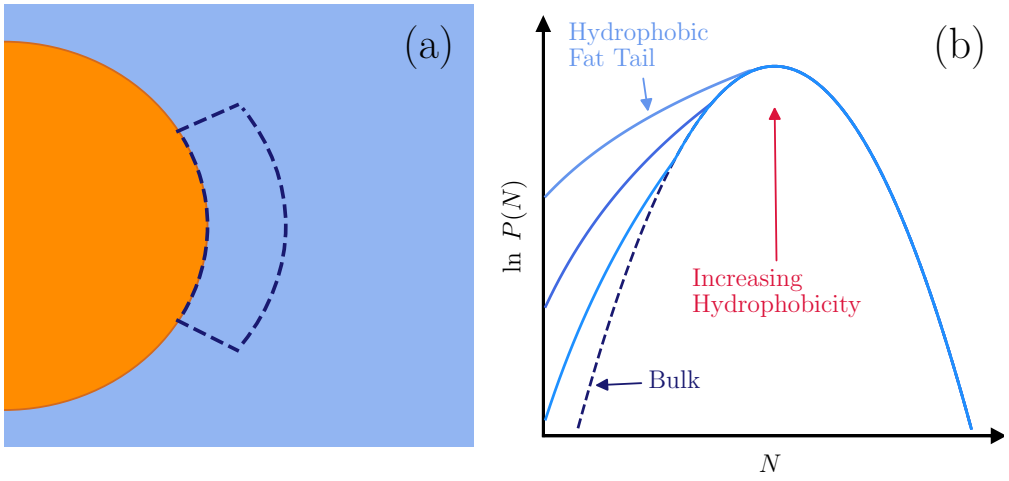

Figure 3.3: (a) A hydrophobic solute, shown in orange, is submerged in water, shown in blue. A volume immediately adjacent to the surface of the solute, enclosed by the dashed lines, represents the volume over which water molecule occupancy probability distributions may be measured. (b) The probability of finding N water molecules in a given enclosed volume. In a bulk fluid, this follows a Gaussian distribution. Near to a hydrophobic solute, the probability of observing fewer water molecules than the mean is enhanced, resulting in a 'fat tail' to the distribution.

not present in bulk water or proximal to hydrophilic solutes.

In addition to acting as a distinct signature of hydrophobicity, density fluctuations proximal to the surface of a hydrophobic solute are thought to play an important role in a variety of chemical and biological processes. For example, ten Wolde and Chandler [30] have shown that fluctuations near extended polymers can lead to their collapse to a coiled form. Their simulations indicated that the process of this collapse involved multiple stages. First, a configuration fluctuation drove hydrophobic segments in the extended chain to cluster together. Thermal fluctuations were then able to nucleate a vapour bubble along the chain, which subsequently facilitated the chain collapse. A later study by Athawale et al. [98] also indicated that the folding of hydrophobic polymers was facilitated by density depletion at the surface of the polymer and found evidence of enhanced local density fluctuations, which were quantified by the variance of the occupation of the first solvation shell.

Within biological contexts, density fluctuations have been used to explain why some biomolecules exhibit significant density depletion in their vicinity whilst others do not. Two commonly compared biomolecules for this are the BphC enzyme [31, 99] and Melittin [31, 80, 100]. During the folding process of the two-domain BphC enzyme, two hydrophobic slab-like domains approach one another. Water density between the domains has been reported to reduce, but only by ten to fifteen percent of the bulk density [99]. In contrast, during the collapse of the Melittin tetramer, water has been found to almost completely evacuate a nano-sized channel formed [100]. Altering the topology or chemical heterogeneity in either system was found to dramatically change the behaviour, either preventing density depletion or encouraging it [80, 99, 100]. This behaviour was rationalised by Patel et al. [31], who considered the occupation probability distributions in volumes adjacent to each of these biomolecules, as opposed to the density profile. Their results showed that both BphC and Melittin exhibit

fat tail distributions like those in figure 3.3(b). In the case of Melittin, bringing two dimers into close proximity greatly enhanced these fat tails, such that a small perturbation would be sufficient to expel any water molecules between them. In contrast, whilst BphC also showed fat tails, these were not as greatly enhanced when two domains were brought together, hence small perturbations were unable to remove the water molecules. Mutating Melittin so as to alter its topology significantly reduced the fat tails, which prevented expulsion of water molecules, whilst removing electrostatic charges between BphC domains significantly enhanced them. The work of Patel et al. [31] therefore highlighted the importance of density fluctuations in understanding hydrophobicity driven biological processes.

3.1.3 Macroscopic Regime

For the same reasons as in the large length scale solvation regime, regions of depleted density are expected to form at a macroscopic hydrophobic surface though, rather than a vapour film, these are typically referred to as a hydrophobic 'gap' [25, 101]. Hydrophobic gaps have been confirmed in both experiment and simulation studies [22–24, 26, 27, 101, 102], however their extent is widely debated. Neutron reflectivity studies have reported hydrophobic gaps of anywhere between 2 nm and 5 nm [103], whilst X-ray reflectivity studies report gaps of between 1Å and 8Å [24, 25, 27, 101]. Results presented within these X-ray reflectivity studies have generated considerable debate, as the exact width appeared to depend heavily on the model used to fit the experimental data [26, 104], and such studies were complicated by their accessible resolutions [27], as well as factors such as radiation damage [26, 27, 104]. Simulation studies, which do not suffer from such problems, have found in favour of gaps of order angstroms [22, 23, 102]. However, such studies typically do not attempt to reproduce realistic surfaces, instead choosing to consider smooth surfaces which usually interact with water via very simple potentials, like that of Lennard-Jones [23, 102]. As such, their relevance to experiment is arguable. There has also been debate over whether the depleted density region even takes the form of a gap, or whether it instead takes the form of 'nanobubbles' on the hydrophobic surface. Atomic Force Microscopy experiments have found in favour of the latter [88, 103], whilst X-ray reflectivity studies the former [27, 101].

The presence of a hydrophobic gap implies the existence of a liquid-vapour like interface and thus dangling bonds. Experimental studies have confirmed that dangling bonds are present near to macroscopic hydrophobic surfaces [16, 20, 21], and that their number is similar to that found at a free liquid-vapour interface [20]. Despite this, liquid-vapour interfaces near macroscopic hydrophobic surfaces differ substantially from a free liquid-vapour interface. For example, water molecules in contact with an impenetrable solid hydrophobic surface have been found to adopt an orderly packing, likened to an ice-like structure [20], which is not present at a free interface. Furthermore, spectra of water in contact with hydrophobic organic liquid surfaces show evidence of weakened hydrogen bonding compared to the free interface [21]. Simulation studies have also found evidence of dangling bonds near hydrophobic surfaces [105], and noted a correspondence between the polarity of a surface, the preferential dangling bond orientation of water molecules, and the contact angle a droplet makes on the surface.

Much like the large length scale solvation regime, hydrophobicity in the macroscopic regime is associated with large density fluctuations, which have been quantified using probability distributions similar to those in figure 3.3(b). Simulations of hydrophobic self-assembled monolayer (SAM) surfaces found these distributions to exhibit fat tails, in agreement with the distributions found around microscopic solutes [31, 73]. Furthermore, these distributions near hydrophilic SAMs were found to be approximately Gaussian [31, 73] and similar to those seen in bulk water. In the macroscopic regime, several additional measures of local density fluctuations, which incorporate spatial resolution, have been proposed. Typically termed local compressibilities, these measures have sought to understand the location of the largest fluctuations relative to the surface, using derivatives of the microscopic density profile. The local compressibility, as defined by Acharya et al. [29], was based on a derivative of the spatially varying density profile with respect to the pressure over a sub-volume adjacent to the surface. Near a hydrophobic surface, this local compressibility was found to exhibit a large peak, several times its bulk value, followed by smaller oscillations [29]. In contrast, hydrophilic surfaces were found to exhibit a local compressibility similar to the bulk value. Acharya et al.'s [29] definition of the local compressibility highlighted the sensitivity of water molecules local to a hydrophobic surface to pressure, however relies on a definition of pressure which is ambiguous [37].

An alternative form of the local compressibility, based on a derivative of the spatially varying density profile with respect to the chemical potential, was presented in section 2.4.1. This measure was rigorously derived from underlying statistical mechanics principles, and removes the limitation of considering a sub-volume, instead allowing for fluctuations over the entire system to be investigated. Evans and Wilding [23] used this measure within their simulation study of water confined between two planar substrates to quantify the local density fluctuations of water near hydrophobic and hydrophilic surfaces. This definition of the local compressibility was found to vary by orders of magnitude compared to its bulk value, indicating that it provided a highly sensitive measure of hydrophobic density fluctuations. Confined between hydrophilic surfaces, these fluctuations showed far less variation, with oscillations which closely followed those observed in the density profile.

Whilst there exist many similarities between hydrophobicity in the macroscopic and large length scale solvation regimes, these have to a large extent been eclipsed by research into other aspects of macroscopic hydrophobicity, most notably, the influence of surface structure. Surface structure has been shown to play a crucial role in natural processes involving hydrophobic surfaces [2, 3] and is of great interest in engineering applications of hydrophobicity. Although only smooth planar surfaces will be considered within the present work, a discussion of macroscopic hydrophobicity would be incomplete without some description of the effect of surface structure, hence is included here.

On a smooth, flat, planar surface, hydrophobicity is naturally defined by Young's contact angle, θ, as shown in in figure 2.3 and defined in equation (2.4.19). However, on an inclined surface, θ alone is insufficient to adequately quantify hydrophobicity, as this measure gives no indication of the adhesion of the droplet to the surface. Because of this, studies of macroscopic

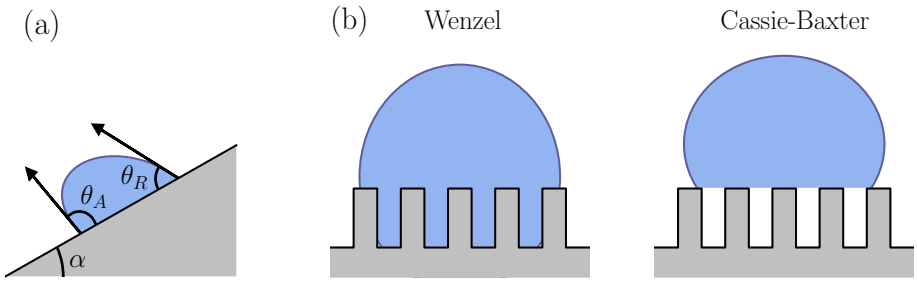

Figure 3.4: (a) A droplet on an incline features two contact angles: the advancing contact angle, θ_A, and the receding contact angle, θ_R. The angle of incline for which the droplet slides down the plane is the sliding angle, α. (b) Illustration of the two possible droplet states on a rough plane. In the Wenzel state, the droplet penetrates the grooves of the surface. In the Cassie-Baxter state, the droplet sits above the grooves, which are instead filled with vapour.

hydrophobicity typically make use of two additional measures. The first is the contact angle hysteresis (CAH), which is the difference between the advancing, θ_A, and receding, θ_R, angles of a droplet on an inclined plane [19, 74]. The second is the sliding angle (SA), also known as the roll-off angle, which is the angle of incline of a plane, α, required before the droplet begins to slide down it [19]. These measures are depicted in figure 3.4(a).

Surfaces which exhibit $150° < \theta < 180°$ and a SA of $\alpha < 5°$ are usually given the special title of superhydrophobic [19]. As the largest θ thought achievable on a smooth surface is $\theta \approx 120°$ [27], it is widely believed that a combination of surface chemistry and topology is necessary for engineering superhydrophobic surfaces [19]. This belief is supported by naturally occurring superhydrophobic surfaces, such as the lotus leaf, which achieves a contact angle of $\theta \approx 162°$ through use of nano sized fibres and micron sized grooves [2, 17, 19]. On structured surfaces, water droplets can take one of two states: they can either fill the grooves in the Wenzel state, or rest above them in the Cassie-Baxter state, as shown in figure 3.4(b) [19, 74, 75]. In the latter state, water droplets are in contact with both the surface and vapour, which lowers surface adhesion [75]. As such, it is the Cassie-Baxter state which is associated with superhydrophobicity.

Of its many potential applications, possibly one of the most interesting uses of superhydrophobicity is in self-cleaning surfaces [106, 107]. Naturally occurring self-cleaning surfaces have been found to utilise hierarchical surface structures to maintain droplets in the Cassie-Baxter state in addition to surface coatings to further lower the surface adhesion [2, 3, 107]. These properties allow droplets to form and move over the surface with ease. In doing so, they 'pick up' particulates on the surface, which feel a stronger force with the droplet than the surface itself due to the low surface adhesion [107]. The naturally low SA of these surfaces means that the droplet can roll off easily, taking the particulates with it. Natural superhydrophobic surfaces have also shown it is possible to tune the direction of the movement of droplets [3]. For example, the wings of butterflies control the amount of vapour trapped within the structured surface, and therefore the adhesion of the droplet, using the tilt of the wing. This property allows directional control over the movement of the droplet, and ensures

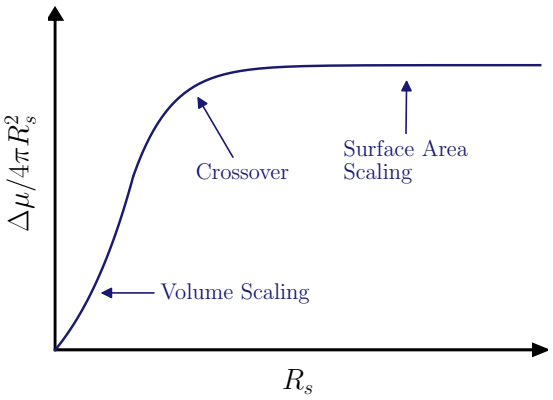

Figure 3.5: Schematic of the variation of the free energy of solvation with radius, R_s, of hydrophobic solute. For solutes approximately the same size as water, the free energy of solvation scales with the volume of the solute. For larger solutes, this scaling is with the surface area. The cross-over between these regimes indicates the cross-over length scale between small and large length scale solvation.

that it runs off the wing away from the butterfly's body [3]. Self-cleaning surfaces have many potential applications, such as self-cleaning glass for windshields, windows, and solar panels, and anticorrosion surfaces [106].

3.1.4 Crossovers between Regimes

Three distinct regimes of hydrophobicity have been presented, however defining the exact length scales which divide these regimes is difficult. The crossover between the small and large length scale solvation regimes has traditionally been taken to be the length scale at which density depletion is observed, and is possibly most easily determined by considering the radius of solute for which the free energy of solvation transitions from scaling with volume of solute to surface area, as shown in figure 3.5. For water, this is widely reported to be around 1 nm [5, 9, 11, 83]. Whilst 1 nm provides a useful gauge in water, it should be noted that the exact crossover length scale depends on both the temperature [78] and pressure [77], as well as the geometry of the solute [11]. Defining a crossover length scale between the large length scale solvation and macroscopic regimes is more difficult, due to the similarities in water's structure and the differing perspectives under which the two regimes are understood. As such, there is no generally agreed consensus on what this should be.

3.2 Hydrophobicity vs Solvophobicity

From section 3.1 it is clear that water's hydrogen bonding network plays a crucial role in the solvation of hydrophobic solutes and the behaviour of water molecules at hydrophobic surfaces. However, it is not clear that it is the actual hydrogen bonding, as opposed to any other form of fluid-fluid interactions, that is important. For example, water molecules appear to straddle small hydrophobic solutes in order to preserve their hydrogen bonds. Whilst other fluids may have weaker van der Waals interactions between molecules, the general argument that they too should wish to conserve these and therefore attempt to straddle the solute can still be made. Similarly, if the solvophobic solute was too large to accommodate

into the van der Waals interactions of the fluid, then it can be argued that fluid molecules would retreat from the surface of the solute towards the more energetically favourable bulk fluid. Furthermore, many fluids other than water form rounded droplets when dropped onto a surface, suggesting a solvophobic response. Therefore, whilst hydrophobicity is abundant and certainly plays many important roles in everyday life, it is not clear that it is a unique interaction, rather than simply a specific case of solvophobicity.

Recent simulation evidence favours the latter conclusion. Dowdle et al. [35] compared the free energy of solvation of three fluids and found that the behaviour in each case was very similar. Each fluid showed a free energy of solvation which scaled with the volume of the solvophobic solute for small solutes and then with the surface area for larger solutes. This was particularly interesting given the very different fluids considered: a simple Lennard-Jones fluid, in which particles interact with one another via a pairwise potential; a more complex Jagla fluid, in which particles interact pairwise but on two characteristic length scales; and water, modelled using an empirical fit to an approximate analytic equation of state. Another study by Wu and Garde [36] found that a polymeric fluid, n-Octane, also showed a free energy of solvation which scaled with volume for small solutes and surface area for larger solutes. This study also noted that, much like water, the probability distributions of finding volumes within n-Octane which could accommodate small solvophobic solutes were Gaussian whilst for larger volumes, exhibited fat tails. Similar probability distributions have also been observed in Lennard-Jones fluids by Huang and Chandler [81].

Dowdle et al. [35] also found that the temperature dependence of the free energy of solvation in water and the Jagla fluid was qualitatively similar, exhibiting a peak upon increasing the temperature for small solutes and a monotonic decrease for larger solutes. Wu and Garde observed similar behaviour in the n-Octane fluid [36]. This behaviour was not found in the simpler Lennard-Jones fluid [35]. In addition to the differences in temperature dependence of the free energy of solvation between fluids, the length-scale at which the free energy transitioned from scaling with volume to surface area also varied between fluids [35, 36].

The similarities between hydrophobicity and solvophobicity are not limited to free energy considerations. Density depletion, reminiscent of that found in studies of water, at the surface of larger solutes and planar surfaces has also been reported in simulation studies of the Lennard-Jones [1, 81, 108] and n-Octane [36] fluids. Furthermore, local density fluctuations, measured by the local compressibility given in equation (2.5.1), have been found to take the same form in simulation studies of planar surfaces in contact with water [23] and a Lennard-Jones fluid [1]. Overall, whilst hydrophobicity is certainly a special interaction, considering all of these similarities, it is unclear whether it is a unique interaction.

3.3 Relation of Hydrophobicity and Solvophobicity to the Drying Surface Phase Transition

The nomenclature surrounding hydrophobicity and solvophobicity is varied, and in some circumstances, misleading. A prominent example of the latter case is the common usage of

terms such as 'dry', 'dewet', 'dewetting transition', and 'drying transition'. These terms are typically used without definition and their meaning appears to vary between studies.

For example, in many studies the term 'dewet', or in some cases 'dewetted', appears to refer to density depletion at the surface of hydrophobic solutes and macroscopic surfaces [11, 24, 31, 109], whilst the phrase 'dewetting transition', also sometimes shortened to 'dewetting', refers to the formation of this depleted density [11, 31, 36, 109]. However, this is not the only usage. In other studies, dewetting transitions seem to refer to the expulsion of water between two hydrophobic objects in close proximity [86, 109, 110]. In one instance, the expulsion of liquid from a slit geometry containing a Lennard-Jones fluid near liquid-vapour coexistence is referred to as a dewetting transition [109], a process which, to other audiences, may be described as capillary evaporation. Dewetting takes a further meaning in studies of macroscopic hydrophobic substrates, with the term being used to describe the transition from the Wenzel to Casse-Baxter states upon application of an external perturbation, for example, mechanical vibration [17].

Furthermore, the terms dewet and dewetting transition are often used interchangeably with the terms dry and drying transition [86]. The latter terms appear to be used colloquially, as studies which invoke them, for example [6, 110], make no mention of the well defined surface phase transitions outlined in section 2.4.5. Despite this, there are instances where authors refer to the tendency of microscopic hydrophobic solutes, such as biomolecules, to expel water between them as a phase transition [31]. Of course, use of the term 'phase transition' is incorrect here, as phase transitions are unable to occur in finite systems. However, the notion that microscopic hydrophobicity may be related to an underlying phase transition does have merit.

From figure 2.8, it can be seen that drying, in its true surface phase transition sense, is critical in systems with SR ff LR sf and LR ff LR sf interactions - circumstances which are pertinent to simulation and experimental studies respectively. Recent work by Evans et al. [1, 32] considered the former system carefully, applying both theoretical and simulation methods. Their systems consisted of a truncated Lennard-Jones fluid either at a planar surface or confined to a slit, with the interaction between the fluid and the surfaces also taking a Lennard-Jones form, however without truncation. In the case of the slit geometry, its width was sufficiently wide that the fluid returned to the bulk liquid density in the centre of the slit, and hence the surfaces could be considered non-interacting. Evans et al. [1, 32] showed that near to critical drying, properties such as the equilibrium vapour film width, ℓ_{eq} and the density fluctuations, as measured by the local compressibility in equation (2.5.1), followed critical scaling relations. Earlier theoretical studies by Stewart and Evans [33, 34] found that the adsorption, Γ, of LR fluids in contact with curved surfaces of very large R_s, also followed a scaling relation. These studies suggest that solvophobicity at curved and planar surfaces are influenced by a nearby drying surface critical point.

As outlined in section 3.2, there is little reason to believe hydrophobicity should be any different from solvophobicity and hence if critical drying may influence solvophobicity, it is equally plausible that it influence hydrophobicity. Furthermore, the extent to which this

possible influence may extend into microscopic length scales can almost immediately be identified by considering the hydrophobic regimes discussed in section 3.1. Hydrophobicity in the small length scale solvation regime was shown in section 3.1.1 to be well described by the bulk properties of water. This regime of hydrophobicity therefore cannot be expected to be related to surface phase behaviour. However, hydrophobicity in the large length scale solvation regime appears to be dominated by interface considerations and hence this regime could well be related to critical drying in the macroscopic regime. Moreover, evidence for critical drying in the macroscopic regime for a water model was recently reported by Evans and Wilding [23]. Critical drying may therefore provide a connection between hydrophobicity and solvophobicity, across length-scales.

Chapter 4

Methods

Hydrophobicity shows clear length scale dependent behaviour, which makes its study challenging. Computational techniques capable of studying the small and large length scale solvation regimes, in addition to the macroscopic regime, are few and tend to be limited in the complexity of the fluids which they are able to represent. In contrast, methods capable of modelling complex fluids are generally computationally demanding and therefore limited in the size of solute they can study. Despite being a simple molecule, water features numerous anomalous behaviours [89] and as such falls under the remit of a complex fluid. This leads to the predicament that methods to study hydrophobicity over vastly different length scales cannot be used in conjunction with water models, whilst methods which can be used with water models cannot be used to study hydrophobicity over such diverse length scales. For this reason, this work utilises two methods.

The first of these methods is classical Density Functional Theory (cDFT), which provides a rigorous statistical mechanical framework to find the equilibrium density profile of a fluid subjected to an external potential via numerical minimisation of the free energy [42, 46, 111]. From the equilibrium density profile, thermodynamic properties such as the surface tension of the fluid can be determined. Due to the simplicity of numerical minimisation, cDFT is highly computationally efficient and can be used to study the behaviour of a fluid around solutes of all sizes and at macroscopic planar surfaces, for a wide range of thermodynamic conditions. However, cDFT requires approximations for the free energy functional, which have proven challenging to develop. Within this work, it is therefore restricted to the exploration of solvophobicity, as opposed to hydrophobicity.

The second method employed within this work is molecular simulation, which aims to find macroscopic properties of a system by sampling microscopic configurations of particles [44]. There are few limitations on the way in which these particles can interact and as such molecular simulation is able to model complex fluids such as water. However, even for simulations of simple bulk fluids, accurate results require several hundred to thousands of particles, which can be computationally demanding, particularly as the complexity of the interaction potentials increases. If solutes are studied, the simulation volume must be large enough to accommodate not only the solute but also a reasonable number of particles to

accurately represent the bulk fluid which, for large solutes, could be in the tens of thousands. Because of this, the computational resource required grows rapidly with solute size and thus molecular simulation studies are limited in the length scales they can realistically study.

Individually, these methods are limited in scope. However, when used in conjunction, they allow for a thorough study of hydrophobicity and solvophobicity over a wide range of length scales. In this chapter, each of these methods is introduced in turn.

4.1 Classical Density Functional Theory

Since its inception in the 1970s, cDFT has been used extensively in a wide range of studies. Many of the original studies of the wetting surface phase transition employed cDFT to understand its nature [52, 55, 59]. More recently, cDFT has been employed in studies of solvophobicity at macroscopic surfaces [1, 32, 37, 112, 113], around solutes [33, 34], and in confined geometries [82]. These studies have allowed identification and quantification of the influence of thermodynamic and geometric properties on solvophobic responses and have been largely enabled by developments in cDFT since the 1970s, the most notable of which is perhaps Rosenfeld's Fundamental Measure Theory (FMT) of hard-spheres [114]. This provided an accurate reference functional on which van der Waals treatments of simple inhomogeneous fluids could be built. cDFT is therefore well established as a method for the study of solvophobicity and surface phase transitions, which in part justifies its use within this work.

4.1.1 Formalism

cDFT was originally borne out of its electronic counterpart, which describes the ground state of an inhomogeneous electron fluid as a functional of the electron density. Whilst the original form of electronic DFT was limited to zero temperature conditions, Mermin [115] showed that it could in fact be extended to non-zero temperatures and introduced a functional of the grand potential to do so. Building on Mermin's formulation, electronic DFT was extended to classical fluids in 1976 [45].

Mermin's proposed functional for the grand potential took the form [46, 115, 116]

$$\Omega[f] = \mathrm{Tr}_{\mathrm{cl}} f \left(\mathcal{H} - \mu N + \beta^{-1} \ln f\right) \tag{4.1.1}$$

where $\mathcal{H}$ is the Hamiltonian, given for a fluid in equation (2.2.1), μ, N, $\mathrm{Tr}_{\mathrm{cl}}$, and $\beta = (k_{\mathrm{B}}T)^{-1}$ take their meanings of previous chapters and f is the probability density distribution of the fluid. At equilibrium, this would take a form like those seen in equations (2.2.5) and (2.2.9) however f as given in equation (4.1.1) does not necessarily represent equilibrium and is thus only restricted in that as a probability, it must obey $\mathrm{Tr}_{\mathrm{cl}}\ f = 1$. Considering the equilibrium case, it can be found that the final term in equation (4.1.1) represents the entropic contribution to the grand potential, $-TS$.

Equation (4.1.1) has many useful properties. For example, at equilibrium when $f = f_o$, $\Omega[f_o] = \Omega$, where Ω is the grand potential of the fluid defined in equation (2.1.4). It can further be proven that Ω is the minimum free energy, and hence that $\Omega[f] > \Omega[f_o]$ when

$f \neq f_o$. The derivation of this is given in Appendix B of [42].

Considering the definition of the Hamiltonian of a fluid given in equation (2.2.1), it can be seen that $f = f[V_{ext}]$. Furthermore, through a proof such as the one in Appendix I of [46], it can be found that V_{ext} is a unique functional of the density profile $\rho(\mathbf{r})$, and hence $V_{ext} = V_{ext}[\rho(\mathbf{r})]$. Together, this implies $f = f[\rho(\mathbf{r})]$, and that equation (4.1.1) can be written as a density functional, as the name cDFT suggests.

From equation (2.1.4), it can be seen that Ω can also be written in terms of the Helmholtz free energy. In density functional form this is [42, 45, 46, 116, 117]

$$\Omega[\rho(\mathbf{r})] = F[\rho(\mathbf{r})] - \mu N = \mathcal{F}[\rho(\mathbf{r})] - \int \mathrm{d}\mathbf{r}(\mu - V_{\mathrm{ext}}(\mathbf{r}))\rho(\mathbf{r}) \tag{4.1.2}$$

where $\mathcal{F}$ is the intrinsic Helmholtz free energy functional, which can be defined in a similar manner as equation (4.1.1) as [46]

$$\mathcal{F}[\rho(\mathbf{r})] = \mathrm{Tr}_{\mathrm{cl}} f\ (\Phi(\mathbf{r}^N) + K(\mathbf{p}^N) + \beta^{-1} \ln f) \tag{4.1.3}$$

where $K(\mathbf{p}^N)$ and $\Phi(\mathbf{r}^N)$ are the kinetic and inter-particle potential energies, as defined in section 2.2.

Equation (4.1.2) has the same properties as equation (4.1.1), which can be summarised as

$$\Omega[\rho_o(\mathbf{r})] = \Omega \qquad\qquad \Omega[\rho(\mathbf{r}) \neq \rho_o(\mathbf{r})] > \Omega \tag{4.1.4}$$

where $\rho_o(\mathbf{r})$ denotes the equilibrium density profile. Combined, these properties also imply a variational principle of the form [42, 45, 46, 116, 117]

$$\left.\frac{\delta\Omega[\rho(\mathbf{r})]}{\delta\rho(\mathbf{r})}\right|_{\rho(\mathbf{r})=\rho_o(\mathbf{r})} = 0 \tag{4.1.5}$$

Solving this variational principle forms the basis of cDFT.

The intrinsic Helmholtz free energy functional can further be separated into its ideal and excess components. The ideal intrinsic Helmholtz free energy functional, $\mathcal{F}_{id}[\rho(\mathbf{r})]$, describes the free energy of an ideal gas, and takes the well-known form [42]

$$\mathcal{F}_{id}[\rho(\mathbf{r})] = \beta^{-1} \int \mathrm{d}\mathbf{r}\rho(\mathbf{r})(\ln \Lambda^3 \rho(\mathbf{r}) - 1) \tag{4.1.6}$$

The excess intrinsic Helmholtz free energy functional, $\mathcal{F}_{ex}[\rho(\mathbf{r})]$, describes all inter-particle interactions within the system and is known exactly in only the case of one-dimensional hard rods. Because of this, $\mathcal{F}_{ex}[\rho(\mathbf{r})]$ must normally be approximated. Finding approximations for $\mathcal{F}_{ex}[\rho(\mathbf{r})]$ for various fluids has been the focus of a vast amount of research and remains an active area of study to this day [118–120].

Substitution of the density functional in equation (4.1.2) into the variational principle of equation (4.1.5) gives an expression for the equilibrium density profile. This requires a

functional derivative which, for a general functional A of function $u(x)$, is defined as [42]

$$A[u(x)+\delta u(x)]-A[u(x)]=\int \mathrm{d}x\frac{\delta A[u(x)]}{\delta u(x)}\delta u(x) \tag{4.1.7}$$

Using this definition, the functional derivative of $\Omega[\rho(\mathbf{r})]$ can be found to be

$$\begin{aligned}\frac{\delta\Omega[\rho(\mathbf{r})]}{\delta\rho(\mathbf{r})} &= \beta^{-1}\ln\Lambda^3\rho(\mathbf{r})-\mu+V_{ext}(\mathbf{r})+\frac{\delta\mathcal{F}_{ex}[\rho(\mathbf{r})]}{\delta\rho(\mathbf{r})}\\ &= \beta^{-1}\ln\Lambda^3\rho(\mathbf{r})-\mu_{id}-\mu_{ex}+V_{ext}(\mathbf{r})+\frac{\delta\mathcal{F}_{ex}[\rho(\mathbf{r})]}{\delta\rho(\mathbf{r})}\\ &= \beta^{-1}\ln\Lambda^3\rho(\mathbf{r})-\beta^{-1}\ln\Lambda^3\rho_b-\mu_{ex}+V_{ext}(\mathbf{r})+\frac{\delta\mathcal{F}_{ex}[\rho(\mathbf{r})]}{\delta\rho(\mathbf{r})}\\ &= \beta^{-1}\ln\frac{\rho(\mathbf{r})}{\rho_b}-\mu_{ex}+V_{ext}(\mathbf{r})+\frac{\delta\mathcal{F}_{ex}[\rho(\mathbf{r})]}{\delta\rho(\mathbf{r})}\end{aligned} \tag{4.1.8}$$

where μ has been decomposed into its ideal, $\mu_{id}=k_\mathrm{B}T\ln\Lambda^3\rho_b$, and excess, μ_{ex}, components, and where ρ_b represents the density of the fluid in the bulk. For the equilibrium density profile, this derivative equals zero. Rearranging this equation therefore gives a formally exact expression for the equilibrium density profile

$$\rho_o(\mathbf{r})=\rho_b e^{(\beta\mu_{ex}-\beta V_{ext}(\mathbf{r})+c^{(1)}(\mathbf{r}))} \tag{4.1.9}$$

where $c^{(1)}(\mathbf{r})$ is the one-body direct correlation function defined as [42, 45, 117]

$$c^{(1)}(\mathbf{r})=-\beta\frac{\delta\mathcal{F}_{ex}[\rho(\mathbf{r})]}{\delta\rho(\mathbf{r})} \tag{4.1.10}$$

This correlation function describes the effects of particle interactions on the density profile [42].

By nature of equations (4.1.9) and (4.1.10), cDFT requires an approximation for $\mathcal{F}_{ex}[\rho(\mathbf{r})]$. One well established approximation is Fundamental Measure Theory (FMT), which describes $\mathcal{F}_{ex}[\rho(\mathbf{r})]$ for hard-sphere mixtures [114]. FMT is particularly useful for the study of van der Waals fluids, as it provides an accurate reference functional for any perturbative approach, like that of section 2.4.3.

4.1.2 Fundamental Measure Theory

FMT is a weighted density approximation for the excess free energy functional of a hard-sphere mixture, which was first proposed by Rosenfeld in 1989. The formalism of cDFT is easily extended to mixtures, by summing over the density distribution of the ν components. The grand potential functional for a mixture becomes [111]

$$\Omega[\{\rho_i(\mathbf{r})\}]=\mathcal{F}[\{\rho_i(\mathbf{r})\}]+\sum_{i=1}^{\nu}\int \mathrm{d}\mathbf{r}\rho_i(\mathbf{r})(V_{ext}^i(\mathbf{r})-\mu_i) \tag{4.1.11}$$

where i represents the species. The description of FMT presented here largely follows that of the review paper by Roth [111].

The interaction potential for a hard-sphere fluid can be written as

$$\phi_{ij}^{HS}(|\mathbf{r}_i - \mathbf{r}_j|) = \begin{cases} \infty & |\mathbf{r}_i - \mathbf{r}_j| < R_i + R_j \\ 0 & \text{otherwise} \end{cases} \tag{4.1.12}$$

where $|\mathbf{r}_i - \mathbf{r}_j|$ represents the distance between the centre of spheres i and j, which are of radius R_i and R_j respectively. The Mayer-f function is defined as [111]

$$f_{ij} = e^{-\beta\phi_{ij}(|\mathbf{r}_i - \mathbf{r}_j|)} - 1 \tag{4.1.13}$$

Substitution of the hard-sphere interaction potential into the Mayer-f function then gives

$$f_{ij}^{HS}(|\mathbf{r}_i - \mathbf{r}_j|) = \begin{cases} -1 & |\mathbf{r}_i - \mathbf{r}_j| < R_i + R_j \\ 0 & \text{otherwise} \end{cases} \tag{4.1.14}$$

which can be identified as a negative Heaviside function, $-\Theta(|\mathbf{r}_i - \mathbf{r}_j| - (R_i + R_j))$. The Mayer-f function for a hard-sphere fluid therefore describes the excluded volume of the fluid [42, 111, 114]. Rosenfeld described this excluded volume in terms of geometrical measures of the individual spheres i and j. He found this to be possible using a deconvolution of the Mayer-f function in terms of four scalar weight functions, ω_α, and two vector weight functions, $\vec{\omega}_\alpha$. Rosenfeld found [114]

$$-f_{ij}(|\mathbf{r}_i - \mathbf{r}_j|) = \omega_3^i \otimes \omega_0^j + \omega_0^i \otimes \omega_3^j + \omega_2^i \otimes \omega_1^j + \omega_1^i \otimes \omega_2^j - \vec{\omega}_2^i \otimes \vec{\omega}_1^j - \vec{\omega}_1^j \otimes \vec{\omega}_2^j \tag{4.1.15}$$

where the three-dimensional convolution is defined as

$$\omega_\alpha^i \otimes \omega_\beta^j(\mathbf{r} = \mathbf{r}_i - \mathbf{r}_j) = \int \mathrm{d}\mathbf{r}' \omega_\alpha^i(\mathbf{r}' - \mathbf{r}_i)\omega_\beta^j(\mathbf{r}' - \mathbf{r}_j) \tag{4.1.16}$$

and the weight functions are defined as

$$\begin{aligned} \omega_3^i(\mathbf{r}) &= \Theta(R_i - r) \\ \omega_2^i(\mathbf{r}) &= \delta(R_i - r) \\ \vec{\omega}_2^i(\mathbf{r}) &= \frac{\mathbf{r}}{r}\delta(R_i - r) \\ \omega_1^i(\mathbf{r}) &= \frac{\omega_2^i(\mathbf{r})}{4\pi R_i} \\ \omega_0^i(\mathbf{r}) &= \frac{\omega_2^i(\mathbf{r})}{4\pi R_i^2} \\ \vec{\omega}_1^i(\mathbf{r}) &= \frac{\vec{\omega}_2^i(\mathbf{r})}{4\pi R_i} \end{aligned} \tag{4.1.17}$$

Integration over each of these scalar weight functions gives a fundamental measure of a sphere, for example, integration over $\omega_3^i(\mathbf{r})$ gives the volume V_i of the sphere i. Integrals over the vector weight functions vanish. The recovery of these fundamental measures is what gives FMT its name [111, 114].

The weighted densities, $n_\alpha(\mathbf{r})$, are defined using these weight functions, as

$$n_\alpha(\mathbf{r}) = \sum_{i=1}^{\nu} \int \mathrm{d}\mathbf{r}' \rho_i(\mathbf{r}') \omega_\alpha^i(\mathbf{r} - \mathbf{r}') \tag{4.1.18}$$

In the bulk limit, where the spatially varying density becomes homogeneous ($\rho_i(\mathbf{r}) \to \rho_b^i$), the scalar weighted densities reduce to the Scaled Particle Theory (SPT) variables, $n_3 \to \sum_{i=1}^{\nu} \rho_b^i 4\pi R_i^3/3$, $n_2 \to \sum_{i=1}^{\nu} \rho_b^i 4\pi R_i^2$, $n_1 \to \sum_{i=1}^{\nu} \rho_b^i R_i$, and $n_0 \to \sum_{i=1}^{\nu} \rho_b^i$. The vector weighted densities, $\mathbf{n}_2$ and $\mathbf{n}_1$, vanish [111].

The basic assumption of FMT is that the excess free energy can be written as

$$\beta \mathcal{F}_{ex}[\{\rho_i(\mathbf{r})\}] = \int \mathrm{d}\mathbf{r}' \Phi_{ex}(\{n_\alpha(\mathbf{r}')\}) \tag{4.1.19}$$

where Φ_{ex}, the reduced free energy density, is a function of the weighted densities. This form of $\mathcal{F}_{ex}[\rho(\mathbf{r})]$ recovers the first order term of the low density expansion of the free energy, which can be written in terms of weighted densities as [111]

$$\lim_{\{\rho_i \to 0\}} \beta \mathcal{F}_{ex}[\{\rho_i\}] = \int \mathrm{d}\mathbf{r} \{n_0(\mathbf{r}) n_3(\mathbf{r}) + n_1(\mathbf{r}) n_2(\mathbf{r}) - \mathbf{n}_1(\mathbf{r}) \cdot \mathbf{n}_2(\mathbf{r})\} \tag{4.1.20}$$

Using dimensional analysis, Rosenfeld found the form of Φ_{ex} to be

$$\Phi_{ex} = f_1(n_3) n_0 + f_2(n_3) n_1 n_2 + f_3(n_3) \mathbf{n}_1 \cdot \mathbf{n}_2 + f_4(n_3) n_2^3 + f_5(n_3) n_2 \mathbf{n}_2 \cdot \mathbf{n}_2 \tag{4.1.21}$$

where $f_1, \ldots, f_5$ are unknown functions of n_3. It should be noted that the deconvolution of the Mayer-f function is not unique. Kierlik and Rosinberg [121] found an equivalent deconvolution which used four distinct scalar weight functions and removed the need for vector weight functions.

It can be found that $f_2(n_3) = -f_3(n_3)$ and $f_5(n_3) = -3f_4(n_3)$. The remaining functions, f_1, f_2, and f_4 can be derived by demanding that Φ_{ex} obey an underlying thermodynamic relation. For this, Rosenfeld chose the exact SPT equation [111]

$$\lim_{R_i \to \infty} \frac{\beta \mu_{ex}^i}{V_i} \to \beta p \tag{4.1.22}$$

where p is the pressure of the system, and can be written as [111, 117, 122]

$$\beta p = n_0 - \Phi_{ex} + \sum_\alpha \frac{\partial \Phi_{ex}}{\partial n_\alpha} n_\alpha \tag{4.1.23}$$

In the bulk limit, the variational principle of cDFT tends to the form

$$\beta \mu_{ex} = \frac{\partial \beta \mathcal{F}_{ex}}{\partial \rho_i} = \frac{\partial \Phi_{ex}}{\partial n_0} + R_i \frac{\partial \Phi_{ex}}{\partial n_1} + 4\pi R_i^2 \frac{\partial \Phi_{ex}}{\partial n_2} + \frac{4\pi}{3} R_i^3 \frac{\partial \Phi_{ex}}{\partial n_3} \tag{4.1.24}$$

In the limit of large R_i, the excess chemical potential can therefore also be expressed as

$$\lim_{R_i\to\infty} \frac{\beta\mu_{ex}^i}{V_i} \to \frac{\partial\Phi_{ex}}{\partial n_3} \tag{4.1.25}$$

Equating the right hand sides of equations (4.1.23) and (4.1.25) gives the SPT differential equation, the solutions of which can be found to be

$$\frac{\partial f_1(n_3)}{\partial n_3} = \frac{1}{1-n_3} \quad \Rightarrow \quad f_1(n_3) = -\ln(1-n_3) + c_1 \tag{4.1.26}$$

$$\frac{\partial f_2(n_3)}{\partial n_3} = \frac{f_2(n_3)}{1-n_3} \quad \Rightarrow \quad f_2(n_3) = \frac{c_2}{1-n_3} \tag{4.1.27}$$

$$\frac{\partial f_4(n_3)}{\partial n_3} = \frac{2f_4(n_3)}{1-n_3} \quad \Rightarrow \quad f_4(n_3) = \frac{c_3}{(1-n_3)^2} \tag{4.1.28}$$

where c_1, c_2, c_3 are integration constants [111, 117].

The further conditions that Φ_{ex} recover the deconvolution of the Mayer-f function and the pair direct correlation function allows for the integration constants to be found to be [111, 117]

$$\begin{aligned} f_1(n_3) &= n_3 + \frac{n_3^2}{2}\mathcal{O}(n_3^3) \\ f_2(n_3) &= 1 + n_3 + \mathcal{O}(n_3^2) \\ f_4(n_3) &= \frac{1}{24\pi} + \mathcal{O}(n_3) \end{aligned} \tag{4.1.29}$$

Substitution of these into equation (4.1.21) then gives the Rosenfeld functional [111, 114, 117]

$$\Phi_{RF} = -n_0\ln(1-n_3) + \frac{n_1n_2 - \mathbf{n}_1\cdot\mathbf{n}_2}{1-n_3} + \frac{n_2^3 - 3n_2(\mathbf{n}_2\cdot\mathbf{n}_2)}{24\pi(1-n_3)^2} \tag{4.1.30}$$

The Rosenfeld functional is the original FMT functional, however subsequently many more have been developed. Popular examples of this include the White-Bear [123] and White-Bear Mark II [120] functionals, which utilise the more accurate Carnahan-Starling equation of state as the underlying thermodynamic relation. Despite their successes in the study of hard-sphere fluids, in their original forms, none of these are able to account for the hard-sphere crystal due to a diverging free energy term in the one-dimensional limit. It was later shown that an accurate description of the hard-sphere crystal required tensorial weighted densities [111]. As the present work is concerned solely with fluids, an accurate description of the freezing transition is not required. Due to its simpler form, the functional used throughout this work is the Rosenfeld functional, given in equation (4.1.30).

FMT provides a means of approximating $\mathcal{F}_{ex}[\{\rho_i\}]$, however it is its derivative that is required to implement cDFT. As FMT makes use of weighted densities, it is more convenient to express this derivative, which gives the one-body direct correlation function, as a functional derivative of the weighted densities themselves. This is possible using the functional version

of the chain rule, defined as [42]

$$\frac{\delta A[u(\mathbf{x})]}{\delta u(\mathbf{x})} = \int \mathrm{d}\mathbf{x}' \frac{\delta A[u(\mathbf{x})]}{\delta v(\mathbf{x}')} \frac{\delta v(\mathbf{x}')}{\delta u(\mathbf{x})} \tag{4.1.31}$$

where $v(\mathbf{x}')$ is a function. Applying this to equation (4.1.19) gives an expression for the one-body direct correlation function [111]

$$c_{HS}^{(1)}(\mathbf{r}) = -\sum_{\alpha} \int \mathrm{d}\mathbf{r}' \frac{\delta \Phi_{ex}(\{n_\alpha\})}{\delta n_\alpha(\mathbf{r}')} \frac{\delta n_\alpha(\mathbf{r}')}{\delta \rho(\mathbf{r})} \tag{4.1.32}$$

As Φ_{ex} is a function of n_α, as opposed to a functional, the first derivative can be simplified to a normal derivative. These derivatives can be calculated analytically, and can be found in appendix A for the Rosenfeld functional.

The present work is concerned only with one-component fluids, hence $\nu = 1$. The pressure of the one-component hard-sphere fluid, described using the Rosenfeld functional, is by design equivalent to the Percus-Yevick compressibility equation of state, which can be written in terms of the packing fraction, $\eta = 4\pi R^3 \rho_b / 3$, as [42]

$$p_{HS} = k_{\mathrm{B}} T \rho_b \frac{1 + \eta + \eta^2}{(1-\eta)^3} \tag{4.1.33}$$

Using equation (4.1.24), the chemical potential of the one-component hard-sphere fluid described by the Rosenfeld functional can be written as

$$\mu_{HS} = \mu_{id} + \mu_{ex} = k_{\mathrm{B}} T \left[\ln(\Lambda^3 \rho_b) + \frac{14\eta - 13\eta^2 + 5\eta^3}{2(1-\eta)^3} - \ln(1-\eta) \right] \tag{4.1.34}$$

4.1.3 Extension of cDFT to Lennard-Jones Fluids

cDFT can be extended from a hard-sphere fluid described by FMT to an attractive fluid using a MFT approach similar to that of section 2.4.3. In addition to being a functional of $\rho(\mathbf{r})$, equation (4.1.2) is also a functional of the ff interaction potential, ϕ. Assuming that ϕ is a pairwise additive interaction potential, such that $\phi \equiv \phi(\mathbf{r}, \mathbf{r}')$, then the functional derivative of $\Omega[\phi(\mathbf{r}, \mathbf{r}')]$ can be found to have the property [42, 45]

$$\frac{\delta \Omega[\phi(\mathbf{r}, \mathbf{r}')]}{\delta \phi(\mathbf{r}, \mathbf{r}')} = \frac{\delta \mathcal{F}_{ex}[\phi(\mathbf{r}, \mathbf{r}')]}{\delta \phi(\mathbf{r}, \mathbf{r}')} = \frac{1}{2} \rho^{(2)}(\mathbf{r}, \mathbf{r}') \tag{4.1.35}$$

where $\rho^{(2)}(\mathbf{r}, \mathbf{r}')$ is the two-particle density given in equation (2.3.4). If $\phi(\mathbf{r}, \mathbf{r}')$ is taken to have the linear perturbation form of equation (2.4.9), integration of equation (4.1.35) at constant one-particle density leads to [42, 45]

$$\mathcal{F}_{ex}[\rho(\mathbf{r})] = \mathcal{F}_o[\rho(\mathbf{r})] + \frac{1}{2} \int_0^\lambda \mathrm{d}\lambda \int \mathrm{d}\mathbf{r} \int \mathrm{d}\mathbf{r}' \rho_\lambda^{(2)}(\mathbf{r}, \mathbf{r}') \phi_{att}(\mathbf{r}, \mathbf{r}') \tag{4.1.36}$$

where $\mathcal{F}_o$ is the excess Helmholtz free energy functional of the purely repulsive reference fluid and other terms take their definitions as in section 2.4.3. Under a MFT approach,

correlations are ignored which equates to assuming $\rho_\lambda^{(2)}(\mathbf{r},\mathbf{r}') \approx \rho(\mathbf{r})\rho(\mathbf{r}')$. If the reference fluid is described using FMT, then $\mathcal{F}_{ex}[\rho(\mathbf{r})]$ can be written as

$$\mathcal{F}_{ex}[\rho(\mathbf{r})] = \mathcal{F}_{ex}^{HS}[\rho(\mathbf{r})] + \frac{1}{2}\int \mathrm{d}\mathbf{r}' \int \mathrm{d}\mathbf{r}\rho(\mathbf{r})\rho(\mathbf{r}')\phi_{att}(\mathbf{r},\mathbf{r}') \tag{4.1.37}$$

where $\mathcal{F}_{ex}^{HS}[\rho(\mathbf{r})]$ is the excess Helmholtz free energy functional of the hard-sphere fluid given in equation (4.1.19). This is often referred to as the standard MFT treatment of attraction within cDFT. Taking the functional derivative of equation (4.1.37) then gives the one-body direct correlation function for an attractive fluid

$$c^{(1)}(\mathbf{r}) = c_{HS}^{(1)}(\mathbf{r}) - \beta \int \mathrm{d}\mathbf{r}'\rho(\mathbf{r}')\phi_{att}(\mathbf{r},\mathbf{r}') \tag{4.1.38}$$

where $c_{HS}^{(1)}(\mathbf{r})$ is obtained using equation (4.1.32)

Utilising a MFT perturbation treatment for the fluid limits the types of fluids which cDFT can be applied to. Notably, the attractive interactions within these fluids must be weak, such that the structure of the fluid is predominantly determined by the packing of the reference fluid [42]. It was recently concluded by Gußmann et al. [119] that it is this condition that has hampered attempts to produce a successful treatment of the Jagla fluid within cDFT. The Jagla fluid has been found to exhibit several properties similar to water and has the advantage that it utilises a far simpler interaction potential compared to most water models. However, the long-ranged attractive perturbation of the Jagla potential was found to be too strong to be accurately described by a simple perturbation theory, particularly one which is truncated to lowest order terms like that considered here. Attempting to extend the perturbation theory treatment to higher order terms requires knowledge or accurate approximations for higher order particle distributions which is typically not realistically possible [42]. Taking an alternative approach, Hughes et al. [118] have proposed a cDFT for water using Statistical Associating Fluid Theory (SAFT). Whilst their functional shows promise, particularly on describing the surface tension of water over a range of temperatures, when compared to molecular simulations of a popular water model, their functional was found to severely overestimate the density of the fluid at the surface of a solute and failed to correctly predict the positions of the solvation shells.

Whilst research into novel cDFT functionals to describe a range of fluids is ongoing, it can be concluded from examples such as these that the inhomogeneous fluids which can be accurately represented in cDFT is currently very limited. One well established inhomogeneous fluid for which cDFT functionals have been shown to be highly accurate is the Lennard-Jones (LJ) fluid [42]. Several perturbation theories for inhomogeneous fluids based on this have been introduced, with the two most notable being the Barker-Henderson and Weeks-Chandler-Anderson (WCA) theories. The latter of these is particularly simple as it allows for a first-order approximation to the perturbation expansion, as used in equation (4.1.37) [119]. Under the WCA scheme, the attractive part of the LJ potential is taken to have the

form [1, 45, 117]

$$\phi_{att}(|\mathbf{r}-\mathbf{r}'|) = \begin{cases} -\varepsilon & |\mathbf{r}-\mathbf{r}'| < r_{min} \\ 4\varepsilon\left[\left(\frac{\sigma}{|\mathbf{r}-\mathbf{r}'|}\right)^{12} - \left(\frac{\sigma}{|\mathbf{r}-\mathbf{r}'|}\right)^{6}\right] & r_{min} < |\mathbf{r}-\mathbf{r}'| < r_c \\ 0 & |\mathbf{r}-\mathbf{r}'| > r_c \end{cases} \tag{4.1.39}$$

where $\mathbf{r}$ and $\mathbf{r}'$ represent the locations of two particles, $r_{min} = 2^{1/6}\sigma$ represents the minimum in the LJ potential, r_c is the cut-off radius of interaction, σ the radius of the fluid particle, and ε is the ff interaction strength.

In the bulk limit, equation (4.1.37) corresponds to the perturbation theory of section 2.4.3. Because of this, the liquid-vapour phase diagram for the LJ fluid within cDFT can be determined using the ideas presented in section 2.4.4. The critical point can be determined using the conditions presented in equation (2.4.18), whilst the coexisting densities of the liquid and vapour phases for a given temperature can be determined by simultaneously solving for equal chemical potential and pressure, using equations (2.4.17) and (2.4.16), where $p_o = p_{HS}$ as given in equation (4.1.33), $\mu_o = \mu_{HS}$ as given in equation (4.1.34), and the attractive component is

$$\begin{aligned} a &= -\frac{1}{2}\int \mathrm{d}\mathbf{r}\phi_{att}(r = |\mathbf{r}-\mathbf{r}'|) \\ &= -\frac{1}{2}\int_0^{2\pi}\mathrm{d}\varphi\int_0^{\pi}\mathrm{d}\theta\sin\theta\int_0^{r_c}\mathrm{d}r\, r^2\phi_{att}(r) \\ &= \frac{2\pi\varepsilon}{3}\left[r_{min}^3 + \frac{4\sigma^{12}}{3}\left(\frac{1}{r_c^9} - \frac{1}{r_{min}^9}\right) - 4\sigma^6\left(\frac{1}{r_c^3} - \frac{1}{r_{min}^3}\right)\right] = \varepsilon c_{LJ} \end{aligned} \tag{4.1.40}$$

4.1.4 Numerical Procedure

Equations (4.1.9), (4.1.32) and (4.1.38) provide the necessary components for finding the equilibrium density profile of an inhomogeneous fluid within cDFT using numerical minimisation. In order to perform this minimisation, it is first necessary to discretise the density profile, $\rho(\mathbf{r})$, into small regions of space of size dr over which the density is constant. dr is typically taken to be in the range $[0.002\sigma, 0.01\sigma]$ and, to ensure numerical stability, should be chosen such that σ/dr is an integer. An initial estimate for the density profile must then be made. If a density profile from a similar system is available, then this can be used. If not, the initial density profile is typically taken to be zero within the solute or substrate, and equal to the bulk density of the fluid, ρ_b, outside. The numerical procedure to find the equilibrium density profile is then

1. Calculate the weighted densities using equations (4.1.18) and (4.1.17).
2. Calculate the one-body direct correlation function according to equation (4.1.38).
3. Propose a new density profile according to equation (4.1.9), where μ_{ex} is found using equations (2.4.17), (4.1.34), and (4.1.40) and the thermal de Broglie wavelength is set

to $\Lambda = \sigma$. To improve numerical stability, this profile is then mixed with the current density profile.

4. Repeat until the maximum difference between the current and proposed density profiles is less than the tolerance, typically taken to be 10^{-12}.

Equations (4.1.18) and (4.1.38) involve convolutions of the density profile with weight functions, or the attractive potential. These are most easily performed using fast Fourier transforms (FFT). For numerical stability, the proposed density profile is mixed with the current profile, using one of two mixing schemes. The first is the Picard scheme, which uses a mixing parameter, α, to mix the current, $\rho_i(\mathbf{r})$, and proposed, $\rho_p(\mathbf{r})$, density profiles, to find the new density profile, $\rho_{i+1}(\mathbf{r})$. This mixing is done according to [111, 117]

$$\rho_{i+1}(\mathbf{r}) = (1-\alpha)\rho_i(\mathbf{r}) + \alpha\rho_p(\mathbf{r}) \tag{4.1.41}$$

The exact value of α that can be used depends on the system in question. For example, the numerical stability of the procedure can be poor for systems very close to drying and hence a smaller mixing parameter is needed. In contrast, further from drying, the numerical procedure is more stable, and hence larger α can be used. In general, the mixing parameter is taken to be in the range $(0, 0.1]$.

An alternative mixing scheme is that of Ng, given in the appendix of [124]. Under this procedure, the new density profile, $\rho_{i+1}(\mathbf{r})$, is a mixture of several trial density profiles. This procedure converges to the equilibrium density profile faster however is less stable. Because of this, Picard and Ng moves are typically used in combination, to ensure that stability is maintained whilst also facilitating fast convergence to the equilibrium density profile.

4.1.5 Implementation of cDFT in Different Geometries

The density profile of an inhomogeneous fluid takes the spatial symmetry of the external potential [111]. Because only smooth surfaces and solutes are considered within the present work, V_{ext} in each case is a function of only one spatial variable. In the case of a macroscopic substrate, the external potential is taken to act along the Cartesian z-axis, which means $V_{ext}(\mathbf{r}) \equiv V_{ext}(z)$ and hence $\rho(\mathbf{r}) \equiv \rho(z)$. For a solute, V_{ext} is taken to act along the radial axis extending from the centre of the solute, hence $V_{ext}(\mathbf{r}) \equiv V_{ext}(r)$ and therefore $\rho(\mathbf{r}) \equiv \rho(r)$. As the density profile in each case is homogeneous in two coordinates, equation (4.1.38) can be evaluated analytically in two dimensions, which improves the speed at which cDFT minimisations can be performed.

The numerical consistency of a cDFT minimisation can be tested using statistical mechanics sum rules. These sum rules provide links between different thermodynamic and microscopic properties of a system. One such sum rule can be constructed using equation (2.1.10), which relates the adsorption to the derivative of the surface tension. Within cDFT, the adsorption and surface tension can be calculated separately, using equation (2.3.11) for the former, and equations (4.1.2) and (2.1.13) for the latter. The agreement between either side of equation (2.1.10) then gives an indication of the consistency of the calculation.

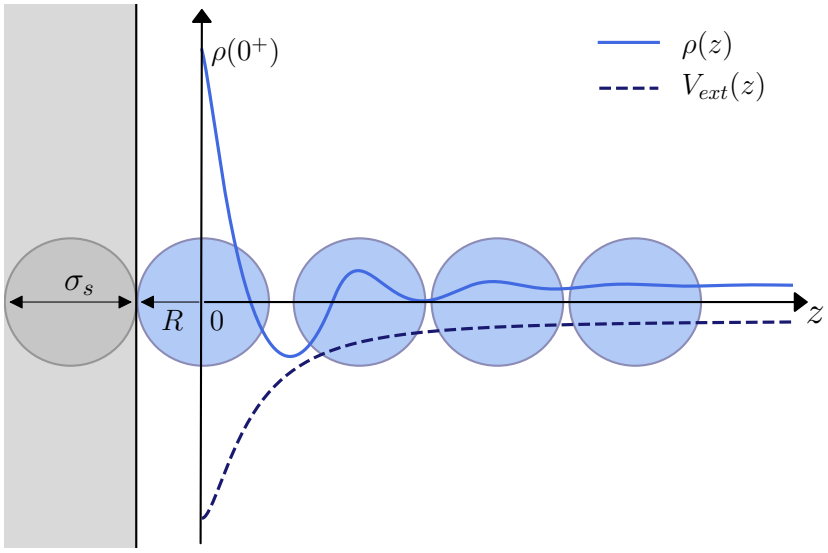

Figure 4.1: Illustration of the layout of a cDFT system consisting of a macroscopic planar substrate, shown in grey, in contact with a fluid, the particles of which are shown in blue and have radius R. The substrate is smooth, impenetrable, assumed to be made of particles of diameter σ_s and homogeneous density ρ_s, and exists where $z < -R$. The substrate and fluid interact via a purely attractive interaction outside of the substrate, which varies only along the z-axis. The density profile of the fluid takes the symmetry of the external potential and also varies only along the z-axis. As the density of the fluid is measured from the centre of the fluid particles, the first non-zero density or contact density, denoted as $\rho(0^+)$, will occur a distance R from the surface. The effective position of the surface is therefore at $z = 0$.

This sum rule is known as the Gibbs' adsorption sum rule. In addition to this sum rule, a second was used to confirm the consistency of the numerical calculations. This was the contact theorem, which relates the pressure of the fluid to the density of the fluid at the surface/solute.

4.1.5.1 Implementation of Planar Substrates

The configuration of a cDFT system for studying macroscopic surfaces within this work can be seen in figure 4.1. The substrate, shown in grey, is assumed to be impenetrable and made of particles of diameter σ_s and homogeneous density, ρ_s, which interact with the fluid particles, shown in blue, via a LJ attraction. The density of the fluid is measured from the centre of the fluid particles and the system arranged such that the first non-zero density to the right of the wall, called the contact density, occurs at $z = 0^+$, where the $+$ represents the approach from the right.

Within such a system, the weighted densities for the one-component hard-sphere fluid described using FMT, as given in equation (4.1.18), can be simplified to [111]

$$n_\alpha(\mathbf{r}) \equiv n_\alpha(z) = \int \mathrm{d}z' \rho(z') \omega_\alpha(z - z') \tag{4.1.42}$$

where the weight functions in equation (4.1.17) can be written as a function of z only as [111]

$$\begin{aligned}
\omega_3(z) &= \pi(R^2 - z^2)\Theta(R - |z|) \\
\omega_2(z) &= 2\pi R\Theta(R - |z|) \\
\vec{\omega}_2(z) &= 2\pi z\Theta(R - |z|)\widehat{\mathbf{k}} \\
\omega_1(z) &= \frac{\omega_2(z)}{4\pi R} \\
\omega_0(z) &= \frac{\omega_2(z)}{4\pi R^2} \\
\vec{\omega}_1(z) &= \frac{\vec{\omega}_2(z)}{4\pi R}
\end{aligned} \tag{4.1.43}$$

and $\widehat{\mathbf{k}}$ is the unit vector along the z-axis.

Calculating the hard-sphere part of $c^{(1)}(\mathbf{r}) \equiv c^{(1)}(z)$ requires the functional derivative of the weighted densities with respect to the density profile. The functional derivative can be found to be

$$\frac{\delta n_\alpha(z')}{\delta\rho(z)} = \omega_\alpha(z' - z) \tag{4.1.44}$$

As the scalar weight functions are even functions, $\omega_\alpha(z' - z) = \omega_\alpha(z - z')$. The vector weight functions are odd functions and hence $\vec{\omega}_\alpha(z' - z) = -\vec{\omega}_\alpha(z - z')$ [111].

Reducing the attractive fluid interaction potential, given in equation (4.1.39), to a function of only $|z - z'|$ requires careful consideration of the piece-wise potential and the intersection of the spherical symmetry of the potential and planar symmetry of the density profile. A derivation for calculating the integrated potential can be found in appendix B.1, with the result being

$$\phi_{att}(|z - z'|) = \begin{cases} \pi\varepsilon\left[|z - z'|^2 - r_{min}^2 + \frac{4}{5}\sigma^{12}\left(\frac{1}{r_{min}^{10}} - \frac{1}{r_c^{10}}\right) - \right. & \\ \qquad \left. 2\sigma^6\left(\frac{1}{r_{min}^4} - \frac{1}{r_c^4}\right)\right] & |z - z'| < r_{min} \\ \pi\varepsilon\left[\frac{4}{5}\sigma^{12}\left(\frac{1}{|z-z'|^{10}} - \frac{1}{r_c^{10}}\right) - 2\sigma^6\left(\frac{1}{|z-z'|^4} - \frac{1}{r_c^4}\right)\right] & r_{min} < |z - z'| < r_c \\ 0 & |z - z'| > r_c \end{cases} \tag{4.1.45}$$

This can then be substituted into equation (4.1.38) along with equation (4.1.32) to obtain $c^{(1)}(z)$.

The homogeneity of the substrate allows for the total attractive interaction felt by a particle at a given distance from the substrate, z, to be calculated by integrating over all particles within the substrate. The attraction between the fluid and substrate is taken to have the form of a LJ potential which has been shifted such that the minimum occurs at the surface of the substrate, $z = 0$. The minimum of the potential is shifted for numerical reasons, as a diverging potential on the approach to the surface can lead to poorly defined behaviour within discretised systems. The derivation for the integration of this potential can

be found in appendix B.2, with the final result taking the form

$$V_{ext}(z) = \begin{cases} \infty & z < 0 \\ \varepsilon_{sf}\left[\frac{2}{15}\left(\frac{\sigma_s}{z+z_{min}}\right)^9 - \left(\frac{\sigma_s}{z+z_{min}}\right)^3\right] & z > 0 \end{cases} \tag{4.1.46}$$

where $\varepsilon_{sf} = 2\pi\rho_s\varepsilon_s\sigma_s^3/3$ is a measure of the substrate-fluid attraction strength, ε_s is the well depth of the sf LJ potential, and $z_{min} = (2/5)^{1/6}\sigma_s$ is the location of the minimum of the interaction potential. For simplicity, σ_s was taken to be $\sigma_s = \sigma$ throughout the present work. This result can then be substituted along with $c^{(1)}(z)$ into equation (4.1.9) to predict the equilibrium density during the numerical minimisation.

Within this geometry, the first test of numerical accuracy was the Gibbs' adsorption sum rule described previously, where the adsorption can be found using

$$\frac{\Gamma}{A} = \int_0^\infty \mathrm{d}z(\rho(z) - \rho_b) \tag{4.1.47}$$

where A is the surface area of the planar substrate. The second test of numerical accuracy is the contact theorem, which in this geometry takes the form [42, 125]

$$p = -\int_{-\infty}^{\infty} \mathrm{d}z\rho(z)\frac{\mathrm{d}V_{ext}(z)}{\mathrm{d}z} \tag{4.1.48}$$

The derivative of $V_{ext}(z)$ is performed in appendix B.3 and gives the contact sum rule within cDFT for a planar substrate to be

$$p = \beta^{-1}\rho(0^+) - \varepsilon_{sf}\int_0^\infty \mathrm{d}z\rho(z)\left[\frac{3\sigma_s^3}{(z+z_{min})^4} - \frac{6\sigma_s^9}{5(z+z_{min})^{10}}\right] \tag{4.1.49}$$

4.1.5.2 Implementation of Solutes

The layout of the cDFT system for studying a solute within this work is shown in figure 4.2. The solute, shown in grey, is assumed to be centred on the origin and to consist of particles of diameter σ_s of homogeneous density ρ_s. The fluid is unable to penetrate the solute and interacts with it via a purely attractive potential where $r > R_s$. As the density of the fluid is measured from the centre of the fluid particles, the first non-zero density, called the contact density, occurs at $\rho(R_s^+)$, where the + represents the approach from the right.

The weighted densities for the one-component hard-sphere reference fluid described by FMT within this geometry are given by [111]

$$n_\alpha(r) = \int \mathrm{d}r' r'^2 \rho(r')\omega_\alpha(r - r') \tag{4.1.50}$$

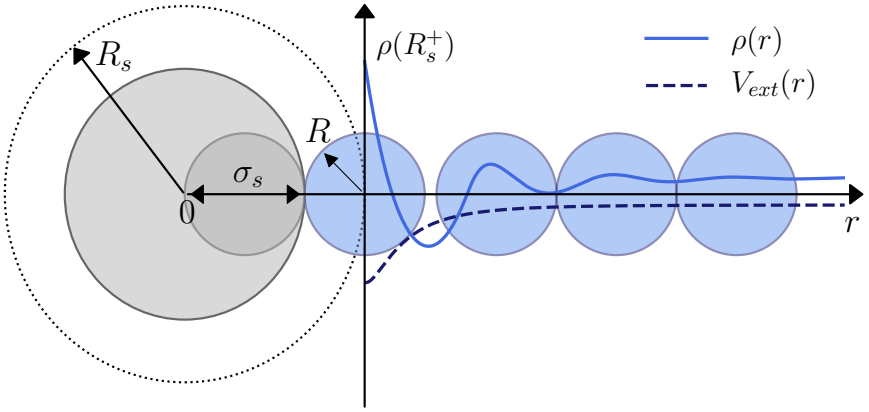

Figure 4.2: Illustration of the layout of cDFT for a system consisting of a solute, shown in grey, in contact with a fluid, shown in blue. The smooth and impenetrable solute is centred on the origin and imagined to consist of smaller particles of diameter σ_s of homogeneous density, ρ_s. Fluid surrounds the solute and is made up of particles, of radius R. The fluid and solute interact via a purely attractive potential, shown by the dashed blue line, which varies only along the radial axis. The density profile of the fluid, shown by the solid blue line, takes the symmetry of the external potential and hence also varies only along the radial axis. As the density of the fluid is measured from the centre of the fluid particles, the first non-zero density or contact density, $\rho(R_s^+)$, will occur a distance R from the surface of the solute. This allows for an effective radius of the solute to be defined as R_s.

where the weight functions are now defined as

$$\begin{aligned}
\omega_3(r-r') &= \frac{\pi}{rr'}(R^2 - |r-r'|^2)\Theta(R-|r-r'|) \\
\omega_2(r-r') &= \frac{2\pi R}{rr'}\Theta(R-|r-r'|) \\
\vec{\omega}_2(r-r') &= \omega_3(r-r')\frac{\hat{\mathbf{k}}}{r} + \frac{2\pi}{rr'}(r-r')\Theta(R-|r-r'|)\hat{\mathbf{k}} \\
\omega_1(r-r') &= \frac{\omega_2(r-r')}{4\pi R} \\
\omega_0(r-r') &= \frac{\omega_2(r-r')}{4\pi R^2} \\
\vec{\omega}_1(r-r') &= \frac{\vec{\omega}_2(r-r')}{4\pi R}
\end{aligned} \tag{4.1.51}$$

and $\widehat{\mathbf{k}}$ is the unit vector along the radial axis. The difference between these and the equivalent planar functions is the factor of $(rr')^{-1}$ within the scalar functions and the notably different form of the vector weights. As the scalar and vector weight functions now take such different forms, so do the functional derivatives of the weighted densities

$$\begin{aligned}
\frac{\delta n_\alpha(r')}{\delta\rho(r)} &= \omega_\alpha(r'-r) \\
\frac{\delta \vec{n}_2(r')}{\delta\rho(r)} &= \frac{\omega_3(r'-r)}{r'} + \frac{2\pi}{rr'}(r'-r)\Theta(R-|r'-r|)\hat{\mathbf{k}}
\end{aligned} \tag{4.1.52}$$

As in the planar case, the scalar weight functions are even functions and hence $\omega_\alpha(r'-r') = \omega_\alpha(r-r')$. The first term in the vector weight function, as a scalar function, is also even.

However, the second term is odd and therefore, when moving from $r'-r$ to $r-r'$, this term in the function must be multiplied by -1.

Reducing $\phi_{att}(|\mathbf{r}-\mathbf{r}'|)$ given in equation (4.1.39) to a function of only the radial distance $|r-r'|$ requires calculation of the intersection of a spherical interaction potential with spherical shells of constant density. The derivation for the integrated potential is given in appendix C.1, with the result being

$$\phi_{att}(|r-r'|) = \begin{cases} \frac{\pi\varepsilon}{rr'}\left[(r-r')^2 - r_{min}^2 + \frac{4}{5}\sigma^{12}\left(\frac{1}{r_{min}^{10}} - \frac{1}{(r+r')^{10}}\right)\right. & |r-r'| < r_{min}, \\ \qquad\left. - 2\sigma^6\left(\frac{1}{r_{min}^4} - \frac{1}{(r+r')^4}\right)\right] & r+r' < r_c \\ \frac{\pi\varepsilon}{rr'}\left[\frac{4}{5}\sigma^{12}\left(\frac{1}{(r-r')^{10}} - \frac{1}{(r+r')^{10}}\right)\right. & r_{min} < |r-r'| < r_c, \\ \qquad\left. - 2\sigma^6\left(\frac{1}{(r-r')^4} - \frac{1}{(r+r')^4}\right)\right] & r+r' < r_c \\ \frac{\pi\varepsilon}{rr'}\left[(r-r')^2 - r_{min}^2 + \frac{4}{5}\sigma^{12}\left(\frac{1}{r_{min}^{10}} - \frac{1}{r_c^{10}}\right)\right. & \\ \qquad\left. - 2\sigma^6\left(\frac{1}{r_{min}^4} - \frac{1}{r_c^4}\right)\right] & |r-r'| < r_{min} \\ \frac{\pi\varepsilon}{rr'}\left[\frac{4}{5}\sigma^{12}\left(\frac{1}{(r-r')^{10}} - \frac{1}{r_c^{10}}\right) - 2\sigma^6\left(\frac{1}{(r-r')^4} - \frac{1}{r_c^4}\right)\right] & r_{min} < |r-r'| < r_c \\ 0 & |r-r'| > r_c \end{cases} \tag{4.1.53}$$

The latter three terms have a very similar form to that of the planar potential, with the additional factor of $(rr')^{-1}$, and represent the cases in which the spherically symmetric attraction intersects the density shells. The first two cases occur only if $2R_s > r_c$, and represent the situation where the entire density shell is encompassed by the interaction potential - see appendix C.1 for further details. Within the present work, these cases are only necessary when considering LR ff potentials. This potential can then be substituted into equation (4.1.38) along with equation (4.1.32) to calculate $c^{(1)}(r)$.

The homogeneity of the solute allows for the total solute-fluid attractive potential felt by a fluid particle a distance r from the centre of the solute to be calculated by integrating over all particles within the solute. As in the planar case, the attraction takes the form of a LJ potential which has been shifted such that the minima occurs at the surface of the solute. A derivation for the integration of the potential can be found in appendix C.2, with the final potential taking the form

$$V_{ext}(r) = \begin{cases} \infty & r < R_s \\ \varepsilon_{sf}\left[\frac{2\sigma_s^9}{15}\left(\frac{1}{(r_+-R_s)^9} - \frac{1}{(r_++R_s)^9}\right) + \frac{3\sigma_s^9}{20r_+}\left(\frac{1}{(r_++R_s)^8} - \frac{1}{(r_+-R_s)^8}\right)\right. & \\ \left. +\sigma_s^3\left(\frac{1}{(r_++R_s)^3} - \frac{1}{(r_+-R_s)^3}\right) + \frac{3\sigma_s^3}{2r_+}\left(\frac{1}{(r_+-R_s)^2} - \frac{1}{(r_++R_s)^2}\right)\right] & r > R_s \end{cases} \tag{4.1.54}$$

where $\varepsilon_{sf} = 2\pi\rho_s\varepsilon_s\sigma_s^3/3$ as in the planar substrate case, and $r_+ = r + r_{min}$. Unlike in the case of a planar substrate, it is very difficult to evaluate the location of r_{min} analytically as it depends on the radius of the solute, R_s. For this reason, it must be found numerically. As for a planar surface, σ_s was taken to be $\sigma_s = \sigma$ throughout this work. In the limit that $R_s \to \infty$, the planar equivalent of this potential is recovered with the substitution $z = r - R_s$.

The adsorption for use in the Gibbs adsorption sum rule for a solute within cDFT can be

calculated using

$$\frac{\Gamma}{A} = \frac{1}{R_s^2}\int_{R_s}^{\infty} \mathrm{d}r r^2(\rho(r) - \rho_b) \tag{4.1.55}$$

where A is the surface area of the solute. The contact sum rule is derived using [117, 126]

$$\left(\frac{\partial \Omega}{\partial R_s}\right)_{T,\mu} = 4\pi \int \mathrm{d}r r^2 \rho(r) \frac{\partial V_{ext}(r)}{\partial R_s} \tag{4.1.56}$$

The left hand side of this equation can be simplified by substituting equation (2.1.6) and noting that $\gamma = \gamma(R_s)$. The differential of $V_{ext}(r)$ is calculated in appendix C.3. The final form of the contact sum rule for a solute is then

$$\begin{aligned} p + \frac{2\gamma(R_s)}{R_s} + \frac{\partial \gamma(R_s)}{\partial R_s} &= k_\mathrm{B} T \rho(R_s^+) + \\ \frac{\varepsilon_{sf}}{R_s^2}\int_{R_s}^{\infty} \mathrm{d}r \rho(r) r^2 \Bigg[\frac{6\sigma_s^9}{5} \Bigg(& \frac{1}{(r_+ - R_s)^{10}} + \frac{1}{(r_+ + R_s)^{10}} - \frac{1}{r_+(r_+ + R_s)^9} - \frac{1}{r_+(r_+ - R_s)^9} \Bigg) \\ & + 3\sigma_s^3 \Bigg(\frac{1}{r_+(r_+ + R_s)^3} + \frac{1}{r_+(r_+ - R_s)^3} - \frac{1}{(r_+ + R_s)^4} - \frac{1}{(r_+ - R_s)^4} \Bigg) \Bigg] \end{aligned} \tag{4.1.57}$$

4.1.6 Measures of Local Density Fluctuations within cDFT

Calculating $\chi_\mu(\mathbf{r})$ and $\chi_T(\mathbf{r})$, given in equation (2.5.1) and (2.5.2), within cDFT requires a simple numerical derivative of the density profile. For example, for $\chi_\mu(\mathbf{r})$ this has the form

$$\chi_\mu(\mathbf{r}) = \frac{\rho(\mathbf{r}; \mu + \Delta\mu) - \rho(\mathbf{r}; \mu)}{\Delta\mu} \tag{4.1.58}$$

where $\Delta\mu$ is some small addition to μ, taken to be $\Delta\mu = 10^{-8}$ within the present work. If instead the temperature is raised by $\Delta T = 10^{-8}$ at constant μ, then equation (4.1.58) gives $\chi_T(\mathbf{r})$. As $\rho(\mathbf{r})$ takes the symmetry of $V_{ext}(\mathbf{r})$, $\chi_\mu(\mathbf{r})$ and $\chi_T(\mathbf{r})$ will also take this symmetry.

The value of $\chi_T(\mathbf{r})$ for the bulk fluid, $\chi_{T,b}$ can be found using the temperature form of equation (4.1.58) by replacing $\rho(\mathbf{r})$ with ρ_b. For $\chi_\mu(\mathbf{r})$, the bulk value can be found using [1]

$$\begin{aligned} \chi_{\mu,b} = \rho_b^2 \kappa_T &= \rho_b \left(\frac{\partial \rho_b}{\partial p}\right)_T \\ &= \rho_b \left(\beta^{-1} \frac{1 + 4\eta + 4\eta^2}{(1-\eta)^4} + \frac{2p_{att}}{\rho_b} \right)^{-1} \end{aligned} \tag{4.1.59}$$

where κ_T is the isothermal compressibility and $p_{att} = -a\rho_b^2$ is the component of pressure of the fluid due to the attractive perturbation. Within this work, a was obtained using equation (4.1.40).

4.2 Monte Carlo Molecular Simulations

Molecular simulation has been utilised extensively in the study of hydrophobicity. Confirmation of the non-Gaussian fat tails in the occupancy probability distributions discussed in section 3.1.2 was achieved by Patel et al. [28] using molecular simulation, whilst the work of Giovambattista et al. [105] utilised molecular simulation to show the relationship between

the contact angle of a droplet, the polarity of the surface and the structure of local water molecules. Furthermore, molecular simulation has often been used in the analysis of experimental data, to enable the better understanding of the structure of water near a hydrophobic object [12, 78]. When performing molecular simulation, one of two methods can be used. The first of these is molecular dynamics, which is concerned with obtaining estimates of observable properties through time averages of microstates. In contrast, Monte Carlo (MC) aims to find estimates of observables through averages over ensembles of microstates. This work utilises the latter method of molecular simulation in conjunction with the Grand Canonical (GC) ensemble. This combination provides a highly efficient method of studying systems with inhomogeneous fluids, particularly those with large differences in the spatially varying density.

The primary aim of MC is to generate microstates over which an ensemble average can be obtained. This is done by performing a random walk through the phase space in which the microstates exist [42–44]. As was discussed in section 2.2, these microstates can be grouped into macrostates of constant E and N, which occur according to probability density distributions like those in equations (2.2.5) and (2.2.9). Considering these, it can be determined that the distribution of macrostates within systems which may be of interest is strongly peaked. Performing a uniform random walk over the ensemble would therefore be highly inefficient, as the low probability tails of the distribution would be sampled as often as the peak. To avoid this and improve efficiency, MC schemes typically make use of biased sampling, known as importance sampling, which acts to sample the peak of the distribution far more often than the tails. Whilst there are many possibilities for the applied bias, the most simple and commonly used is the equilibrium probability distribution of the statistical mechanics ensemble in which the macrostates exist, for example, equations (2.2.5) and (2.2.9) [43, 44].

The random walk itself takes the form of a Markov chain, whose limiting distribution is equal to the equilibrium probability distribution of the underlying ensemble. Each step in the Markov chain is generated in a multi-stage process, which involves first proposing a trial configuration of particles, known as a move, and then determining whether to accept or reject the move according to some acceptance criteria. The random walk must also obey the conditions of [42–44]

Ergodicity - It must be possible to reach every accessible state within a finite number of moves from any other state.

Detailed Balance - Once thermodynamic equilibrium is reached, it must not be destroyed. Therefore, at equilibrium, the average number of moves into a state must equal the average number of moves out of the state.

Ergodicity can be ensured by using an acceptance criteria scheme which obeys it, for example, the Metropolis scheme. This method in particular also ensures detailed balance by imposing the stricter condition, known as microscopic reversibility, that the number of moves in and out a microstate must be exactly equal [42, 43].

4.2.1 Metropolis Acceptance Criteria

Consider an initial microstate, i and a final microstate f. Microscopic reversibility under the Metropolis scheme requires that the number of moves from $i \to f$ exactly equal the number of moves $f \to i$. Let $\mathcal{N}(i)$ represent the probability of finding the system in i, $\mathcal{N}(f)$ the probability of finding it in f, and π the transition matrix of probability of moving from $i \to f$ and $f \to i$. Microscopic reversibility can then be expressed as [44]

$$\mathcal{N}(i)\pi(i \to f) = \mathcal{N}(f)\pi(f \to i) \tag{4.2.1}$$

The transition matrix can also be written as the product of the two stages of a Monte Carlo move [44]

$$\pi(i \to f) = \alpha(i \to f)P_{acc}(i \to f) \tag{4.2.2}$$

where $\alpha(i \to f)$ is the probability of generating the microstate f starting from i and $P_{acc}(i \to f)$ is the probability of accepting the move. Under the Metropolis scheme, α is chosen to be symmetric, such that $\alpha(i \to f) = \alpha(f \to i)$. This allows the condition of microscopic reversibility to be simplified to [44]

$$\frac{\mathcal{N}(f)}{\mathcal{N}(i)} = \frac{P_{acc}(i \to f)}{P_{acc}(f \to i)} \tag{4.2.3}$$

Whilst there are many forms of P_{acc} which would obey this, Metropolis chose [44]

$$P_{acc}(i \to f) = \begin{cases} \frac{\mathcal{N}(f)}{\mathcal{N}(i)} & \mathcal{N}(f) < \mathcal{N}(i) \\ 1 & \mathcal{N}(f) \geq \mathcal{N}(i) \end{cases} \tag{4.2.4}$$

Specifically, this choice ensures that the probability of acceptance will never exceed 1. Physically, this condition also means that, if $\mathcal{N}(f)$ is more probable than $\mathcal{N}(i)$, which would imply it is a lower energy macrostate, then the MC move should always be accepted. Otherwise, the decision of whether to accept or reject a move is taken by comparing $P_{acc}(i \to f)$ to a uniform random number in the range $[0, 1]$ [44].

The Metropolis acceptance criteria requires knowledge of only the relative probability of two macrostates. This is important for the implementation of MC in statistical mechanics ensembles, as calculating the absolute probability of each macrostate would require knowledge of the partition function, which is generally not possible. Using the relative probability conveniently overcomes this, as the factor of the partition function cancels [44].

4.2.2 Acceptance Probabilities within the Grand Canonical Ensemble

P_{acc} is dependent on the ensemble in which the microstates exist. In the present work, this is the GC ensemble. Within this ensemble, the simulation volume, or box, of constant volume V, is imagined to be in contact with a reservoir. The reservoir and simulation box are in thermal and chemical equilibrium, such that they share the same (μ, T). Throughout the simulation, the simulation box and reservoir are able to exchange both particles and heat, using one of the following moves [44]

1. The reservoir could give a particle to the simulation box. This is called an insertion move.
2. The simulation box could give a particle to the reservoir. This is called a deletion move.
3. The reservoir and simulation box could exchange energy. This is achieved by moving a single particle in the simulation box and therefore altering the inter-particle and external potential energies. This is known as a translation move.

The latter of these moves is not strictly necessary, as the deletion and later insertion of a particle is effectively equivalent to having translated the particle [68]. Because of this, only deletion and insertion moves are employed within the present work.

As discussed in section 4.2.1, there are multiple components to a MC move. For example, components of a MC insertion move can be written as [44]

$$K(N \to N+1) = \mathcal{N}(N)\alpha(N \to N+1)P_{acc}(N \to N+1) \tag{4.2.5}$$

where N is the current number of particles within the system. Using equation (2.2.9), $\mathcal{N}(N)$ within the GC ensemble can be identified as

$$\mathcal{N}_{GC}(N) = \frac{e^{-\beta(\mathcal{H}_N - \mu N)}}{\Xi} \tag{4.2.6}$$

where $\mathcal{H}_N$ is the Hamiltonian for, in this case, the fluid of N particles. Physically, $\alpha(N \to N+1)$ represents the probability of picking a specific location to insert a particle. Assuming every location is equally likely to be chosen, this can be identified as

$$\alpha(N \to N+1) = \frac{\Lambda^3}{V} \tag{4.2.7}$$

where Λ is the thermal de Broglie wavelength, and Λ^3 is an estimate of the volume which a single particle occupies. Substituting these into equation (4.2.5) then leads to

$$K(N \to N+1) = \frac{e^{-\beta(\mathcal{H}_N - \mu N)}}{\Xi}\frac{\Lambda^3}{V}P_{acc}(N \to N+1) \tag{4.2.8}$$

Under microscopic reversibility, this must equal the reverse move, which, using similar reasoning, can be written as

$$K(N+1 \to N) = \frac{e^{-\beta(\mathcal{H}_{N+1} - \mu(N+1))}}{\Xi}\frac{1}{N+1}P_{acc}(N+1 \to N) \tag{4.2.9}$$

where $\alpha(N+1 \to N) = 1/(N+1)$ is the probability of picking a single particle at random to delete, and assumes each particle is equally likely to be chosen. Equating equations (4.2.8) and (4.2.9) and rearranging then leads to the ratio of acceptance probabilities

$$\frac{P_{acc}(N \to N+1)}{P_{acc}(N+1 \to N)} = \frac{V}{\Lambda^3(N+1)}e^{-\beta(\Delta E - \mu)} \tag{4.2.10}$$

where $\Delta E = \mathcal{H}_{N+1} - \mathcal{H}_N$. Within a MC simulation, this specifically is the difference in the

inter-particle and external potential energies of the configurations with N and $N+1$ particles.

Using similar reasoning, the ratio of acceptance probabilities for a deletion move, $P_{acc}(N \to N-1)/P_{acc}(N-1 \to N)$, can also be obtained. Invoking the Metropolis result given in equation (4.2.4) then leads to the acceptance probabilities of moves within GCMC [44]

$$\begin{aligned} P_{acc}(N \to N+1) &= \min\left[1, \frac{V}{\Lambda^3(N+1)} e^{-\beta(\Delta E - \mu)}\right] \\ P_{acc}(N-1 \to N) &= \min\left[1, \frac{\Lambda^3 N}{V} e^{-\beta(\Delta E + \mu)}\right] \end{aligned} \tag{4.2.11}$$

As is standard in GCMC, Λ was taken to be the diameter of a particle throughout the present work.

4.2.3 Implementation

The general procedure to implement a MC move within the GC ensemble is as follows [44]

1. Choose at random whether to attempt to insert or delete a particle.
2. Calculate the energy that the inserted/deleted particle contributes to the system. This energy will include that of interactions with other particles as well as any external potential applied.
3. Calculate the probability of accepting the move according to equation (4.2.11).
4. Accept/reject the move by comparing the acceptance probability to a uniform random number and update the system to reflect the decision taken.

This process is repeated typically millions of times, during which samples of the system are taken for use in the calculation of properties, such as the average density. Due to the large number of times in which the system will undergo this process, moves within MC tend to be grouped into sweeps, where the definition of a sweep can vary between studies.

Within a MC move, it is the process of calculating the energy which a chosen particle contributes or would contribute to the system which is computationally demanding, and constitutes the majority of the simulation time. As such many schemes exist to reduce this computation, and therefore to increase the speed at which simulations can be performed. One such method, which is particularly useful for SR pairwise potentials like those considered within this work, is that of cell lists [44]. Consider a particle to be inserted within the system, which interacts with other particles using such a potential. In order to determine the energy that this single particle contributes, it is in theory necessary to consider every particle within the system. However, the particles within the system interact over a finite range, denoted as r_c, which means that many particles will not interact with that to be inserted, and hence searching the entire system is wasteful. Instead, it would be better to only search for particles a distance r_c from the particle to be inserted. One way to ensure that only this nearby distance is searched is to segment the simulation box into cubes of side length r_c,

called cells. Particles will only interact with those within their cell, or within a neighbouring cell, hence instead of searching the entire system for particles which interact with that to be inserted, it is sufficient to search only particles in neighbouring cells. This greatly reduces the computational cost of computing the energy contribution of a particle to the system. Within this work, the use of cells allows for the definition of a sweep as a move attempt per number of cells within the simulation box.

If the particle interaction potential is finite ranged, but now consists of an additional three-body component, then searching only neighbouring cells for interacting particles is insufficient. This is best understood by considering figure 4.3. Consider particle i, which interacts via a three-body interaction with a particle k through an intermediate particle j. Particle k is not within a neighbouring cell of i, and hence if only neighbouring cells were searched for interacting particles, this interaction would go undetected. The consequence of this is that, for potentials with three-body components, it is necessary to search both neighbouring, and next-neighbouring cells.

Another important factor to consider in molecular simulation is the finite nature of the simulation box. Specifically, what to do to at the edges of the box. If the sides and edges of the box are considered impenetrable then particles in cells which exist at the edge of the box will have fewer nearest neighbours than particles near the centre of the box. The sides of the box then act as an external potential, from which particles may retreat. This prevents the simulation results from accurately representing, for example, a bulk fluid. One method to overcome this, if a bulk fluid representation is desirable, is to implement periodic boundary conditions. These assume that, at the edge of the box, an exact replica of the box exists, and thus each particle, irrespective of its location, will have the same number of nearest neighbours [44]. If cell lists are used, implementing periodic boundary conditions is further simplified, as it is only necessary for there to be a replica of one cell at the edge of the box, rather than the entire box. Practically, periodic boundary conditions then amounts to searching the cells on the opposing side of the simulation box, from the one in which the particle of interest exists, to find interacting particles [44].

Finally, when starting a MC simulation, it is necessary to consider the initial configuration of particles. There are several ways to approach this, for example, the simulation box could be empty to begin with, and then allowed to fill with particles, or a configuration obtained from a similar simulation could be used. Within this work, the bulk fluid of interest is a liquid, which is very near liquid-vapour coexistence. In this case, it is necessary that the initial configuration of particles be that of a liquid. One way to ensure this is to run a short simulation in a fairly dense liquid, far from liquid-vapour coexistence. However, as this initial liquid configuration is generated at a different set of parameters, which are far from liquid-vapour coexistence, it will not be initially in equilibrium at the thermodynamic parameters, μVT, to be considered within the simulation. It is therefore necessary to perform a number of sweeps before measuring observables, to allow the system to reach equilibrium, in a process aptly known as equilibration. After equilibration, samples for the evaluation of the observable can be taken. Although each MC move generates a new configuration, which

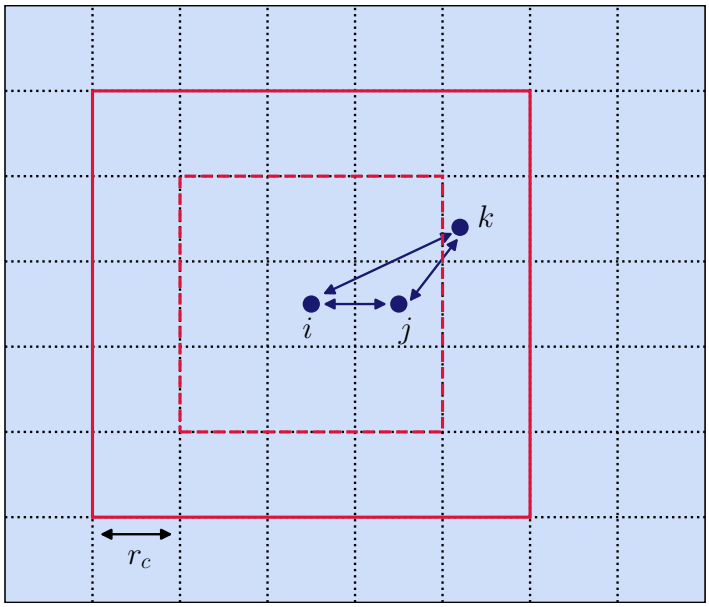

Figure 4.3: Example of a simulation box which has been divided into cubic cells of side length, r_c, where r_c is the maximum distance over which a pair of particles interact. If the interaction potential is purely pairwise, then every particle which interacts with particle i will fall within a neighbouring cell of i, which are indicated by the red dashed line. If instead the interaction potential is three-body, then i may interact with a particle k which falls outside these neighbouring cells via an intermediate particle j. Particles which interact with i in this case will fall within the solid red box.

constitutes a valid sample, configurations near one another will be fairly similar and highly correlated. Hence it is best to allow several sweeps to occur before sampling the observable.

4.2.4 Multicanonical and Transition Matrix Methods

Under certain circumstances, accepting and rejecting moves according to the GC acceptance probabilities given in equation (4.2.11) is inadequate to fully explore the available macrostates. For example, consider a fluid at liquid-vapour coexistence far below the critical point. Figure 4.4(a) shows an illustration of the free energy per particle, E/N, for such a fluid. Two troughs of equal depth, which represent the equilibrium free energies of the liquid and vapour phases, are separated by a large free energy barrier, shown by the red arrow. Due to the favourable free energy, the probability of the system being in the liquid or vapour phases will be high. Similarly, due to the unfavourable free energy the probability of being in an intermediate phase, which is a mixture of the liquid and vapour phases, is low. This is shown in figure 4.4(b) by the solid line. This low probability prevents the simulation from moving between the liquid and vapour phases, thus hampering the sampling. Under such conditions, it is necessary to bias the underlying acceptance probabilities, such that it becomes more favourable to be in the mixed-phase macrostate. One method in which to do this is to use the multicanonical ensemble [44, 68].

Under the multicanonical ensemble, a bias is applied to the probability, $\mathcal{N}$, of finding the system in macrostate m, such that the biased probability, $\tilde{\mathcal{N}}(m)$, becomes [44, 68]

$$\tilde{\mathcal{N}}(m) = \frac{\mathcal{N}(m)e^{\eta_m}}{\tilde{\Xi}} \tag{4.2.12}$$

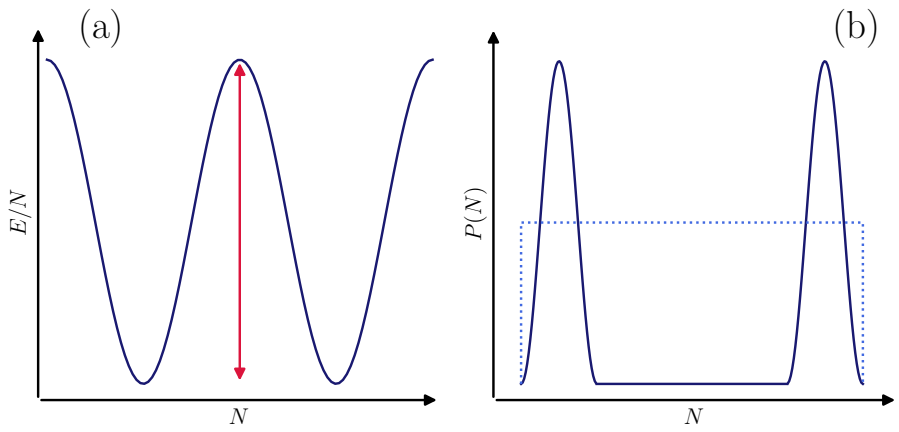

Figure 4.4: (a) Illustration of the variation of the free energy per particle with number of particles for a fluid at liquid-vapour coexistence. Two troughs of equal depth represent the liquid and vapour phases. A large free energy barrier, indicated by the red arrow, exists between the phases. (b) Solid Line - corresponding probability distribution of the number of particles within the system. The large free energy barrier results in a low probability of the fluid being in a mixed phase. Dotted line - example probability distribution achieved by the multicanonical ensemble for the same system.

where $\tilde{\Xi}$ is the grand partition function required to normalise $\tilde{\mathcal{N}}(m)$, and η_m is the applied bias, which can be freely chosen. For circumstances such as studying liquid-vapour coexistence, the aim of applying a bias is to sample the mixed-phase region frequently, so as to allow the system to move between phases. A simple way to achieve this is to apply a bias which makes it equally likely for the system to be in any available macrostate, such that $\tilde{\mathcal{N}}(m)$ is a constant, as shown by the dotted line in figure 4.4(b). An example of a bias which accomplishes this is [68]

$$\eta_m = -\ln \mathcal{N}(m) + D \tag{4.2.13}$$

where $D = ln\ \tilde{\Xi}\ \tilde{\mathcal{N}}(m)$ is a constant whose only role is to shift the bias linearly, and can therefore be omitted.

Equation (4.2.13) shows that it is possible to implement the multicanonical ensemble under the caveat that the probability distribution, $\mathcal{N}(m)$, of macrostates is known apriori. However, this is often exactly the distribution that a simulation aims to find and therefore it is not known apriori. To overcome this, it is necessary to instead estimate $\mathcal{N}(m)$ which can be done during the course of a simulation using the transition matrix method [127–129]. Under this scheme, $\mathcal{N}(m)$ is approximated by monitoring the transitions between macrostates with different numbers of particles, N.

The transition matrix method consists of several stages. First, for every MC move attempt, the unbiased probability of accepting the move, $P_{acc}(N \to N')$, is calculated. The cumulative results of these are stored in the collection matrix, $\mathcal{C}$, according to [127–129]

$$\begin{aligned} \mathcal{C}(N \to N') &= \mathcal{C}(N \to N') + P_{acc}(N \to N') \\ \mathcal{C}(N \to N) &= \mathcal{C}(N \to N) + (1 - P_{acc}(N \to N')) \end{aligned} \tag{4.2.14}$$

The transition matrix, π, is then formed using

$$\pi(N \to N') = \frac{\mathcal{C}(N \to N')}{\sum_{N'} \mathcal{C}(N \to N')} \tag{4.2.15}$$

Microscopic reversibility demands that $\mathcal{N}(N)\pi(N \to N') = \mathcal{N}(N')\pi(N' \to N)$ and thus the relative probabilities of finding the system in a state with $N+1$ particles compared to N particles can be written as

$$\mathcal{N}(N+1) = \frac{\pi(N \to N+1)}{\pi(N+1 \to N)}\mathcal{N}(N) \tag{4.2.16}$$

Equation (4.2.13) relates the multicanonical bias to $\mathcal{N}(N)$ if $m = N$. This equation can therefore be written in terms of the multicanonical bias as

$$\begin{aligned}
\eta(N+1) &= -\ln \mathcal{N}(N+1) \\
&= -\ln\left[\frac{\pi(N \to N+1)}{\pi(N+1 \to N)}\mathcal{N}(N)\right] \\
&= \eta(N) - \ln\left[\frac{\pi(N \to N+1)}{\pi(N+1 \to N)}\right]
\end{aligned} \tag{4.2.17}$$

The transition matrix method therefore provides an iterative method to determine the necessary bias within the multicanonical ensemble such that all macrostates are equally likely to occur, provided that $\eta(N=0)$ is known. However, as the bias $\eta(N+1)$ is determined relative to the bias $\eta(N)$, $\eta(N=0)$ can in fact be chosen freely. For simplicity, within this work, this is chosen to be $\eta(N=0) = 1$.

The multicanonical acceptance probabilities are then determined by substituting $\tilde{\mathcal{N}}(N)$ for $\mathcal{N}(N)$ during the derivation of the GC acceptance probabilities in section 4.2.2, which leads to

$$\begin{aligned}
P_{acc}(N \to N+1) &= \min\left[1, \frac{V}{\Lambda^3(N+1)} e^{-\beta(\Delta E - \mu) + (\eta(N+1) - \eta(N))}\right] \\
P_{acc}(N-1 \to N) &= \min\left[1, \frac{\Lambda^3 N}{V} e^{-\beta(\Delta E + \mu) + (\eta(N-1) - \eta(N))}\right]
\end{aligned} \tag{4.2.18}$$

As the underlying probability distribution for a multicanonical ensemble simulation is by definition biased, any results collected must then have the bias removed. This is done by inverting equation (4.2.12).

4.2.5 Histogram Reweighting

As discussed in section 4.2.3, MC is computationally expensive, in part due to the sheer number of samples of an observable required to accurately predict its behaviour. This limits the number of simulations which can realistically be performed, and therefore the thermodynamic parameters which can be explored. Fortunately there exists a scheme in which the behaviour of an observable at one set of parameters can be used to predict the behaviour of the same observable at a different set of parameters. This scheme is known as histogram

reweighting [130, 131].

The premise of histogram reweighting is that the histogram of an observable can be written as

$$h_\beta(E) \propto n(E)e^{-\beta E} \tag{4.2.19}$$

where $n(E)$ is the density of microstates with energy E and $e^{-\beta E}$ is the macrostate probability of the system having energy E at temperature T. A histogram at another temperature, T', with $\beta' = (k_\mathrm{B}T')^{-1}$, would have the form

$$h_{\beta'}(E) \propto n(E)e^{-\beta' E} \sim h_\beta e^{-(\beta'-\beta)E} \tag{4.2.20}$$

where the density of microstates has been substituted for. The probability of the system with temperature T' having energy E is then

$$P_{\beta'}(E) = \frac{h_{\beta'}(E)}{\sum_E h_{\beta'}(E)} = \frac{h_\beta e^{-(\beta'-\beta)E}}{\sum_E h_\beta(E)e^{-(\beta'-\beta)E}} \tag{4.2.21}$$

This provides the probability distribution of a system at T'. Data collected for an observable, $\mathcal{O}$, at T can therefore be used to predict the expectation value of $\mathcal{O}$ at the different temperature T' using

$$\langle\mathcal{O}\rangle_{\beta'} = \sum_E \mathcal{O}_\beta P_{\beta'}(E) \tag{4.2.22}$$

In the GC ensemble, data for an observable can be reweighted in both E and μ. When reweighting from μ to μ', the probability takes the form

$$P_{\mu'}(N) = \frac{h_\mu(N)e^{\beta(\mu'-\mu)N}}{\sum_N h_\mu(N)e^{\beta(\mu'-\mu)N}} \tag{4.2.23}$$

When simultaneously reweighting in (μ, T), the probability takes the form

$$P_{\mu',\beta'}(N,E) = \frac{h_{\mu,\beta}(N,E)e^{-(\beta'-\beta)E+\beta(\mu'-\mu)N}}{\sum_{N,E} h_{\mu,\beta}(N,E)e^{-(\beta'-\beta)E+\beta(\mu'-\mu)N}} \tag{4.2.24}$$

4.2.6 Models of Water

Considering its numerous thermodynamic anomalies and tetrahedral structure, it is no surprise that water is exceedingly difficult to model. To date, there is no water model which is able to accurately reproduce the behaviour of water in all three phases, despite the over one hundred water models currently in existence [132]. These models can largely be grouped by the method in which they represent water, for example, as a flexible or rigid, polarisable or non-polarisable molecule. Each model is also parameterised such that it reproduces a select few experimental characteristics of water, for example, the density at ambient conditions or the vaporisation enthalpy [133, 134]. Because no model can reproduce all the characteristics, it is necessary to choose a model which best reproduces the characteristics of water which are most important to that specific study.

From section 3.1, it is sensible to conclude that two important properties for a water model to reproduce for the study of hydrophobicity are the structure, and surface tension of water. The former is justified due to the apparent connections between the tetrahedrality of water and its abilities to solvate small and large solutes, whilst the latter is justified due to the clear importance of the formation of a liquid-vapour like interface in the large length scale solvation and macroscopic hydrophobicity regimes.

These properties are reproduced to a good degree of accuracy in several of the rigid non-polarisable models of water, for example, SPC/E, TIP4P and TIP4P/2005. These models represent water as a rigid molecule, with Lennard-Jones interactions between oxygen atoms and electronic interactions between charge sites, the position of which vary between models. For SPC/E, a positive charge is centered on each hydrogen atom, and the negative charge is centered on the oxygen atom. For TIP4P and TIP4P/2005, the positive charge sites again fall on the hydrogen atoms however the negative charge site occurs on the perpendicular bisector between the hydrogen and oxygen atoms. These models are then parameterised to reproduce various characteristics of water, for example, SPC/E and TIP4P are parameterised to reproduce the experimental density of water at ambient conditions, whilst TIP4P/2005 is parameterised to reproduce the pressure isobar densities [133, 134]. By design, all three models therefore reproduce the structure of water well at ambient conditions and their calculated liquid-vapour surface tensions are also the closest to the experimental value of water of all the rigid non-polarisable water models [133, 134]. Of these three models, SPC/E is the most computationally tractable due to the reduced number of interaction sites, and has been used extensively in studies of hydrophobicity [22, 23, 28, 29, 31, 77, 79, 83, 97, 102, 135–137].

Although more tractable, SPC/E is still a fairly computationally demanding model due to its use of long-ranged electrostatic interactions to reproduce the tetrahedral structure of water. A recent model, proposed by Molinero and Moore [132], has shown that it is possible to reproduce this structure without the need for such computationally expensive electrostatics. This model, named monatomic water (mW), coarse-grains the water molecule into a single particle and reproduces the tetrahedral structure of water using a three-body potential which penalises non-tetrahedral angles. The SR nature of mW makes it highly computationally efficient and simulations involving mW have been shown to be over one hundred times faster than similar simulations utilising SPC/E [132]. mW at ambient conditions has also been shown to exhibit a liquid-vapour surface tension closer to that of experimental values than SPC/E [132, 138]. Being a fairly new model, mW has been used in only a few studies of hydrophobicity to date [138–140], however shows great promise as an efficient and realistic model for hydrophobic behaviour. For these reasons, it is used within the present work.

4.2.7 Monatomic Water

mW is based on a reparameterisation of the Stillinger-Weber potential, which was used originally to model elements such as silicon and germanium that exhibit similar tetrahedral structures to that of water. Molinero and Moore chose to parameterise mW to reproduce the melting temperature, vaporisation enthalpy, and density of water at ambient conditions.

Based on this parameterisation, the form of the interaction potential is [132]

$$\phi_{mw}(\mathbf{r}_i, \mathbf{r}_j, \mathbf{r}_k, \theta_{ijk}) = \sum_i \sum_{j>i} \phi_{mw,2}(\mathbf{r}_i, \mathbf{r}_j) + \sum_i \sum_{j\neq i} \sum_{k>j} \phi_{mw,3}(\mathbf{r}_i, \mathbf{r}_j, \mathbf{r}_k, \theta_{ijk}) \tag{4.2.25}$$

where the two-body, $\phi_{mw,2}$ and three-body, $\phi_{mw,3}$, potentials are

$$\phi_{mw,2}(\mathbf{r}_i, \mathbf{r}_j) = A\varepsilon_{mw}\left[B\left(\frac{\sigma_{mw}}{r}\right)^4 - 1\right]\exp\left(\frac{\sigma_{mw}}{|\mathbf{r}_i - \mathbf{r}_j| - a\sigma_{mw}}\right) \tag{4.2.26}$$

$$\phi_{mw,3}(\mathbf{r}_i, \mathbf{r}_j, \mathbf{r}_k, \theta_{ijk}) = \lambda\varepsilon_{mw}\left[\cos\theta_{ijk} - \cos\theta_0\right]^2 \exp\left(\frac{\gamma\sigma_{mw}}{|\mathbf{r}_i - \mathbf{r}_j| - a\sigma_{mw}}\right)\exp\left(\frac{\gamma\sigma_{mw}}{|\mathbf{r}_i - \mathbf{r}_k| - a\sigma_{mw}}\right) \tag{4.2.27}$$

and $A = 7.049556277$, $B = 0.6022245584$, $\gamma = 1.2$ are constants which determine the form and scale of the potential, $\lambda = 23.15$ is the tetrahedrality parameter, $\theta_0 = 109.47°$ is the angle favoured between waters, $a = 1.8$ is the cut-off radius, $\sigma_{mw} = 2.3925\mathring{A}$ is the diameter of a mW particle, and $\varepsilon_{mw} = 6.189\text{kcal mol}^{-1}$ is the mW-mW interaction strength.

4.2.8 Liquid-Vapour Phase Diagram

In contrast to cDFT, the treatment of fluids within MC is not van der Waals like and as such the coexistence curve cannot be calculated according to section 2.4.4. Instead, the liquid-vapour coexistence curve must be calculated from simulations themselves. Within the GC ensemble, the most robust way in which to do this is to follow the methods presented by Wilding in [68]. These methods utilise the multicanonical ensemble and histogram reweighting to accurately gather coexistence values of (μ, T, ρ_l, ρ_v), where ρ_l and ρ_v are the liquid and vapour densities respectively. This approach requires only a few simulations to trace the entire liquid-vapour bulk coexistence curve and is therefore highly efficient. Alternative methods to calculate the liquid-vapour coexistence curve include use of the Gibbs' ensemble and Gibbs-Duhem integration [44]. The latter of these allows for the curve to be traced from only one simulation. However this method is not robust, as it provides no method of estimating the uncertainty in any state point and is also prone to numerical errors.

4.2.8.1 Critical Point

The liquid-vapour critical point within GCMC can be found by comparing the distribution of the scaling variable, $\mathcal{M}$, to the equivalent distribution of the three dimensional Ising model. Universality arguments mean that these should be equal at the critical point. Whilst $\mathcal{M}$ within the Ising model represents the magnetisation, within a fluid, $\mathcal{M}$ takes the form [68, 141]

$$\mathcal{M} = \rho - su \tag{4.2.28}$$

where ρ is the density, u is the reduced energy density, and s is a system specific mixing parameter.

The process of finding the critical point then consists of running a simulation at a set of

parameters, (μ, T) which are believed to be close to those of the critical point, and regularly sampling ρ and u. Once sufficient statistics have been gathered, these values can be used to generate the scaling variable distribution of equation (4.2.28) which can then be compared to the three dimensional Ising distribution. The latter of these has been found to a high degree of accuracy in several studies, for example [142]. The distribution of $\mathcal{M}$ can then be tuned using histogram reweighting to find the parameters (μ_c, T_c, s) for which the distribution of $\mathcal{M}$ best matches the three dimensional Ising distribution [68].

However, as was discussed in section 2.4.6, any simulation performed near the critical point will be subject to FS effects due to the divergence of the correlation length, ξ. This means that parameters such as T_c and μ_c are in fact functions of the size of the system which, assuming the simulation box is cubic, is quantified by the length of the simulation box, L. In order to find the infinite volume critical parameters, it is necessary that these FS effects be accounted for. This can be achieved by finding the critical parameters in simulations of several box sizes and plotting these against the predicted scaling relations, which can be found in the work of Wilding [68]. Performing a linear fit to the relation and extrapolating to the infinite volume limit, then gives an estimate of the true critical parameters.

4.2.8.2 Liquid-Vapour Coexistence

Close to liquid-vapour coexistence, the probability distribution of the density samples collected during a GCMC simulation will feature two peaks representing the vapour and liquid phases. If the phases within the distribution are separated by the mean density, then exactly at coexistence the area under each peak should be equal [68]. Physically, this represents that either phase is equally likely to occur, and therefore the system must be at liquid-vapour coexistence.

Using this knowledge, the liquid-vapour coexistence curve can be found using the multicanonical ensemble and histogram reweighting through the following procedure

1. First, a simulation is performed at a set of parameters (μ, T) believed to be near coexistence and samples of the density collected. To overcome the free energy barrier between phases, the multicanonical ensemble can be used.

2. These samples are then placed into a histogram to find the probability distribution of the density of the system.

3. The density histogram is then reweighted in μ until the equal peak area criteria is met. This then gives the coexistence μ for a given T.

4. The density histogram can then be reweighted in temperature and step 3 performed again to find another coexistence state point.

5. Step 4 can be repeated until the reweighted density distributions become too noisy to give accurate results.

The accuracy of the state points obtained through histogram reweighting can be confirmed by running a simulation at the predicted state point. An efficient method to do this is to

trace the coexistence curve from the critical point. Starting at near critical parameters, the procedure can be performed down to a temperature T', below which noise prevents any further reweighting. The next simulation is performed at T' using the coexistence μ' predicted by histogram reweighting. The accuracy of the histogram reweighting is confirmed by directly comparing the predicted density histogram to that obtained through the simulation and the procedure repeated until the entire coexistence curve has been traced. This procedure therefore provides a method to trace the entire coexistence curve and confirm its accuracy, with only a few simulations.

4.2.9 Introduction of Solutes

Molecular simulation studies of hydrophobicity take one of two approaches when modelling a solute. If the aim of the study is to understand water's response to a specific hydrophobic solute, then careful consideration of the interaction potential, V_{ext}, between the solute and the water molecules is necessary. Studies which may fall into this category include those interested in understanding biological processes, for example [29, 31]. If instead the aim of the study is to understand hydrophobicity more generally, then such care over interaction potentials is unnecessary. Studies which fall into this category include those interested in general features of hydrophobic density fluctuations, for example [23, 28]. As the present work is concerned with understanding the relationships between hydrophobicity and a possible underlying surface critical point, it falls into the latter category. Because of this, the V_{ext} chosen is of little importance. The present work therefore makes use of the simplest choice of V_{ext}, which is a LJ potential like that used within cDFT. This choice is in part motivated by the direct comparison it then allows between MC and cDFT results and in part justified by its use in previous studies, for example [1, 79].

The simulation box set-up during studies of hydrophobic solvation consisted of a single, smooth, spherical solute, which was placed in the centre of the cubic box of side length L with periodic boundary conditions. The radius of the solute, R_s, was measured in units of σ_{mw}. In order to ensure that there were sufficient mW particles to represent a bulk fluid, the length of the box was chosen to satisfy $L \geq 2(R_s + 3a\sigma_{mw})$, where $a\sigma_{mw}$ was the cut-off radius of interaction of mW fluid particles. Short simulations in larger boxes were also performed initially, however presented no different results to those in the smaller box size. This confirmed that the condition that $L \geq 2(R_s + 3a\sigma_{mw})$ was large enough to accommodate the solute and to accurately represent the bulk fluid.

As in the case of cDFT, the solute was modelled as impenetrable and imagined to be made up of smaller particles of diameter σ_s of homogeneous density ρ_s, which individually interacted with the fluid particles via a LJ potential. Under the same reasoning as within cDFT, the interaction potential was reduced to a variable of only the radial distance from the centre of the solute and therefore took the form of equation (4.1.54). To allow for a direct comparison between cDFT and MC results, the potential was shifted such that the minimum occurred at the surface of the solute. However, as stated in section 4.1.5.2, it is exceedingly difficult to determine this minimum analytically. To overcome this, the minimum was approximated as that expected for the equivalent planar potential, and therefore took

the form $r_{min} = (2/5)^{1/6}\sigma_s$. For simplicity, throughout the present work σ_s was chosen to be $\sigma_s = \sigma_{mw}$.

4.2.10 Measures

Several examples of observables which may be sampled during the course of a MC simulation have been mentioned so far, for example the density and energy of the system. In addition to these, there are many other measures which may be of interest specifically in the case of hydrophobicity. These measures fall into two main categories: bulk measures which refer to those sampled in bulk systems and spatially varying measures which provide detailed information about the local response of mW particles to a hydrophobic solute or surface.

4.2.10.1 Bulk Measures

The main bulk measure of interest within this work is the density, ρ_b. The process of finding this has been discussed previously and involves collecting samples of the density throughout the simulation and using these to form a histogram. Under the central limit theorem [43], provided that sufficient samples have been collected, this histogram should have a Gaussian form. If the system is near coexistence, such that the density histogram features two peaks, each of these should individually take a Gaussian form. The most probable density of the system, and therefore the true density of the system, can be found by fitting a Gaussian to the histogram,. The peak of the Gaussian fit, which will be the mean, is the density of the system.

4.2.10.2 Spatially Varying Measures

Examples of spatially varying measures of interest in the study of hydrophobicity are the spatially varying density profiles, as measured from the centre of the solute. The measurement of these within MC is achieved by sampling the positions of all particles regularly throughout the simulation. The distances between each particle and the centre of the solute are then calculated, and placed into a histogram. This histogram provides the density profile $\rho(r)$. For a bulk simulation, a similar method can be used to measure the radial distribution function, $g(r)$. However, in this case, the origin of the distribution for the measurement can be centred on any particle within the system. As such, $g(r)$ can be calculated for each particle during each sampling.

The local compressibility, as presented in equation (2.5.1), can be calculated during the course of a simulation, by using histogram reweighting to reweight the density profile, $\rho(r)$, to a slightly larger chemical potential. At the end of the simulation, this can be compared to the density profile at the simulation chemical potential, and a numerical derivative performed. The difference in chemical potential for the reweighting process should be small to ensure an accurate numerical derivative is achieved. Within this work, the chemical potential was reweighted by a difference $\beta \mathrm{d}\mu = 10^{-6}$. To confirm this gave an accurate result, tests were also performed at larger and smaller $d\mu$.

4.2.11 Estimation of Uncertainties

All of the MC measures presented here take the form of histograms with approximately Gaussian distributions. The uncertainty in each measure can therefore be found by calculating the standard error according to [43]

$$error = \frac{s}{\sqrt{(N)}} \tag{4.2.29}$$

where s is the standard deviation and N is the number of independent samples. This latter is important, as it is highly likely that not every sample collected will be independent and thus N not equal to the total number of samples [43].

Samples are considered independent when they are decorrelated. This decorrelation happens naturally over the course of a simulation, hence one method to estimate the number of independent samples is to divide the total number of samples by the number of samples it takes for two samples to naturally decorrelate. The number of samples it takes for decorrelation to occur is known as the correlation time, τ_c, and can be calculated using the autocorrelation of samples [44]. However, calculating this can be computationally intensive, as it requires performing operations over every sample. Alternative methods, such as block averages [43], have been introduced to overcome this.

Alternatively, the number of independent samples can be estimated by considering the physics of the system. For example, consider a simulation of a fluid at liquid-vapour coexistence. Throughout the simulation, the system will pass through both the liquid and vapour phases multiple times. Whilst τ_c in the former phase may be very long, in the latter it will be very short and hence the system can be considered to decorrelate almost immediately if it passes through the vapour phase. An estimate of the number of independent samples can then be made by dividing the total number of samples by the number of times the system passed through the vapour phase.

If instead the fluid exhibits a small oversaturation, it will not pass through the vapour. As the fluid is a liquid in bulk, τ_c will be very long and therefore samples of properties of the system, such as spatially varying profiles, will change little over large periods of the simulation. The computational time required to secure adequate decorrelated samples may therefore be infeasibly long. In this case, one method in which to ensure independent samples is to perform multiple simulations in parallel. As MC operates on random sampling, these systems will evolve differently throughout the course of the simulations and hence each individual simulation constitutes an independent sample. For spatially varying measures, such as the density and local compressibility profiles, which are themselves histograms, equation (4.2.29) can then be calculated for each bin within the profile, by finding s for each bin and dividing by the square root of the number of parallel simulations.

Chapter 5

Effective Interface Potential Analysis for Critical Drying

As was discussed in section 3.3, evidence of enhanced fluctuations local to the surfaces of both macroscopic planar substrates and microscopic solutes indicates the potential relation between critical drying, and hydrophobicity and solvophobicity. However, as was presented in section 2.4.1, diverging fluctuations are but one feature of a critical point. If critical drying truly influences hydrophobicity and solvophobicity, other characteristic behaviours of criticality, such as the existence of critical exponents and scaling function forms of observables, should also be present. For an interfacial system, these behaviours are related to non-analytic features of the surface free energy. An analysis of the surface free energy of a solvophobic system near to a potential drying critical point should therefore allow for the prediction of critical behaviour, such as the critical exponents and forms of scaling functions.

A surface free energy, also termed effective interface potential, approach was applied in early studies of wetting of van der Waals fluids at macroscopic planar substrates [143, 144]. These studies used such an approach to predict the critical exponents for various properties on the approach to both critical and complete wetting [41, 50]. Later studies of drying showed that it was also possible to construct an effective interface potential for a large curved substrate, or effectively a large solute [33, 34]. In these studies, which focused specifically on LR LJ fluids, the predicted critical exponents were compared to numerical results from cDFT, and excellent agreement was found. More recently, an effective interface potential approach has been used to predict the way in which local density fluctuations in a SR LJ fluid at a macroscopic planar substrate, as measured by χ_μ defined in equation (2.5.1), diverge on the approach to critical drying [1, 32]. When compared to both cDFT and MC results, again, excellent agreement was found.

In addition to confirming critical behaviours, the effective interface potential approach provides a method of interpreting results obtained from simulation and cDFT, by relating different measures of proximity to the drying critical point to the expected behaviour of observables such as ℓ_{eq} and χ_μ. Whilst previous studies have demonstrated its usefulness and applicability, each was focused on the influence of a particular measure of proximity to

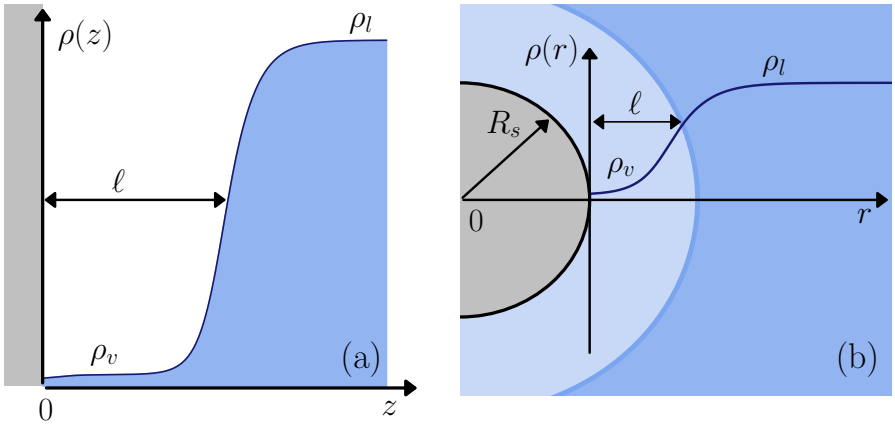

Figure 5.1: Illustration of systems which are considered within this chapter. (a) A macroscopic planar substrate is in contact with a fluid, which is in its liquid phase in the bulk. A film of vapour of width ℓ separates the substrate from the bulk liquid. (b) A large solute, or curved substrate, of radius R_s is in contact with a fluid which is in its liquid phase in bulk. A film of vapour, of width ℓ, separates the surface of the substrate from the bulk liquid. In both (a) and (b), ρ_l and ρ_v represent the densities of the liquid and vapour phases of the fluid at coexistence.

critical drying, such as the substrate/solute-fluid attraction [1] or the curvature of the solute [33, 34]. Within this work, all measures of proximity to critical drying are investigated, and hence the analysis presented within this chapter builds on these previous studies to provide a more comprehensive understanding, particularly of the interplay between measures. To do this, two systems are considered. The first is shown in figure 5.1(a) and consists of a macroscopic planar substrate in contact with a fluid, which is in its liquid phase in the bulk. The second is shown in figure 5.1(b), and consists of a large solute surrounded by a fluid, which is also in its liquid phase in bulk. Whilst critical drying was shown to occur in three of the four surface phase diagrams for a planar substrate in figure 2.8, this work is limited to systems with SR ff LR sf and LR ff LR sf interactions, as these are the relevant combinations for most simulation and experimental studies respectively. Finally, throughout this chapter, the behaviour of observables along two specific paths in parameter space will be considered frequently. These paths are shown in figure 5.2(a), along with the expected behaviour of ℓ_{eq} for each in figures 5.2(b) and 5.2(c) respectively. For convenience, within this chapter, path (a) will be referred to as the approach to critical drying, whilst path (b) as the approach to complete drying. It should be noted that these paths and terms are used simply for convenience and represent only one of the possible paths to critical/complete drying. In particular, whilst complete drying is used here to refer to the path at $T = T_D$, in much of the literature, complete drying refers to any path for which $T_D < T < T_c$.

5.1 Effective Interface Potential for Drying

The construction of an effective interface potential for wetting or drying can be approached in several ways. Authors such as Dietrich [50] and Schick [41] have presented these clearly, and the reader is directed to either of these for detailed derivations. Irrespective of method, the excess grand potential, which is the natural free energy to consider, for a planar substrate

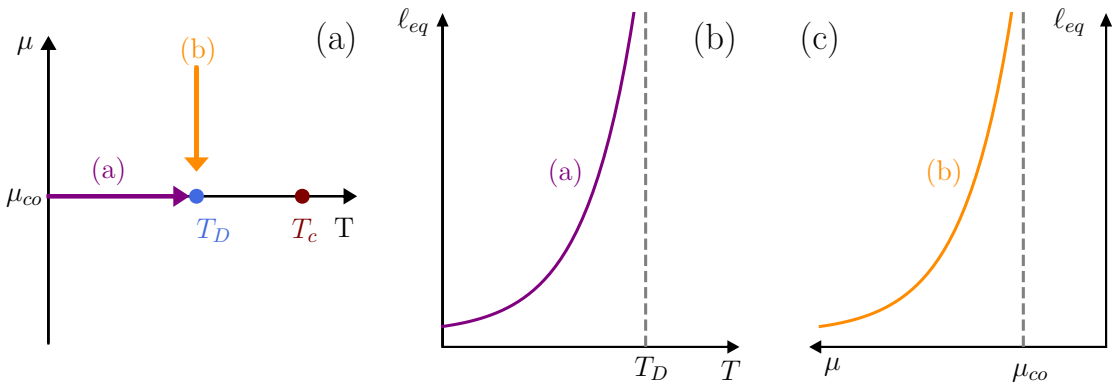

Figure 5.2: (a) Illustration of phase paths considered within this chapter. The approach to the drying critical point along path (a) is referred to as the approach to critical drying, whilst the approach along path (b) as complete drying. These terms are used for convenience only, as there are many such approaches to critical and complete drying. Note, this diagram is purely illustrative, and does not reflect the true shape of the coexistence curve. (b) Behaviour of equilibrium film width, ℓ_{eq}, on the approach to critical drying along path (a). (c) Behaviour of ℓ_{eq} on the approach to complete drying along path (b).

in contact with a liquid at coexistence with its vapour phase can be found to be [41, 50]

$$\Omega_{ex} = \gamma_{sv}A + \gamma_{lv}A + \omega(\ell)A \tag{5.1.1}$$

where γ represents the surface tension, A the surface area, and the subscripts sv and lv substrate-vapour and liquid-vapour respectively. The final term, $\omega(\ell)$, is the binding potential, which describes the free energy required to bind the liquid-vapour interface to the surface of the substrate at a distance ℓ. Dividing through by A simplifies equation (5.1.1) to

$$\frac{\Omega_{ex}}{A} \equiv \gamma_{sl} = \gamma_{sv} + \gamma_{lv} + \omega(\ell) \tag{5.1.2}$$

where γ_{sl} is the substrate-liquid surface tension. Comparing this to Young's equation given in equation (2.4.19) shows that in the limit of drying, $\omega(\ell \to \infty) \to 0$.

Equation (5.1.1) assumes the fluid is at liquid-vapour coexistence, in which case there is no free energy difference between the liquid and vapour phases. If instead the fluid has a small oversaturation, then the vapour phase will be metastable with respect to the liquid phase. In this case, equation (5.1.1) acquires an additional free energy term, which describes the pressure difference between the liquid and vapour phases. This term can be rewritten in terms of the chemical potential, μ, by expanding the pressures of the liquid and vapour phases about the coexisting chemical potential, μ_{co}, and utilising the Gibbs-Duhem relation. Doing so leads to

$$\Omega_{ex} = \gamma_{sv}A + \gamma_{lv}A + \omega(\ell)A + \delta\mu\Delta\rho A\ell \tag{5.1.3}$$

where $\Delta\rho = (\rho_l - \rho_v)$, $\delta\mu = \mu - \mu_{co}$, and $A\ell$ is the volume of the vapour film. This expression can then be rewritten as [41, 50, 117]

$$\frac{\Omega_{ex}}{A} = \omega_{ex}(\ell) = \gamma_{sv} + \gamma_{lv} + \omega(\ell) + \delta\mu\Delta\rho\ell \tag{5.1.4}$$

If instead of a planar substrate, the system consists of a large solute, as shown in figure 5.1(b), then the effective interface potential takes the form [34, 117, 145]

$$\Omega_{ex} = \gamma_{sv}(R_s)A_{sv} + \gamma_{lv}(R_s + \ell)A_{lv} + \omega(\ell; R_s)A_{sv} + \delta\mu\Delta\rho V_v \tag{5.1.5}$$

where $\omega(\ell; R_s)$ is the curvature dependent binding potential. In this case, the substrate-vapour surface area is $A_{sv} = 4\pi R_s^2$, the liquid-vapour surface area is $A_{lv} = 4\pi(R_s + \ell)^2$, and the volume of the vapour film is $V_v = 4\pi((R_s + \ell)^3 - R_s^3)/3$. Substituting these gives

$$\Omega_{ex} = \gamma_{sv}(R_s)A_{sv} + \gamma_{lv}(R_s + \ell)A_{sv}\left(1 + \frac{2\ell}{R_s} + \frac{\ell^2}{R_s^2}\right) + \omega(\ell; R_s)A_{sv} + \delta\mu\Delta\rho A_{sv}\ell\left(1 + \frac{\ell}{R_s} + \frac{\ell^2}{3R_s^2}\right) \tag{5.1.6}$$

This can be simplified using two assumptions. Firstly, it is assumed that R_s is very large, such that the surface tension terms can be approximated by their values at a planar substrate, $\gamma_{sv}(R_s) \approx \gamma_{sv}$ and $\gamma_{lv}(R_s + \ell) \approx \gamma_{lv}$. Secondly, if it is assumed that $R_s \gg \ell$, then terms of order $\mathcal{O}(\ell^2/R_s^2)$ can be neglected. Under these assumptions, equation (5.1.6) reduces to

$$\frac{\Omega_{ex}}{A_{sv}} = \omega_{ex}(\ell; R_s) \approx \gamma_{sv} + \gamma_{lv}\left(1 + \frac{2\ell}{R_s}\right) + \omega(\ell; R_s) + \delta\mu\Delta\rho\ell \tag{5.1.7}$$

5.2 Equilibrium Drying Film Width

As was discussed in section 2.4.5, the equilibrium film width, ℓ_{eq}, is the film width for which the surface free energy is minimum. This can be found by minimising the effective interface potential. For the case of the planar substrate, minimising $\omega_{ex}(\ell)$ given in equation (5.1.4) leads to

$$\left.\frac{\partial\omega_{ex}(\ell)}{\partial\ell}\right|_{\ell=\ell_{eq}} = 0 = \left.\frac{\partial\omega(\ell)}{\partial\ell}\right|_{\ell=\ell_{eq}} + \delta\mu\Delta\rho \tag{5.2.1}$$

For the case of the solute, minimising $\omega_{ex}(\ell; R_s)$ given in equation (5.1.7) leads to

$$\left.\frac{\partial\omega_{ex}(\ell; R_s)}{\partial\ell}\right|_{\ell=\ell_{eq}} = 0 = \left.\frac{\partial\omega(\ell; R_s)}{\partial\ell}\right|_{\ell=\ell_{eq}} + \frac{2\gamma_{lv}}{R_s} + \delta\mu\Delta\rho \tag{5.2.2}$$

The term $2\gamma_{lv}/R_s$ can be identified as the Laplace pressure, which arises due to the curvature of the liquid-vapour interface [89]. The final two terms in equation (5.2.2) can be combined to define the effective pressure as

$$\tilde{p} = \frac{2\gamma_{lv}}{R_s} + \delta\mu\Delta\rho \tag{5.2.3}$$

which implies an equivalence between the effects of substrate curvature and oversaturation. Such an equivalence has been noted by other authors, for example, Stewart and Evans [34] and Evans et al. [146].

5.3 Local Fluctuations

On the approach to the drying critical point, density fluctuations are expected diverge according to some power law [41, 50]. Unlike the case of a bulk fluid, the faster divergence of the correlation length parallel to the surface of the substrate or solute, $\xi_{||}$, compared to the perpendicular correlation length, $\xi_{\perp}$, means that on the approach to critical and complete drying, these fluctuations are localised to the surface of the substrate or solute [69]. Spatially resolved measures of these density fluctuations, like χ_μ and χ_T presented in section 2.5, have been shown to peak near the liquid-vapour interface at ℓ_{eq} [1, 23, 37, 113]. This can be rationalised by the fact that the main effect of small changes in the local parameters of a system with such an interface is to move the interface.

The behaviour of the density fluctuations on the approach to critical and complete drying can therefore be understood by considering $\chi_\mu(\ell_{eq})$ and $\chi_T(\ell_{eq})$. Making the assumption that the density profile takes the form of a smooth function, $\rho(z) \equiv S(z-\ell)$ like that shown in figure 5.1(a), $\chi_\mu(\ell_{eq})$ for a planar substrate can be written as [1]

$$\chi_\mu(\ell_{eq}) = \left.\frac{\partial \rho(z)}{\partial \mu}\right|_{T,\ell=\ell_{eq}} = \left.\frac{\partial S(z-\ell)}{\partial (z-\ell)}\,\frac{\partial (z-\ell)}{\partial \mu}\right|_{T,\ell=\ell_{eq}} = -\rho'(\ell_{eq})\left.\frac{\partial \ell_{eq}}{\partial \mu}\right|_{T} \tag{5.3.1}$$

where $\rho'(\ell_{eq})$ represents the spatial derivative of the density profile evaluated at ℓ_{eq}, and it has been used that $\ell = \ell(\mu, T)$. Similarly, $\chi_T(\ell_{eq})$ for a planar substrate can be written as

$$\chi_T(\ell_{eq}) = -\rho'(\ell_{eq})\left.\frac{\partial \ell_{eq}}{\partial T}\right|_{\mu} \tag{5.3.2}$$

For a large solute, the density profile is instead assumed to be a smooth function of $\rho(r) \equiv S(r-(R_s+\ell))$. In this case, using similar reasoning, $\chi_\mu(\ell_{eq}; R_s)$ and $\chi_T(\ell_{eq}; R_s)$ can be written as

$$\chi_\mu(\ell_{eq}; R_s) = -\rho'(R_s+\ell_{eq})\left.\frac{\partial \ell_{eq}}{\partial \mu}\right|_{T} \tag{5.3.3}$$

$$\chi_T(\ell_{eq}; R_s) = -\rho'(R_s+\ell_{eq})\left.\frac{\partial \ell_{eq}}{\partial T}\right|_{\mu} \tag{5.3.4}$$

The similarity in forms of equation (5.3.1) and (5.3.2) imply a similarity in the behaviour of the divergence of different measures of local density fluctuations on the approach to critical drying. Writing these as a ratio gives

$$\frac{\chi_T(\ell_{eq})}{\chi_\mu(\ell_{eq})} = \left(\frac{\partial \ell_{eq}}{\partial T}\right)_{\mu}\left(\frac{\partial \ell_{eq}}{\partial \mu}\right)_{T}^{-1} \tag{5.3.5}$$

In the case of a planar substrate, $\ell_{eq} \equiv \ell_{eq}(\mu, T)$. Writing this in the more convenient form of $\ell_{eq} \equiv \ell_{eq}(\delta\mu, T)$, the temperature derivative of ℓ_{eq} can be written as

$$\left(\frac{\partial \ell_{eq}}{\partial T}\right)_{\mu} = \left(\frac{\partial \ell_{eq}}{\partial T}\right)_{\delta\mu} + \left(\frac{\partial \ell_{eq}}{\partial \delta\mu}\right)_{T}\left(\frac{\partial \delta\mu}{\partial T}\right)_{\mu} \tag{5.3.6}$$

Within $\delta\mu$, only μ_{co} is a function of temperature, hence this simplifies to

$$\left(\frac{\partial \ell_{eq}}{\partial T}\right)_{\mu} = \left(\frac{\partial \ell_{eq}}{\partial T}\right)_{\delta\mu} - \left(\frac{\partial \ell_{eq}}{\partial \delta\mu}\right)_{T}\left(\frac{\partial \mu_{co}}{\partial T}\right) \tag{5.3.7}$$

Near to the drying critical point, both terms within this expression will diverge. If the first were to diverge more slowly than the second, then equation (5.3.5) would reduce to

$$\frac{\chi_T(\ell_{eq})}{\chi_\mu(\ell_{eq})} \sim -\frac{\partial \mu_{co}}{\partial T} \tag{5.3.8}$$

If this were to be the case, then it would imply that both $\chi_\mu(\ell_{eq})$ and $\chi_T(\ell_{eq})$ diverge in the same way on the approach to critical drying. By definition, this would also imply that $\chi_*(\ell_{eq})$, defined in equation (2.5.3), diverge in the same way.

A condition for when it is true that the first term in equation (5.3.7) diverges more slowly than the second can be found by considering the behaviour of the adsorption of the system, which is related to ℓ_{eq} via equation (2.4.20). Substituting this relation gives a form of equation (5.3.5) dependent on the adsorption

$$\frac{\chi_T(\ell_{eq})}{\chi_\mu(\ell_{eq})} = \left(\frac{\partial \Gamma}{\partial T}\right)_{\mu}\left(\frac{\partial \Gamma}{\partial \mu}\right)^{-1}_{T} \tag{5.3.9}$$

Using similar reasoning that $\Gamma \equiv \Gamma(\delta\mu, T)$, the total derivative can be written as

$$\left(\frac{\partial \Gamma}{\partial T}\right)_{\mu} = \left(\frac{\partial \Gamma}{\partial T}\right)_{\delta\mu} - \left(\frac{\partial \Gamma}{\partial \delta\mu}\right)_{T}\left(\frac{\partial \mu_{co}}{\partial T}\right) \tag{5.3.10}$$

Hence, as before, if the first term diverges more slowly than the second, then equation (5.3.8) is obtained.

As was discussed in section 2.1, the adsorption, Γ is related to γ_{sl} via

$$\frac{\Gamma}{A} = -\left(\frac{\partial \gamma_{sl}}{\partial \mu}\right)_{T} \tag{5.3.11}$$

Near to the drying critical point, the singular part of γ_{sl}, denoted as γ_{sing}, is expected to have a scaling function form, with a scaling variable of $\delta\mu/\tilde{t}^{\Delta}$, where $\tilde{t}$ is the reduced temperature defined as $\tilde{t} = (T - T_D)/T_D$, and Δ is the gap exponent. γ_{sing} can therefore be written as [41, 50]

$$\gamma_{sing} = \gamma_{sl} - \gamma_{sv} - \gamma_{lv} \sim |\tilde{t}|^{2-\alpha_s}\Sigma\left(\frac{\delta\mu}{|\tilde{t}|^{\Delta}}\right) \tag{5.3.12}$$

where α_s is the surface equivalent of the bulk heat capacity critical exponent, α, on the approach to critical drying and Σ is a scaling function. Taking the derivative of equation (5.3.12) with respect to μ allows for the singular part of the adsorption, Γ_{sing}, to be written as

$$|\Gamma_{sing}| \sim |\tilde{t}|^{2-\alpha_s-\Delta}\mathcal{L}\left(\frac{\delta\mu}{|\tilde{t}|^{\Delta}}\right) \tag{5.3.13}$$

where $\mathcal{L}$ is the first derivative of Σ, and is itself a scaling function.

Utilising the scaling form of Γ_{sing}, the T and μ derivatives of Γ_{sing} can be written as

$$\left(\frac{\partial|\Gamma_{sing}|}{\partial T}\right)_{\delta\mu} \sim |\tilde{t}|^{1-\alpha_s-\Delta}\mathcal{L}\left(\frac{\delta\mu}{|\tilde{t}|^{\Delta}}\right) + |\tilde{t}|^{1-\alpha_s-\Delta}\left(\frac{\delta\mu}{|\tilde{t}|^{\Delta}}\right)\mathcal{L}'\left(\frac{\delta\mu}{|\tilde{t}|^{\Delta}}\right)$$
$$\left(\frac{\partial|\Gamma_{sing}|}{\partial\mu}\right)_{T} \sim |\tilde{t}|^{2-\alpha_s-2\Delta}\mathcal{L}'\left(\frac{\delta\mu}{|\tilde{t}|^{\Delta}}\right) \tag{5.3.14}$$

where $\mathcal{L}'$ is the first derivative of $\mathcal{L}$, and the term $(\delta\mu/|\tilde{t}|^{\Delta})\mathcal{L}'(\delta\mu/|\tilde{t}|^{\Delta})$ can be recognised as a scaling function. Comparing the exponents, it is possible to deduce that, for the second term in equation (5.3.10) to diverge faster than the first, $\Delta > 1$. By nature of definition of ℓ_{eq}, this condition should also apply to equation (5.3.7).

A potential relation between the divergence of different measures of density fluctuations on the approach to critical drying is not limited to the case of a planar substrate. Considering equations (5.3.3) and (5.3.4), it can be deduced that

$$\frac{\chi_T(\ell_{eq};R_s)}{\chi_\mu(\ell_{eq};R_s)} = \left(\frac{\partial\ell_{eq}}{\partial T}\right)_{\mu}\left(\frac{\partial\ell_{eq}}{\partial\mu}\right)_{T}^{-1} \tag{5.3.15}$$

should also hold. Considering equation (5.2.2), it can be seen that in the case of a curved substrate, $\ell_{eq} \equiv \ell_{eq}(\tilde{p},T)$. This can be rewritten in the more convenient form $\ell_{eq} \equiv \ell_{eq}(\tilde{p}',T)$, where $\tilde{p}' = \tilde{p}/\Delta\rho$, in which case the temperature derivative of ℓ_{eq} becomes

$$\begin{aligned}\left(\frac{\partial\ell_{eq}}{\partial T}\right)_{\mu} &= \left(\frac{\partial\ell_{eq}}{\partial T}\right)_{\delta\mu} + \left(\frac{\partial\ell_{eq}}{\partial\tilde{p}'}\right)_{T}\left(\frac{\partial\tilde{p}'}{\partial T}\right)_{\mu} \\ &= \left(\frac{\partial\ell_{eq}}{\partial T}\right)_{\delta\mu} + \left(\frac{\partial\ell_{eq}}{\partial T}\right)_{\mu}\left(\frac{2}{R_s}\frac{\partial}{\partial T}\left(\frac{\gamma_{lv}}{\Delta\rho}\right) - \frac{\partial\mu_{co}}{\partial T}\right)\end{aligned} \tag{5.3.16}$$

As $R_s \to \infty$, this must tend to the relation for a planar substrate, given in equation (5.3.8). It can therefore be expected that, as in the planar case, the second term diverges faster than the first provided $\Delta > 1$, and as such, equation (5.3.15) can be expected to follow

$$\frac{\chi_T(\ell_{eq};R_s)}{\chi_\mu(\ell_{eq};R_s)} \sim \left(\frac{2}{R_s}\frac{\partial}{\partial T}\left(\frac{\gamma_{lv}}{\Delta\rho}\right) - \frac{\partial\mu_{co}}{\partial T}\right) \tag{5.3.17}$$

This again implies a simple relationship between all measures of density fluctuations on the approach to critical drying. However, this relationship also suggests that curvature constrains these density fluctuations, and therefore true divergence of $\chi_\mu(\ell_{eq};R_s)$ and $\chi_T(\ell_{eq};R_s)$ is only possible as $R_s \to \infty$.

5.4 Forms of the Binding Potential

The effective interface potentials given in equations (5.1.4) and (5.1.7) imply that the binding potential, $\omega(\ell)$ or $\omega(\ell;R_s)$, determines the nature of drying within a system. Considering the case of a planar substrate, for first-order drying, $\omega(\ell)$ must have two minima located at finite and infinite ℓ_{eq}, as shown in figure 5.3(a). When $T < T_D$, the minimum for a finite ℓ_{eq} is deeper, and hence a microscopic vapour film is favoured. In contrast, when $T > T_D$, the minimum at infinite ℓ_{eq} is deeper, and hence a macroscopic vapour film is favoured. Exactly

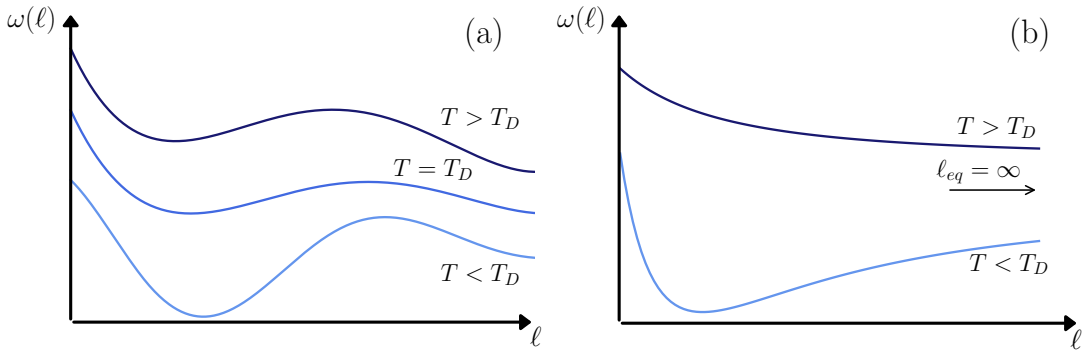

Figure 5.3: Forms of the binding potential for a fluid at coexistence in contact with a planar substrate, $\omega(\ell)$, for the cases of (a) first-order drying and (b) critical drying. Similar forms are expected to exist for the binding potential for a curved substrate, $\omega(\ell; R_s)$.

at $T = T_D$, the two minima are equal, and hence first-order drying can occur [50]. For the case of critical drying, $\omega(\ell)$ has only one minimum, as shown in figure 5.3(b). Below T_D, this occurs at finite ℓ, and hence a microscopic film is favoured. As $T \to T_D$, this minimum moves to increasingly larger ℓ and exactly at $T = T_D$, the minimum occurs at $\ell = \infty$, at which point a macroscopic vapour film is favoured [50]. By nature of the similarity of the forms of equations (5.1.4) and (5.1.7), the same forms must exist for $\omega(\ell; R_s)$.

As indicated in the surface phase diagrams presented in figure 2.8, the nature of drying is dependent on the ranges of interactions within the system, which implies that the form of $\omega(\ell)$, which determines the surface phase diagrams of figure 2.8, also varies depending on the range of interactions within the system. This form is generally derived by using statistical mechanics to find an approximation for $\omega_{ex}(\ell)$, which can then be compared to equation (5.1.1) in order to determine terms which contribute to $\omega(\ell)$. The precise statistical mechanics approach to finding $\omega_{ex}(\ell)$ varies depending on the system of interest. Here, only the final form of $\omega(\ell)$ is presented, and the reader is directed to [41] in the case of SR ff LR sf, and [50] in the case of LR ff LR sf, for more detailed derivations. Within these texts, it can be seen that the binding potential can be separated into two components, dependent on the ff and sf interactions respectively. Within this section, the binding potential for a planar substrate for each case of interactions is discussed. This is followed by a discussion of how the binding potential can be expected to change when the substrate is instead curved.

5.4.1 SR ff LR sf Interactions

As has been discussed, $\omega(\ell)$ has two components, relating to the effects of the ff and sf interactions respectively. In the SR ff LR sf interactions case, the ff component is derived by utilising a Landau-Ginzburg approximation for the density profile [41, 147]. This is typically constructed using magnetic language, and fluid-Ising magnet universality applied to translate the result back into fluid language. As Landau-Ginzburg theory is used, this approximation is mean field. Following the derivations found in [41] and [147], the ff component of $\omega(\ell)$ can be found to be

$$\omega_{SR,ff}(\ell) = a(T)e^{-\ell/\xi} + b'(T)e^{-2\ell/\xi} + H.O.T \tag{5.4.1}$$

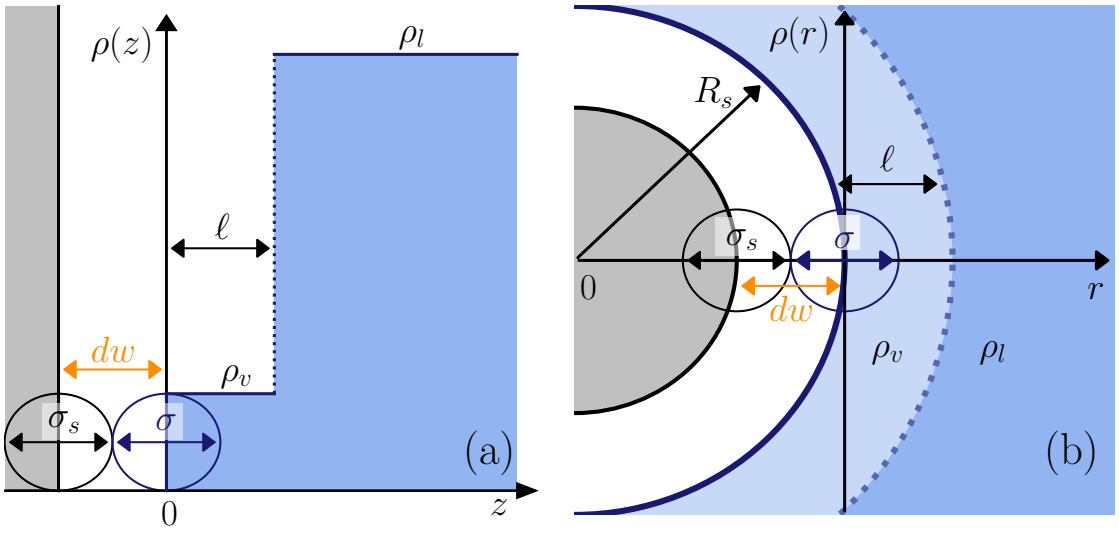

Figure 5.4: Illustration of sharp-kink (SK) approximation for the systems considered. (a) Under a SK approximation for a planar substrate, the system is assumed to consist of three slabs, representing the substrate (grey), vapour and liquid (both blue), the latter of which are taken to have the coexisting densities ρ_v and ρ_l respectively. The width of the vapour slab is taken to be ℓ. The density and interaction of the fluid and surface are measured from the centre of the fluid and surface particles respectively. This leads to a region of excluded volume of width dw. (b) Under a SK approximation for a curved substrate, the system is assumed to consist of a large solute (grey), a vapour shell (light blue) of width ℓ, and a liquid shell (darker blue). A region of excluded volume (white) of width dw exists between the solute and vapour due to the finite size of the particles. This leads to an effective radius of R_s.

where ξ is the correlation length of the bulk vapour, $a(T)$ and $b'(T)$ are constants, and $H.O.T$ stands for higher order terms. This exponential form indicates that the bound liquid-vapour interface and the substrate interact through the exponentially decaying tails of the density profile [41]. It is also interesting to note that the derivations of this found in [41] and [147] do not specify a form for the ff interaction potential. In fact, $\omega_{SR,ff}(\ell)$ contains no information of the microscopic interactions, and instead only requires that they be SR [144].

In order to evaluate the sf component, it is necessary to specify the density profile. However, to find this, it is typically necessary to perform a numerical study using a method such as cDFT. As this is time consuming, and gives no analytic solution, $\rho(z)$ is approximated. One way in which to do this would be to use the result of the Landau-Ginzburg treatment used for the ff component, however this form of the density profile also does not typically lead to an analytic solution for $\omega_{sf}(\ell)$. Instead, the simpler approximation of a sharp-kink (SK) profile, which has the form [143]

$$\rho(z) = \begin{cases} \rho_v & 0 < z < \ell \\ \rho_l & \ell < z \end{cases} \tag{5.4.2}$$

is used. The form of this profile is shown in figure 5.4(a). The profile is assumed to consist of two fluid slabs of constant density, with the nearest to the substrate taking the coexisting vapour density, ρ_v, and the slab furthest from the substrate taking the coexisting liquid

density, ρ_l. At a distance ℓ, there is a sharp transition between the two densities. Due to the finite size of the fluid and substrate particles, there exists a region of excluded volume between the substrate and the vapour slab, which has width dw, and is as shown in figure 5.4(a).

Using such a profile, the sf component of $\omega(\ell)$ can be found to be [41, 117]

$$\omega_{LR,sf}(\ell) = \Delta\rho\rho_s \int_{\ell+dw}^{\infty} \mathrm{d}z V_{ext}(z) \tag{5.4.3}$$

Within the present work, $V_{ext}(z)$ is assumed to take the form given in equation (4.1.46), though it should be noted that the factor of ρ_s in the prefactor of equation (4.1.46) is the same ρ_s as in the equation above. Substitution of V_{ext} into equation (5.4.3) leads to a form of the sf component of $\omega(\ell)$ of

$$\omega_{LR,sf}(\ell) = \frac{2\pi\sigma_s^3}{3}\Delta\rho\rho_s\varepsilon_s \left[\frac{\sigma_s^9}{60(\ell + (dw + z_{min}))^8} - \frac{\sigma_s^3}{2(\ell + (dw + z_{min}))^2}\right] \tag{5.4.4}$$

where ρ_s is the density of the substrate, and ε_s the sf attraction strength. Further details of this derivation can be found in appendix D.1.

This expression can be rewritten as an inverse power series in ℓ, by performing a Taylor expansion of $(\ell + dw)^{-2}$ and $(\ell + dw)^{-8}$. Retaining only leading order terms from both equations (5.4.1) and (5.4.4) then gives $\omega(\ell)$ for the case of SR ff LR sf interactions as

$$\omega_{SR}(\ell) = \omega_{SR,ff}(\ell) + \omega_{LR,sf}(\ell) = a(T)e^{-\ell/\xi} + \frac{b(T)}{\ell^2} + H.O.T \tag{5.4.5}$$

where $b(T)$ is a constant with dimensions of energy which is defined as

$$b(T) = -b_o\rho_s\varepsilon_s\sigma_s^6 \tag{5.4.6}$$

with $b_o = \pi\Delta\rho/3$.

5.4.2 LR ff LR sf Interactions

The derivation for $\omega(\ell)$ in the case of LR ff LR sf interactions typically utilises cDFT to construct a density functional of the excess grand potential, which can then be minimised for a given ℓ to find the equilibrium density profile [50]. This then gives a form of the excess grand potential which is a function of ℓ, which can be compared to equation (5.1.1) to find $\omega(\ell)$ [50]. However, as was discussed in section 4.1, minimising the grand potential must normally be done numerically. To avoid this, and instead allow for an analytic form of $\omega(\ell)$, a SK approximation like that in equation (5.4.2) is usually made for the density profile [143, 144].

Following the derivations of [50], [143] and [144], $\omega(\ell)$ for the case of LR ff LR sf interactions can be found to be

$$\omega_{LR}(\ell) = \Delta\rho\left(\rho_s \int_{\ell+dw}^{\infty} \mathrm{d}z V_{ext}(z) - \rho_v \int_{\ell}^{\infty} \mathrm{d}z\phi(z)\right) \tag{5.4.7}$$

where $\phi(z)$ is the attraction felt by a single particle due to the ff interaction with all other particles, and takes the form

$$\phi(z) = \int_z^\infty \mathrm{d}z'' \phi_{att}(z'' = |z' - \tilde{z}|) \tag{5.4.8}$$

The first term of equation (5.4.7) can be recognised as equation (5.4.3), and represents the sf component of $\omega(\ell)$, whilst the second term represents the ff component.

V_{ext} is assumed to have the form of equation (4.1.46), with ρ_s having been pulled out of the prefactor of equation (4.1.46) in equation (5.4.7), whilst the attraction between fluid particles is assumed to take the form of equation (4.1.45). Using these, $\omega_{LR}(\ell)$ can be found to be

$$\omega_{LR}(\ell) = \frac{2\pi}{3}\Delta\rho\left(\rho_s\varepsilon_s\sigma_s^3\left[\frac{\sigma_s^9}{60(\ell + (dw + z_{min}))^8} - \frac{\sigma_s^3}{2(\ell + (dw + z_{min}))^2}\right] - \rho_v\varepsilon\sigma^3\left[\frac{\sigma^9}{60\ell^8} - \frac{\sigma^3}{2\ell^2}\right]\right) \tag{5.4.9}$$

For further details, see appendix D.2. Performing a Taylor expansion of $(\ell + dw)^{-2}$ and $(\ell + dw)^{-8}$ about ℓ then allows this to be written as

$$\omega_{LR}(\ell) = \frac{b(T)}{\ell^2} + \frac{c(T)}{\ell^3} + H.O.T \tag{5.4.10}$$

where the constants $b(T)$ and $c(T)$ take the forms

$$b(T) = b_o(\rho_v\varepsilon\sigma^6 - \rho_s\varepsilon_s\sigma_s^6) \qquad c(T) = 2(dw + z_{min})\rho_s\varepsilon_s\sigma_s^6 b_o \tag{5.4.11}$$

and b_o is defined as before.

5.4.3 Effect of Curvature

If instead of a planar substrate, the system consists of a large solute, then the binding potential will acquire terms proportional to the curvature. Despite this, $\omega(\ell; R_s)$ can be derived in much the same way as in the preceding section. Considering first the case of LR ff LR sf interactions, similar reasoning as in the planar substrate case leads to a form of the binding potential very similar to that of equation (5.4.7) [145]

$$\omega_{LR}(\ell; R_s) = \Delta\rho\left(\rho_s\int_{R_s+\ell}^\infty \mathrm{d}r\left(\frac{r}{R_s}\right)^2 V_{ext}(r; R_s - dw) - \rho_v\int_{R_s+\ell}^\infty \mathrm{d}r\left(\frac{r}{R_s}\right)^2 \phi(r; R_s)\right) \tag{5.4.12}$$

where, the SK approximation described in figure 5.4(b) has been used, and is written as

$$\rho(r) = \begin{cases} \rho_v & R_s < r < R_s + \ell \\ \rho_l & R_s + \ell < r \end{cases} \tag{5.4.13}$$

In the case of a solute, $V_{ext}(r; R_s - dw)$ takes the form of equation (4.1.54), without the

factor of ρ_s in ε_{sf}, and $\phi(r;R_s)$ takes the form

$$\phi(r;R_s) = \int_{|r|\leq R_s} \mathrm{d}r'' \phi_{att}(r'' = |r' - \tilde{r}|) \tag{5.4.14}$$

where ϕ_{att} is as given in equation (4.1.53). Substituting these into equation (5.4.12) and evaluating leads to [34, 117]

$$\omega_{LR}(\ell;R_s) = \omega_{LR}(\ell)\left(1 + \frac{\ell}{R_s} + \mathcal{O}\left(\frac{\ell^2}{R_s^2}\ln\left(\frac{\ell}{2R_s}\right)\right)\right) \tag{5.4.15}$$

where $\omega_{LR}(\ell)$ is the binding potential for a planar substrate, as given in equation (5.4.10).

In the case of SR ff LR sf interactions, the ff component is unchanged by the curvature of the surface. The sf component takes the same form as above, and therefore obtains the same curvature corrections as in equation (5.4.15). Within the construction of the effective interface potential for a solute, it is assumed that R_s is very large, and therefore it can also be assumed that $R_s \gg \ell$. Hence $\omega(\ell;R_s)$ in both the cases of LR ff LR sf and SR ff LR sf interactions can be approximated as the equivalent binding potential at a planar substrate

$$\omega(\ell;R_s) \approx \omega(\ell) \tag{5.4.16}$$

5.5 Critical Drying in SR ff LR sf Systems

SR ff LR sf interactions best describe those found in numerical or molecular simulation studies. Throughout this section, the expected behaviour of ℓ_{eq} and $\chi_\mu(\ell_{eq};R_s)$ is investigated in detail for such systems, first with a planar substrate then with a curved substrate. Several previous studies have considered the former case [1, 32, 37], whilst the latter case has been the focus of fewer studies [146]. The study by Evans et al. [146] in particular considered only a hard solute and the behaviour of ℓ_{eq}.

5.5.1 Planar Substrate

Substitution of equation (5.4.5) into equation (5.1.4) gives $\omega_{ex}(\ell)$ for a system consisting of a planar substrate in contact with an oversaturated fluid. Considering only leading order terms, this is

$$\omega_{ex}(\ell) = \gamma_{sv} + \gamma_{lv} + a(T)e^{-\ell/\xi} + \frac{b(T)}{\ell^2} + \delta\mu\Delta\rho\ell \tag{5.5.1}$$

where $a(T)$ and $b(T)$ are temperature dependent constants with dimensions of energy per area and energy respectively, and $b(T)$ takes the specific the form

$$b(T) = -b_o\rho_s\varepsilon_s\sigma_s^6, \qquad b_o = \frac{\pi}{3}\Delta\rho$$

Substitution of $\omega_{ex}(\ell)$ into equation (5.2.1) allows the equilibrium vapour film width, ℓ_{eq}, to be identified as

$$-\frac{\ell_{eq}}{\xi} = \ln\left(\frac{\xi}{a}\right) + \ln\left(\delta\mu\Delta\rho - \frac{2b}{\ell_{eq}^3}\right) \tag{5.5.2}$$

where the temperature dependence of the constants a and b has been omitted. The divergence of ℓ_{eq} on the approach to critical or complete drying is determined by the second term and, due to the logarithmic nature, must be slow. It can be seen that ℓ_{eq} diverges only when both $\delta\mu \to 0$ and $\varepsilon_s \to 0$, hence the drying critical point in the case of SR ff LR sf interactions must exist at $(\delta\mu = 0, \varepsilon_s = 0)$. The first of these conditions is expected, however the second implies a lack of temperature dependence of the drying critical point. It can therefore be concluded that critical drying occurs for all temperatures below the bulk critical temperature, T_c. This agrees with the findings of Evans et al. [1, 38].

On the approach to critical drying along path (a) in figure 5.2(a), equation (5.5.2) predicts that $\ell_{eq} \sim -\ln\varepsilon_s + 3\ln\ell_{eq}$. This relationship was previously reported by Evans et al. [1], who also provided numerical evidence for such a relationship using cDFT for a truncated LJ fluid. Considering the approach to complete drying along path (b) in figure 5.2(a), equation (5.5.2) indicates that $\ell_{eq} \sim -\ln\delta\mu$. This agrees with the result expected for complete wetting with SR forces [50].

Substitution of equation (5.5.2) into equation (5.3.1) gives an expression for $\chi_\mu(\ell_{eq})$. First evaluating the derivative of ℓ_{eq} gives

$$\frac{\partial \ell_{eq}}{\partial \mu} = -\xi\Delta\rho\left(\delta\mu\Delta\rho - \frac{2b}{\ell_{eq}^3}\left(1 - \frac{3\xi}{\ell_{eq}}\right)\right)^{-1} \tag{5.5.3}$$

Substitution of this then gives $\chi_\mu(\ell_{eq})$ to be

$$\chi_\mu(\ell_{eq}) = \xi\Delta\rho\rho'(\ell_{eq})\left(\delta\mu\Delta\rho - \frac{2b}{\ell_{eq}^3}\left(1 - \frac{3\xi}{\ell_{eq}}\right)\right)^{-1} \tag{5.5.4}$$

This indicates a power law divergence of density fluctuations on the approach to the drying critical point, where $\delta\mu$ and $b(T)$ vanish, as expected. Considering first the approach to critical drying, it can be deduced that $\chi_\mu(\ell_{eq}) \sim \varepsilon_s^{-1}$. This is the same result as was obtained by Evans et al. [1, 32], who confirmed it for a SR LJ fluid using cDFT and MC. On the approach to complete drying, $\chi_\mu(\ell_{eq}) \sim \delta\mu^{-1}$. This relationship was previously reported by Evans and Stewart [37], who confirmed it using cDFT for a SR LJ fluid.

Substitution of equation (5.5.2) into equation (5.3.2) gives $\chi_T(\ell_{eq})$. First evaluating the derivative of ℓ_{eq} gives

$$-\frac{\partial \ell_{eq}}{\partial T} = \left(1 - \frac{\ell_{eq}}{\xi}\right)\frac{\partial \xi}{\partial T} + \xi\left(\frac{1}{\Delta\rho}\frac{\partial \Delta\rho}{\partial T} - \frac{1}{a}\frac{\partial a}{\partial T}\right) + \xi\left(\delta\mu\Delta\rho - \frac{2b}{\ell_{eq}^3}\right)^{-1}\left(-\Delta\rho\frac{\partial \mu_{co}}{\partial T} + \frac{6b}{\ell_{eq}^4}\frac{\partial \ell_{eq}}{\partial T}\right) \tag{5.5.5}$$

Assuming that the system is far below T_c, ξ will be small and not expected to grow quickly. Because of this, the term proportional to its derivative can be neglected. From the Landau-Ginzburg derivation of $\omega_{SR,ff}(\ell)$, it can be found that the temperature dependence of a arises because $a \propto \Delta\rho$ [41]. With this knowledge, the second term on the right is zero. $\chi_T(\ell_{eq})$ can

then be found to be

$$\chi_T(\ell_{eq}) = -\xi\Delta\rho\rho'(\ell_{eq})\left(\delta\mu\Delta\rho - \frac{2b}{\ell_{eq}^3}\left(1 - \frac{3\xi}{\ell_{eq}}\right)\right)^{-1}\frac{\partial\mu_{co}}{\partial T} = -\chi_\mu(\ell_{eq})\left(\frac{\partial\mu_{co}}{\partial T}\right) \tag{5.5.6}$$

This follows the relationship predicted in equation (5.3.8). It is therefore expected that in the case of SR ff LR sf interactions and a planar substrate, all measures of density fluctuations diverge in the same way on the approach to the drying critical point.

5.5.2 Curved Substrate

Substitution of equation (5.4.5) into equation (5.1.7) gives $\omega_{ex}(\ell; R_s)$ for a curved substrate, or solute, in contact with an oversaturated fluid. Considering only leading order terms, this is

$$\omega_{ex}(\ell; R_s) = \gamma_{sv} + \gamma_{lv} + a(T)e^{-\ell/\xi} + \frac{b(T)}{\ell^2} + \tilde{p}(T)\ell \tag{5.5.7}$$

where $\tilde{p}(T)$ is defined in equation (5.2.3) as

$$\tilde{p} = \delta\mu\Delta\rho + \frac{2\gamma_{lv}}{R_s}$$

Substitution of this into equation (5.2.2) gives an expression for ℓ_{eq} of

$$-\frac{\ell_{eq}}{\xi} = \ln\left(\frac{\xi}{a}\right) + \ln\left(\tilde{p} - \frac{2b}{\ell_{eq}^3}\right) \tag{5.5.8}$$

where the temperature dependence is now omitted. This has the same form as in the case of a planar substrate, as given in equation (5.5.2), with the only difference being that $\delta\mu\Delta\rho$ has been replaced with $\tilde{p}$. This highlights that the effects of curvature within such systems are equivalent to the effects of oversaturation. Considering the form of $\tilde{p}$, it can be seen that as $R_s \to \infty$, equation (5.5.2) is recovered from equation (5.5.8), as expected. This then gives the further condition that the drying critical point for a system with SR ff LR sf interactions must exist where $(\delta\mu = 0, \varepsilon_s = 0, R_s = \infty)$. The latter condition is expected as true phase transitions cannot occur in finite systems.

On the approach to critical drying along path (a) in figure 5.2(a), ℓ_{eq} can be seen to take the form

$$\ell_{eq}(\delta\mu = 0; R_s) \sim -\ln\left(\frac{2\gamma_{lv}}{R_s} - \frac{2b}{\ell_{eq}^3}\right) \tag{5.5.9}$$

Depending on the relative magnitudes of $2\gamma_{lv}/R_s$ and $2b/\ell_{eq}^3$, two scaling regimes can be identified as

$$\ell_{eq}(\delta\mu = 0; R_s) \sim \begin{cases} \ln R_s & R_s \ll \frac{\gamma_{lv}\ell_{eq}^3}{|b|} \\ -\ln\varepsilon_s + 3\ln\ell_{eq} & \frac{\gamma_{lv}\ell_{eq}^3}{|b|} \ll R_s \end{cases} \tag{5.5.10}$$

In the second case, the expected behaviour is identical to that of a planar substrate. This indicates that the effects of curvature of the substrate are only relevant when R_s is smaller than a certain length scale. However, determining such a length scale is difficult, due to the occurrence of ℓ_{eq} within the condition. Substitution of $\ell_{eq} \sim \ln R_s$ and $|b| = b_o\Delta\rho\rho_s\varepsilon_s\sigma_s^3$ into

this condition gives an estimate that, for curvature to be the dominant influence on ℓ_{eq} on the approach to critical drying, $R_s(\ln R_s)^{-1} \ll 3\gamma_{lv}/b_o\rho_s\varepsilon_s\sigma_s^3$.

On the approach to complete drying along path (b) in figure 5.2(a), equation (5.5.8) indicates that $\ell_{eq} \sim -\ln\tilde{p}$. Again, two scaling regimes can be identified, however in this case, it is far easier to determine the length scale which separates them. This is because $\tilde{p}$ can be rewritten as

$$\tilde{p} = \delta\mu\Delta\rho\left(1 + \frac{2\gamma_{lv}}{\delta\mu\Delta\rho R_s}\right) = \delta\mu\Delta\rho\left(1 + \frac{R_c}{R_s}\right) \tag{5.5.11}$$

where $R_c = 2\gamma_{lv}/\delta\mu\Delta\rho$ [146]. This can be identified as the same length scale for which an oversaturated liquid subject to confinement will evaporate, the process of which is called capillary evaporation [42]. Using this, the two scaling regimes of ℓ_{eq} on the approach to complete drying along path (b) of figure 5.2(a) can be identified as

$$\ell_{eq}(\varepsilon_s = 0; R_s) \sim \begin{cases} \ln R_s & R_s \ll R_c \\ -\ln\delta\mu & R_c \ll R_s \end{cases} \tag{5.5.12}$$

Such scaling regimes have previously been predicted by Evans et al. [146]. In the first case, the same scaling as in the first case of equation (5.5.10) is recovered, whilst in the second case, the scaling expected at a planar substrate is recovered. This indicates that again, the effects of curvature are only relevant for R_s smaller than a specific length scale. Considering these cases in conjunction with those of critical drying given in equation (5.5.10), it can be seen that the individual effects of $(\delta\mu, \varepsilon_s, R_s)$ are each dominant in a region of parameter space about the drying critical point, and that each is a measure of deviation from the critical point.

Substitution of equation (5.5.8) into equation (5.3.3) gives $\chi_\mu(\ell_{eq}; R_s)$. First evaluating the derivative of ℓ_{eq} gives

$$\frac{\partial\ell_{eq}}{\partial\mu} = -\xi\Delta\rho\left(\tilde{p} - \frac{2b}{\ell_{eq}^3}\left(1 - \frac{3\xi}{\ell_{eq}}\right)\right)^{-1} \tag{5.5.13}$$

which, when substituted, gives $\chi_\mu(\ell_{eq}; R_s)$ to be

$$\chi_\mu(\ell_{eq}; R_s) = \xi\Delta\rho\rho'(R_s + \ell_{eq})\left(\tilde{p} - \frac{2b}{\ell_{eq}^3}\left(1 - \frac{3\xi}{\ell_{eq}}\right)\right)^{-1} \tag{5.5.14}$$

Again, this expression is equivalent to that of a planar substrate, given in equation (5.5.4), as $R_s \to \infty$.

Considering first the approach to critical drying, substitution of $\ell_{eq}(\delta\mu = 0; R_s)$ allows two regimes of $\chi_\mu(\ell_{eq})$ to be identified

$$\chi_\mu(\ell_{eq}(\delta\mu = 0); R_s) \sim \begin{cases} R_s & R_s \ll \frac{\gamma_{lv}\ell_{eq}^3}{|b|} \\ \varepsilon_s^{-1} & \frac{\gamma_{lv}\ell_{eq}^3}{|b|} \ll R_s \end{cases} \tag{5.5.15}$$

This identifies that, for large R_s, $\chi_\mu(\ell_{eq}; R_s)$ diverges in the same way as if the substrate were

planar, whilst for small R_s, the density fluctuations grow as the radius of the substrate or solute is increased. On the approach to complete drying, the two scaling regimes are

$$\chi_\mu(\ell_{eq}(\varepsilon_s = 0); R_s) \sim \begin{cases} R_s & R_s \ll R_c \\ \delta\mu^{-1} & R_c \ll R_s \end{cases} \tag{5.5.16}$$

Again, the expected divergence of $\chi_\mu(\ell_{eq})$ for a planar substrate is recovered for sufficiently large R_s. For small R_s, $\chi_\mu(\ell_{eq}(\varepsilon_s = 0); R_s)$ diverges in the same way as $\chi_\mu(\ell_{eq}(\delta\mu = 0); R_s)$. As in the case of ℓ_{eq}, it can therefore be seen that there exist three regions of parameter space in which the behaviour of $\chi_\mu(\ell_{eq}; R_s)$ is largely determined by the parameters $(\delta\mu, \varepsilon_s, R_s)$ individually.

Substitution of equation (5.5.8) into equation (5.3.4) gives $\chi_T(\ell_{eq}; R_s)$. First evaluating the derivative of ℓ_{eq} gives

$$\begin{aligned} -\frac{\partial \ell_{eq}}{\partial T}\left(\tilde{p} - \frac{2b}{\ell_{eq}^3}\left(1 - \frac{3\xi}{\ell_{eq}}\right)\right)\left(\tilde{p} - \frac{2b}{\ell_{eq}^3}\right)^{-1} & \\ = \frac{\partial \xi}{\partial T}\left(1 - \frac{\ell_{eq}}{\xi}\right) + \xi\left(\frac{1}{\Delta\rho}\frac{\partial \Delta\rho}{\partial T} - \frac{1}{a}\frac{\partial a}{\partial T}\right) & \\ + \xi\left(\tilde{p} - \frac{2b}{\ell_{eq}^3}\right)^{-1}\left(\frac{2}{R_s}\left(\frac{\partial \gamma_{lv}}{\partial T} - \frac{\gamma_{lv}}{\Delta\rho}\frac{\partial \Delta\rho}{\partial T}\right) - \Delta\rho\frac{\partial \mu_{co}}{\partial T}\right) & \end{aligned} \tag{5.5.17}$$

This can be simplified using the same assumptions as in the case of a planar substrate - that the first term on the right can be neglected whilst the second term vanishes. Furthermore, the chain rule can be used to simplify the third term on the right, and hence the local thermal susceptibility can be written as

$$\chi_T(\ell_{eq}; R_s) = \xi\Delta\rho\rho'(R_s + \ell_{eq})\left(\tilde{p} - \frac{2b}{\ell_{eq}^3}\left(1 - \frac{3\xi}{\ell_{eq}}\right)\right)^{-1}\left(\frac{2}{R_s}\frac{\partial}{\partial T}\left(\frac{\gamma_{lv}}{\Delta\rho}\right) - \frac{\partial \mu_{co}}{\partial T}\right) \tag{5.5.18}$$

Once again, this has a similar form as that of $\chi_\mu(\ell_{eq}; R_s)$ given in equation (5.5.14), allowing $\chi_T(\ell_{eq}; R_s)$ to be rewritten as

$$\chi_T(\ell_{eq}; R_s) = \chi_\mu(\ell_{eq}; R_s)\left(\frac{2}{R_s}\frac{\partial}{\partial T}\left(\frac{\gamma_{lv}}{\Delta\rho}\right) - \frac{\partial \mu_{co}}{\partial T}\right) \tag{5.5.19}$$

which is in agreement with the predictions of equation (5.3.17).

5.5.3 Validity of MFT Approach

The relations presented thus far have been obtained using MFT, hence fluctuations, such as those in the shape of the liquid-vapour interface, have been ignored. To understand whether this is a valid approach, it is important to calculate the upper critical dimension, d^*, of the system. This can be done in a similar way as was done in section 2.4.2 for a bulk fluid. Each approach to the critical point, either by path (a) for critical drying or path (b) for complete drying in figure 5.2(a), features its own upper critical dimension, denoted d_s^* and d_{com}^* respectively, which are considered in turn.

Considering first the case of critical drying approached along path (a), and a planar substrate, the singular part of the surface free energy, given in equation (5.5.1), can be written as

$$\omega_{sing}(\delta\mu = 0) = \omega_{ex}(\ell_{eq}(\delta\mu = 0)) - \gamma_{sv} - \gamma_{lv} = \frac{b}{\ell_{eq}^2}\left(1 - \frac{2\xi}{\ell_{eq}}\right) \tag{5.5.20}$$

where the exponential term has been substituted for. Typically, this would be expected to diverge as $\omega_{sing} \sim |\tilde{t}|^{2-\alpha_s}$ [1, 41], where α_s and $\tilde{t}$ are as defined in section 5.3. However, as has been shown, critical drying occurs for all $T < T_c$ for systems with SR ff LR sf interactions, hence a more appropriate measure of deviation from the critical point for this system is $\delta\varepsilon_s = \varepsilon_s - \varepsilon_c$, where ε_c is the critical sf attraction which, for a system with SR ff LR sf interactions, is $\varepsilon_c = 0$. Using this, ω_{sing} can instead be written as

$$\omega_{sing} \sim |\delta\varepsilon_s|^{2-\alpha_s} \sim |\delta\varepsilon_s| \tag{5.5.21}$$

where the second expression arises directly from equation (5.5.20), as $b \propto \varepsilon_s$. This allows for α_s to be identified as $\alpha_s = 1$ [1].

The energy of a thermal fluctuation within this system can be found using

$$\omega_{fluc} = \frac{k_{\mathrm{B}}T}{\xi_{||}^{(d-1)}} \tag{5.5.22}$$

where k_{B} is Boltzmann's constant, $d = 3$ is the dimension of the system, and the parallel correlation length, $\xi_{||}$ can be found using [50]

$$\xi_{||} \sim \left(\frac{\partial^2\omega_{sing}}{\partial\ell^2}\right)^{-1/2}_{\ell=\ell_{eq}(\delta\mu=0)} \tag{5.5.23}$$

Evaluating this for the case of SR ff LR sf interactions gives

$$\xi_{||} \sim \left(\frac{2b}{\ell_{eq}^3}\left(\frac{3}{\ell_{eq}} - \frac{1}{\xi}\right)\right)^{-1/2} \tag{5.5.24}$$

This is expected to vary as $\xi_{||} \sim |\delta\varepsilon_s|^{-\nu_{||,s}}$, on the approach to critical drying, hence $\nu_{||,s} = 1/2$ [1]. The upper critical dimension for this interfacial system is then found by equating the critical exponents of ω_{sing} and ω_{fluc}, which gives [1]

$$2 - \alpha_s = (d_s^* - 1)\nu_{||,s} \tag{5.5.25}$$

Substituting for α_s and $\nu_{||,s}$ gives the upper critical dimension of a system with SR ff LR sf interactions to be $d_s^* = 1 + \nu_{||,s}^{-1}(2 - \alpha_s) = 3$. This is the same as the physical dimension of the system, hence the case of SR ff LR sf interactions is on the edge of the applicability of MFT. Because of this previous studies have carried out detailed renormalisation group theory calculations. These concluded that fluctuations alter only the amplitude, as opposed to the critical exponents, of observables, and hence a MFT approach is valid [1].

Equation (5.5.25) is also expected to apply to the case of complete drying, with the critical drying critical exponents replaced with the equivalent exponents for complete drying. These can be found in much the same way as above, by substituting, for example, $\ell_{eq}(\varepsilon_s = 0)$ into ω_{sing} and equation (5.5.23), and considering the behaviour with $\delta\mu$ as opposed to $\delta\varepsilon_s$. Doing so leads to the conclusion that the complete drying critical exponents are $\alpha_{com} = 1$ and $\nu_{||,com} = 1/2$, which gives $d^*_{com} = 3$. As this is equal to the dimension of the system, the case of complete drying at $\varepsilon_s = 0$ in the case of SR ff LR sf interactions is again on the edge of the applicability of MFT. As such, it is expected that there will be corrections to the amplitude of observables, however the critical exponents should be correct.

Using α_s, the gap exponent, which was shown in section 5.3 to provide a condition for the validity of equations (5.3.8) and (5.3.17), can be determined. Noting that the adsorption, Γ, is proportional to ℓ_{eq}, a scaling form for ℓ_{eq} similar to that of equation (5.3.13) can be written as

$$\ell_{eq} \sim |\delta\varepsilon_s|^{2-\alpha_s-\Delta}\mathcal{L}\left(\frac{\delta\mu}{|\delta\varepsilon_s|^{\Delta}}\right) \sim |\delta\varepsilon_s|^{\beta_s} \tag{5.5.26}$$

where the reduced temperature has been replaced with the appropriate parameter, $\delta\varepsilon_s$, for this system. As seen in the second expression, this is expected to go as $|\delta\varepsilon_s|^{\beta_s}$, where β_s is the surface critical exponent for the adsorption [1]. Equating the relations gives [41]

$$\Delta = 2 - \alpha_s - \beta_s \tag{5.5.27}$$

The scaling of $\ell_{eq}(\delta\mu = 0)$ was previously found to be logarithmic in ε_s, hence β_s can be identified as $\beta_s = 0$. Substitution of $\alpha_s = 1$ and $\beta_s = 0$ into this therefore gives the gap exponent for a system with SR ff LR sf interactions as $\Delta = 1$. The condition for the validity of equations (5.3.8) and (5.3.17) was that $\Delta > 1$, hence the case of SR ff LR sf interactions is a marginal case for the applicability of these relations according to the analysis of section 5.3. It is therefore necessary to resort to a microscopic analysis, like that of the preceding sections, to confirm the applicability of these relationships. Equation (5.5.6) shows that such a relationship is indeed followed for the case of a planar substrate, whilst equation (5.5.19) shows this for a curved substrate.

5.6 Critical Drying in LR ff LR sf Systems

The case of LR ff LR sf interactions, relevant to experiment, is difficult to implement efficiently within numerical and computational studies. Approximations such as the SK approximation have therefore been utilised extensively in previous studies of such systems [41, 50, 143, 145]. Whilst these studies focused on the case of critical wetting, many of their results are equally applicable to critical drying, due to the view that drying can be thought of as wetting by a vapour, discussed in section 2.4.5. Because of this, various critical exponents and forms of ℓ_{eq} are well known. There have also been several studies of the effects of the drying critical point in systems with solutes [33, 34, 117, 145], however these studies were limited to discussion of ℓ_{eq} and the corresponding $\omega_{ex}(\ell)$.

5.6.1 Planar Substrates

For LR ff LR sf interactions in the case of a planar substrate, substitution of equation (5.4.10) into equation (5.1.4) leads to

$$\omega_{ex}(\ell) = \gamma_{sv} + \gamma_{lv} + \frac{b(T)}{\ell^2} + \frac{c(T)}{\ell^3} + \delta\mu\Delta\rho\ell \tag{5.6.1}$$

where $b(T)$ and $c(T)$ are given in equation (5.4.11) as

$$b(T) = b_o(\rho_v\varepsilon\sigma^6 - \rho_s\varepsilon_s\sigma_s^6) \qquad c(T) = 2(dw + z_{min})\rho_s\varepsilon_s\sigma_s^6 b_o$$

and $b_o = \pi\Delta\rho/3$. Considering these forms, it can be seen that $c(T)$ is positive for all temperatures. Assuming ρ_s is held constant, $b(T)$ will move from negative to positive upon increasing T, and therefore ρ_v. Because of this, $b(T)$ is the quantity which determines the location of the minimum in $\omega_{ex}(\ell)$. The drying temperature, T_D, can therefore be determined as the temperature for which $b(T_D) = 0$. Using this condition, the critical substrate attraction strength, ε_c, can be found to be

$$\varepsilon_c = \frac{\rho_v\sigma^6}{\rho_s\sigma_s^6}\varepsilon \tag{5.6.2}$$

which is the same result as that of Evans et al. [38]. The behaviour of the system can then be determined by $b(T)$. When $T < T_D$, $b(T) < 0$, and hence the minimum of $\omega_{ex}(\ell)$ occurs for a finite value of ℓ, which equates to the system favouring a microscopic vapour film. In contrast, when $T > T_D$, $b(T) > 0$ and hence the only possible location of the minimum is $\ell = \infty$. This equates to a macroscopic vapour film being favoured [50].

Considering this behaviour, it can be deduced that $b(T)$ follows the same behaviour as the reduced temperature on the approach to the drying critical point from below. This allows for the definition of a more convenient dimensionless measure of deviation from the drying critical point of

$$t' = (\rho_v\varepsilon\sigma^6 - \rho_s\varepsilon_s\sigma_s^6)\varepsilon^{-1}\sigma^{-3} \quad \sim \tilde{t} \text{ as } \tilde{t} \to 0 \tag{5.6.3}$$

named here as the effective reduced temperature. This is a similar definition to the effective reduced temperature used by Stewart and Evans [33] within their work. The convenience of this measure arises from the fact that $b(T) \propto t'$.

Substitution of equation (5.6.1) into equation (5.2.1) gives an equation for ℓ_{eq} of

$$\frac{2b(T)}{\ell_{eq}^3} + \frac{3c(T)}{\ell_{eq}^4} = \delta\mu\Delta\rho \tag{5.6.4}$$

Omitting the explicit temperature dependence for convenience, on the approach to critical drying along path (a) in figure 5.2(a), ℓ_{eq} takes the form

$$\ell_{eq}(\delta\mu = 0) = -\frac{3c}{2b} \tag{5.6.5}$$

which agrees with the result presented by Stewart and Evans [33], and is the drying equivalent of earlier results for wetting [41]. As $b(T) \propto t'$, this result implies $\ell_{eq}(\delta\mu = 0) \sim |t'|^{-1}$, which

allows the critical exponent, β_s to be identified as $\beta_s = -1$. This agrees with the exponent predicted for the case of critical wetting in systems with LR ff LR sf interactions [41, 50].

On the approach to complete drying along path (b) in figure 5.2(a), equation (5.6.4) predicts that

$$\ell_{eq}(t' = 0) = \left(\frac{3c}{\delta\mu\Delta\rho}\right)^{1/4} \tag{5.6.6}$$

which implies that $\ell_{eq}(t' = 0) \sim \delta\mu^{-1/4}$. This agrees with previous results reported by, for example, [50].

Taking the derivative of equation (5.6.4) with respect to μ gives

$$\frac{\partial \ell_{eq}}{\partial \mu} = -\Delta\rho \left(\frac{6b}{\ell_{eq}^4} + \frac{12c}{\ell_{eq}^5}\right)^{-1} \tag{5.6.7}$$

Substituting this into equation (5.3.1) gives $\chi_\mu(\ell_{eq})$ as

$$\chi_\mu(\ell_{eq}) = \Delta\rho\rho'(\ell_{eq})\frac{\ell_{eq}}{3}\left(\delta\mu\Delta\rho + \frac{c}{\ell_{eq}^4}\right)^{-1} \tag{5.6.8}$$

Here, terms proportional to $b(T)$ have been substituted for using equation (5.6.4). On the approach to critical drying along path (a) of figure 5.2(a), substitution of $\ell_{eq}(\delta\mu = 0)$ reduces this to

$$\chi_\mu(\ell_{eq}(\delta\mu = 0)) = -\Delta\rho\rho'(\ell_{eq})\left(\frac{81c^4}{32b^5}\right) \tag{5.6.9}$$

This implies that $\chi_\mu(\ell_{eq}(\delta\mu = 0)) \sim |t'|^{-5}$, which indicates an incredibly fast power law divergence of density fluctuations on the approach to critical drying. On the approach to complete drying

$$\chi_\mu(\ell_{eq}(t' = 0)) = \frac{\Delta\rho\rho'(\ell_{eq})}{4}\frac{(3c)^{1/4}}{(\delta\mu\Delta\rho)^{5/4}} \tag{5.6.10}$$

which implies $\chi_\mu(\ell_{eq}(t' = 0)) \sim \delta\mu^{-5/4}$.

$\chi_T(\ell_{eq})$ is found by first taking the temperature derivative of equation (5.6.4). This can be greatly simplified by recognising that each term contains a factor of $\Delta\rho$ and that it is this term which gives $c(T)$ its temperature dependence. Rewriting $b(T) = \tilde{b}(T)\Delta\rho$ and $c(T) = \tilde{c}\Delta\rho$ allows equation (5.6.4) to be simplified to

$$\frac{2\tilde{b}(T)}{\ell_{eq}^3} + \frac{3\tilde{c}}{\ell_{eq}^4} = \delta\mu \tag{5.6.11}$$

Taking the temperature derivative then leads to

$$\begin{aligned}\frac{\partial \ell_{eq}}{\partial T} &= \left(\frac{6\tilde{b}(T)}{\ell_{eq}^4} + \frac{12\tilde{c}}{\ell_{eq}^5}\right)^{-1}\left(\frac{2\pi\sigma^6\varepsilon}{3\ell_{eq}^3}\frac{\partial \rho_v}{\partial T} + \frac{\partial \mu_{co}}{\partial T}\right) \\ &= \Delta\rho\frac{\ell_{eq}}{3}\left(\delta\mu\Delta\rho + \frac{c}{\ell_{eq}^4}\right)^{-1}\left(\frac{2\pi\sigma^6\varepsilon}{3\ell_{eq}^3}\frac{\partial \rho_v}{\partial T} + \frac{\partial \mu_{co}}{\partial T}\right)\end{aligned} \tag{5.6.12}$$

where, in the first line, the temperature dependence has been made explicit for clarity, and in the second line, the constants have been written in their original forms and $b(T)$ substituted for using equation (5.6.4). Considering this form, it can be seen that

$$\chi_T(\ell_{eq}) = -\chi_\mu(\ell_{eq})\left(\frac{2\pi\varepsilon\sigma^6}{3\ell_{eq}^3}\frac{\partial\rho_v}{\partial T} + \frac{\partial\mu_{co}}{\partial T}\right) \tag{5.6.13}$$

The terms within the brackets imply that $\chi_T(\ell_{eq})$ diverges in two ways however, due to the factor of ℓ_{eq}^{-3} in the first term, it can be seen that the second will always diverge faster. This can be seen explicitly by considering the individual cases of critical and complete drying.

Considering first the approach to critical drying along path (a) of figure 5.2(a), substitution of $\ell_{eq}(\delta\mu = 0)$ and $\chi_\mu(\ell_{eq}(\delta\mu = 0))$ into equation (5.6.13) gives

$$\begin{aligned}\chi_T(\ell_{eq}(\delta\mu = 0)) &= \Delta\rho\rho'(\ell_{eq})\left[-\left(\frac{\pi\varepsilon\sigma^6 c}{2b^2}\right)\frac{\partial\rho_v}{\partial T} + \left(\frac{81c^4}{32b^5}\right)\frac{\partial\mu_{co}}{\partial T}\right] \\ &\sim -\chi_\mu(\ell_{eq}(\delta\mu = 0))\frac{\partial\mu_{co}}{\partial T}\end{aligned} \tag{5.6.14}$$

as the first term diverges more slowly. Similarly, substitution of $\ell_{eq}(t' = 0)$ and $\chi_\mu(\ell_{eq}(t' = 0))$ into equation (5.6.13) gives

$$\begin{aligned}\chi_T(\ell_{eq}(t' = 0)) &= -\Delta\rho\rho'(\ell_{eq})\left[\left(\frac{\pi\varepsilon\sigma^6}{2(3)^{3/2}c^{1/2}(\delta\mu\Delta\rho)^{1/2}}\right)\frac{\partial\rho_v}{\partial T} + \left(\frac{(3c)^{1/4}}{4(\delta\mu\Delta\rho)^{5/4}}\right)\frac{\partial\mu_{co}}{\partial T}\right] \\ &\sim -\chi_\mu(\ell_{eq}(t' = 0))\frac{\partial\mu_{co}}{\partial T}\end{aligned} \tag{5.6.15}$$

Hence, in both the cases of critical and complete drying, the divergence of $\chi_T(\ell_{eq})$ follows that of $\chi_\mu(\ell_{eq})$, and the predicted relationship given in equation (5.3.8) is recovered.

5.6.2 Curved Substrates

Substitution of equation (5.4.10) into equation (5.1.7) gives $\omega_{ex}(\ell; R_s)$ for a curved substrate, or solute, in a system with LR ff LR sf interactions to be

$$\omega_{ex}(\ell; R_s) = \gamma_{sv} + \gamma_{lv} + \frac{b(T)}{\ell^2} + \frac{c(T)}{\ell^3} + \tilde{p}\ell \tag{5.6.16}$$

where $\tilde{p}$, given in equation (5.2.3), is

$$\tilde{p} = \delta\mu\Delta\rho + \frac{2\gamma_{lv}}{R_s}$$

and $b(T)$ and $c(T)$ are as defined in the case of a planar substrate. Comparing equation (5.6.16) to the equivalent expression for a planar substrate given in equation (5.6.1) shows that, once again, the only difference is the substitution of $\delta\mu\Delta\rho$ in the latter for $\tilde{p}$ in the former. As such, as $R_s \to \infty$, $\omega_{ex}(\ell; R_s) \to \omega_{ex}(\ell)$ as expected.

Omitting the explicit temperature dependence and substituting equation (5.6.16) into

equation (5.2.2) gives

$$\frac{2b}{\ell_{eq}^3} + \frac{3c}{\ell_{eq}^4} = \tilde{p} \tag{5.6.17}$$

which again, differs only by the replacement of $\delta\mu\Delta\rho$ for $\tilde{p}$ compared to the equivalent expression for a planar substrate given in equation (5.6.4). Due to the complexity of the resulting expression, little understanding can be gained by considering the approach to critical drying along path (a) of figure 5.2(a).

On the approach to complete drying along path (b) of figure 5.2(a), $\ell_{eq}(t' = 0; R_s)$ becomes

$$\ell_{eq}(t' = 0; R_s) = \left(\frac{3c}{\tilde{p}}\right)^{1/4} \tag{5.6.18}$$

This agrees with the expression obtained by Stewart and Evans [34], who further confirmed this relation using cDFT. Using that $\tilde{p}$ can be written in terms of the length scale R_c as given in equation (5.5.11), two scaling regimes can be identified as

$$\ell_{eq}(t' = 0; R_s) \sim \begin{cases} R_s^{1/4} & R_s \ll R_c \\ \delta\mu^{-1/4} & R_c \ll R_s \end{cases} \tag{5.6.19}$$

The first of these cases has been confirmed using cDFT by Stewart and Evans [33], whilst the second case again shows that, for sufficiently large R_s, the scaling expected at a planar substrate is recovered.

Taking the derivative of equation (5.6.17) with respect to μ gives

$$\frac{\partial \ell_{eq}}{\partial \mu} = -\Delta\rho \frac{\ell_{eq}}{3} \left(\tilde{p} + \frac{c}{\ell_{eq}^4}\right)^{-1} \tag{5.6.20}$$

where terms proportional to b have been substituted for using equation (5.6.17). Substituting this into equation (5.3.3) then gives $\chi_\mu(\ell_{eq}; R_s)$ to be

$$\chi_\mu(\ell_{eq}; R_s) = \Delta\rho\rho'(R_s + \ell_{eq}) \frac{\ell_{eq}}{3} \left(\tilde{p} + \frac{c}{\ell_{eq}^4}\right)^{-1} \tag{5.6.21}$$

As with ℓ_{eq} little understanding is gained by considering $\chi_\mu(\ell_{eq}(\delta\mu = 0); R_s)$.

On the approach to complete drying along path (b) of figure 5.2(a), $\chi_\mu(\ell_{eq}(t' = 0); R_s)$ can be written as

$$\chi_\mu(\ell_{eq}(t' = 0); R_s) = \frac{\Delta\rho\rho'(R_s + \ell_{eq})}{4} \frac{(3c)^{1/4}}{\tilde{p}^{5/4}} \tag{5.6.22}$$

Using equation (5.5.11) this can be written as two scaling regimes as

$$\chi_\mu(\ell_{eq}(t' = 0); R_s) \sim \begin{cases} R_s^{5/4} & R_s \ll R_c \\ \delta\mu^{-5/4} & R_c \ll R_s \end{cases} \tag{5.6.23}$$

Again, this shows that for large R_s, the scaling expected at a planar substrate is recovered, and hence the influence of curvature on the growth of density fluctuations is limited to small

R_s.

Dividing equation (5.6.17) by $\Delta\rho$ to eliminate the temperature dependence of $c(T)$ as in the planar case and taking the temperature derivative gives

$$\frac{\partial \ell_{eq}}{\partial T} = -\Delta\rho \frac{\ell_{eq}}{3}\left(\tilde{p} + \frac{c}{\ell_{eq}^4}\right)^{-1}\left(\frac{2}{R_s}\frac{\partial}{\partial T}\left(\frac{\gamma_{lv}}{R_s}\right) - \frac{\partial \mu_{co}}{\partial T} - \frac{2\pi\varepsilon\sigma^6}{3\ell_{eq}^3}\frac{\partial \rho_v}{\partial T}\right) \tag{5.6.24}$$

Substituting this into equation (5.3.4) gives $\chi_T(\ell_{eq}; R_s)$ to be

$$\begin{aligned}\chi_T(\ell_{eq}; R_s) &= \Delta\rho\rho'(R_s + \ell_{eq})\frac{\ell_{eq}}{3}\left(\tilde{p} + \frac{c}{\ell_{eq}^4}\right)^{-1}\left(\frac{2}{R_s}\frac{\partial}{\partial T}\left(\frac{\gamma_{lv}}{\Delta\rho}\right) - \frac{\partial \mu_{co}}{\partial T} - \frac{2\pi\varepsilon\sigma^6}{3\ell_{eq}^3}\frac{\partial \rho_v}{\partial T}\right) \\ &= \chi_\mu(\ell_{eq}; R_s)\left(\frac{2}{R_s}\frac{\partial}{\partial T}\left(\frac{\gamma_{lv}}{\Delta\rho}\right) - \frac{\partial \mu_{co}}{\partial T} - \frac{2\pi\varepsilon\sigma^6}{3\ell_{eq}^3}\frac{\partial \rho_v}{\partial T}\right)\end{aligned} \tag{5.6.25}$$

As in the planar case, the first two terms on the right diverge faster than the last, and hence as in the case of SR ff LR sf interactions, it is expected that

$$\frac{\chi_T(\ell_{eq}; R_s)}{\chi_\mu(\ell_{eq}; R_s)} \sim \left(\frac{2}{R_s}\frac{\partial}{\partial T}\left(\frac{\gamma_{lv}}{\Delta\rho}\right) - \frac{\partial \mu_{co}}{\partial T}\right) \tag{5.6.26}$$

which is in agreement with the predictions of equation (5.3.16).

5.6.3 Validity of MFT Approach

As in section 5.5.3, the validity of the MFT approach taken here can be assessed by calculating the upper critical dimension of the system using equation (5.5.25). For critical drying, the exponent, α_s, is found by substituting equation (5.6.5) into the singular part of equation (5.6.1). Doing so gives

$$\omega_{sing}(\delta\mu = 0) = \omega_{ex}(\ell_{eq}) - \gamma_{lv} - \gamma_{sv} = \frac{4b^3}{27c^2} \tag{5.6.27}$$

which is in agreement with that found by Stewart [117]. From this, it can be seen that $\omega_{sing} \sim |t'|^3$, and hence $\alpha_s = -1$, as was found for critical wetting in [41]. The exponent $\nu_{||,s}$ is found by calculating $\xi_{||}$ using equation (5.5.23), which gives

$$\xi_{||} \sim \left.\frac{\partial^2 \omega_{ex}(\ell)}{\partial \ell^2}\right|^{-1/2}_{\ell=\ell_{eq}(\delta\mu=0)} = \left(-\frac{32}{81}\frac{b^5}{c^4}\right)^{-1/2} \tag{5.6.28}$$

From this, it can be determined that $\nu_{||} = 5/2$, again as given in [41]. Substituting α_s and $\nu_{||}$ into equation (5.5.25) then gives $d_s^* = 11/5$. As this is smaller than the spatial dimension of the system, $d = 3$, a MFT approach is expected to yield the correct critical exponents [41, 50].

For the case of complete drying, $\omega_{sing}(t' = 0)$ is found by substituting equation (5.6.18) into the singular part of equation (5.6.1), which gives

$$\omega_{sing}(t' = 0) = (\delta\mu\Delta\rho)^{3/4} c^{1/4}\left(3^{1/4} + \frac{1}{3^{3/4}}\right) \tag{5.6.29}$$

This varies as $\omega_{sing}(t'=0) \sim \delta\mu^{3/4}$ and hence α_{com} can be identified as $\alpha_{com} = 5/4$, which agrees with the result presented for wetting with LR forces in [50]. The parallel correlation length exponent, $\nu_{||,com}$ can be identified to be

$$\xi_{||} \sim \left.\frac{\partial^2 \omega_{ex}(\ell)}{\partial \ell^2}\right|^{-1/2}_{\ell=\ell_{eq}(t'=0)} = \frac{12^{-1/2}}{3^{5/8}} c^{1/8} (\delta\mu\Delta\rho)^{-5/8} \tag{5.6.30}$$

which allows $\nu_{||,com}$ to be identified as $\nu_{||,com} = 5/8$, which agrees again with [50]. Substituting this and α_{com} into the hyperscaling relation then gives an upper critical dimension for complete drying of $d^*_{com} = 11/5$. As this is less than the dimension of the system, $d = 3$, a MFT approach is expected to yield the correct critical exponents for complete drying in the LR ff LR sf regime.

Using the same approach as in section 5.5.3, the gap exponent can be calculated using equation (5.5.27), and is found to be $\Delta = 4$. This agrees with the results presented in [41], and implies that equations (5.3.8) and (5.3.17) are expected to be valid for systems with LR ff LR sf interactions, in agreement with the findings of equations (5.6.15) and (5.6.26).

5.6.4 Scaling Function Forms

As was discussed in section 5.3, it is possible to write Γ_{sing}, and therefore ℓ_{eq}, in terms of a scaling function. In section 5.3, this was done for a planar substrate, and the scaling variable was stated to be $\delta\mu/|\tilde{t}|^{\Delta}$. Considering equation (5.6.4), and noting that $\tilde{t} \propto t'$, it can be seen that this is the natural scaling variable, as ℓ_{eq} cannot be written as a function of $\delta\mu$ and $|t'|$ separately [41]. Furthermore, it was previously shown in section 5.6.3 that $\Delta = 4$. ℓ_{eq} for the case of LR ff LR sf interactions and a planar substrate can therefore be written as

$$\ell_{eq} = \frac{\sigma}{|t'|} \mathcal{L}\left(\frac{\delta\mu}{\varepsilon|t'|^4}\right) \tag{5.6.31}$$

where $\mathcal{L}$ is a scaling function, and the appropriate critical exponents have been substituted for. This has the same form as that in [41]. This scaling function, $\mathcal{L}$, must obey equation (5.6.4) and hence it is possible to numerically calculate the form of $\mathcal{L}$, as was done in [33].

Taking the derivative of equation (5.6.31) with respect to μ and substituting into equation (5.3.1) gives a scaling function form of $\chi_\mu(\ell_{eq})$ of

$$\chi_\mu(\ell_{eq}) = \frac{\sigma}{\varepsilon|t'|^5} \rho'(\ell_{eq}) \mathcal{L}'\left(\frac{\delta\mu}{\varepsilon|t'|^4}\right) \tag{5.6.32}$$

where $\mathcal{L}'$ is the derivative of $\mathcal{L}$, and is itself a scaling function, which must follow equation (5.6.8). $\chi_T(\ell_{eq})$ can be found in a similar way to be

$$\chi_T(\ell_{eq}) = -\frac{\sigma}{\varepsilon|t'|^5} \rho'(\ell_{eq}) \mathcal{L}'\left(\frac{\delta\mu}{\varepsilon|t'|^4}\right) \frac{\partial \mu_{co}}{\partial T} - \frac{\sigma}{\varepsilon|t'|^2} \rho'(\ell_{eq}) \left(\mathcal{L}\left(\frac{\delta\mu}{\varepsilon|t'|^4}\right) + 4\left(\frac{\delta\mu}{\varepsilon|t'|^4} \mathcal{L}'\left(\frac{\delta\mu}{\varepsilon|t'|^4}\right)\right)\right) \tag{5.6.33}$$

where $\mathcal{L}'$ is again the derivative of $\mathcal{L}$, which must obey equation (5.6.25), and $(\delta\mu/\varepsilon|t'|^4)\mathcal{L}'(\delta\mu/\varepsilon|t'|^4)$ is a scaling function. The first term in this expression for $\chi_T(\ell_{eq})$ shows a much faster divergence than the remaining, and hence $\chi_T(\ell_{eq})$ can be written as

$$\chi_T(\ell_{eq}) \sim -\frac{1}{|t'|^5}\rho'(R_s+\ell_{eq})\mathcal{L}'\left(\frac{\delta\mu}{|t'|^4}\right)\frac{\partial\mu_{co}}{\partial T} = -\chi_\mu(\ell_{eq})\frac{\partial\mu_{co}}{\partial T} \tag{5.6.34}$$

If instead the substrate is curved, similar scaling functions can be found. The difference between the expressions for ℓ_{eq} in the planar and curved substrate cases is the replacement of $\delta\mu\Delta\rho$ in the former for $\tilde{p}$ in the latter. It is therefore sensible to suggest that the scaling function form of ℓ_{eq} for a curved substrate be

$$\ell_{eq} = \frac{\sigma}{|t'|}\mathcal{L}\left(\frac{\tilde{p}}{\varepsilon\Delta\rho|t'|^4}\right) \tag{5.6.35}$$

where $\mathcal{L}$ now obeys equation (5.6.17). Furthermore, in the limit of $R_s \to \infty$, this expression recovers equation (5.6.31). Stewart and Evans [33] proposed a similar form for the case of $\delta\mu = 0$, and found excellent agreement between cDFT results for ℓ_{eq}, and the calculated scaling function from equation (5.6.17).

Following the same procedure as in the planar case, $\chi_\mu(\ell_{eq};R_s)$ can be written in a scaling form as

$$\chi_\mu(\ell_{eq};R_s) = -\rho'(R_s+\ell_{eq})\frac{\sigma}{|t'|^5}\mathcal{L}'\left(\frac{\tilde{p}}{\varepsilon\Delta\rho|t'|^4}\right) \tag{5.6.36}$$

whilst $\chi_T(\ell_{eq};R_s)$ can be found to be

$$\begin{aligned}\chi_T(\ell_{eq};R_s) &\sim \rho'(R_s+\ell_{eq})\frac{\sigma}{\varepsilon|t'|^5}\mathcal{L}'\left(\frac{\tilde{p}}{\varepsilon\Delta\rho|t'|^4}\right)\left(\frac{2}{R_s}\frac{\partial}{\partial T}\left(\frac{\gamma_{lv}}{\Delta\rho}\right)-\frac{\partial\mu_{co}}{\partial T}\right)\\ &= \chi_\mu(\ell_{eq};R_s)\left(\frac{2}{R_s}\frac{\partial}{\partial T}\left(\frac{\gamma_{lv}}{\Delta\rho}\right)-\frac{\partial\mu_{co}}{\partial T}\right)\end{aligned} \tag{5.6.37}$$

where, as before, only the most strongly diverging terms are considered.

5.7 Discussion

Within this chapter, a comprehensive effective interface potential analysis has been presented for the case of critical drying in systems with both planar and curved substrates with SR ff LR sf and LR ff LR sf interactions. This analysis has focused specifically on how a drying critical point can be expected to influence the behaviour of the equilibrium vapour film width, ℓ_{eq}, and the local compressibility and thermal susceptibility evaluated at ℓ_{eq}, $\chi_\mu(\ell_{eq})/\chi_\mu(\ell_{eq};R_s)$ and $\chi_T(\ell_{eq})/\chi_T(\ell_{eq};R_s)$. A MFT approach has been applied, and has been proven to yield the correct critical exponents in both the cases of SR ff LR sf and LR ff LR sf interactions. The analysis presented within this chapter builds on previous work such as [1, 33, 34, 41, 50, 143, 145, 146], extending these analyses to consider all parameters which influence ℓ_{eq}, $\chi_\mu(\ell_{eq})/\chi_\mu(\ell_{eq};R_s)$ and $\chi_T(\ell_{eq})/\chi_T(\ell_{eq};R_s)$ in the vicinity of the drying critical point.

Throughout this chapter, the behaviour of ℓ_{eq} and $\chi_\mu(\ell_{eq})/\chi_\mu(\ell_{eq};R_s)$ has been found

to depend on three parameters: the oversaturation, $\delta\mu = (\mu - \mu_{co})$, the sf attraction, ε_s and the radius of the solute/curved substrate, R_s. It has been found that each of these act as the dominant influence over ℓ_{eq} and $\chi_\mu(\ell_{eq})/\chi_\mu(\ell_{eq}; R_s)$ in separate regions of parameter space. In some cases, this region has been found to be well defined. For example, in the case of $\varepsilon_s = 0$ for both SR ff LR sf and LR ff LR sf interactions, it was found that the behaviour of ℓ_{eq} and $\chi_\mu(\ell_{eq})/\chi_\mu(\ell_{eq}; R_s)$ depended solely on R_s for $R_s < R_c$ and solely on $\delta\mu$ where $R_s > R_c$, where $R_c = 2\gamma_{lv}/\delta\mu\Delta\rho$ has been identified as the length scale of capillary evaporation. This behaviour highlighted that the R_s exerts a strong influence over the behaviour of the system only when it is small, and furthermore that behaviour expected at a planar substrate is recovered when $R_s \to \infty$. This provides a direct connection between the behaviour of ℓ_{eq} and $\chi_\mu(\ell_{eq})/\chi_\mu(\ell_{eq}; R_s)$ around solutes to that at planar substrates, and thus supports the assertion in the postulates of chapter 1, that hydrophobicity and solvophobicity on microscopic and macroscopic length scales are related by the influence of a drying critical point. Furthermore, as R_c acts as a length scale which divides curvature dependent and independent behaviour, it is possible that it provides a good crossover length scale between the large length scale solvation and macroscopic regimes described in section 3.1.

Comparing the predicted growth of ℓ_{eq}, $\chi_\mu(\ell_{eq})$ and $\chi_T(\ell_{eq})$ on the approach to critical drying for the cases of SR ff LR sf and LR ff LR sf interactions, it can be seen that the divergences are much faster in the latter. For example, ℓ_{eq} grows as a logarithm in the case of SR ff LR sf interactions, whilst as a power law in the case of LR ff LR sf interactions. The divergence of $\chi_\mu(\ell_{eq})$ at a planar substrate is particularly fast in the case of LR ff LR sf interactions on the approach to critical drying, diverging as $|t'|^{-5}$. In the equivalent SR ff LR sf case, this divergence is $|\delta\varepsilon_s|^{-1}$. In terms of general behaviour, systems with SR ff LR sf and LR ff LR sf interactions show little difference. For example, both cases of interactions show evidence of scaling regimes dependent on the individual parameters $(\delta\mu, \varepsilon_s, R_s)$, and it is possible to write the measures ℓ_{eq} and $\chi_\mu(\ell_{eq})/\chi_\mu(\ell_{eq}; R_s)$ in terms of scaling functions in each.

The ability to write ℓ_{eq} and $\chi_\mu(\ell_{eq}; R_s)$ as scaling functions is particularly useful for the case of LR ff LR sf interactions. Throughout this chapter, a SK approximation has been applied to the density profile, in order to find analytic forms for ℓ_{eq}, $\chi_\mu(\ell_{eq}; R_s)$ and $\chi_T(\ell_{eq}; R_s)$. This approximation gives the constants $b(T)$ and $c(T)$ to have the forms presented in equation (5.4.11). Whilst the expression found for $b(T)$ is expected to be valid beyond a SK approximation, $c(T)$ is expected to depend on the exact form of the density profile [144], and hence is not strictly valid beyond a SK approximation. This means that testing the predictions of equations (5.6.17) and (5.6.21) would require numerical evaluation of $c(T)$. Stewart [117] has previously presented a method to do this, however this required studying cDFT systems very close to critical drying. Such systems are often not practical to implement, due to their slow convergence. Hence, a scaling function form for ℓ_{eq}, $\chi_\mu(\ell_{eq})$ and $\chi_T(\ell_{eq})$ which avoids the factor of $c(T)$, and therefore prevents the need to study such difficult systems, is useful. It should be noted that if $c(T)$ is known, it is possible to calculate the form of the scaling function, $\mathcal{L}$, explicitly, and therefore make predictions for observables such as ℓ_{eq}.

In addition to considering the behaviour of $\chi_\mu(\ell_{eq})/\chi_\mu(\ell_{eq}; R_s)$ and $\chi_T(\ell_{eq})/\chi_T(\ell_{eq}; R_s)$ near to the drying critical point, it was predicted that a relationship should exist between them. This relationship is presented in equation (5.3.8) for the case of a planar substrate and equation (5.3.17) for the case of a curved substrate, and indicates that all measures of density fluctuations diverge in the same way on the approach to the drying critical point. Initially, it was shown that such a general relationship can be obtained by considering surface thermodynamics. Detailed effective interface potential analyses, which consider the microscopic interactions, also confirmed such a relationship should exist.

Chapter 6

Influence of Critical Drying in the Solvophobic Response of a Lennard-Jones Fluid

Verification of the effective interface potential predictions made in chapter 5 is best achieved using cDFT as described in section 4.1. The simplicity of the numerical minimisation utilised within this method allows for a wide range of parameters to be explored with very little computational cost, which is advantageous as the effective interface potential analysis highlighted that $\delta\mu$, ε_s and R_s are all expected to significantly influence the behaviour of systems near to the drying critical point. Perhaps because of this, cDFT has been used extensively in previous studies of solvophobicity, for example [1, 32–34, 37, 112, 113, 146].

However, as has been discussed, cDFT within this thesis is limited to the study of LJ fluids, and hence this chapter focuses specifically on solvophobicity. Both solutes and planar surfaces are considered, and their solvophobic response is quantified using ℓ_{eq} and $\chi_\mu(\ell_{eq}; R_s)$ as defined in sections 5.2 and 5.3 respectively. It should be noted that planar surfaces correspond to the case where $R_s = \infty$. Predictions for the behaviour of ℓ_{eq} and $\chi_\mu(\ell_{eq}; R_s)$ are found in sections 5.5 and 5.6 for the cases of SR ff LR sf and LR ff LR sf interactions respectively, and will be referred to frequently throughout this chapter.

In addition to considering the predictions of the effective interface potential analysis, a detailed study of the influence of parameters $(\delta\mu, \varepsilon_s, R_s)$ on the density profiles, $\rho(r)/\rho(z)$ and local compressibility profiles, $\chi_\mu(r)/\chi_\mu(z)$ is presented within this chapter, as this provides a more physical understanding of the influence of critical drying on solvophobicity than the predictions of chapter 5 alone. Furthermore, to provide a more physical interpretation of the degree of solvophobicity of each solute and planar surface considered, the Young's contact angle, found using equation (2.4.19), for each ε_s considered is given. It should be appreciated that this provides only an indication of the solvophobicity, as Young's contact angle is strictly defined in the limit of a smooth planar surface in contact with a fluid at liquid-vapour coexistence.

Finally, it should be noted that the purpose of this chapter is not to test every relation presented in chapter 5 - as has been discussed previously, many of these have already been confirmed. Instead, this chapter focuses on understanding specifically the similarities and differences between the behaviour of LJ fluids around solvophobic solutes and planar substrates, and explores the potential influence of a drying critical point on each, with the purpose of evaluating the accuracy of postulate 2 presented in chapter 1.

6.1 State Points and Bulk Parameters

Implementing cDFT as described in section 4.1.4 and analysing the behaviour of ℓ_{eq} and $\chi_\mu(\ell_{eq}; R_s)$ according to the predictions of chapter 5 requires knowledge of many properties of the bulk LJ fluid. It is the purpose of this section to present these properties, which are given to a high degree of precision for two reasons. Firstly, near to the drying critical point, small variations in parameters are expected to have a large influence on ℓ_{eq} and $\chi_\mu(\ell_{eq}; R_s)$, due to their diverging behaviour. Secondly, the numerical consistency of all results presented was tested using the appropriate sum rules presented in sections 4.1.5.1 and 4.1.5.2. For high levels of consistency, it was necessary to have a high level of precision.

As a MFT approximation is used to describe the LJ fluids within cDFT in this thesis, the bulk liquid-vapour phase diagram can be obtained using the methods presented in section 2.4.4. The cut-off radius of the ff interaction potential in systems described as being SR ff was taken to be $r_c = 2.5\sigma$, whilst in LR ff systems to be $r_c = 200\sigma$, where σ was the diameter of a fluid particle. The dimensionless bulk critical temperature, $k_\mathrm{B}T_c/\varepsilon$, was found using the conditions given in equation (2.4.18), whilst the sub-critical liquid-vapour phase diagram was obtained using a program by Wilding [148]. The latter gave the coexisting liquid, ρ_l, and vapour, ρ_v, densities, which allowed for $\Delta\rho = (\rho_l - \rho_v)$ to be calculated. The liquid-vapour surface tension was obtained using cDFT, by finding the equilibrium density profile when the liquid and vapour phases of a fluid at coexistence were brought into contact. By constraining the system such that both phases remained present and in contact, a free liquid-vapour interface naturally formed. γ_{lv} was then calculated using equations (2.1.7) and (4.1.2). All fluids considered within this chapter were oversaturated. Their bulk density, ρ_b, was found using a simple root finding algorithm which, starting at ρ_l, searched for the density, ρ_b, for which a given chemical potential deviation, measured using the dimensionless parameter $\beta\delta\mu$, was satisfied. The corresponding $\chi_{\mu,b}$ was then be found by substituting ρ_b into equation (4.1.59). It should be noted that the SR and LR fluids considered within this chapter obeyed a law of corresponding states, such that when the liquid-vapour phase diagram of each was scaled by their respective bulk critical temperatures, the coexistence curves collapsed onto one another. As $\chi_{\mu,b}$ depended only on ρ_b and the temperature, T, it also obeyed a law of corresponding states.

The value of ε_s for which critical drying occurs was found in chapter 5 to be $\varepsilon_c = 0$ for the case of SR ff LR sf interactions, and as given in equation (5.6.2) for the case of LR ff LR sf interactions. Within the geometry specific cDFT methods presented in sections 4.1.5.1 and 4.1.5.2, this parameter enters the sf attraction potential, given in equations (4.1.46) and (4.1.54) for the cases of planar surfaces and solutes respectively, through the variable

$\varepsilon_{sf} = 2\pi\rho_s\varepsilon_s\sigma_s^3/3$. Within the present work, ε_{sf} was defined as $\varepsilon_{sf} = \tilde{\varepsilon}_{sf}\,\varepsilon$, such that it was a fraction of the ff attraction strength, ε. For a SR ff LR sf system, the critical sf attraction was therefore $\varepsilon^c_{sf,SR} = \tilde{\varepsilon}^c_{sf,SR}\,\varepsilon = 0$, which meant $\tilde{\varepsilon}^c_{sf,SR} = 0$. For a LR ff LR sf system, it is necessary to rearrange equation (5.6.2). Doing so leads to

$$\varepsilon^c_{sf,LR} = \tilde{\varepsilon}^c_{sf,LR}\,\varepsilon = \frac{2\pi}{3}\rho_v\sigma^3\varepsilon \tag{6.1.1}$$

and hence $\tilde{\varepsilon}^c_{sf,LR} = 2\pi\rho_v\sigma^3/3$. This agrees with the result obtained by Evans et al. [38], and is remarkably simple.

Using the methods outlined, the bulk critical temperature for the SR LJ fluid considered was found to be $k_\mathrm{B}T_c/\varepsilon = 1.319441624248$. Table 6.1 gives the coexistence state point parameters for this fluid for the temperature considered, $T = 0.775T_c$. This temperature was chosen to reflect that used in previous work, for example [1, 32]. In addition, γ_{lv} and $\tilde{\varepsilon}^c_{sf,SR}$ are given. Table 6.2 gives the liquid state points and parameters for the same fluid at $T = 0.775T_c$, for the various finite $\beta\delta\mu$ studied.

The bulk critical temperature for the LR LJ fluid studied was found to be $k_\mathrm{B}T_c/\varepsilon = 1.415390136786$. In contrast to the SR ff LR sf case, multiple temperatures were considered, the coexisting properties of which can be found in table 6.3 along with γ_{lv}. Due to its dependence on ρ_v, $\tilde{\varepsilon}^c_{sf,LR}$ in the LR ff LR sf case is also temperature dependent, and its value for each temperature considered is also given in table 6.3. As before, these temperatures were chosen to reflect those used in previous work, for example [1, 32, 33, 37]. Table 6.4 gives the off-coexistence state points used for the LR ff LR sf case. Unlike the SR ff LR sf case, only $\beta\delta\mu = 10^{-3}$ was considered. This value was chosen to reflect approximately that of water [96].

Table 6.1: Relevant liquid-vapour coexistence state points and properties for the MFT SR LJ fluid, which had truncation $r_c = 2.5\sigma$, used within this work. The critical substrate-fluid attraction, $\tilde{\varepsilon}^c_{sf}$, is also given.

T/T_c	$k_\mathrm{B}T/\varepsilon$	$\rho_l\sigma^3$	$\rho_v\sigma^3$	$\beta\sigma^2\gamma_{lv}$	$\tilde{\varepsilon}^c_{sf}$
0.775	1.0225672588	0.597844705492	0.0343066397783	0.2573683657	0.0

Table 6.2: Relevant off-coexistence state points and properties for the bulk MFT SR LJ fluid, with truncation $r_c = 2.5\sigma$, used within this work. The temperature of all state points was $T = 0.775T_c$.

$\beta\delta\mu$	$\rho_b\sigma^3$	$\beta^{-1}\sigma^3\chi_{\mu,b}$
10^{-3}	0.5980277945	0.1829266785
10^{-4}	0.597863029	0.1832189495
10^{-5}	0.597846538	0.1832482423
10^{-6}	0.5978448887	0.1832511723

Table 6.3: Relevant liquid-vapour coexistence state points and properties of the MFT LR LJ fluid, with truncation $r_c = 200\sigma$, considered within this work. The critical substrate-fluid attraction, $\tilde{\varepsilon}^c_{sf}$, is also given.

T/T_c	$k_\mathrm{B}T/\varepsilon$	$\rho_l\sigma^3$	$\rho_v\sigma^3$	$\beta\sigma^2\gamma_{lv}$	$\tilde{\varepsilon}^c_{sf}$
0.7	0.9907730958	0.667378745414	0.0180259142506	0.5451849116	0.0377533865
0.775	1.096927356	0.597844705492	0.0343066397783	0.3208420804	0.0718151658
0.85	1.203081616	0.521924905174	0.0603159413095	0.1603760082	0.1263254119

Table 6.4: Relevant state points and properties for the bulk MFT LR LJ fluid, with truncation $r_c = 200\sigma$, considered. For each state point, $\beta\delta\mu = 10^{-3}$.

T/T_c	$\rho_b\sigma^3$	$\beta^{-1}\sigma^3\chi_{\mu,b}$
0.7	0.6675006410	0.1218310834
0.775	0.5980277945	0.1829266785
0.85	0.5222273831	0.3019506502

Throughout this chapter, Young's contact angle is used to indicate the solvophobicity of a solute or planar substrate. This was calculated using equation (2.4.19). Firstly, γ_{lv} was calculated as discussed above. γ_{sv}/γ_{sl} were then calculated using cDFT, by finding the equilibrium density profile of a system consisting of a planar substrate with given ε_{sf} in contact with a vapour/liquid at liquid-vapour coexistence. The surface tension was the evaluated using equations (4.1.2) and (2.1.7).

6.2 Density and Fluctuation Profiles

Many previous solvophobicity studies have sought to understand the influence of various parameters on the density profile [1, 34, 37, 81, 108, 113]. Far fewer have considered the local compressibility profile [1, 32, 37, 113], of which all considered only planar surfaces. Therefore, in addition to providing a physical understanding of solvophobic behaviour under varying conditions, this section investigates for the first time how curvature of a surface influences the spatial form of the local compressibility. Also, in contrast to many of these previous studies, a large number of combinations of non-zero parameters $(\beta\delta\mu, R_s, \varepsilon_{sf})$ were considered. This section therefore provides a comprehensive understanding of the competing influence of parameters on the density and local compressibility profiles in solvophobic systems.

6.2.1 Influence of Solute Size

The influence of solute size on $\rho(r)$ has been considered in several previous studies of solvophobicity [34, 81, 108]. Huang and Chandler [81], and Moody and Attard [108] both used simulations of a SR LJ fluid to investigate small hard solutes with $R_s \leq 3\sigma$. For solutes of order $R_s = \sigma$, the density at the surface of the solute was found to be enhanced, and oscillations, indicative of liquid packing effects, were pronounced. As the solute size increased, both the density at the surface and the oscillations in the density profile depleted. Stewart and Evans [34] used cDFT of a LR LJ fluid to investigate much larger hard solutes,

of up to $R_s \approx 10^6\sigma$. $\rho(r)$ around these larger solutes showed significant depleted density regions, or vapour films, near the surface of the solute, the width of which grew as the solute size was increased. Furthermore, this study highlighted the equivalence of the effects of oversaturation and curvature of substrate, as indicated by $\tilde{p}$ given in equation (5.2.3), by comparing the density profiles of an oversaturated fluid at a planar substrate, to those of a saturated fluid around a solute. If $\delta\mu$ was chosen such that $\delta\mu = 2\gamma_{lv}/R_s\Delta\rho$, it was found that the density profiles around the solute and at the planar substrate could not be distinguished.

To our knowledge, no previous studies have considered the behaviour of $\chi_\mu(r)$ around solutes of varying size. However, considering that the form of the density profile around a very large solute differs little from that at a planar substrate [34], and that $\chi_\mu(r)$ is the derivative of this density profile, it can be expected that $\chi_\mu(r)$ take a similar form around a solute as is found at a planar substrate. At smooth planar substrates, $\chi_\mu(z)$ has been found to exhibit a smooth peak near to the liquid-vapour like interface portion of the density profile, the latter of which occurs at ℓ_{eq} [1, 37].

Figures 6.1 and 6.2 show the density (lower) and local compressibility (upper) profiles for systems with SR ff LR sf and LR ff LR sf interactions respectively, for a variety of R_s and $\delta\varepsilon_{sf} = (\tilde{\varepsilon}_{sf} - \tilde{\varepsilon}^c_{sf})$ for the conditions $T = 0.775T_c$ and $\beta\delta\mu = 10^{-3}$. It should be noted that whilst $\rho(r)$ is plotted on a linear scale, $\chi_\mu(r)$ is plotted on a logarithmic scale. In each case, the density profiles follow the behaviour observed by Stewart and Evans [34] for a hard solute as R_s grows. Firstly, the contact density reduces towards that of the planar substrate, which can be seen in equation (4.1.49) to be fixed by the pressure of the system. As the planar contact density is neared, the width of the vapour film begins to increase. Increasing $\delta\varepsilon_{sf}$ can be seen to increase the contact density, as well as reduce the width of the vapour film.

As expected, the local compressibility profile around a solute differs little in form from that at a planar substrate. Each profile exhibits a smooth peak located near the liquid-vapour interface of the density profile, which grows as R_s grows. For very small solutes of $R_s = 10\sigma$, the peak of χ_μ is ten times the bulk value, whilst for larger solutes, it is almost one thousand times. This indicates that χ_μ is a highly sensitive measure of density fluctuations in solvophobic systems with solutes, in agreement with the findings of previous studies of planar surfaces [1, 32, 37].

For both $\rho(r)$ and $\chi_\mu(r)$, increasing R_s causes the profile to tend to that found at a planar substrate. Considering figures 6.1 and 6.2, there appears to be an upper limit of R_s for which profiles at a curved substrate can be distinguished from those at a planar substrate. For example, when $\delta\varepsilon_{sf} = 0.0$, it is impossible to distinguish the density profile of a substrate with $R_s = 10^4\sigma$ from that of a planar substrate, and only just possible to distinguish the local compressibility profile. This indicates that the influence of R_s on $\rho(r)$ and $\chi_\mu(r)$ is only strongly felt when R_s is small, which agrees with the predictions of chapter 5. Increasing $\delta\varepsilon_{sf}$ limits the range of R_s for which $\rho(r)$ and $\chi_\mu(r)$ can be distinguished from those at a planar substrate. For example, for $\delta\varepsilon_{sf} = 0.2$ in both the cases of SR ff LR sf and LR ff LR sf interactions, it is no longer possible to distinguish profiles for $R_s = 10^4\sigma$ from those at the

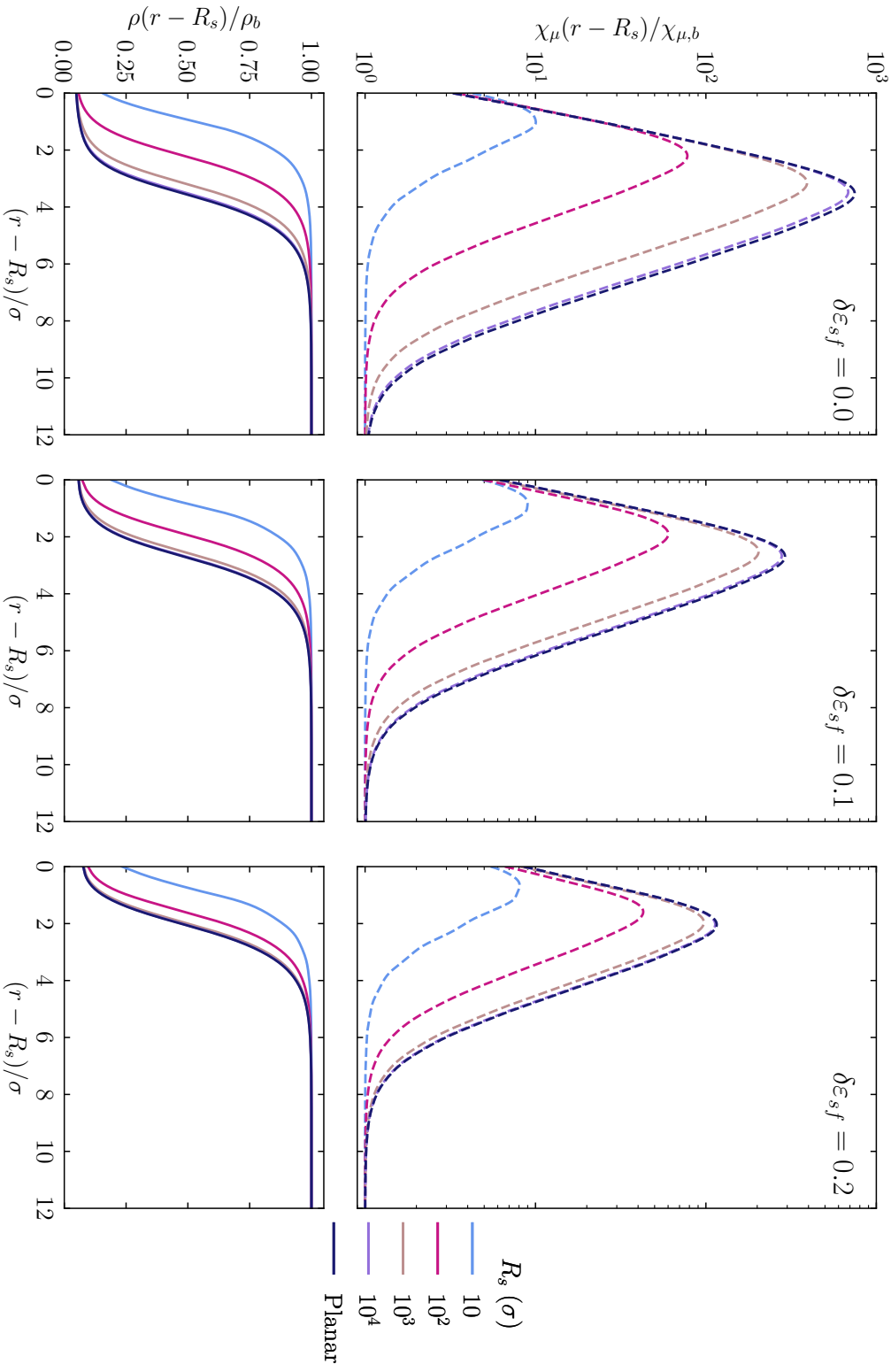

Figure 6.1: Density (lower) and local compressibility (upper) profiles, scaled by their bulk values, for systems with SR ff LR sf interactions at $T = 0.775T_c$ and $\beta\delta\mu = 10^{-3}$, for varying radii of substrate. The deviation of the sf attraction from its value at the drying critical point is increased when moving from left to right and is given in the top right corner. The equivalent Young's contact angles for these $\delta\varepsilon_{sf}$ are $\theta \approx 180.0°, 173.9°, 169.0°$ when moving from left to right.

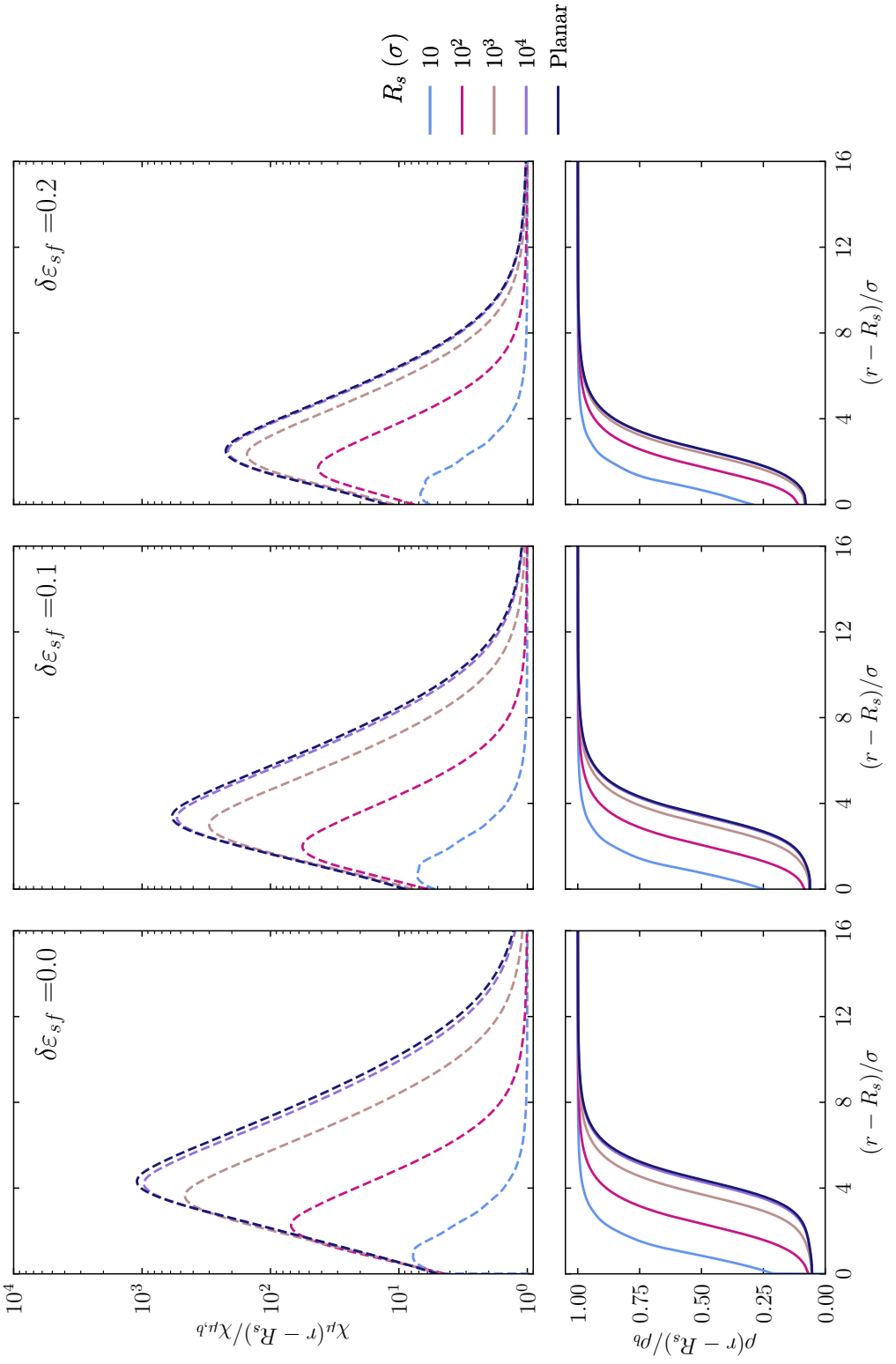

Figure 6.2: Density (lower) and local compressibility (upper) profiles, scaled by their bulk values, for systems with LR ff LR sf interactions at $T = 0.775T_c$ and $\beta\delta\mu = 10^{-3}$, for varying radii of substrate. The deviation of the sf attraction from its value at drying critical point is increased when moving from left to right, and is given in the top right corner. The equivalent Young's contact angles for these $\delta\varepsilon_{sf}$ would be $\theta \approx 180.0°, 176.8°, 173.1°$ when moving from left to right.

planar substrate.

Comparing figures 6.1 and 6.2, it can be seen that there is little difference in the behaviour of systems with SR ff LR sf and LR ff LR sf interactions. The latter exhibit slightly larger vapour films for smaller $\delta\varepsilon_{sf}$, and slightly larger peaks in $\chi_\mu(r)$, in agreement with the predicted behaviours of chapter 5.

6.2.2 Influence of Substrate-Fluid Attraction

The influence of $\delta\varepsilon_{sf}$ on $\rho(r)$ and $\chi_\mu(r)$ can be seen more clearly in figures 6.3 and 6.4, which show profiles for SR ff LR sf and LR ff LR sf systems respectively. Considering first the density profiles, increasing $\delta\varepsilon_{sf}$ can be seen to initially deplete the vapour film, before leading to an increase in contact density, and the appearance of substantial oscillations, indicating local packing of particles. The general forms of the density profile vary little with R_s, with the main effect instead being reduced film widths. Similar patterns are observed in the local compressibility profiles. Increasing $\delta\varepsilon_{sf}$ reduces the magnitude of the fluctuations within the system, and for large $\delta\varepsilon_{sf}$, clear oscillations are observed. These follow those observed in the density profile, as has been discussed by Evans et al. previously [1]. Again, the general forms differ little between different values of R_s.

This depletion in magnitude of χ_μ with decreasing R_s is most evident for small $\delta\varepsilon_{sf}$, indicating that R_s has a larger influence on χ_μ than $\delta\varepsilon_{sf}$ in this region. However, for $\delta\varepsilon_{sf} > 0.4$ in the SR ff LR sf case, and $\delta\varepsilon_{sf} > 0.6$ in the LR ff LR sf case, the differences in profiles between different values of R_s is far less noticeable. This indicates that in this region, $\delta\varepsilon_{sf}$ has a larger influence over the magnitude of the fluctuations than R_s. This observation of two regimes in which the dominant influence on the density and local compressibility are R_s and $\delta\varepsilon_{sf}$ respectively agrees with the predictions of sections 5.5.2 and 5.6.2. Furthermore, when $\delta\varepsilon_{sf} > 0.4$ and $\delta\varepsilon_{sf} > 0.6$ in the cases of figures 6.3 and 6.4 respectively, the form of the density and local compressibility profile can be seen to change, with the latter in particular exhibiting clear oscillations. Such a change in behaviour suggests a region in which the effects of the drying critical point can be felt more strongly. It is interesting to note that these values of $\delta\varepsilon_{sf}$ correspond to Young's contact angles of $\theta > 158.1°$ and $153.4°$ respectively.

Despite the differing appearances of $\rho(r)$ and $\chi_\mu(r)$ upon increasing $\delta\varepsilon_{sf}$, all $\delta\varepsilon_{sf}$ considered in figures 6.3 and 6.4 are solvophobic. Each gives an equivalent Young's contact angle of $\theta > 90°$, and all but $\delta\varepsilon_{sf} = 1.2$ show a depleted contact density. Considering the density profile, the solutes and planar substrate with $\delta\varepsilon_{sf} = 1.2$ may be thought to be solvophilic, due to the enhancement of the fluid at the surface of the solute or substrate. However, considering $\chi_\mu(r)$, this can be seen not to be the case. Whilst $\chi_\mu(r)$ shows oscillations and a much smaller variation from the bulk value than for other $\delta\varepsilon_{sf}$, its form differs substantially from that expected at a solvophilic surface. In the latter, the oscillations in $\chi_\mu(r)$ are centred on $\chi_{\mu,b}$. This agrees with observations of other measures of density fluctuations discussed in chapter 3, in that it is far easier to distinguish solvophobic and solvophilic behaviours in the density fluctuations than in the density profile.

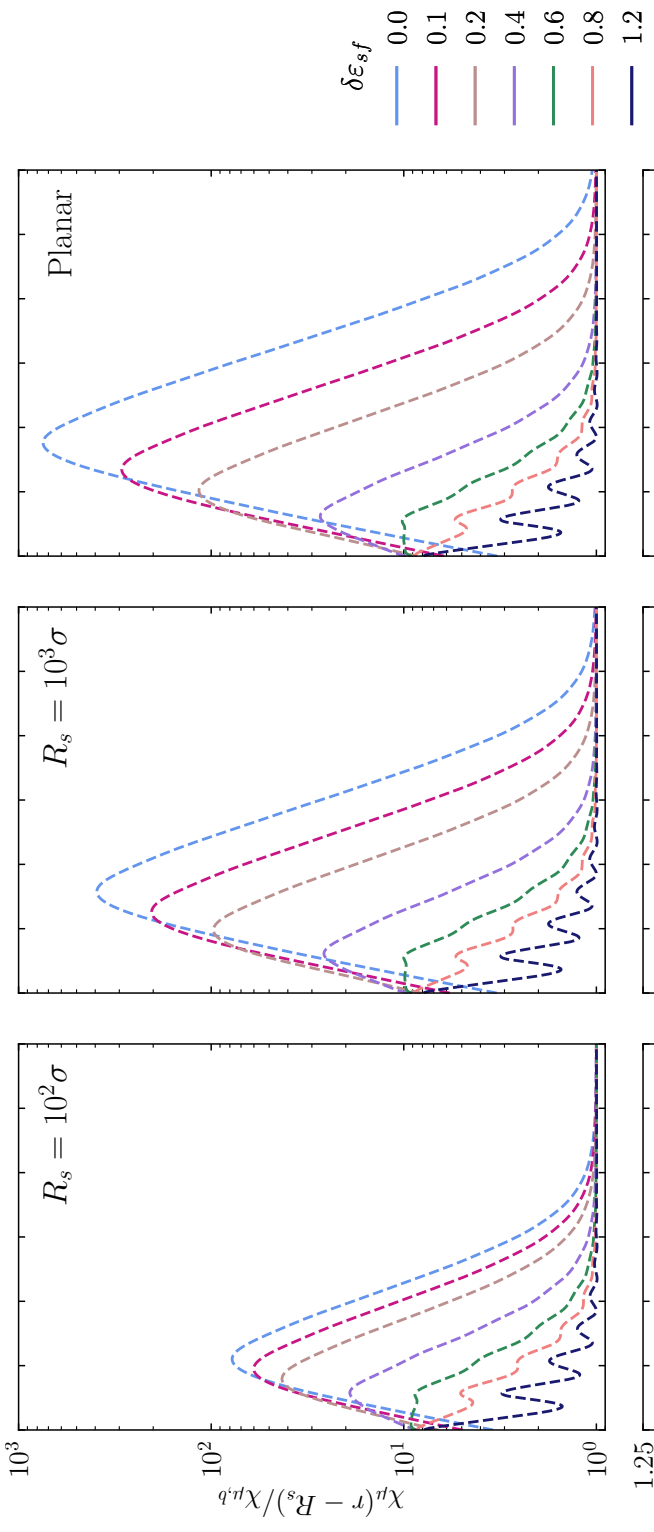

Figure 6.3: Density (lower) and local compressibility (upper) profiles, scaled by their bulk values, for systems with SR ff LR sf interactions at $T = 0.775T_c$ and $\beta\delta\mu = 10^{-3}$, for varying $\delta\varepsilon_{sf}$ and R_s. The $\delta\varepsilon_{sf}$ from smallest to largest correspond to Young's contact angles of $\theta \approx 180.0°, 173.9°, 169.0°, 158.1°, 146.0°, 133.5°, 107.4°$.

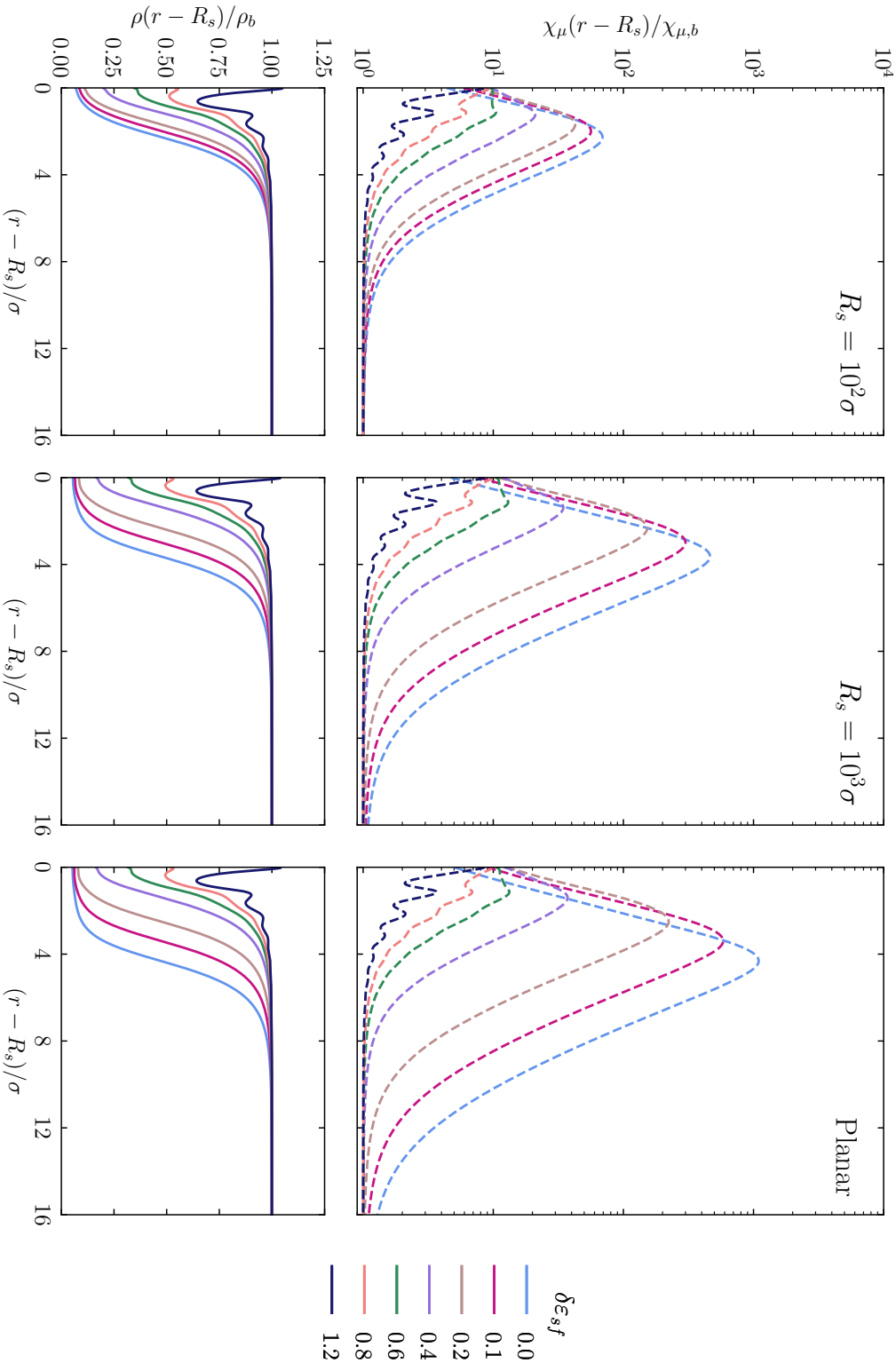

Figure 6.4: Density (lower) and local compressibility (upper) profiles, scaled by their bulk values, for systems with LR ff LR sf interactions at $T = 0.775T_c$ and $\beta\delta\mu = 10^{-3}$, for varying $\delta\varepsilon_{sf}$ and R_s. The $\delta\varepsilon_{sf}$ from smallest to largest correspond to Young's contact angles of $\theta \approx 180.0^\circ, 176.8^\circ, 173.1^\circ, 163.7^\circ, 153.4^\circ, 143.0^\circ, 122.1^\circ$.

6.2.3 Competing Influence of Solute Size and Chemical Potential Deviation

It was previously reported by Evans et al. [146] in a study of a hard solute immersed in a SR square well fluid that there exist two regimes of ℓ_{eq} in which the behaviour depends independently on $\delta\mu$ and R_s. Stewart and Evans [34] made a similar observation for the case of LR ff interactions, in a study of hard solute immersed in a LJ fluid. Such a prediction was also made for both SR and LR ff interactions in the effective interface potential analysis of chapter 5, and it was further shown in equations (5.5.16) and (5.6.23) that such regimes should also exist for $\chi_\mu(\ell_{eq}; R_s)$. In all cases, these regimes were found or predicted to be separated by the length scale of capillary evaporation, $R_c = 2\gamma_{lv}/\delta\mu\Delta\rho$. This suggests a length scale above which the curvature of the substrate has little influence over the behaviour of $\rho(r)$ and $\chi_\mu(r)$. If this were the case, then for $R_s \gg R_c$, it should not be possible to distinguish the density and local compressiblility profiles found around solutes from those found at the planar substrate.

Figure 6.5 tests this assertion for a system with SR ff LR sf interactions, by considering the density (lower) and local compressibility (upper) profiles around solutes of varying size for varying $\beta\delta\mu$. In each case, $\delta\varepsilon_{sf} = 0$. For $\beta\delta\mu = 10^{-3}$, $R_c \approx 913\sigma$, and hence for $R_s \gg 913\sigma$, it should be difficult to distinguish profiles around solutes from those obtained at planar substrates. Considering figure 6.5, this can indeed be seen to be the case. For $R_s = 10^3\sigma$, $\rho(r)$ and $\chi_\mu(r)$ are clearly different from those at the planar substrate. However, by $R_s = 10^4\sigma$, it is near impossible to distinguish the profiles. Similar behaviours can be seen for $\beta\delta\mu = 10^{-4}$, for which $R_c \approx 9134\sigma$ and for $\beta\delta\mu = 10^{-5}$, for which $R_c \approx 91340\sigma$. In agreement with the conclusions of previous studies [146], R_c appears to distinguish between sizes of solutes for which R_s influences the behaviour of the system, and for which it does not.

6.2.4 Influence of Temperature

Although temperature does not enter explicitly into the predictions of chapter 5, it implicitly effects the behaviour of solvophobic systems through terms such as γ_{lv}, $\Delta\rho$ and in the case of LR ff LR sf interactions, $\tilde{\varepsilon}^c_{sf}$. In section 5.6.4 it was also shown that ℓ_{eq} and $\chi_\mu(\ell_{eq}; R_s)$ for the LR ff LR sf case can be written in a scaling function form, which obey equations (5.6.17) and (5.6.21) respectively. These equations have temperature dependent constants $b(T)$ and $c(T)$, and hence the scaling functions can be expected to vary with temperature. This is in contrast to bulk scaling function forms like those presented in section 2.4.1, which instead take only two forms, for below and above the bulk critical temperature respectively. It is therefore interesting to consider the variation in the density and local compressibility profiles with temperature.

Figure 6.6 shows the variation in $\rho(r)$ (lower) and $\chi_\mu(r)$ (upper) for a system with LR ff LR sf interactions with $\beta\delta\mu = 10^{-3}$, $\delta\varepsilon_{sf} = 0$, and for varying T and R_s. As the temperature is increased, the liquid-vapour interface in the density profile broadens, and the vapour film grows in width. As the predictions of chapter 5 make use of a SK approximation for the

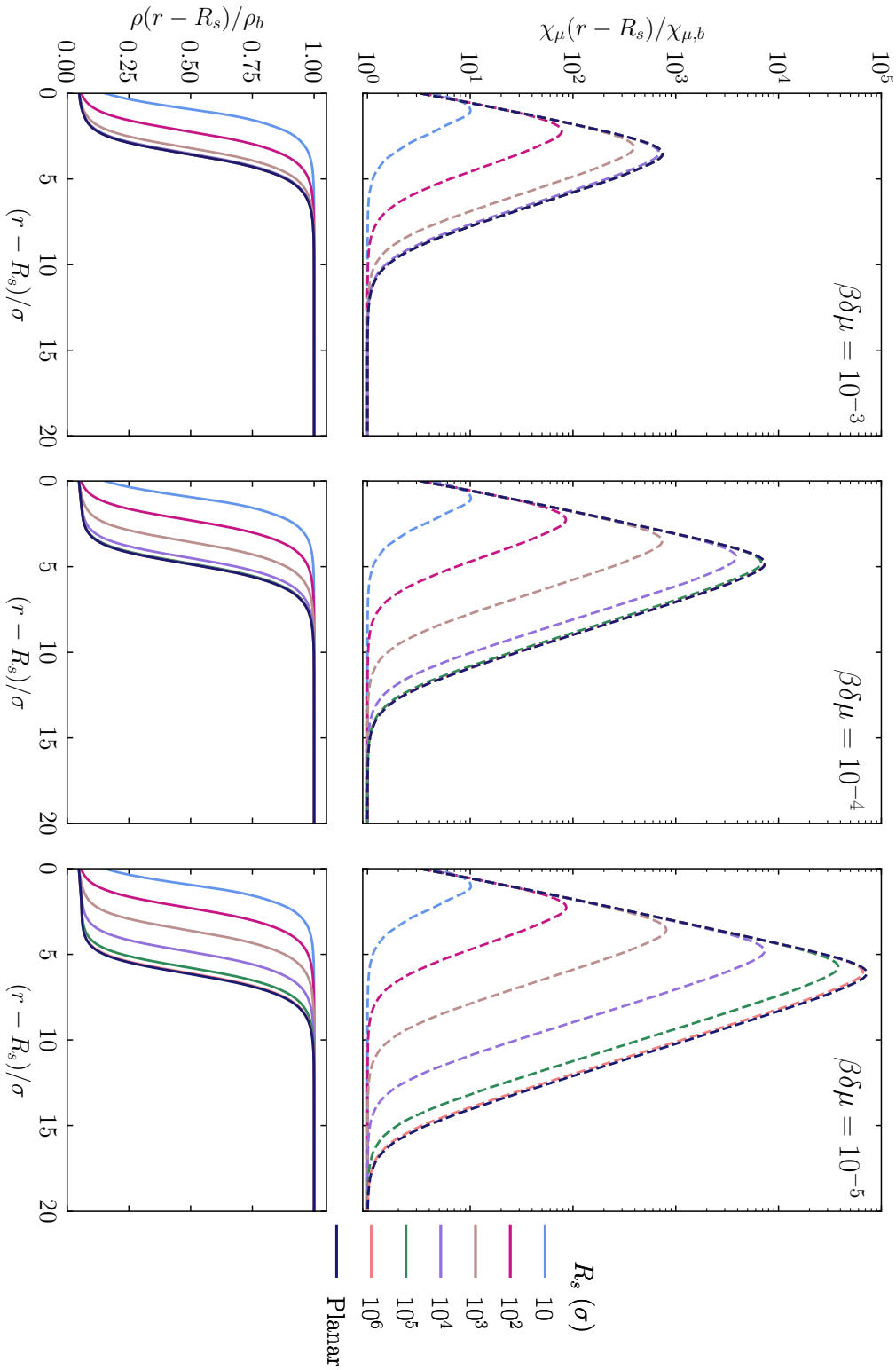

Figure 6.5: Density (lower) and local compressibility (upper) profiles, scaled by their bulk values, for systems with SR ff LR sf interactions at $T = 0.775T_c$ and $\delta\varepsilon_{sf} = 0.0$, for varying $\beta\delta\mu$ and R_s.

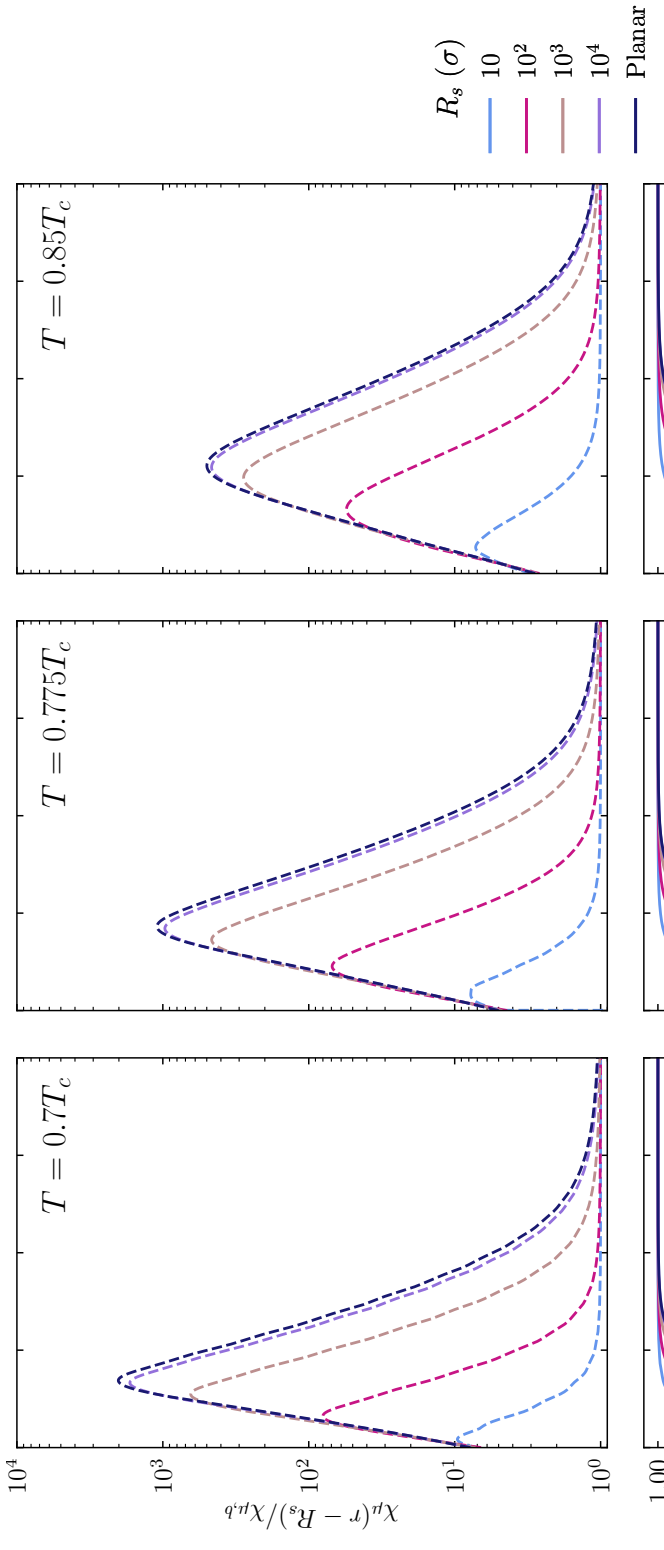

Figure 6.6: Density (lower) and local compressibility (upper) profiles, scaled by their bulk values, for a system with LR ff LR sf interactions at $\delta\varepsilon_{sf} = 0.0$ and $\beta\delta\mu = 10^{-3}$, for varying temperature and R_s.

density profile, this indicates that lower temperatures should provide more accurate results. Lower temperatures are also associated with sharper peaks in the local compressibility profile, as well as larger fluctuations in magnitude. Despite this, it can be seen that the predictions of section 6.2.3, that R_c acts as a boundary on the ability to distinguish profiles around hard solutes from those at a hard planar substrate, is largely followed at all temperatures considered in figure 6.6. This indicates that although the SK approximation is not as reliable at higher temperatures, many of the predictions made using it are.

6.3 Effective Interface Potential Predictions

Within this section, the predictions for the behaviour of ℓ_{eq} and $\chi_\mu(\ell_{eq}; R_s)$ made in chapter 5 are investigated in detail. For all systems considered, ℓ_{eq} was calculated using the equilibrium density profile obtained from cDFT according to equation (2.4.20), where the adsorption per unit area, Γ/A_{sv}, was found using equation (4.1.55) in the case of a solute and equation (4.1.47) in the case of a planar substrate. $\chi_\mu(\ell_{eq}; R_s)$ was taken to be the first value in the local compressibility profile which satisfied $r > R_s + \ell_{eq}$ when increasing r from $r = 0$. For planar surfaces considered, $\chi_\mu(\ell_{eq}; R_s = \infty)$ was the first value in the local compressibility profile which satisfied $z > \ell_{eq}$, when increasing z from $z = 0$. It should be noted that all fluids considered within this chapter were oversaturated and therefore ℓ_{eq} and $\chi_\mu(\ell_{eq}; R_s)$ in all cases remained finite.

6.3.1 Equilibrium Film Width

Figure 6.7 compares the effective interface potential prediction for the behaviour of ℓ_{eq} for the case of SR ff LR sf interactions, given in equation (5.5.8), to values of ℓ_{eq} obtained from cDFT. All results in figure 6.7 were obtained at $T = 0.775T_c$, whilst other parameters varied in the ranges ($10^{-6} \leq \beta\delta\mu \leq 10^{-3}, 0.0 \leq \delta\varepsilon_{sf} \leq 1.0, 10\sigma \leq R_s \leq 10^8\sigma$). Results obtained for a planar substrate are also shown. Colour is used to indicate the value of $\delta\varepsilon_{sf}$, and associated Young's contact angle.

For $\delta\varepsilon_{sf} < 0.4$, there is clear agreement between the predictions of the effective interface potential and the results obtained from cDFT for a wide range of $(\beta\delta\mu, R_s)$. The few exceptions to this are predominantly found where $\ln(\beta\sigma^3(\tilde{p} - 2b/\ell_{eq}^3)) > -3$, and correspond to solutes of size $R_s < 20\sigma$. This indicates a limit in R_s for which the predicted relationship is applicable, which could be related to the crossover between the small and large length scale solvation regimes discussed in section 3.1.4. The agreement between the predictions of the effective interface potential and cDFT results is poorer for $\delta\varepsilon_{sf} > 0.4$. Considering the profiles of figure 6.3, this is unsurprising, as for $\delta\varepsilon_{sf} > 0.4$, the density profile is no longer reasonably described by a SK approximation, which was a basic assumption of the derivations of section 5.5.

The predicted behaviour of ℓ_{eq} for the case of LR ff LR sf interactions is given in equation (5.6.17) however, as discussed in section 5.7, it is not practical to use this form of ℓ_{eq}, due to the difficulties involved in calculating the temperature dependent constant $c(T)$. For this reason, figure 6.8 instead compares the predicted scaling function form of ℓ_{eq}, given in equation (5.6.35), to results obtained from cDFT. Systems at three temperatures, $T =$

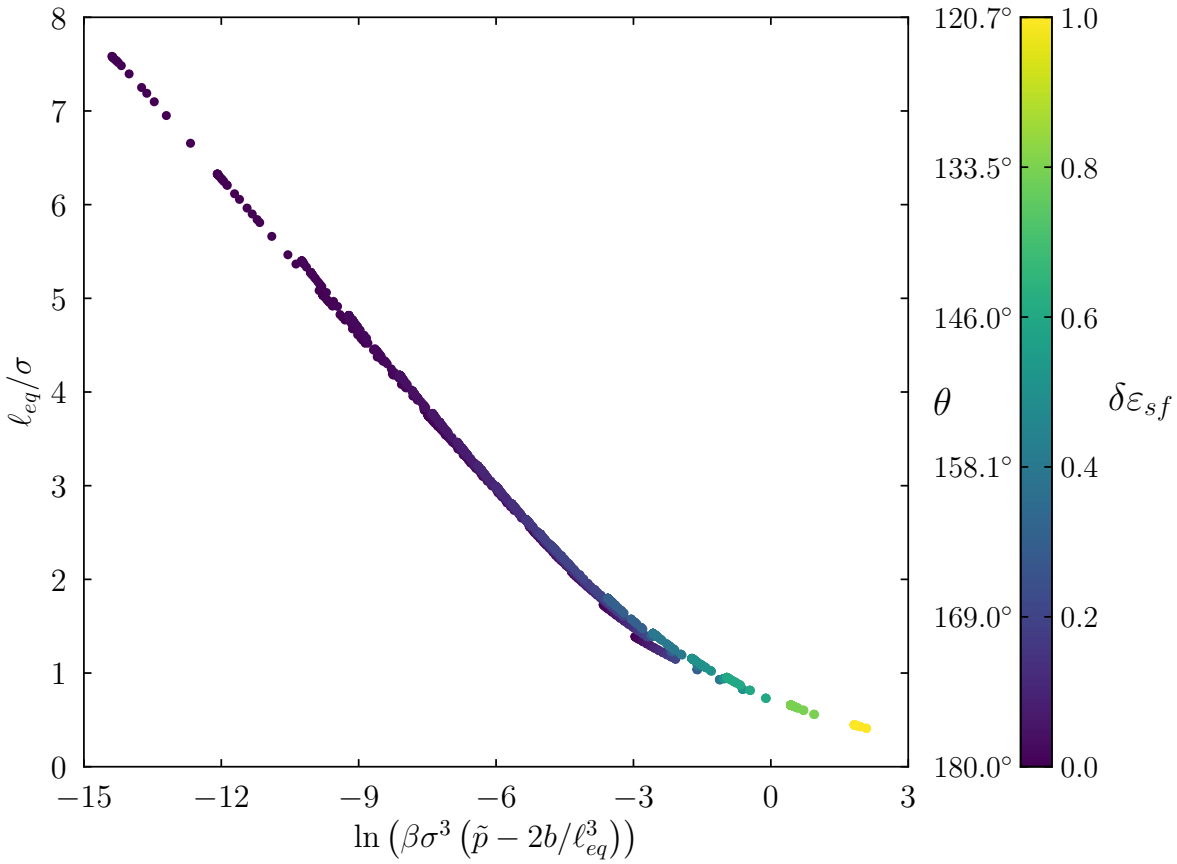

Figure 6.7: Comparison of the predictions of equation (5.5.8) and results for ℓ_{eq} obtained from cDFT, using equation (2.4.20), for the case of SR ff LR sf interactions. The temperature was held constant at $T = 0.775T_c$, whilst other parameters varied in the range ($10^{-6} \leq \beta\delta\mu \leq 10^{-3}, 0.0 \leq \delta\varepsilon_{sf} \leq 1.0, 10\sigma \leq R_s \leq 10^8\sigma$). The value of $\delta\varepsilon_{sf}$ and associated Young's contact angle θ, for each result is indicated by the colour.

$0.7T_c, 0.775T_c$ and $0.85T_c$, are shown, with the arrow indicating the direction of increasing temperature. At each temperature, the chemical potential deviation was taken to be $\beta\delta\mu = 10^{-3}$, whilst other parameters varied in the ranges ($0.0 \leq \delta\varepsilon_{sf} \leq 1.0, 10\sigma \leq R_s \leq 10^8\sigma$). Again, colour is used to indicate the value of $\delta\varepsilon_{sf}$, whilst the associated Young's contact angle for each value of $\delta\varepsilon_{sf}$ for each temperature is given in the inset.

As predicted, the values of ℓ_{eq} obtained from cDFT fall onto three temperature dependent curves, which each represent a temperature dependent scaling function that obeys equation (5.6.17). If $c(T)$ were known, the exact form of this scaling function could be predicted from equation (5.6.17). This was done by Stewart and Evans [33] for the case of $\delta\mu = 0$, who found excellent agreement between the calculated scaling function, and results obtained from cDFT.

As was found in the case of SR ff LR sf interactions, there appears to be a limit in R_s for which the expected relation is obeyed. This can be seen most clearly by the small deviations from the apparent scaling function when $\ln(\tilde{p}/\varepsilon\Delta\rho|t'|^4) > 10$, which correspond to solutes of $R_s < 20\sigma$. Values of ℓ_{eq} obtained for $\delta\varepsilon_{sf} > 0.6$ also appear not to obey the scaling function. This can be seen most clearly by considering the yellow or light green results in figure 6.8,

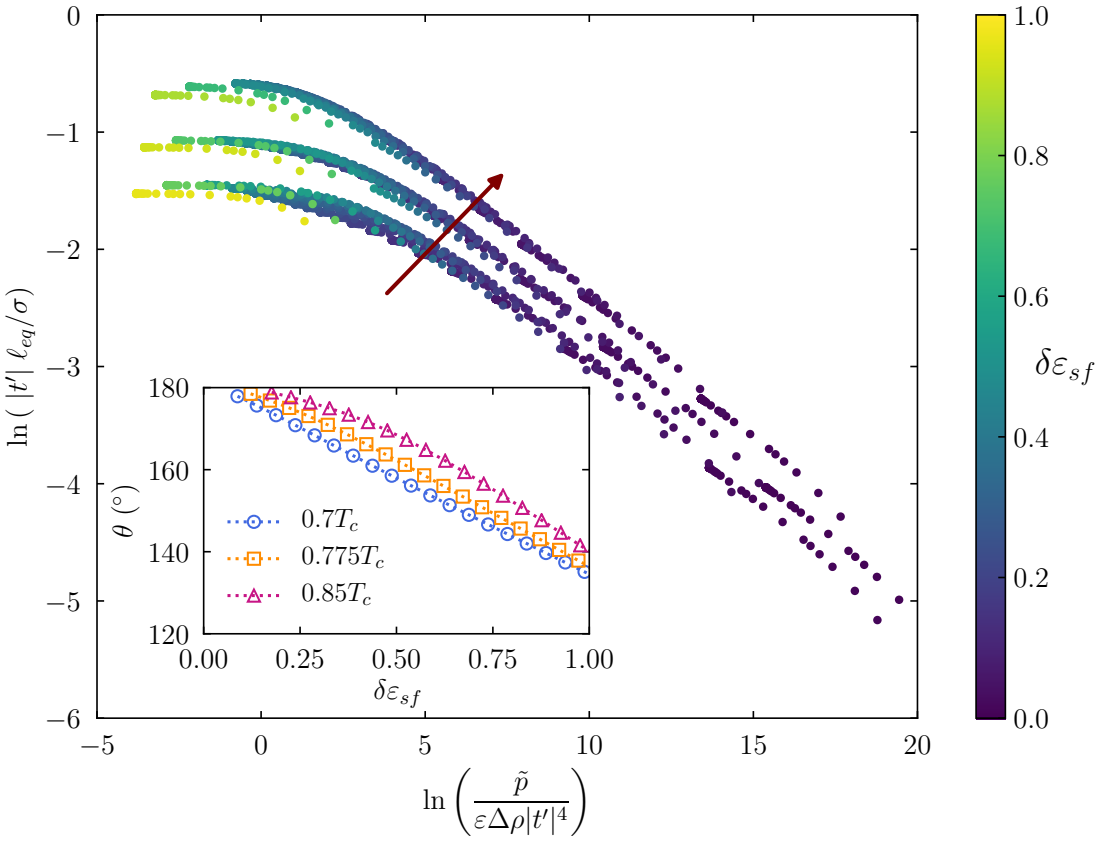

Figure 6.8: Comparison of results for ℓ_{eq} obtained from cDFT to the predicted scaling function relationship for LR ff LR sf interactions given in equation (5.6.35). Results obtained from three temperatures, $T = 0.7T_c, 0.775T_c$ and $0.85T_c$ are shown, with the red arrow indicating the direction of increasing temperature. Each result was obtained at $\beta\delta\mu = 10^{-3}$, with other parameters falling in the range $(0.0 \leq \delta\varepsilon_{sf} \leq 1.0, 10\sigma \leq R_s \leq 10^8\sigma)$. $\delta\varepsilon_{sf}$ is indicated by the colour. The inset shows the Young's contact angles for each $\delta\varepsilon_{sf}$ and temperature considered.

which correspond to $\delta\varepsilon_{sf} > 0.8$, as these clearly fall below the apparent scaling function curve. As was found in the SR ff LR sf case, the density profiles for $\delta\varepsilon_{sf} > 0.6$ in figure 6.4 are not well described by a SK approximation, and hence the predictions of the effective interface potential cannot be expected to be applicable for this region.

The influence of the parameters $(\beta\delta\mu, \delta\varepsilon_{sf}, R_s)$ on ℓ_{eq} can be better visualised by considering figure 6.9, which presents cDFT results for systems with SR ff LR sf interactions at $T = 0.775T_c$ in the form of contour plots. Figures 6.9(a) and 6.9(b) compare the influence of the curvature, R_s^{-1}, and $\delta\varepsilon_{sf}$ on ℓ_{eq}, for systems at constant $\beta\delta\mu = 10^{-4}$ and $\beta\delta\mu = 10^{-6}$ respectively. In both cases, a very similar shape of contour is observed. For $\sigma/R_s > 10^{-3}$, the contours are largely horizontal, which suggests ℓ_{eq} is most heavily influenced by the curvature of the solute. In contrast, for $\sigma/R_s < 10^{-3}$, the contours are almost vertical, and hence it appears that $\delta\varepsilon_{sf}$ exerts the greatest influence over ℓ_{eq}. The region in which the contour changes from near horizontal to near vertical gives an indication of the length scale for which the behaviour of ℓ_{eq} crosses over from being curvature dependent to curvature independent. These observations are in agreement with the predictions of equation (5.5.10), however it should be noted that the fluids considered in figure 6.9 are oversaturated.

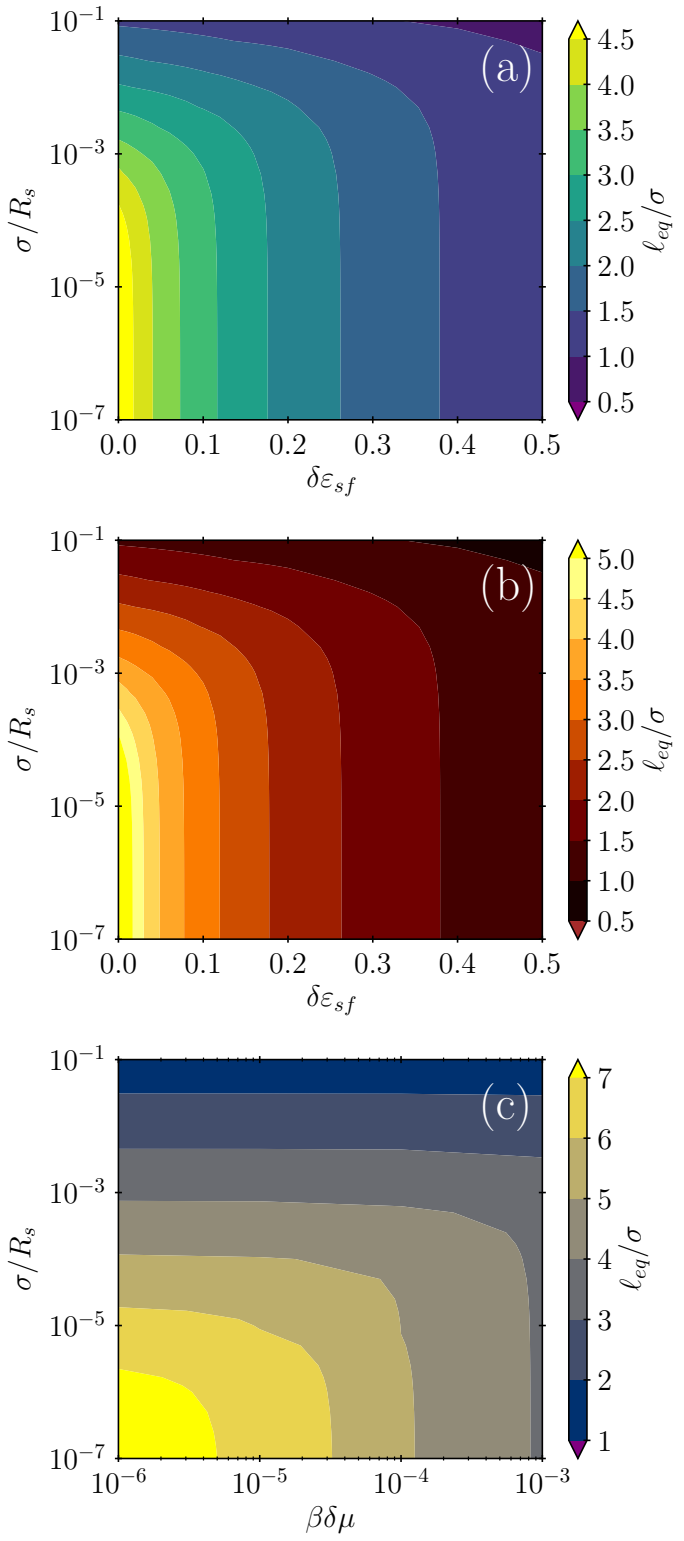

Figure 6.9: Comparison of ℓ_{eq} in systems with SR ff LR sf interactions for varying R_s, and $\delta\varepsilon_{sf}$ at constant (a) $\beta\delta\mu = 10^{-4}$ and (b) $\beta\delta\mu = 10^{-6}$, and (c) for varying R_s and $\beta\delta\mu$ at constant $\delta\varepsilon_{sf} = 0.0$.

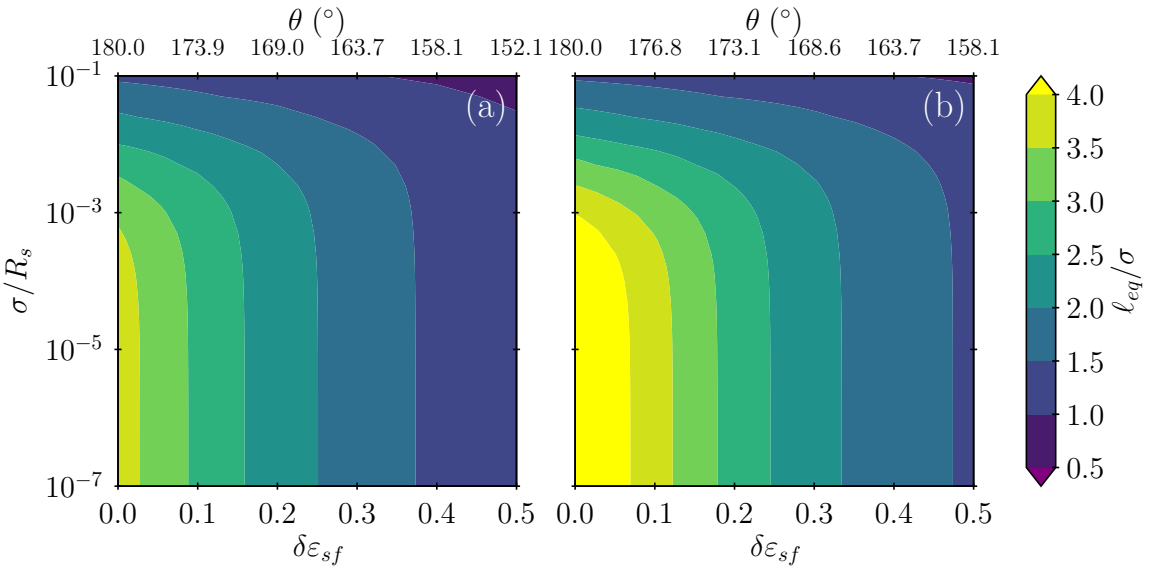

Figure 6.10: Influence of $(\delta\varepsilon_{sf}, R_s)$ on ℓ_{eq}, for the cases of (a) SR ff LR sf and (b) LR ff LR sf interactions, at $T = 0.775T_c$ and $\beta\delta\mu = 10^{-3}$. An indication of the solvophobicity of each $\delta\varepsilon_{sf}$ is given on the top axes by the equivalent Young's contact angle.

Figure 6.9(c) compares the influence of R_s^{-1} and $\beta\delta\mu$ for $\delta\varepsilon_{sf} = 0.0$ and, as expected, agrees with the predictions of equation (5.5.12). For large σ/R_s, the contours are almost completely horizontal, hence ℓ_{eq} is almost solely dependent on σ/R_s. In contrast, for small σ/R_s, the contours are near vertical, and hence ℓ_{eq} depends almost solely on $\beta\delta\mu$. The curve in the contour, which represents the crossover between regimes, is expected to occur at $R_s = R_c$. For $\beta\delta\mu = 10^{-3}$, this is $R_c \approx 913\sigma$, which equates to $\sigma/R_s \approx 10^{-3}$. This is in excellent agreement with figure 6.9(c).

The behaviour visualised in figure 6.9 for systems with SR ff LR sf interactions is also expected for the case of LR ff LR sf interactions. Figure 6.10 compares contour plots for the cases of (a) SR ff LR sf and (b) LR ff LR sf interactions at $T = 0.775T_c$ and $\beta\delta\mu = 10^{-3}$, for varying $(\delta\varepsilon_{sf}, R_s)$. As expected, the shapes of figures 6.10(a) and 6.10(b) are very similar. The largest difference between figures 6.10(a) and 6.10(b) is the generally larger values of ℓ_{eq} in the case of LR ff LR sf interactions, which is most easily observed by comparing the left of each figure. This is in agreement with the predictions of chapter 5, which indicate ℓ_{eq} grows as a logarithm in the case of SR ff LR sf interactions, whilst as an inverse power law in the case of LR ff LR sf interactions.

6.3.2 Local Density Fluctuations

Figure 6.11 compares the effective interface potential predictions for $\chi_\mu(\ell_{eq}; R_s)$ for the case of SR ff LR sf interactions, given in equation (5.5.14), to results obtained using cDFT. All results presented in figure 6.11 were obtained for a temperature of $T = 0.775T_c$, with other parameters taking values in the ranges $(10^{-6} \leq \beta\delta\mu \leq 10^{-3}, 0.0 \leq \delta\varepsilon_{sf} \leq 0.3, 10\sigma \leq R_s \leq 10^8\sigma)$. Results obtained for a planar substrate are also shown. Within figure 6.11, the cDFT results are coloured according to $\delta\varepsilon_{sf}$.

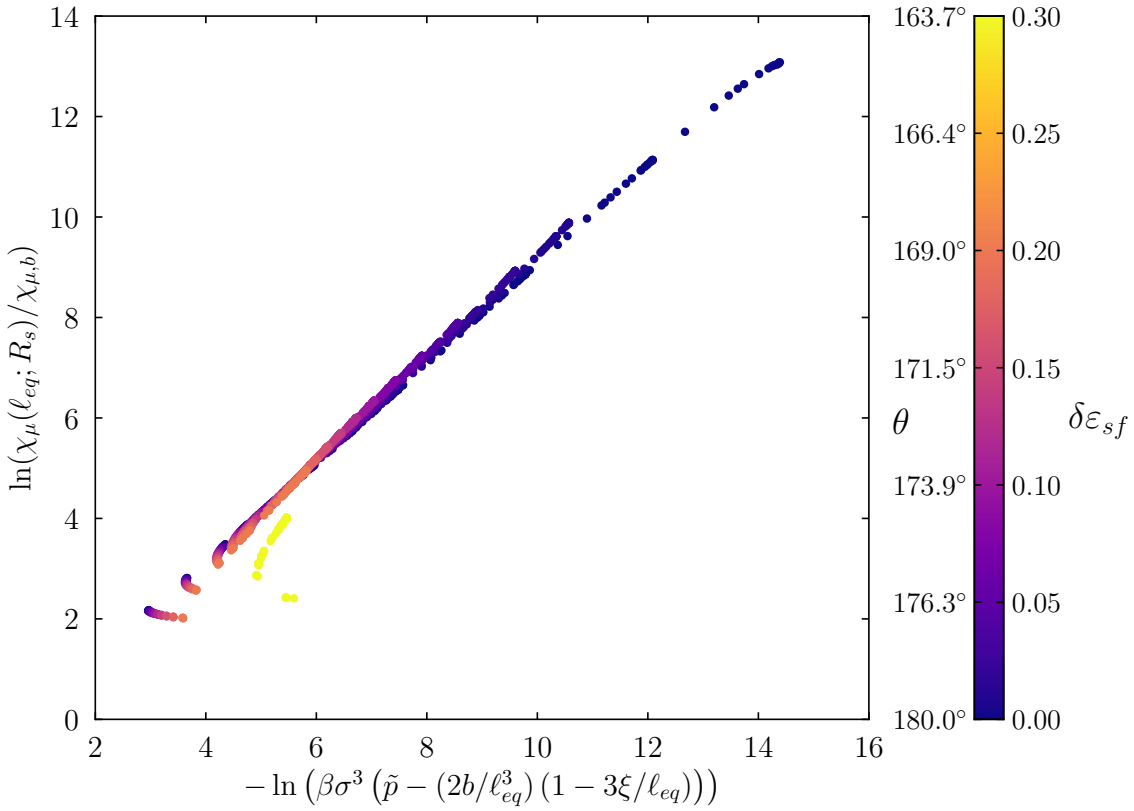

Figure 6.11: Comparison of effective interface potential prediction for $\chi_\mu(\ell_{eq}; R_s)$ given in equation (5.5.14), and results obtained from cDFT. All cDFT results were collected at $T = 0.775T_c$, for parameters in the range $(10^{-6} \leq \beta\delta\mu \leq 10^{-3}, 0.0 \leq \delta\varepsilon_{sf} \leq 0.3, 10\sigma \leq R_s \leq 10^8\sigma)$. The value of $\delta\varepsilon_{sf}$ for each result is indicated by the colour, and equivalent Young's contact angles are given as an indication of the solvophobicity.

In general, figure 6.11 shows excellent agreement between the predictions of equation (5.5.14) and the results obtained using cDFT when $\delta\varepsilon_{sf} \leq 0.2$. Some deviation from the predicted relationship is apparent in the lower left of figure 6.11, which corresponds to results from systems in which $R_s < 20\sigma$. This is the same range of R_s for which deviation from the predicted relationship of ℓ_{eq} was found in figure 6.7, and hence is unsurprising. There is also some notable deviation in the top right of figure 6.11, where the results appear to curve. These results relate to systems very close to the drying critical point, where $\chi_\mu(\ell_{eq}; R_s)/\chi_{\mu,b}$ can be seen to be of order 10^6. This deviation from the predicted behaviour is therefore most likely due to numerical errors in evaluating such large fluctuations.

For $\delta\varepsilon_{sf} = 0.3$, there is clear disagreement between the predicted relationship and results obtained using cDFT. Considering figure 6.7, it can be seen that systems with $\delta\varepsilon_{sf} \geq 0.3$ typically feature vapour films of width $\ell_{eq} < 2\sigma$. As the effective interface potential analysis assumes a thick vapour film, which is clearly not the case of $\delta\varepsilon_{sf} \geq 0.3$, it is perhaps unsurprising that the predictions are no longer obeyed. Alternatively, it could be that higher order terms in the binding potential, which were neglected in chapter 5, become important for such systems. This can be understood by considering the term $1 - 3\xi/\ell_{eq}$ within the predicted relationship of equation (5.5.2), where $\xi = 0.51\sigma$ is the correlation length of the bulk

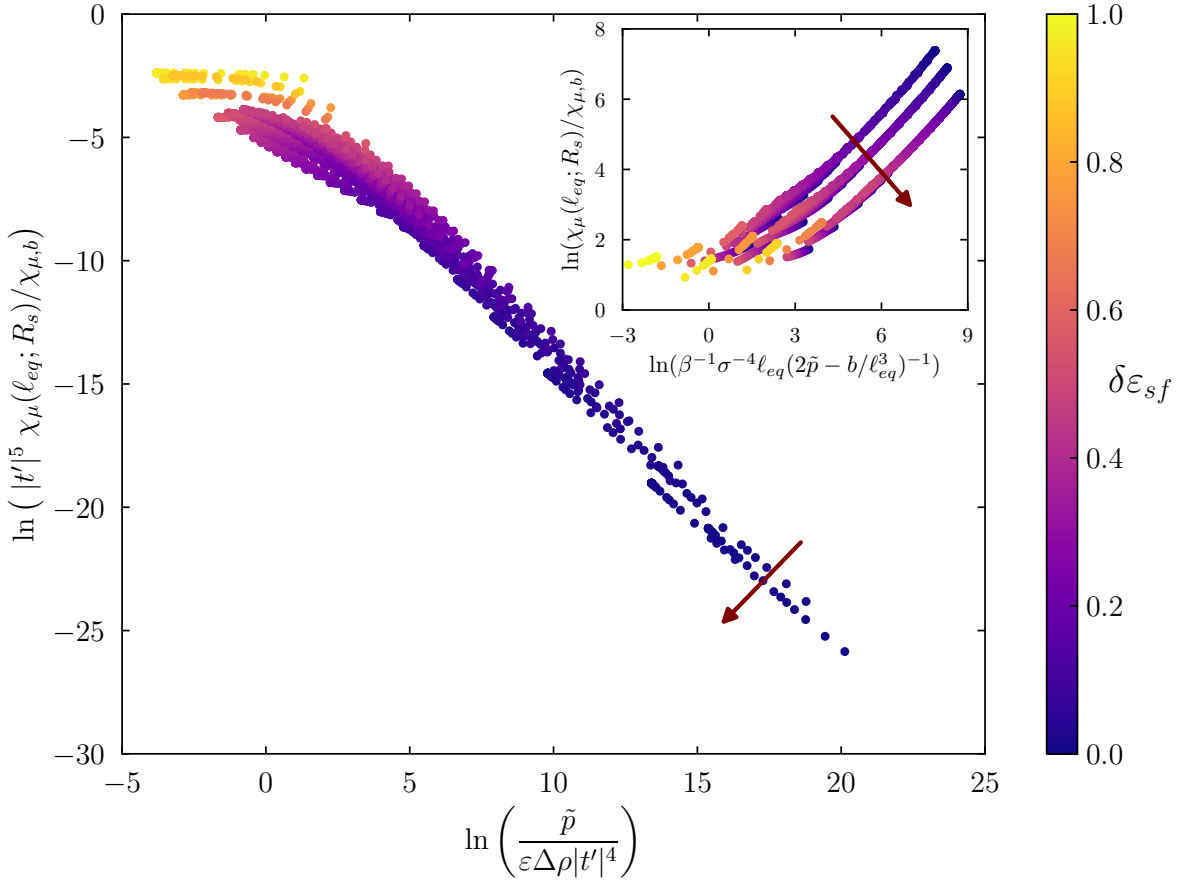

Figure 6.12: Comparison of effective interface potential predictions for the scaling function form of $\chi_\mu(\ell_{eq};R_s)$, given in equation (5.6.36), and cDFT results for LR ff LR sf interactions. The inset compares an alternative form of these predictions, given in equation (6.3.1), to cDFT results. For all cDFT results, $\beta\delta\mu = 10^{-3}$, whilst other parameters fell in the range $(0.0 \leq \delta\varepsilon_{sf} \leq 1.0, 10\sigma \leq R_s \leq 10^8\sigma)$. Three temperatures, $T = 0.7T_c, 0.775T_c$ and $0.85T_c$ are shown, with the arrows indicating the direction of increasing temperature. The cDFT results are coloured according to the value of $\delta\varepsilon_{sf}$ at which they were obtained. Equivalent Young's contact angles for these can be found in the inset of figure 6.8

.

vapour, and can be found numerically by comparing cDFT results to equation (5.5.2). When $\ell_{eq} < 3\xi = 1.53\sigma$, $1 - 3\xi/\ell_{eq}$ becomes negative and thus the agreement in figure 6.11 breaks down. If higher order terms were included in the binding potential, it is possible that the relationship would not become negative. However, such terms are likely to feature constants which depend on the shape of the liquid-vapour interface within the density profile, and are thus likely to be difficult to evaluate.

The predicted behaviour of $\chi_\mu(\ell_{eq};R_s)$ for the case of LR ff LR sf interactions is given in equation (5.6.21) and as in the case of ℓ_{eq}, contains a term proportional to $c(T)$, which is difficult to evaluate numerically. However, unlike the case of ℓ_{eq}, it is possible to remove this term using equation (5.6.17). Doing so leads to an alternative form of the predicted behaviour of $\chi_\mu(\ell_{eq};R_s)$ for LR ff LR sf interactions of

$$\chi_\mu(\ell_{eq};R_s) = \Delta\rho\;\rho'(R_s+\ell_{eq})\frac{\ell_{eq}}{2}\left(2\tilde{p}-\frac{b}{\ell_{eq}^3}\right)^{-1} \tag{6.3.1}$$

where all variables take their meanings as in section 5.6.2.

Figure 6.12 compares the predictions of the effective interface potential for $\chi_\mu(\ell_{eq}; R_s)$ to results obtained using cDFT, for both the scaling function form (main figure) given in equation (5.6.36), and form given in equation (6.3.1) (inset). For all results, $\beta\delta\mu$ was held constant at $\beta\delta\mu = 10^{-3}$, whilst other parameters varied in the ranges ($0.0 \leq \delta\varepsilon_{sf} \leq 1.0, 10\sigma \leq R_s \leq 10^8\sigma$). As in figure 6.8, three temperatures, $T = 0.7T_c, 0.775T_c$ and $0.85T_c$ were considered, and the arrows in figure 6.12 indicate the direction of increasing temperature. The cDFT results are again coloured according to the value of $\delta\varepsilon_{sf}$ at which they were obtained. Equivalent Young's contact angles can be found in the inset of figure 6.8. Considering first the predicted scaling function form of $\chi_\mu(\ell_{eq}; R_s)$, it can be seen that for small $\delta\varepsilon_{sf}$, the cDFT results appear to collapse onto three temperature dependent curves. These are much closer to one another than in the case of ℓ_{eq} in figure 6.8, and are most clearly distinguished in the lower right of the figure. For $\delta\varepsilon_{sf} > 0.4$, it is much less clear whether there is agreement between the predicted relationship and the results obtained from cDFT, and whether there are three scaling functions. Considering instead the predictions of equation (6.3.1) given in the inset, it appears as though there is excellent agreement between the effective interface potential predictions and cDFT results when $\delta\varepsilon_{sf} < 0.6$ at $T = 0.775T_c$ and $T = 0.85T_c$, and when $\delta\varepsilon_{sf} < 0.4$ at $T = 0.7T_c$. Comparing these values of $\delta\varepsilon_{sf}$ to the expected Young's contact angles in the inset of figure 6.8, it can be seen that all correspond to $\theta > 150°$. Careful inspection of the inset in figure 6.12 shows some disagreement between the predicted relationship and cDFT results even at small $\delta\varepsilon_{sf}$, though these results typically relate to values of $R_s < 20\sigma$, where disagreement was also found for the predictions of ℓ_{eq} in figure 6.8.

As in the case of ℓ_{eq}, the influence of individual parameters ($\beta\delta\mu, \delta\varepsilon_{sf}, R_s$) is best visualised using contour plots. Figures 6.14(a) and 6.14(b) compare the influence of R_s and $\delta\varepsilon_{sf}$ on $\chi_\mu(\ell_{eq}; R_s)$ for $\beta\delta\mu = 10^{-4}$ and $\beta\delta\mu = 10^{-6}$ respectively, whilst figure 6.14(c) compares the influence of $\beta\delta\mu$ and R_s for $\delta\varepsilon_{sf} = 0$. All are for the case of SR ff LR sf interactions, at $T = 0.775T_c$.

Much the same patterns as observed in figure 6.9 can be seen in figure 6.14, which is unsurprising given that $\chi_\mu(\ell_{eq}; R_s)$ is related to the derivative of ℓ_{eq}, and that all behavioural regimes predicted for ℓ_{eq} were also predicted from $\chi_\mu(\ell_{eq}; R_s)$ in section 5.5.2. Considering first figures 6.14(a) and 6.14(b), it is clear that there exists a region of parameter space for which R_s largely determines $\chi_\mu(\ell_{eq}; R_s)$, and a region for which $\delta\varepsilon_{sf}$ does, as was predicted in equation (5.5.15). The crossover between these regions seems to be very similar to that for ℓ_{eq} seen in figures 6.9(a) and 6.9(b). In figure 6.14(c), the shapes of each contour are near identical to those seen in figure 6.9(c), with the crossover between R_s and $\delta\mu$ regimes occurring near R_c. It is worth noting the incredibly large values of $\chi_\mu(\ell_{eq}; R_s)$ seen in figure 6.14, which are up to 10^6 times their bulk value very close to the drying critical point, and rarely fall below 10 times their bulk value. This highlights the sensitivity of $\chi_\mu(\ell_{eq}; R_s)$ as a measure of density fluctuations.

As with ℓ_{eq}, the regimes of $\chi_\mu(\ell_{eq}; R_s)$ observed for a system with SR ff LR sf interactions

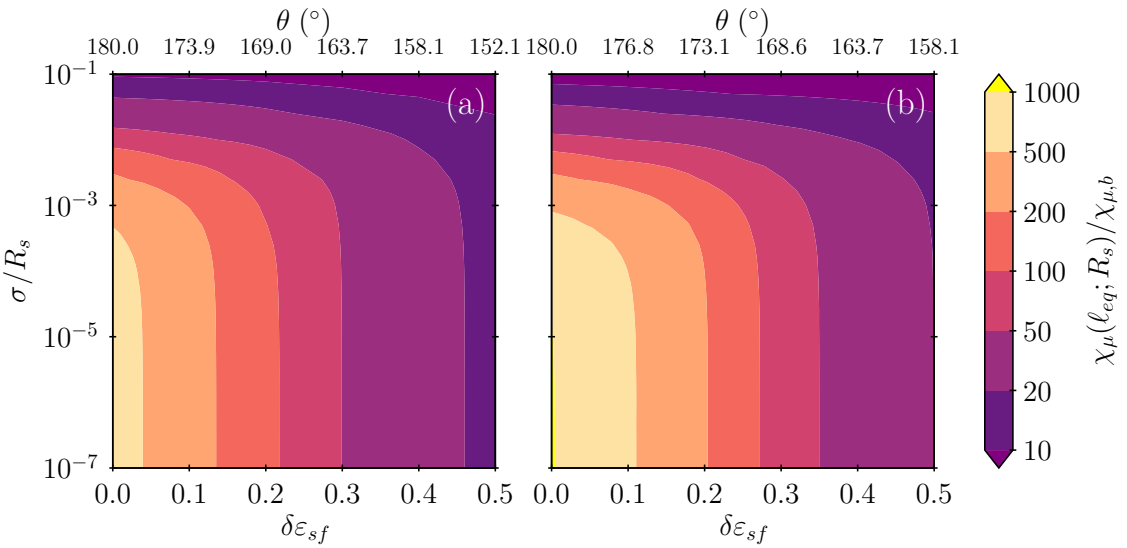

Figure 6.13: Comparison of influence of R_s and $\delta\varepsilon_{sf}$ on $\chi_\mu(\ell_{eq};R_s)$ in systems with (a) SR ff LR sf and (b) LR ff LR sf interactions, at $T = 0.775T_c$ and $\beta\delta\mu = 10^{-3}$. The equivalent Young's contact angle for each $\delta\varepsilon_{sf}$ is given on the top axes.

in figure 6.14 are also expected for systems with LR ff LR sf interactions. Figure 6.13 confirms this, by comparing the influence of R_s and $\delta\varepsilon_{sf}$ for $\beta\delta\mu = 10^{-3}$ in systems with (a) SR ff LR sf and (b) LR ff LR sf interactions, at $T = 0.775T_c$. In general, $\chi_\mu(\ell_{eq};R_s)$ is larger in the case of LR ff LR sf interactions, which is in agreement with the predictions of chapter 5, due to the more rapid divergence in the case of LR ff LR sf interactions compared to SR ff LR sf interactions.

6.4 Discussion

The purpose of this chapter was to confirm the assertion made in postulate 2 of chapter 1, that the physical mechanism underlying solvophobicity is a drying surface critical point. This has been done by comparing the predictions for the behaviour of ℓ_{eq} and $\chi_\mu(\ell_{eq};R_s)$ presented in the effective interface potential analysis of chapter 5 to results for a large number of systems of varying $(\beta\delta\mu, \delta\varepsilon_{sf}, R_s, T)$, obtained using cDFT. As the predictions of chapter 5 specifically relate the behaviour of ℓ_{eq} and $\chi_\mu(\ell_{eq};R_s)$ to the existence of a drying critical point, verification of their accuracy acts as strong evidence in favour of the assertion. These predictions have been tested for systems with SR ff LR sf interactions, which best reflect conditions of molecular simulation, and systems with LR ff LR sf interactions, which best reflect conditions of experiment.

Figures 6.7, 6.8, 6.11 and 6.12 confirm the predictions of chapter 5 are obeyed for both systems with SR ff LR sf and LR ff LR sf interactions, when $R_s > 20\sigma$ for a limited range of $\delta\varepsilon_{sf}$. The range of $\delta\varepsilon_{sf}$ for which the predictions are obeyed has been shown to vary with temperature, range of interactions and measure (ℓ_{eq} or $\chi_\mu(\ell_{eq};R_s)$) considered. However, in each case, the range of $\delta\varepsilon_{sf}$ for which the predictions are obeyed corresponds to Young's contact angles of $\theta > 150°$. As has been discussed, Young's contact angle is strictly only defined in the limit of a fluid at liquid-vapour coexistence in contact with a smooth planar

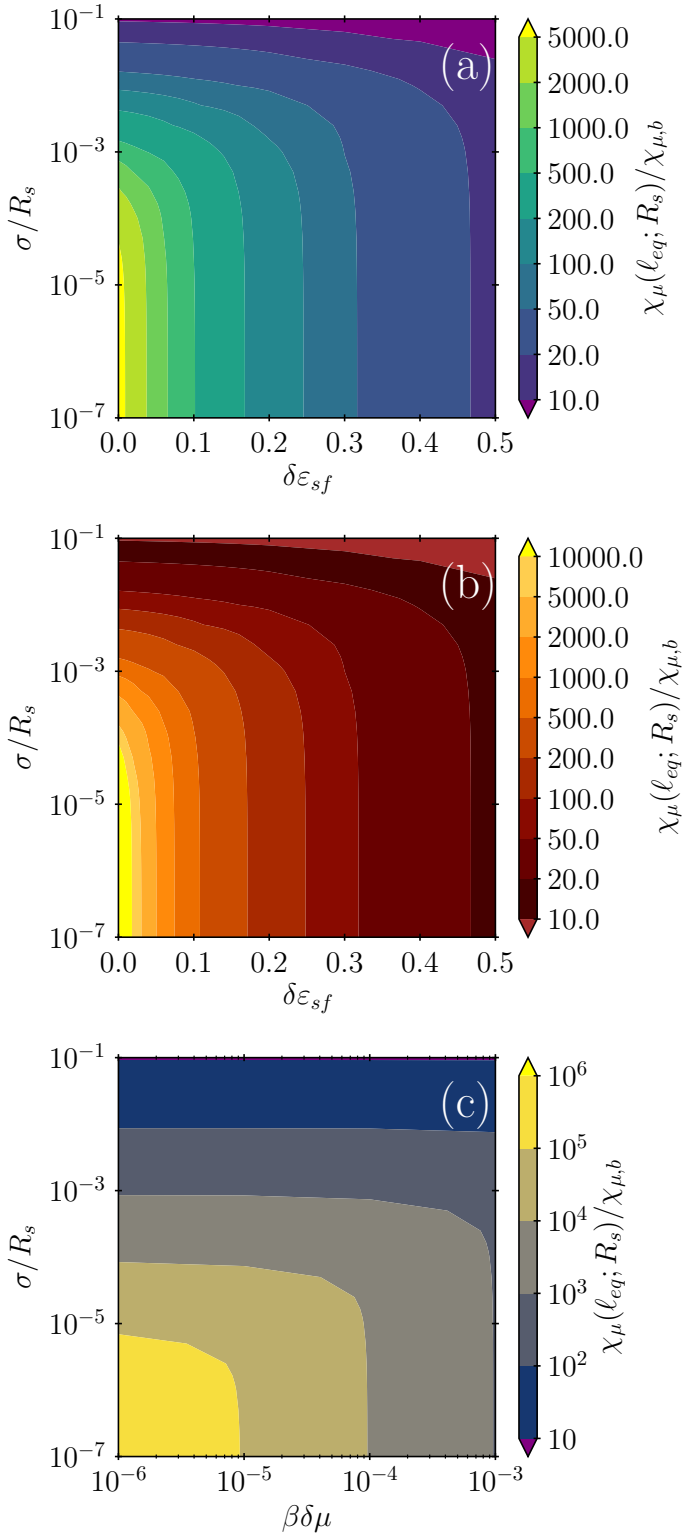

Figure 6.14: Behaviour of $\chi_\mu(\ell_{eq}; R_s)$ with varying (a) R_s and $\delta\varepsilon_{sf}$ at $\beta\delta\mu = 10^{-4}$, (b) R_s and $\delta\varepsilon_{sf}$ at $\beta\delta\mu = 10^{-6}$ and (c) R_s and $\beta\delta\mu$ at $\delta\varepsilon_{sf} = 0.0$, for the case of SR ff LR sf interactions. All results were obtained at $T = 0.775T_c$.

surface, which is a description not applicable to the systems considered here. Despite this, it is interesting to note that the range of θ for which the predictions were obeyed is equivalent to the range for 'superhydrophobic' behaviour discussed in section 3.1.3. The results presented here therefore suggest that the influence of the drying critical point is most strongly felt in the analogous 'supersolvophobic' regime.

Although weak to little agreement was found between the predictions of the effective interface potential analysis and cDFT results for systems with $\theta < 150°$, there is reason to believe that the drying critical point may exert some limited influence on these solvophobic systems. This can be understood most clearly by considering the local compressibility profiles for $\delta\varepsilon_{sf} = 1.2$ in figures 6.3 and 6.4. As was noted in section 6.2.2, although there are clear oscillations, and $\chi_\mu(r)/\chi_{\mu,b}$ is comparably smaller in magnitude than profiles for corresponding lower $\delta\varepsilon_{sf}$, these local compressibility profiles take a form distinct from that expected in the bulk or at a solvophilic substrate, as the oscillations are not centred on $\chi_{\mu,b}$. This potentially indicates that the density fluctuations around weakly solvophobic solutes and at weakly solvophobic planar surfaces are remnants of the critical fluctuations observed in systems nearer to the drying critical point.

Figures 6.1 and 6.2 analysed the influence of R_s on the density and local compressibility profiles of solvophobic systems with SR ff LR sf and LR ff LR sf interactions respectively. For all cases of $\delta\varepsilon_{sf}$ in each figure, it was found that as R_s increased, the profiles tended to those expected at a planar substrate. This indicates that solvophobicity on microscopic length scales is related to that on macroscopic length scales, which is to be expected as solvophobicity on both of these length scales has been shown to be influenced by the drying critical point. Within figures 6.1 and 6.2 there appears to be an upper limit of R_s, above which the profiles could not be distinguished from those at a planar substrate. Such a limit suggests a length scale which divides systems into those in which the behaviour is dependent on curvature and those in which it is not. This corresponds to the idea of a crossover length scale between the large length scale solvation and macroscopic regimes of hydrophobicity described in section 3.1. Whilst such a length scale should exist, there does not appear to be any definition used commonly in the literature, as mentioned in section 3.1.4. It was suggested in chapter 5 that a candidate for this was the length scale of capillary evaporation, R_c. At $\delta\varepsilon_{sf} = 0.0$, there is strong evidence in favour of this, as can be seen in figures 6.5, 6.9(c) and 6.14(c). However, when both $\beta\delta\mu > 0$ and $\delta\varepsilon_{sf} > 0$, R_c does not accurately describe the crossover, as can be seen in figures 6.9(a), 6.9(b), 6.14(a) and 6.14(b). In each of these figures, the curves in the contours, which represents the crossover between curvature dependent and independent behaviour, can be seen to largely occur for the same length scales, despite the different $\beta\delta\mu$. Hence, from these results, it is not possible to define a length scale which separates the large length scale solvation and macroscopic regimes of solvophobicity.

Finally, from the results presented within this chapter, two interesting observations with potential consequences for hydrophobicity can be made. Firstly, many of the systems considered featured the oversaturation predicted for water at ambient conditions, $\beta\delta\mu = 10^{-3}$, and hence it has been confirmed that such an oversaturation is sufficiently close to the drying

critical point to feel its effects. Secondly, density fluctuations in systems with $\beta\delta\mu = 10^{-3}$ with both SR ff LR sf and LR ff LR sf interactions presented in figure 6.13 are predominantly influenced by the curvature of the system when $R_s < 1000\sigma$. Density fluctuations in such systems with $R_s < 1000\sigma$ are therefore not expected to vary substantially when exposed to small changes in other parameters, $(\beta\delta\mu, \delta\varepsilon_{sf})$, and considering figure 6.6, when exposed to small changes in the temperature. This is an interesting observation, because many of the biological processes discussed in section 3.1.2, which are believed to involve density fluctuations, would be expected to occur on these length scales.

Chapter 7

Influence of Critical Drying in the Hydrophobic Response of Water

Examination of the validity of the predictions of the effective interface potential analysis of chapter 5 for hydrophobic systems can be achieved using GCMC, as was presented in section 4.2. As discussed in section 4.2.7, this thesis makes use of a water model which features only SR ff interactions, and models the sf interaction using the LR LJ potential described in section 4.2.9. As such, the hydrophobic systems considered within this thesis have SR ff LR sf interactions, and are thus expected to obey the predictions of section 5.5.

Due to the computational demand of GCMC, it was not possible to perform as detailed a study for hydrophobicity as was performed for solvophobicity in chapter 6. Instead, this chapter focuses on examining a smaller number of systems, and is limited to consideration of solutes only. In particular, studying systems with planar substrates requires careful consideration of the FS effect premature drying, discussed in section 2.4.6, which was not feasible within the present work. Despite this, results presented within this chapter are expected to allow for accurate conclusions on the validity of postulate 1 of chapter 1 for several reasons. Firstly, if the predicted behaviour of ℓ_{eq} and $\chi_\mu(\ell_{eq}; R_s)$ occurs around the small solutes considered here, there is no reason to believe it would not occur around larger solutes or in the planar limit. Secondly, a previous study by Evans and Wilding [23] has considered the influence of the drying critical point on hydrophobic systems with a planar slit geometry. Although this study did not consider effective interface potential predictions, it does provide density and local compressibility profiles with which results for solutes can be compared. Finally, if the results presented within this chapter indicate that hydrophobicity of microscopic solutes is related to a drying critical point, then postulate 2 of chapter 1 is expected to be valid. In this case, all general conclusions presented in chapter 6 for solvophobicity can be expected to be applicable also for hydrophobicity.

This chapter proceeds in much the same way as chapter 6, presenting the state points and bulk properties of mW required for the study, then considering density and local compressibility profiles and finally testing the predictions of section 5.5. Following this, the process by which the depleted density region at the surface of hydrophobic solutes forms is investigated,

and compared to previous results of both simulation and experiment. This chapter is then concluded with a discussion of the implications of the results presented with respect to the postulates of chapter 1.

7.1 State Points and Bulk Properties

Water at ambient conditions exhibits a small oversaturation of approximately $\beta\delta\mu \approx 10^{-3}$ [96]. To accurately model water, it is essential that this value be reproduced. As mW is a relatively new model, many of its bulk properties are not yet widely reported, of which an example is a highly accurate $\mu - T$ coexistence curve. Because of this, it was necessary to carefully trace the liquid-vapour coexistence curve of mW prior to considering hydrophobicity, which was done using the GCMC methods presented in section 4.2.8. This also provided an opportunity to assess the suitability of mW for the study of hydrophobicity through comparisons to real water and a popular water model SPC/E, which is presented in Appendix E.

Figure 7.1 shows the liquid-vapour phase diagrams of mW relevant to this thesis. In each case, ρ and T are given in both physical and reduced units. The physical density of the fluid was obtained in units of gcm^{-3} using $\rho =< N > M/VN_{\mathrm{A}}$, where $M = 18.015$g is the molar weight of water, N_{A} is Avagadro's number, V was the volume of the simulation box, and $< N >$ the average number of particles [132]. The filled points represent state points obtained from simulation, whilst the hollow points represent state points obtained through histogram reweighting, as described in section 4.2.5. In figure 7.1(a), the dotted curve represents the mean density. In both figures 7.1(a) and 7.1(b), the critical point is represented by the larger filled point. In all cases, the uncertainty, obtained using the methods described in section

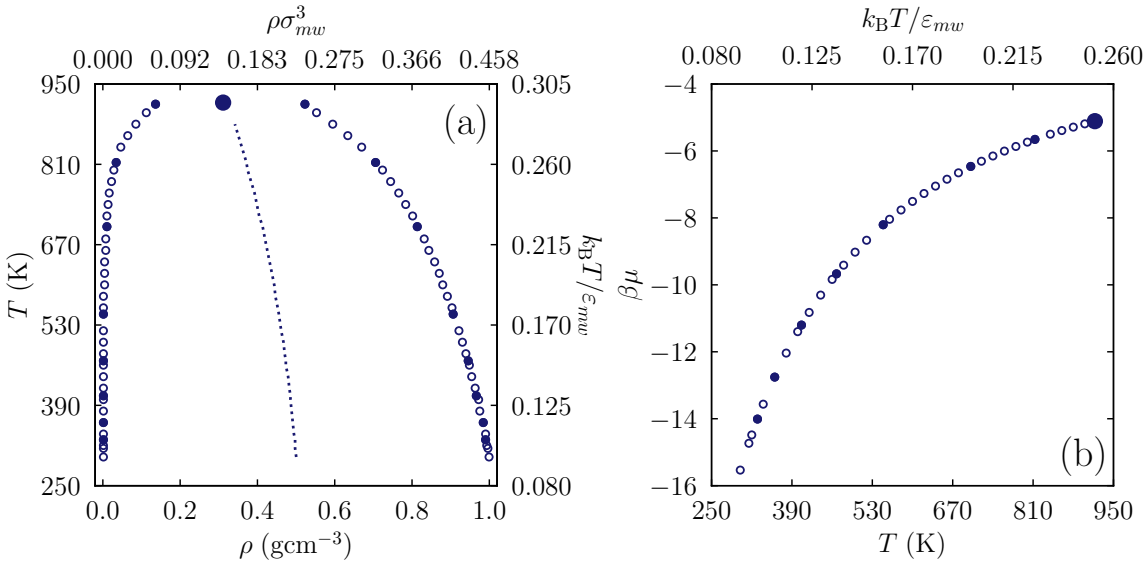

Figure 7.1: Liquid-vapour phase diagrams of mW, obtained using the methods of section 4.2.8. The filled points represent simulation data, whilst the hollow points represent state points obtained using histogram reweighting. The uncertainty of simulation points did not exceed symbol size. The critical point is given by the larger filled point. Both physical and reduced units are given. In the latter, $\sigma_{mw} = 2.3925$Å, whilst $\varepsilon_{mw} = 6.189$kcal/mol.

4.2.11, did not exceed symbol size.

From figure 7.1(a), it can be seen that mW grossly over-predicts the bulk critical temperature of water. Accounting for FS effects, mW was found to have a bulk critical temperature of $T_{c,mw} = 917.6$K, which is similar to previous estimates by Xu and Molinero [138], and by Russo et al. [141], though it should be noted that these previous studies do not make clear whether FS effects were taken into account. Interestingly, despite a large over prediction in T_c, mW performs well when reproducing the critical density. Accounting for FS effects, this was found to be $\rho_{c,mw} = 0.311\text{gcm}^{-3}$, which compares favourably to that of water, $\rho_{c,w} = 0.322\text{gcm}^{-3}$ [133]. This suggests that mW may more accurately reproduce the liquid-vapour phase diagram of water if all temperatures and densities were scaled by their bulk critical values.

Despite the larger $T_{c,mw}$, mW can be seen in figure 7.1(a) to reproduce the phase diagram of water well near ambient conditions. Detailed analysis by Molinero and Moore [132] found that the density of mW in fact agrees to within 1% of the experimental value of water between the temperatures $250\text{K} \leq T \leq 350\text{K}$. In addition, mW has previously been reported to have a liquid-vapour surface tension at ambient conditions closer to that of water than other leading water models [132], and it has been reported by Xu and Molinero [138] that mW reproduces the liquid-vapour surface tension of water almost exactly at 360K. As these two properties were discussed and argued in section 4.2.6 to be those important for the study of hydrophobicity, this suggests that collecting results at either ambient conditions, taken to be $T = 300$K, or at $T = 360$K, is sensible.

However, realistically it was not possible to do so because of the low move acceptance ratio, defined as the number of accepted insertion and deletion moves compared to the total number of moves proposed, of GCMC at these temperatures. Bulk simulations of mW at 300K and a realistic oversaturation of $\beta\delta\mu = 10^{-3}$ [96] showed move acceptance ratios of $\approx 0.1\%$, whilst at 360K and $\beta\delta\mu = 10^{-3}$, move acceptance was $\approx 0.3\%$. Although these acceptance ratios may be expected to improve with the addition of hydrophobic solutes which induce depleted density regions, even in this case, move acceptance at 300K and $\beta\delta\mu = 10^{-3}$ never exceeded 0.2%. This can be rationalised by considering figure 7.1(b). Below 400K, the coexistence chemical potential, μ_{co}, decreases rapidly, indicating that it becomes progressively more difficult to insert particles into the system.

It was therefore not feasible to perform a comprehensive study of hydrophobicity using mW at temperatures below 400K. Instead, a strategy was devised to collect the majority of results at the higher temperature of $T = 426$K, which was chosen to reflect the ratio of ambient temperature to bulk critical temperature of water, $T/T_c \approx 0.46$. This approach can be justified using figure 7.2, which compares the phase diagrams of water and mW (a) in physical units and (b) when scaled by the bulk critical temperature and density. Whilst the phase diagrams in physical units show little similarity above 350K, the scaled phase diagrams show remarkable agreement, particularly at $T/T_c = 0.46$, which is marked by the grey dotted line. This implies mW has a comparable bulk structure to that of real water at corresponding T/T_c and ρ/ρ_c.

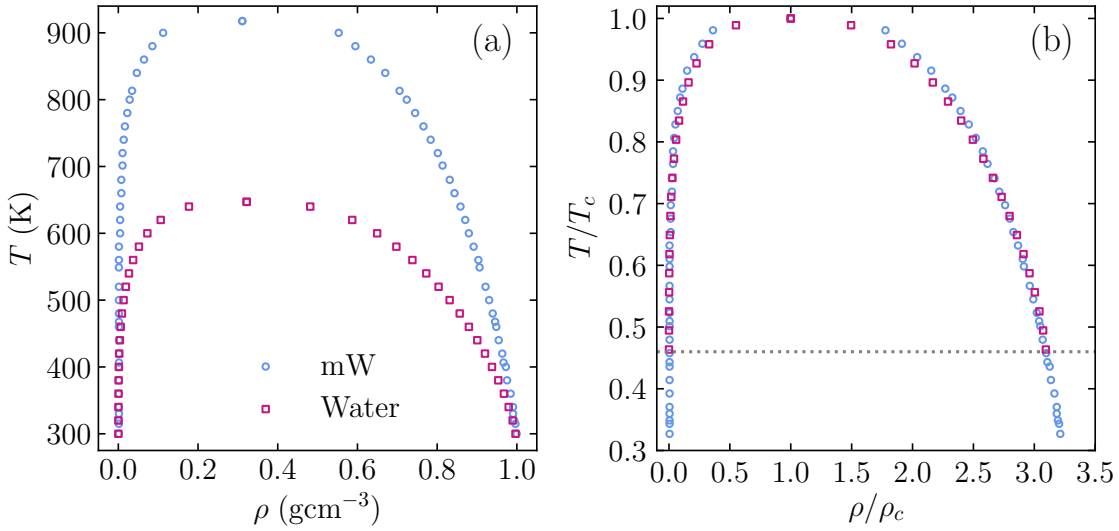

Figure 7.2: Comparison of the liquid-vapour phase diagrams of water (pink squares) and mW (blue circles) (a) in physical units and (b) when units are scaled by their bulk critical values. The dotted grey line represents the T/T_c ratio for water. Results for water were taken from [149].

Three temperatures were therefore considered within this chapter. The majority of the results, particularly those used to verify the predictions of the effective interface potential, were collected at 426K, where the move acceptance ratio was closer to 1%. Limited results were collected at 300K and 360K, where move acceptance was low, for comparison. Table 7.1 provides details of the coexistence state points for each of these temperatures. Parameters and bulk properties for mW at these temperatures for an oversaturation can be found in table 7.2. In each case, ρ_b was found according to section 4.2.10.1. $\chi_{\mu,b}$ was obtained by using histogram reweighting to find ρ_b at a higher μ and then performing a numerical derivative. Due to the discretisation of the density within the simulation box into units of an integer number of particles, it was not possible to distinguish ρ_b and $\chi_{\mu,b}$ at $\beta\delta\mu = 0, 10^{-3}, 10^{-4}$, and hence the same value is given for each.

The systems considered within this chapter consisted of SR ff LR sf interactions, hence the critical sf attraction in each was expected to be $\varepsilon_c = 0.0$. As in chapter 6, the sf attraction was defined to be a fraction of the ff attraction, $\varepsilon_{mw} = 6.189$ kcal/mol, such that $\varepsilon_{sf} = \tilde{\varepsilon}_{sf}\varepsilon_{mw}$.

Table 7.1: State points of mW at liquid-vapour coexistence for the temperatures used within this work.

T (K)	$\beta\mu_{co}$
300	−15.53438
360	−12.75623
426	−10.66336

Table 7.2: State points and bulk properties of mW for various temperatures at non-zero $\beta\delta\mu$, which are used within this work.

T (K)	$\beta\delta\mu$	ρ_b (gcm^{-3})	$\beta^{-1}\sigma_{mw}^3\chi_{\mu,b}$
300	10^{-3}	0.99821	0.01190
360	10^{-3}	0.98175	0.01557
426	$10^{-3}, 10^{-4}$	0.95981	0.02060

7.2 Density and Local Compressibility Profiles

The behaviour of the density profile of water local to hydrophobic solutes and planar substrates has been discussed in several previous studies of hydrophobicity. Using simulations of SPC/E, Huang and Chandler [9] investigated the behaviour of the density profile in the small length scale solvation regime discussed in section 3.1.1. For solutes of R_s approximately the same size as a SPC/E molecule, an enhanced contact density and prominent packing effects were observed, as expected. As R_s was increased, Huang and Chandler [9] found that the contact density decreased and oscillations within the density profile were depleted. Huang and Chandler [9] extended their study to consider the large length scale solvation regime using LCW theory, and found that for a hard solute, as $R_s \to \infty$, the contact density depleted further, and smooth vapour films formed. This is the same behaviour as for both SR and LR LJ fluids, presented in section 6.2. Furthermore, Huang and Chandler [9] found that introducing a sf attraction suppressed the emergence of a vapour film, in a similar fashion to that observed for solvophobicity in section 6.2.2. Simulation studies by Mamatkulov et al. [22] and Mittal and Hummer [95] reported similar behaviour, and went further to consider the effects of varying thermodynamic conditions such as temperature and pressure. Increasing the temperature was found to encourage the growth of the vapour film [22], in agreement with the findings for solvophobicity presented in section 6.2.4, whilst increasing the pressure was found to suppress it [22, 95]. In a simulation study of SPC/E confined to a hydrophobic slit, Evans and Wilding [23] also found evidence of vapour-like films at the surfaces of the slit, which were suppressed upon increasing sf attraction.

To the best of our knowledge, no previous studies have considered the form of the local compressibility around hydrophobic solutes. Despite this, its form is easily reasoned. Previous studies of solutes and planar surfaces have reported similar behaviour in the density profiles [9, 22, 23, 95]. As the local compressibility is simply the derivative of these density profiles, it can therefore also be expected to be similar around solutes and planar surfaces.

7.2.1 Influence of Solute Size and Substrate-Fluid Attraction Strength

Figure 7.3 shows the density (lower) and local compressibility (upper) profiles of mW, at $T = 426$K and $\beta\delta\mu = 10^{-3}$, around solutes of radii $\sigma_{mw} \leq R_s \leq 17\sigma_{mw}$ for four values of ε_{sf}, given as a fraction of ε_{mw} in the upper legend, and in physical units in the lower. The bottom axis gives the distance measured from the centre of the solute in real units, whilst the upper in units of σ_{mw}. The vertical grey dotted lines represent the surface of each solute considered. The uncertainty of each profile was found according to section 4.2.11. For the

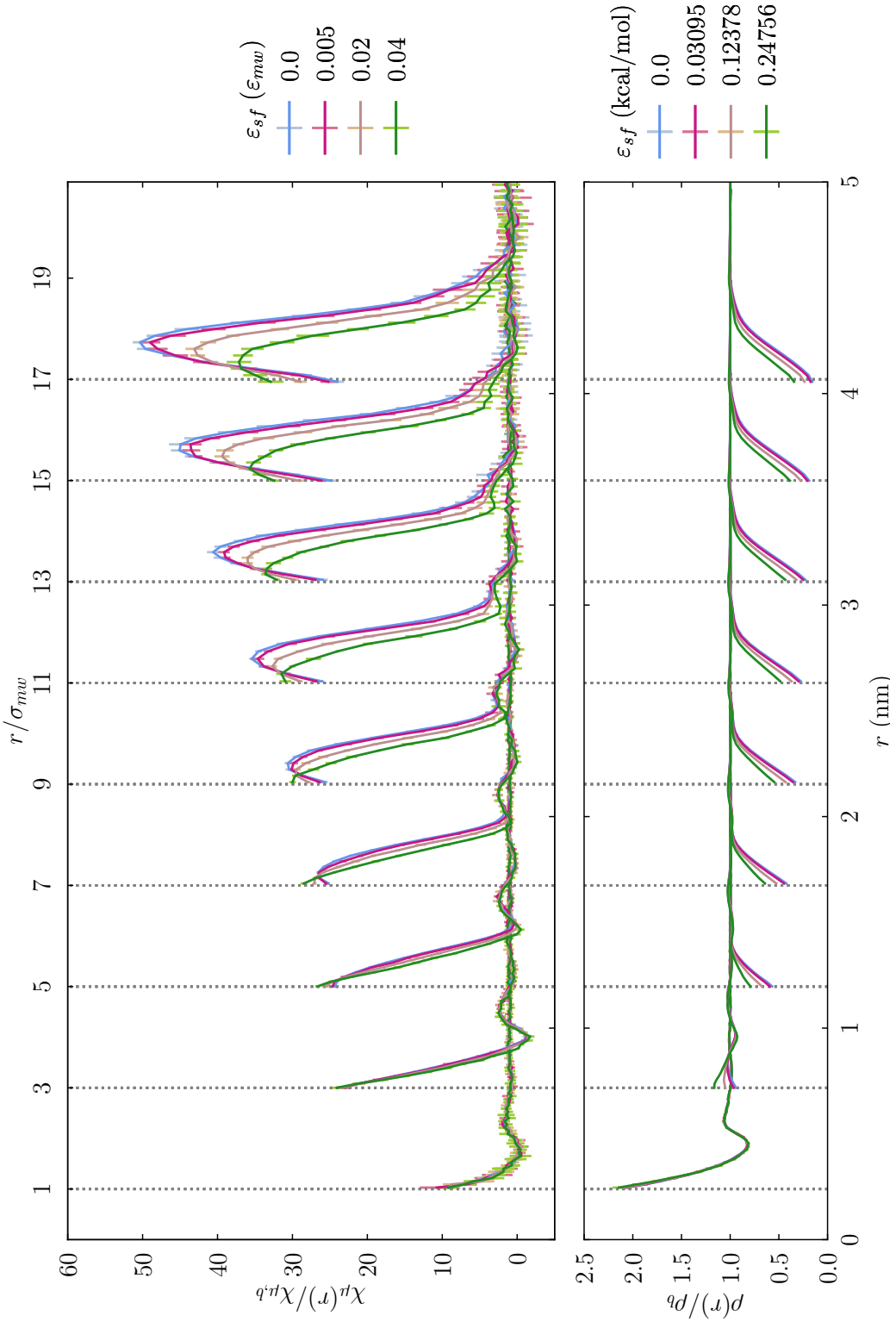

Figure 7.3: Density (lower) and local compressibility (upper) profiles, scaled by their bulk values, for mW at $T = 426$K and $\beta\delta\mu = 10^{-3}$ around solutes of various radii. The colour represents the sf attraction strength, and is given as a fraction of the ff attraction, ε_{mw}, in the upper legend, as well as in physical units in the lower. The location of the surface of each solute is represented by the vertical grey dotted lines. Uncertainties were found according to section 4.2.11, and for the density did not exceed line width.

density profile, this did not exceed the line width.

For the smallest value of R_s considered, $R_s = \sigma_{mw} \approx 0.24$nm, the density profile shows the behaviour expected of the small length scale solvation regime described in section 3.1.1, and found by Huang and Chandler [9]. There is an enhanced contact density with clear oscillations, and increasing the sf attraction has little influence. The local compressibility profile follows the form of the density profile, and again shows little variation with sf attraction. This also agrees with the behaviour expected in the small length scale solvation regime, in which fluctuations are expected to be well described by those found in bulk water, and therefore not enhanced.

Upon increasing R_s, figure 7.3 shows that the contact density reduces, eventually falling below that of the bulk between $3\sigma_{mw} < R_s < 5\sigma_{mw}$. For R_s larger than this, a region of depleted density, termed here a vapour film for simplicity, emerges. The emergence of this vapour film is accompanied by a change in the behaviour of the local compressibility, which can be seen to exhibit a large peak centred on the interface between the depleted density region and bulk liquid within the density profile. As R_s grows, oscillations in the density profile are suppressed, which is also reflected in the local compressibility. For $R_s > 5\sigma_{mw}$, the oscillations within the local compressibility are no longer centred on $\chi_{\mu,b}$. This behaviour was specifically noted to differentiate solvophilic and solvophobic behaviour in section 6.2.2. Increasing the sf attraction suppresses the vapour film, and thus suppresses the emergence of a peak in the local compressibility profile. All of these behaviours are in good agreement with those expected of the large length scale solvation regime, described in section 3.1.2, and for the density profile, those reported in previous studies [9, 22, 95]. Interestingly, the crossover between the small and large length scale solvation regimes occurs near 1nm, which is the same length scale reported for water at ambient conditions in previous studies. [5, 9, 11, 83].

The density and local compressibility profiles presented in figure 7.3 have near identical forms to those found at planar surfaces in the study by Evans and Wilding [23]. Whilst their study used a slit geometry, for most values of sf attraction considered, the surfaces of the slit could be considered independent or non-interacting, and hence the profile at each treated as one expected to occur at a single planar surface. It is also worth noting the magnitude of the local compressibility for the largest solutes in figure 7.3. For $R_s = 17\sigma_{mw} \approx 4.07$nm and $\varepsilon_{sf} < 0.04\varepsilon_{mw}$, the peak in the local compressibility is more than fifty times that in the bulk. This should be compared to the depleted density region of the density profile, which does not vary substantially from its bulk value, and extends less than a diameter of a mW particle from the surface of the solute.

7.2.2 Influence of Chemical Potential Deviation

For mW at $T = 426$K and $\beta\delta\mu = 10^{-3}$, the length scale of capillary evaporation can be calculated to be $R_c = 2\gamma_{lv}/\delta\mu\Delta\rho = 0.583\mu$m, whilst for $\beta\delta\mu = 10^{-4}$, $R_c = 5.83\mu$m. According to the general predictions of the effective interface potential analysis, the behaviour of $\rho(r)$ and $\chi_\mu(r)$ around solutes of $R_s < R_c$ and $\varepsilon_{sf} = 0.0$ should be largely determined by R_s, and hence profiles for $\beta\delta\mu = 10^{-3}$ and $\beta\delta\mu = 10^{-4}$ should exhibit little difference. This

predicted behaviour was found to be true for a LJ fluid in section 6.2.3.

Figure 7.4 shows the density (lower) and local compressibility (upper) profiles, scaled by their bulk values, around solutes of $R_s < R_c$ for $\varepsilon_{sf} = 0.0$ and $T = 426$K, and two values of $\beta\delta\mu$. In agreement with predictions, there is very little difference in $\rho(r)$ and $\chi_\mu(r)$ for the two $\beta\delta\mu$ considered, despite the order of magnitude difference. Figure 7.4 therefore provides first evidence that hydrophobicity may obey the scaling relations presented in section 5.5. For completeness, it would be pertinent to test the further prediction that for $R_s \gg R_c$, the density and local compressibility profiles for varying R_s become indistinguishable, as was confirmed for a solvophobicity in section 6.2.3. However, due to the large values of R_s this would require, it is simply not feasible here.

7.2.3 Influence of Temperature

In section 7.1, three temperatures were proposed as sensible state points. The first was $T = 300$K, at which mW reproduces the density of water well. Molinero and Moore [132] also showed that at 298K, the radial and angular distributions of mW are in excellent agreement with experiment, hence this state point most accurately reproduces the structure of water. The second temperature suggested was $T = 360$K, which is the temperature at which mW reproduces the liquid-vapour surface tension of water almost exactly. Finally, the third state point was $T = 426$K, which is expected to correspond to that of water at ambient conditions, as shown in figure 7.2(b). Although the majority of results collected were at the latter

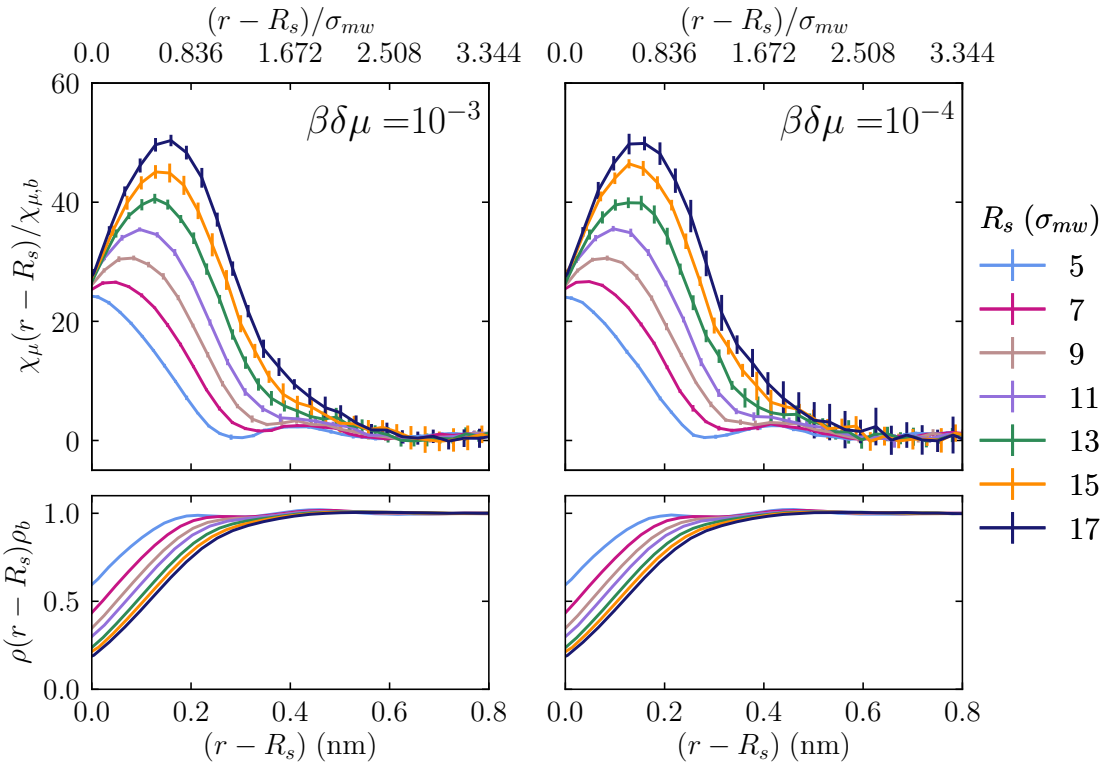

Figure 7.4: Density (lower) and local compressibility (upper) profiles, scaled by their bulk values, for mW at $T = 426$K and $\varepsilon_{sf} = 0.0$, and for varying R_s and $\beta\delta\mu$. The uncertainty in each profile was calculated according to section 4.2.11, and did not exceed line width in the case of the density.

temperature, as each state point represents a different property expected to be important for accurately modelling hydrophobicity, it is interesting to ask how hydrophobicity differs at each of these temperatures.

Figure 7.5 shows the density (lower) and local compressibility (upper) profiles, scaled by their bulk values, for solutes of $\varepsilon_{sf} = 0$ and three radii, for the state points discussed. Due to the lower move acceptance ratios at lower temperatures, the uncertainty in these profiles is larger, particularly for $T = 300$K. This further justifies the majority use of $T = 426$K. For all temperatures considered, the density and local compressibility profiles take much the same form. As R_s is increased, a region of depleted density and a peak in the local compressibility emerge at the surface of the solutes, and oscillations indicative of liquid packing effects are suppressed. These packing effects do not disappear completely at lower temperatures, which is in contrast to $R_s = 17\sigma_{mw}$ and $T = 426$K, where packing effects are no longer visible in either the density and local compressibility profiles. At lower temperatures, the interface in the density profile and the peak in the local compressibility profile can be seen to be sharper. This same behaviour was also observed for the case of LR ff LR sf interactions for solvophobicity, presented in section 6.2.4. Overall, the general behaviour for each of these state points can be seen to be the same, and hence results collected at any of these can be expected to accurately represent hydrophobic behaviour.

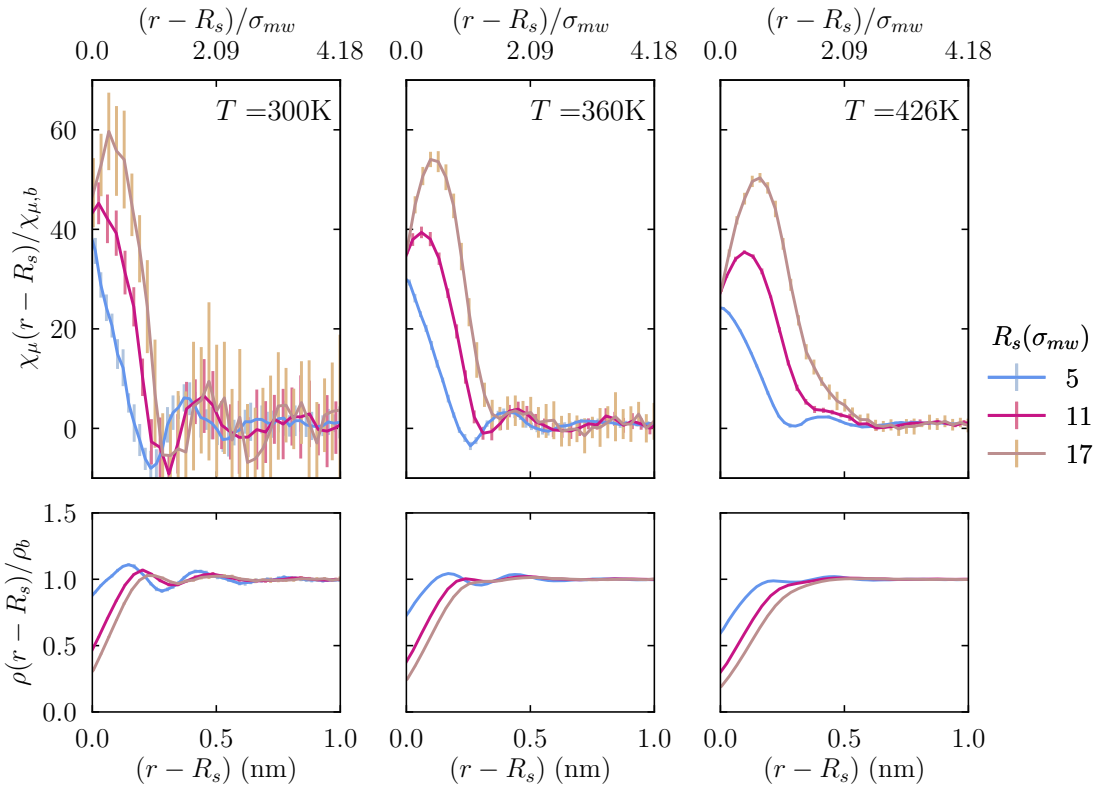

Figure 7.5: Density (lower) and local compressibility (upper) profiles, scaled by their bulk values, for mW around solutes of varying radii with $\varepsilon_{sf} = 0.0$. The temperature of the system is given in the top right of each plot. In all cases, $\beta\delta\mu = 10^{-3}$. Uncertainties were calculated as described in section 4.2.11, and in the case of the density did not exceed line width.

7.3 Effective Interface Potential Predictions

Unlike cDFT, the GCMC methods used within this chapter do not lend themselves to as thorough a study of the predictions of the effective interface potential analysis, as was performed for SR ff LR sf interactions for solvophobicity in figures 6.7 and 6.11. There are several reasons for this. Firstly, within cDFT it is possible to use fine grids for the density profile to obtain accurate results. For GCMC, it is not possible to use such fine grids when calculating the density profile according to the methods of section 4.2.10.2, for reasons including the large statistical noise which would be introduced and the unreasonable computational resource it would require. The consequence of this is that calculations of the adsorption per unit area using equation (4.1.55), which require numerical integration, have a higher uncertainty compared the cDFT. As the predictions of both ℓ_{eq} and $\chi_\mu(\ell_{eq}; R_s)$, given in equations (5.5.8) and (5.5.14) respectively, contain factors of ℓ_{eq}, their calculated values will also have a larger uncertainty. In addition, table 7.2 shows that it is not possible to distinguish ρ_l from ρ_b at $T = 426$K due to the discretisation of the density and the limited number of mW particles which can reasonably be simulated. As both the predictions of ℓ_{eq} and $\chi_\mu(\ell_{eq}; R_s)$, and the calculation of ℓ_{eq} itself from equation (2.4.20), contain factors of $\Delta\rho$, this limitation introduces further inaccuracy. Furthermore, the prediction of the behaviour of $\chi_\mu(\ell_{eq}; R_s)$ requires an accurate estimate of the correlation length of the bulk vapour, ξ, for mW. It was described in section 6.3 that an accurate prediction for this is most easily obtained numerically by considering a planar substrate. Plotting numerical results for systems very close to the drying critical point against the predictions of equation (5.5.2) permits an estimate of ξ to be obtained from the gradient. As it was not possible to study systems with planar substrates close to critical drying within the present work, an accurate estimate for ξ could not be obtained.

Any attempt to test the predictions of ℓ_{eq} and $\chi_\mu(\ell_{eq}; R_s)$ of equations (5.5.8) and (5.5.14) for mW was therefore likely to be difficult. Instead, the present work tests the simpler predictions given in equations (5.5.12) and (5.5.16), that in the limit of $R_s < R_c$ and $\varepsilon_{sf} = 0.0$, the predicted behaviour of ℓ_{eq} and $\chi_\mu(\ell_{eq}; R_s)$ reduces to $\ell_{eq} \sim \ln R_s$ and $\chi_\mu(\ell_{eq}; R_s) \sim R_s$. For $T = 426$K and $\beta\delta\mu = 10^{-3}$, the conditions used throughout most of this chapter, the length scale of capillary evaporation is $R_c \approx 0.583\mu$m. As this is far larger than the largest solute considered within the present work, $R_s = 17\sigma_{mw} \approx 4.07$nm, all solutes considered can be expected to obey these relations.

Figure 7.6(a) compares the prediction for ℓ_{eq} to data obtained from mW at $T = 426$K and $\beta\delta\mu = 10^{-3}$. ℓ_{eq} was calculated in the same way as for the LJ fluid in chapter 6, using equation (2.4.20). The adsorption was calculated by numerically integrating the density profile using the trapezium rule, and the uncertainty taken to be $\mathcal{O}(\mathrm{d}r^2)$, where d$r$ was the width of each histogram bin within the density profile. Due to the inability to distinguish the coexisting liquid density, ρ_l, from that of ρ_b given in table 7.2, and the fact that the coexisting vapour density of a water model is expected to be several orders of magnitude lower than the liquid density, $\Delta\rho$ was approximated as $\Delta\rho \approx \rho_b$.

For $R_s > 5\sigma_{mw}$, excellent agreement is found between the predictions of the effective

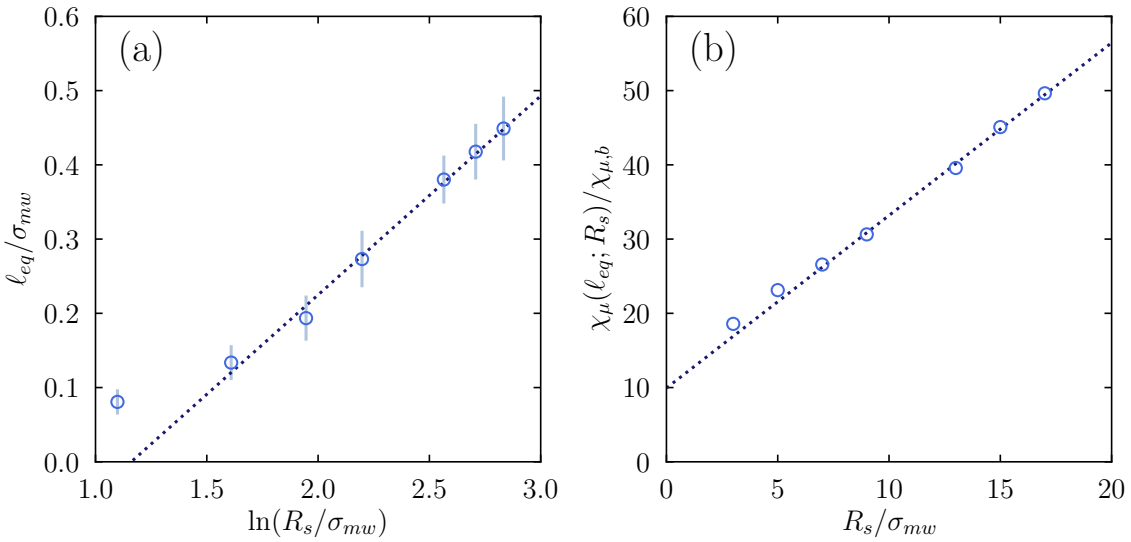

Figure 7.6: (a) Comparison of predicted growth of ℓ_{eq} with R_s, given in equation (5.5.12), for the case of $R_s < R_c$, to results obtained using GCMC simulations of mW. The uncertainty was taken to be that associated with the calculation of the adsorption, Γ. (b) Comparison of predicted growth of $\chi_\mu(\ell_{eq};R_s)$ as given in equation (5.5.16) for the case of $R_s < R_c$, to data obtained using GCMC simulations of mW. Uncertainty was calculated as described within the text, and did not exceed symbol size. In both (a) and (b), the parameters were $T = 426$K, $\beta\delta\mu = 10^{-3}$ and $\varepsilon_{sf} = 0.0$. The dotted lines are linear fits to the simulation data.

interface potential analysis and the results for ℓ_{eq} obtained from GCMC, particularly for $R_s \geq 9\sigma_{mw}$. Considering the left of figure 7.4, it can be seen that these values of R_s correspond to density profiles with clear vapour films and limited packing effects. It is interesting to note the values of ℓ_{eq} found, as even for $R_s = 17\sigma_{mw} \approx 4.07$nm, $\ell_{eq} < \sigma_{mw}$. This indicates that although regions of depleted density do form at the surface of the hydrophobic solutes, their width is very limited. It is therefore extraordinary that the predictions of the effective interface potential analysis, which specifically assumes a thick vapour film, appear to be obeyed.

Figure 7.6(b) compares the predicted relationship for $\chi_\mu(\ell_{eq};R_s)$ to the results obtained from mW for the same conditions as figure 7.6(a). In each case, $\chi_\mu(\ell_{eq};R_s)$ was taken to be the first value in the $\chi_\mu(r)$ profile for which $r > R_s + \ell_{eq}$. The uncertainty was found using the standard error, defined in equation (4.2.29), in the value of $\chi_\mu(\ell_{eq};R_s)$ between the multiple parallel simulations performed, and did not exceed the symbol size. Again, excellent agreement is found for $R_s > 5\sigma_{mw}$. This indicates that the scaling relationship predicted in equation (5.5.16) is obeyed by these hydrophobic systems.

For solvophobicity, it was noted in section 6.3 that R_s remains the dominant influence over ℓ_{eq} and $\chi_\mu(\ell_{eq};R_s)$ for a region of parameter space where $\beta\delta\mu > 0$ and $\varepsilon_{sf} > 0$. This can be seen by considering values of $R_s < 1000\sigma$ in figures 6.9(a), 6.9(b), 6.14(a) and 6.14(b). As hydrophobicity has been shown to exhibit comparable behaviour to solvophobicity throughout this chapter, it is reasonable to assume that such a region of parameter space should also exist for hydrophobicity. It is therefore plausible that all systems with $R_s > 5\sigma_{mw}$ presented

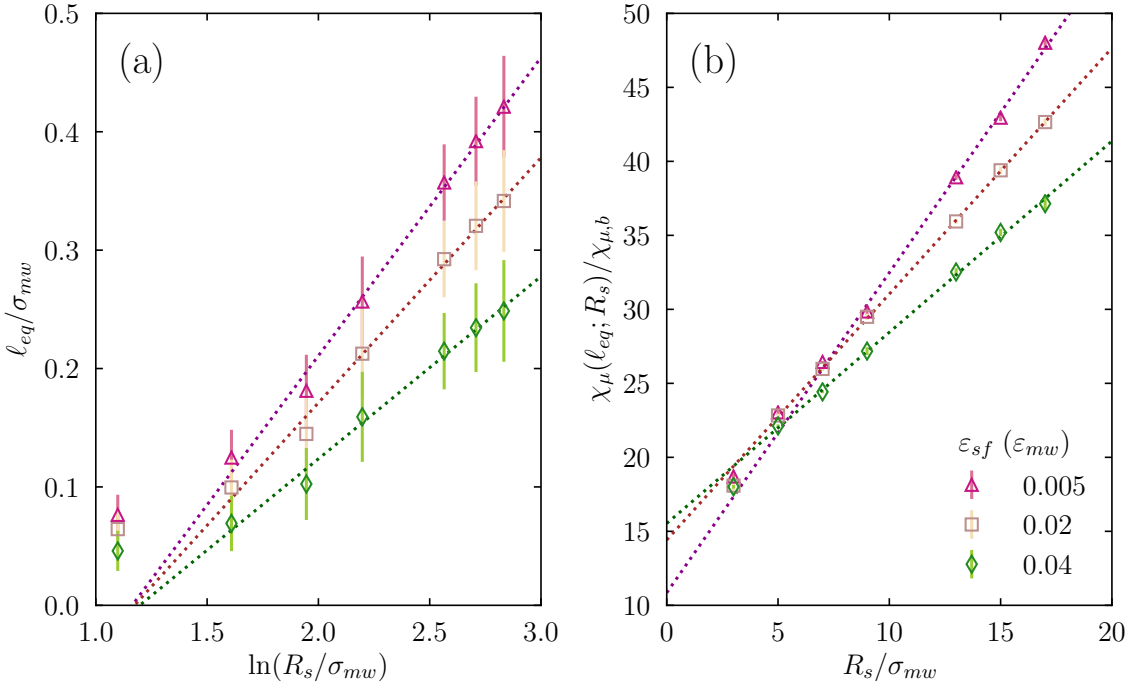

Figure 7.7: Comparison of the prediction that systems with $\varepsilon_{sf} > 0$ obey the same relationships as figure 7.6 to results obtained from GCMC for (a) ℓ_{eq} and (b) $\chi_\mu(\ell_{eq}; R_s)$. The parameters of each system were $T = 426$K and $\beta\delta\mu = 10^{-3}$, whilst ε_{sf} is given by the symbol. Uncertainty was as calculated in figure 7.6. Dotted lines are linear fits.

in figure 7.3 exhibit the scaling found for the case of $\varepsilon_{sf} = 0.0$ in figures 7.6(a) and 7.6(b).

Figures 7.7(a) and 7.7(b) test this proposition for mW at $T = 426$K and $\beta\delta\mu = 10^{-3}$ for three values of $\varepsilon_{sf} > 0.0$. In all cases, linear behaviour is found for $R_s > 5\sigma_{mw}$, in agreement with predictions. This indicates that ℓ_{eq} and $\chi_\mu(\ell_{eq}; R_s)$ are indeed predominantly influenced by R_s in this regime, in agreement with the contour plots presented for solvophobicity in section 6.3.

7.4 Form of Depleted Density Region

Throughout this chapter, the depleted density region observed in the density profiles of figures 7.3, 7.4 and 7.5 has been referred to as a vapour film. However, as was discussed in section 3.1.3 for the macroscopic regime of hydrophobicity, there is substantial debate as to whether the form of the depleted density region at the surface of a planar substrate is that of a film or 'gap', or whether it instead takes the form of 'nanobubbles'. As the density and local compressibility profiles for hydrophobic solutes presented here and for macroscopic substrates presented in [37] show little difference, it is reasonable to expect that this debate extend to solutes. Figures 7.8 and 7.9 show snap-shots of cross-sections through the centre of the simulation box for all nine solute sizes considered. For both figures 7.8 and 7.9, the temperature was held constant at $T = 426$K and the chemical potential deviation at $\beta\delta\mu = 10^{-3}$, whilst the sf attraction was taken to be $\varepsilon_{sf} = 0.0$ in the former and $\varepsilon_{sf} = 0.02\varepsilon_{mw}$ in the latter. In each cross-section, the ratio of the size of the mW particles, shown in blue, to the size of the solute, shown in purple, is to scale. The depth of each mW particle is

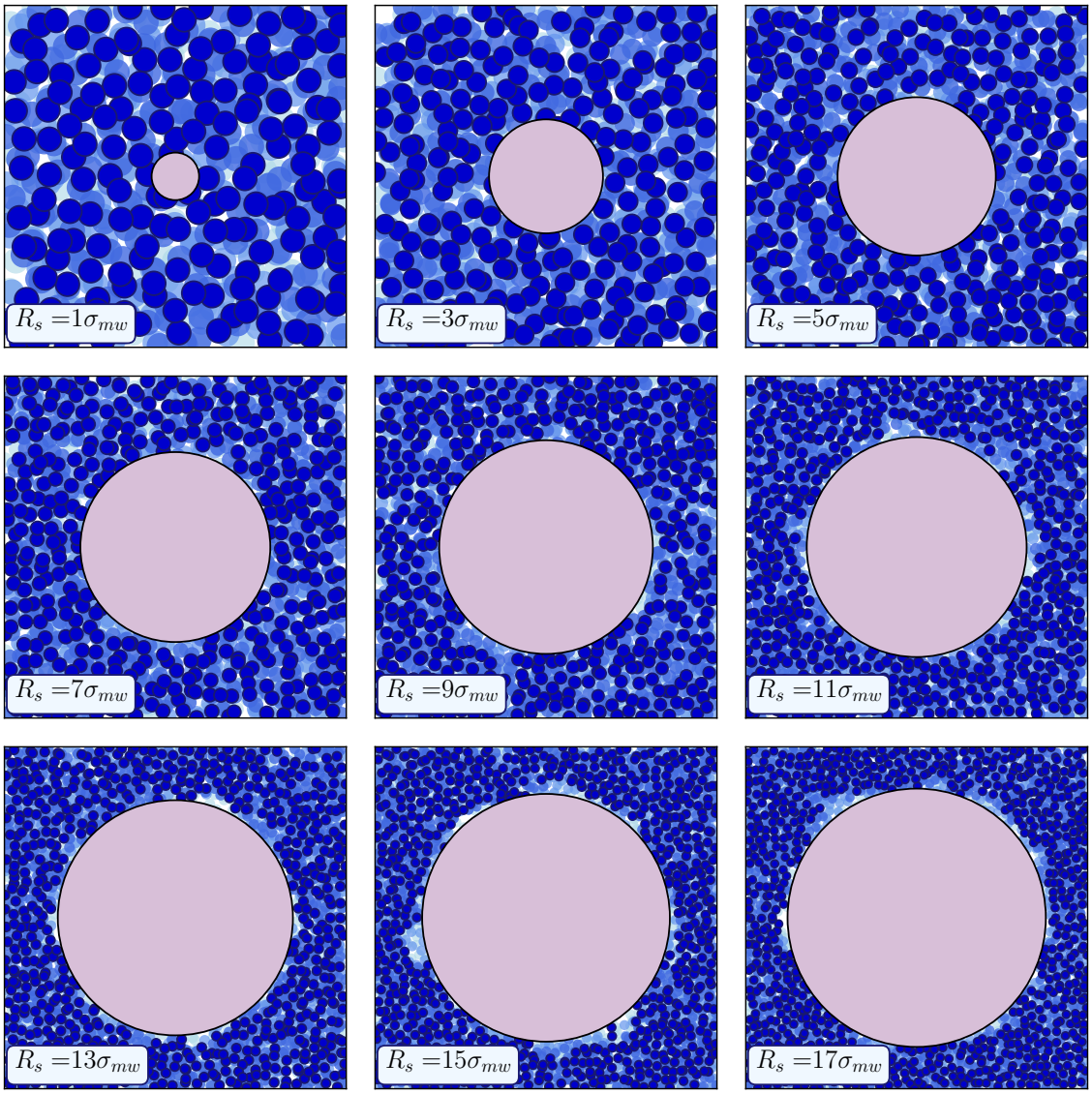

Figure 7.8: Cross-sections through centre of simulation box showing a snapshot of the positions of mW particles (blue) with respect to the solute (purple). The ratio of the size of the mW particles to the solute is to scale in each case. Darker blue mW particles represent particles closer to the foreground, whilst lighter mW particles represent those closer to the background. The parameters of each system were $T = 426$K, $\beta\delta\mu = 10^{-3}$ and $\varepsilon_{sf} = 0.0$. The radius of each solute is given in the lower left of each cross-section.

represented by the shade of blue, with lighter shades indicating particles further away.

Figures 7.8 and 7.9 support the nanobubble view for the form of the depleted density region around solutes. Considering first figure 7.8, it can be seen that for small $R_s < 5\sigma_{mw}$, there is little evidence that the hydrophobic solute disrupts the behaviour of mW particles, in agreement with the behaviour expected from the small length scale solvation regime. However, as R_s increases, small bubbles begin to appear at the surface of the solute. For $R_s = 7\sigma_{mw}$ and $R_s = 9\sigma_{mw}$, these bubbles can be observed in the lower left of the solute. They do not extend far from the surface of the solute, and appear to be limited in depth. By $R_s = 11\sigma_{mw}$, the bubbles appear to be more spread over the surface, and can be observed

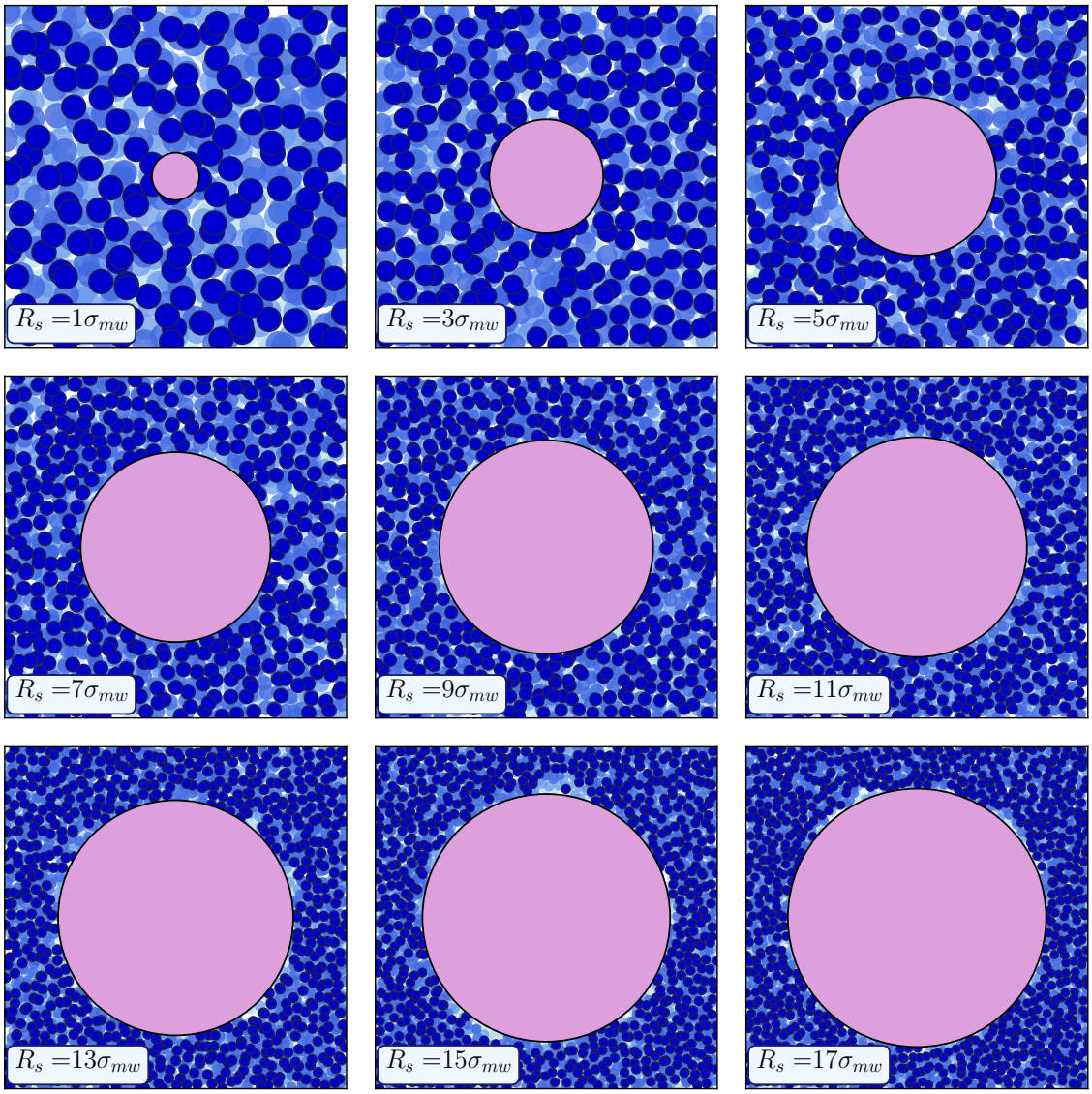

Figure 7.9: Cross-sections through centre of simulation box showing a snapshot of the positions of mW particles (blue) with respect to the solute (purple). The ratio of the size of the mW particles and solute is to scale in each case. Darker blue mW particles represent particles closer to the foreground, whilst lighter mW particles represent those closer to the background. The parameters of each system were $T = 426$K, $\beta\delta\mu = 10^{-3}$ and $\varepsilon_{sf} = 0.02\varepsilon_{mw}$. The radius of each solute is given in the lower left of each cross-section.

most clearly in the upper right of the solute. Lighter blue mW particles can be seen easily here, which indicates that these bubbles have more depth. For $R_s > 11\sigma_{mw}$, nanobubbles can be observed extensively over the surfaces of the solutes. However, these again do not extend very far from the surface of the solute. This is in agreement with the expectation that the parallel correlation length diverge more quickly than the perpendicular correlation length, in systems near to the critical drying surface phase transition. Figure 7.9 shows much the same behaviour though, as would be expected for system with larger ε_{sf}, the bubbles appear to be more suppressed.

Over the course of a simulation, these nanobubbles fluctuate in shape, location and form.

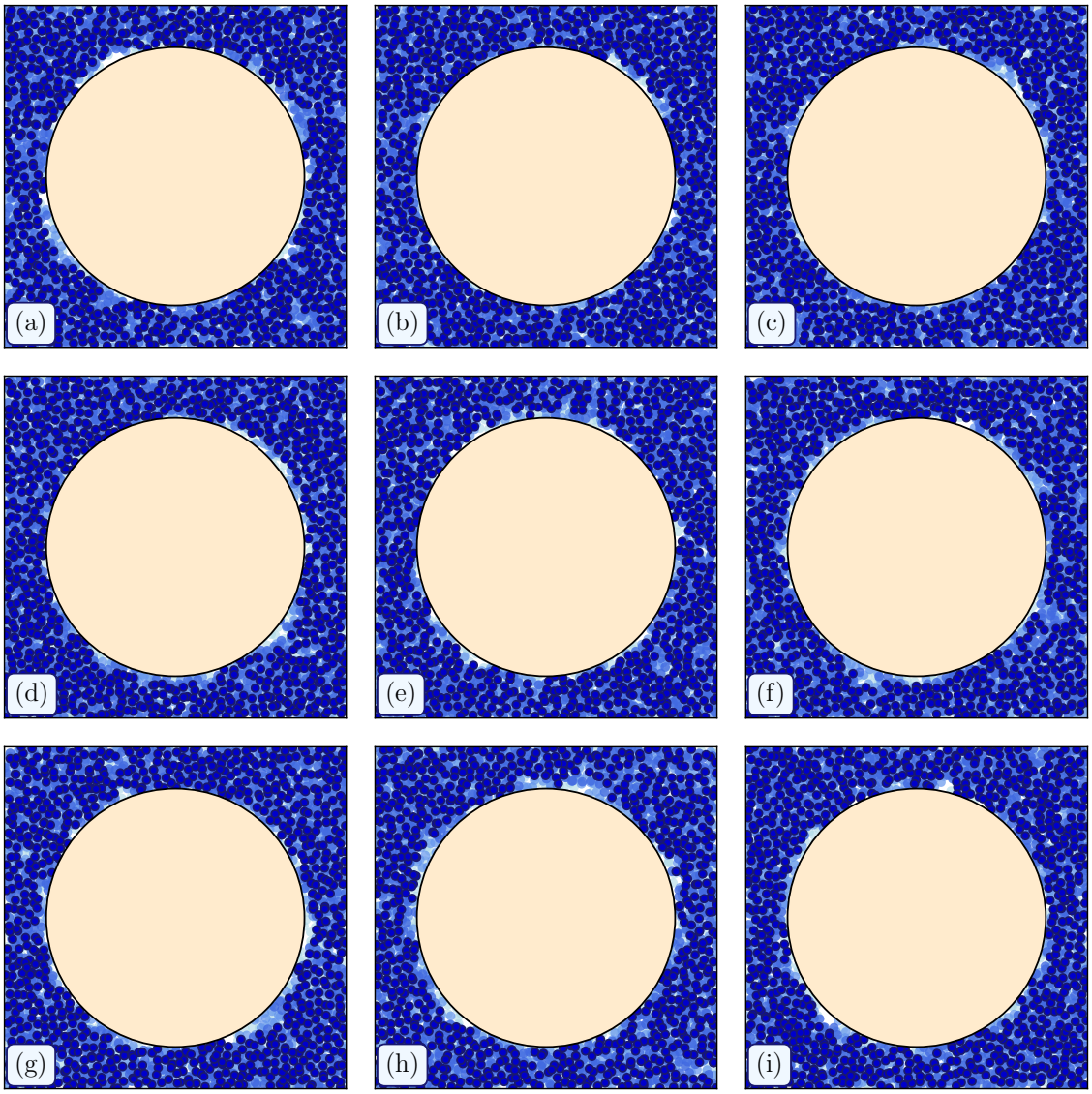

Figure 7.10: Cross-sections through centre of simulation box showing snapshots of the positions of mW particles (blue) with respect to a solute (yellow) of radius $R_s = 17\sigma_{mw}$ during the course of a simulation. The ratio of the size of the mW particles and solute is to scale in each case. Darker blue mW particles represent particles closer to the foreground, whilst lighter mW particles represent those closer to the background. The parameters of the system were $T = 426$K, $\beta\delta\mu = 10^{-3}$ and $\varepsilon_{sf} = 0.0$.

This can be seen in figure 7.10, which shows snap-shots of cross-sections for a system consisting of a solute of radius $R_s = 17\sigma_{mw}$, over the course of a simulation. As in figures 7.8 and 7.9, the temperature and chemical potential deviation were held constant at $T = 426$K and $\beta\delta\mu = 10^{-3}$ respectively. The sf fluid attraction was $\varepsilon_{sf} = 0.0$. Whilst in all snap-shots nanobubbles are clearly visible, in some they are more widespread than others. For example, in figures 7.10(f) and 7.10(h), the nanobubbles can be seen to cover the surface of the solute substantially, indicating a somewhat film-like depleted density region. In contrast, in figures 7.10(b) and 7.10(d), the nanobubbles are far more localised. This variation highlights the large density fluctuations present around hydrophobic solutes. Whilst these nanobubbles grow and shrink frequently, on average they lead to a region of depleted density at the surface

of the solute, as indicated by the corresponding density profile of this system, shown in figure 7.3.

The emergence of nanobubbles on the surface of a planar substrate in contact with a LJ fluid has been reported previously in simulations by Evans et al. [32]. These were found to cover large areas of the surface, however to extend only a few fluid particle diameters perpendicularly, in agreement with the experimental AFM findings for water by Tyrrell and Attard [88] and Steitz et al. [103]. The results presented within this thesis suggest that these nanobubbles are also present around hydrophobic solutes of $R_s > 1\text{nm}$.

7.5 Discussion

Within this chapter, GCMC simulations have been used to study hydrophobic systems with the purpose of evaluating the validity of postulate 1 and 2 presented in chapter 1. Density and local compressibility profiles around solutes of nine different radii have been presented, for a range of parameters $(\beta\delta\mu, \varepsilon_{sf}, T)$, and several of the predictions of the effective interface potential analysis for systems with SR ff LR sf interactions have been tested. In addition, the form of the depleted density region around solutes has been considered, and compared to the forms reported at planar substrates in experiment [88, 103].

All results presented within this chapter support postulate 1. The density and local compressibility profiles presented for solutes in figure 7.3 have near identical forms to those found at planar substrates by Evans and Wilding [23] for the water model SPC/E, indicating that hydrophobicity on microscopic length scales behaves in the same way as hydrophobicity on macroscopic length scales. Figures 7.4, 7.6 and 7.7 provide evidence that microscopic hydrophobic systems obey the predictions of the effective interface potential, and are therefore influenced by a drying critical point. Evans and Wilding [23] provided evidence that macroscopic hydrophobic systems are also influenced by a drying critical point. Combined, these results are strong evidence in support of the mechanism underlying hydrophobicity on microscopic and macroscopic length scales being a drying surface critical point.

Although the values of R_s investigated for hydrophobicity within this chapter differ from those investigated for solvophobicity in chapter 6, similar forms of the density and local compressibility profiles have been observed in each case. These forms have also been found to exhibit similar behaviour when varying the temperature and chemical potential deviation. Furthermore, evidence provided in sections 7.3 and 6.3 supports both hydrophobicity and solvophobicity being related to a drying critical point. Overall, this is overwhelming evidence in favour of postulate 2, that hydrophobicity is no more than a specific case of solvophobicity. This suggests that all qualitative conclusions drawn in chapter 6 for solvophobicity, should be equally applicable to hydrophobicity. Of course, quantitative conclusions drawn in chapter 6, for example that the effects of the drying critical point in solvophobic systems is only felt when $R_s > 20\sigma$, do not apply to hydrophobicity.

The study presented within this chapter has been limited both by computational resource and FS effects. It has not been possible to test many of the predictions of section 5.5 due to the limited systems sizes which could reasonably be simulated, the onset of premature

drying in systems with planar substrates, and due to the inaccuracies introduced through limited knowledge of the precise values of ρ_v, ρ_l, ξ, as was outlined in section 7.3. Whilst it would be pertinent to test more of the predictions of the effective interface potential analysis, particularly in the planar limit, there is no reason to believe that the conclusions drawn here would change. These conclusions are therefore expected to be accurate, despite the limitations within the present study.

Finally, it is worth returning to the observation made in section 6.4, that density fluctuations in systems with solutes of similar size ratios of biomolecules to water molecules are largely uninfluenced by changes in local conditions. It has been shown in figure 7.4 that varying $\beta\delta\mu$ has very little influence on the local compressibility. Varying the temperature by over 100K in figure 7.5 can be seen to only marginally influence the local compressibility. Increasing the sf attraction between the solutes and water can be seen to have a larger impact on the local compressibility in figure 7.3, as can varying R_s. Hence, whilst changes in local thermodynamic conditions do not appear to have much influence on the local density fluctuations, changes in geometric or solute chemical conditions do. This is interesting for several reasons. Firstly, if a uniform hydrophobic polymer chain partially collapses, part of the chain will then have a larger physical size compared to the stretched parts, and also a different sf attraction strength. From the results presented here, these two effects can be expected to enhance local density fluctuations in the collapsed region of the chain, which may facilitate further collapse. These observations are in agreement with previous findings [30, 98]. Secondly, topology and chemical heterogeneity have been widely reported to be influential in many biological processes, such as protein folding [73]. Although several studies have investigated density fluctuations in the processes mentioned [30, 31, 98], the measures of density fluctuations the authors used did not include the spatial information that the local compressibility offers. A study of the changes in the local compressibility during the hydrophobic polymer collapse or biological assembly could therefore be very interesting.

Chapter 8

Comparison of Measures of Fluctuations on the Approach to Critical Drying

In section 2.5, three measures of local density fluctuations, the local compressibility χ_μ, the local thermal susceptibility χ_T, and the reduced density χ_*, were introduced. The first two of these were then shown to be related to one another on the approach to critical drying, through equation (5.3.8) in the case of a planar substrate, and equation (5.3.17) in the case of a curved substrate or solute. Specifically, this was predicted to be the case if the gap exponent satisfied $\Delta > 1$. Whilst this was confirmed to be the case for LR ff LR sf interactions, it was found that $\Delta = 1$ for the case of SR ff LR sf interactions. As a case of the edge of the applicability of the relation, a full microscopic analysis was required to confirm that systems with SR ff LR sf interactions obey the expected relations. Such an analysis was presented in section 5.5, and confirmed that equations (5.3.8) and (5.3.17) were expected to be obeyed in the case of SR ff LR sf interactions.

After this, all further results considered only χ_μ. This is justified if a relationship does indeed exist between χ_μ and χ_T in the limit of critical drying, as knowledge of one effectively gives knowledge of the other. Equation (2.5.3) shows that χ_* is defined with respect to χ_μ and χ_T, and hence knowledge of χ_μ alone then also gives χ_*. However, as yet the relationships in equations (5.3.8) and (5.3.17) have not been tested. Furthermore, no justification has been made for the choice of χ_μ, as opposed to χ_T, utilised extensively in chapters 6 and 7. Within this chapter, the choice of χ_μ is justified, and the predicted relations between χ_μ and χ_T for both planar substrates and solutes verified.

8.1 State Points and Bulk Properties

Within this chapter, systems with SR ff LR sf interactions are used to test the accuracy of the relations presented in equations (5.3.8) and (5.3.17). With a gap exponent of $\Delta = 1$, these systems are expected to be on the edge of the applicability of these relations. If the relations are obeyed in such a marginal case, then they can then also be expected to be

obeyed in all systems with $\Delta > 1$, for example, those with LR ff LR sf interactions. All results within this chapter were collected using cDFT as described in section 4.1. Table 8.1 presents the bulk properties of the state points for systems with SR ff LR sf interactions at $k_{\mathrm{B}}T/\varepsilon = 0.775 k_{\mathrm{B}}T_c/\varepsilon = 1.0225672588$ considered within this chapter. The bulk density, ρ_b, was found in the same way as in section 6.1, whilst $\chi_{\mu,b}$ was found using equation (4.1.59). $\chi_{T,b}$ was found by performing a numerical derivative of ρ_b with respect to temperature within cDFT, whilst $\chi_{*,b}$ followed naturally from equation (2.5.3).

Table 8.1: Bulk properties of the state points for a system with SR ff LR sf interactions at $k_{\mathrm{B}}T/\varepsilon = 0.775 k_{\mathrm{B}}T_c/\varepsilon = 1.0225672588$ considered within this chapter.

$\beta\delta\mu$	$\rho_b\sigma^3$	$\varepsilon\sigma^3\chi_{\mu,b}$	$\varepsilon\sigma^3\chi_{T,b}/k_{\mathrm{B}}$	$\sigma^3\chi_{*,b}$
10^{-3}	0.5980277945	0.1788896299	-0.8757469527	2.1734350790
10^{-4}	0.597863029	0.1791754507	-0.8765597781	2.1753526845
10^{-5}	0.597846538	0.1792040971	-0.8766412340	2.1755448811
10^{-6}	0.5978448887	0.1792069624	-0.8766493631	2.1755640868

8.2 Comparison of Profile Behaviour Near to Critical Drying

By definition, the behaviour of χ_μ and χ_T is dependent on the behaviour of the density profile. Near to critical drying, the density profile takes the form of a depleted density region or vapour-like film, with a liquid-vapour like interface with the bulk. In sections 6.2 and 7.2, it was found that increasing the chemical potential, μ, moved this interface towards the surface of the solute or planar substrate - a behaviour rationalised by the fluid moving further from liquid-vapour coexistence. The resultant derivative, χ_μ, then took the form of a smooth positive peak. Using similar reasoning, the effect of increasing the temperature, T, should be to move the fluid towards liquid-vapour coexistence, and hence the liquid-vapour interface away from the surface of the solute or planar substrate. In this case, the derivative is also expected to take the form of a smooth peak, however is now expected to be negative. χ_T is therefore expected to follow a similar shape and form to χ_μ, but with opposite sign, as would be expected from the relationships predicted from the effective interface potential analysis in equations (5.3.8) and (5.3.17). By nature of its definition in equation (2.5.3), χ_* should also take this form and be positive. It should be noted that, because the behaviour of changing (μ, T) is to move the liquid-vapour interface in opposite directions, the peaks in χ_μ and χ_T are not expected to align exactly.

Figure 8.1 compares $\chi_\mu(z)$, $\chi_T(z)$ and $\chi_*(z)$ for a system with SR ff LR sf interactions and a planar substrate at parameters $T = 0.775T_c$, $\beta\delta\mu = 10^{-3}$ and $\delta\varepsilon_{sf} = 0.0$. The latter of these parameters for the case of SR ff LR sf interactions equates to considering a hard substrate. Each profile is scaled by its bulk value in the main figure, whilst the inset shows the dimensionless raw profiles. The density profile, scaled by its bulk value, is also given in the lower figure for comparison. From the raw profiles within the inset, it is clear that the expected behaviour is observed. χ_μ and χ_T show very similar forms with opposite sign, whilst χ_* features a smooth peak and is positive. In terms of magnitude, χ_μ and χ_T appear similar, whilst χ_* is much larger. However, when scaled by their bulk value, χ_μ can be seen to vary far more than χ_T or χ_*. This indicates that χ_μ is the most sensitive measure of density

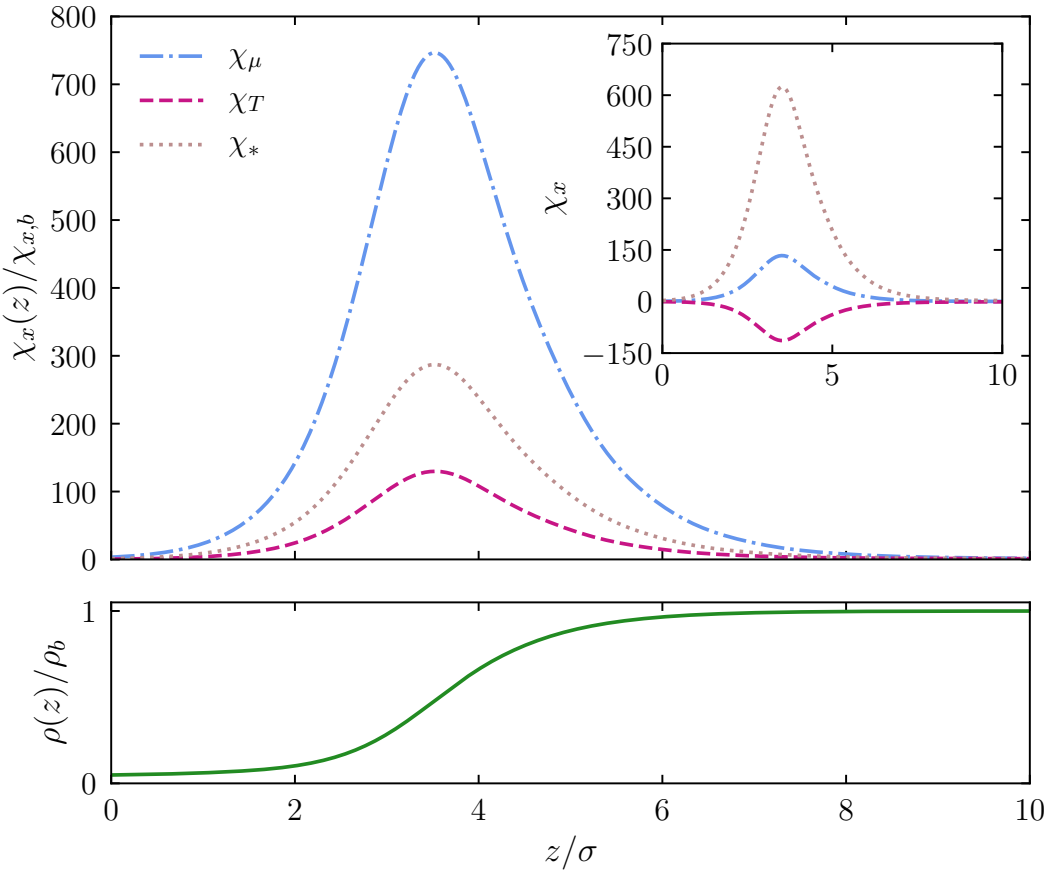

Figure 8.1: Fluctuation (upper) and density (lower) profiles, scaled by their bulk values, for a system with a hard planar substrate and SR ff LR sf interactions. The measure of density fluctuation is denoted as χ_x, where $x = \mu, T, *$. The parameters for the system were $T = 0.775T_c$, $\beta\delta\mu = 10^{-3}$ and $\delta\varepsilon_{sf} = 0.0$. Raw fluctuation profiles are given in the inset, and have been made dimensionless by multiplying by $\varepsilon\sigma^3$, $\varepsilon\sigma^3/k_\mathrm{B}$ and σ^3 in the cases of χ_μ, χ_T and χ_* respectively.

fluctuations near to critical drying, and hence justifies its use in previous chapters.

It was found in chapter 6 that χ_μ took the same form around solutes as it did at planar surfaces, which is expected as the density profile also takes the same form in both cases. As χ_T and χ_* show the same behaviour as χ_μ, it is natural to assume that they also take the same forms around solutes as they do at planar surfaces. Increasing the curvature of the substrate acts to move the system away from the drying critical point, and thus the liquid-vapour interface in the density profile closer to the surface of the solute. The effect of curvature on the fluctuation profiles should therefore be to move the peaks closer to the surface of the solute, and to reduce their magnitude.

Figure 8.2 compares the fluctuation and density profiles for two radii of solutes for the same parameters as in figure 8.1. The two radii of solutes shown were chosen such that they demonstrated the behaviour when $R_s = 10^2\sigma < R_c$ and $R_s = 10^4\sigma > R_c$, where $R_c = 2\gamma_{lv}/\delta\mu\Delta\rho$ is the length scale of capillary evaporation discussed previously and was previously discussed in chapter 6 to separate regimes in which curvature is expected to influence the behaviour of the density fluctuations near to critical drying ($R_s < R_c$) and in which it is not ($R_s > R_c$). The dimensionless raw profiles are shown on a linear scale in the inset, whilst

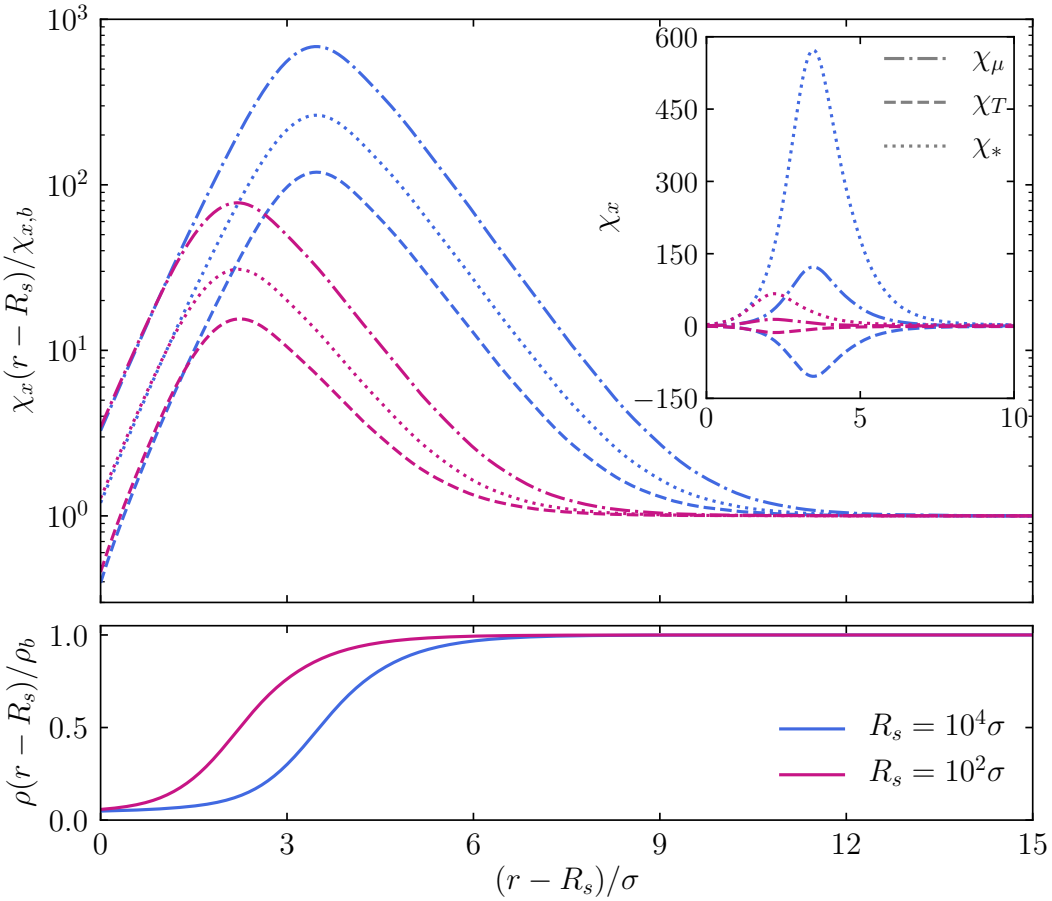

Figure 8.2: Fluctuation (upper) and density (lower) profiles, scaled by their bulk values, for two hard solutes of radius $R_s = 10^2\sigma$ (pink) and $R_s = 10^4\sigma$ (blue) in systems with SR ff LR sf interactions. The measure of density fluctuation is denoted as χ_x, where $x = \mu, T, *$. The parameters for each system were $T = 0.775T_c$, $\beta\delta\mu = 10^{-3}$ and $\delta\varepsilon_{sf} = 0.0$. Raw fluctuation profiles are given in the inset and have been made dimensionless by multiplying by $\varepsilon\sigma^3$, $\varepsilon\sigma^3/k_\mathrm{B}$ and σ^3 in the cases of χ_μ, χ_T and χ_* respectively.

in the main figure, the profiles are shown scaled by their bulk values on a logarithmic scale. For comparison, the density profiles for each radii of solute, scaled by their bulk values, are shown in the lower figure.

Considering first the case of $R_s = 10^4\sigma$, the influence of curvature can be seen to be muted, as expected for a solute which falls into the curvature independent scaling regime. The magnitude of the fluctuations is reduced only slightly compared to those found at the equivalent planar substrate in figure 8.1, and the peak is moved only marginally closer to the surface of the solute. For $R_s = 10^2\sigma$, the curvature of the substrate can be seen to have a much larger influence over the behaviour of the density fluctuations. Whilst the general form of the profiles remains unchanged as expected, the magnitude of each measure is depleted substantially compared to $R_s = 10^4\sigma$, and the peak in each profile moved far closer to the surface of the solute. As in the planar case, χ_μ can be seen to vary the most from its bulk value for both radii of solutes.

8.3 Effective Interface Potential Predictions

The effective interface potential analysis predicts that the ratio of χ_T to χ_μ follow the specific forms given in equations (5.3.8) and (5.3.17) for the cases of planar and curved substrates respectively. These are repeated here for convenience. For a planar substrate, it is expected that

$$\frac{\chi_T(\ell_{eq})}{\chi_\mu(\ell_{eq})} \sim -\frac{\partial \mu_{co}}{\partial T} \tag{8.3.1}$$

whilst for a curved substrate or solute, the expectation is

$$\frac{\chi_T(\ell_{eq}; R_s)}{\chi_\mu(\ell_{eq}; R_s)} \sim \left(\frac{2}{R_s} \frac{\partial}{\partial T} \left(\frac{\gamma_{lv}}{\Delta\rho} \right) - \frac{\partial \mu_{co}}{\partial T} \right) \tag{8.3.2}$$

Defining the left hand side of each relation as the 'ratio' and the right as the 'expected', the disagreement in each relation, δ_e, can be defined as

$$\delta_e = \frac{|\text{Ratio} - \text{Expected}|}{|\text{Expected}|} \tag{8.3.3}$$

These relations are valid in the vicinity of the drying critical point, therefore δ_e can be expected to reduce as the drying critical point is approached. For the case of SR ff LR sf interactions, this drying critical point is expected to occur at the parameters ($\beta\delta\mu = 0.0, \delta\varepsilon_{sf} = 0.0, R_s = \infty$). The gradient of the coexistence curve was found using the program by Wilding [148], previously used in section 6.1, and was evaluated to be

$$\left. \frac{\partial \mu_{co}}{\partial T} \right|_{T=0.775T_c} = 0.8339999979(5) k_{\mathrm{B}}^{-1}$$

Figure 8.3(a) compares δ_e for a planar substrate in systems with varying $\beta\delta\mu$ and $\delta\varepsilon_{sf}$. As the drying critical point parameters are approached, δ_e can be seen to tend towards zero, which confirms that the relation given in equation (8.3.1) is obeyed in the vicinity of the drying critical point. Very close to critical drying, for example when $\beta\delta\mu = 10^{-5}$ and $\delta\varepsilon_{sf} = 0.0$, δ_e appears to increase. For such parameters, χ_μ and χ_T are expected to be thousands of times their bulk values, and rapidly varying. It should therefore be noted that an increase in δ_e very close to the drying critical point does not imply a break down in the relation, but instead highlights the difficulty in accurately evaluating the large and rapidly varying density fluctuations. As $\delta\varepsilon_{sf}$ is increased, δ_e also increases. By $\delta\varepsilon_{sf} = 0.2$, $\delta_e > 0.12$ for all $\beta\delta\mu$ considered, and hence the relation presented in equation (8.3.1) is no longer obeyed well. This is to expected, as it was shown in figure 6.11 that the drying critical point has limited influence in systems with SR ff LR sf interactions when $\delta\varepsilon_{sf} > 0.2$.

Figure 8.3(b) compares δ_e for systems with solutes of varying size at $\beta\delta\mu = 10^{-4}$ for two values of $\delta\varepsilon_{sf}$. This value of $\beta\delta\mu$ was chosen as figure 8.3(a) shows that it is suitably close to the drying critical point to give low δ_e in the planar limit, however far enough away to allow for accurate numerical evaluation of the density fluctuations. Considering the relation in equation (8.3.2), and the behaviour shown in figure 8.2, two regimes of δ_e can be expected to exist. For large R_s, the second curvature independent term in equation (8.3.2) is expected to

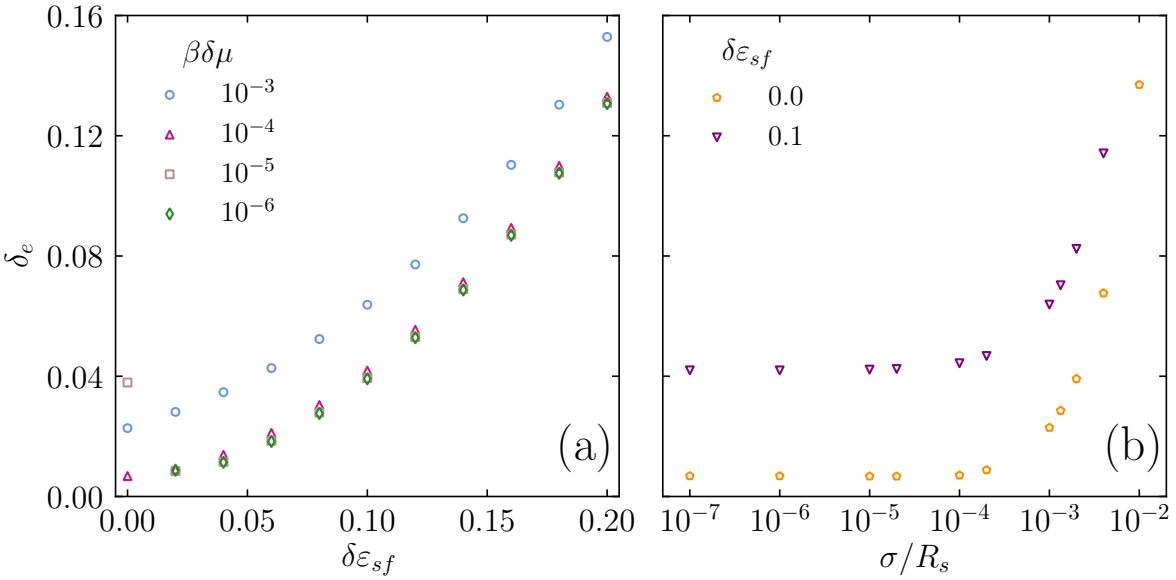

Figure 8.3: Variation in δ_e on the approach to critical drying in a system with SR ff LR sf interactions and (a) a planar substrate or (b) a curved substrate. In both cases, $T = 0.775T_c$, whilst in (b), $\beta\delta\mu = 10^{-4}$.

dominate. In this case, equation (8.3.2) should reduce to equation (8.3.1) and hence δ_e in this regime should be constant and similar to the value for the equivalent parameters $(\beta\delta\mu, \delta\varepsilon_{sf})$ in figure 8.3(a). For small R_s, the first curvature dependent term in equation (8.3.2) can be expected to dominate.

This does appear to be the case in figure 8.3(b). For $R_s > 10^4\sigma$ for both $\delta\varepsilon_{sf} = 0.0$ and $\delta\varepsilon_{sf} = 0.1$, δ_e can be seen to be fairly constant, and similar to the values for the planar substrate in figure 8.3(a). For $R_s < 10^4\sigma$, δ_e can be seen to increase, becoming particularly large when $R_s = 10^2\sigma$. To some extent, large δ_e is not unexpected at such small values of R_s. Firstly, these values of R_s represent systems very far from the drying critical point, where equation (8.3.2) cannot be expected to be obeyed. Secondly, from the left of figure 6.11, it can be seen that the predictions of the effective interface potential analysis are not well obeyed for small values of R_s, particularly as $\delta\varepsilon_{sf}$ is increased. It is worth noting the value of R_s for which δ_e changes behaviour in figure 8.3(b) corresponds well to the length scale of capillary evaporation, which for $\beta\delta\mu = 10^{-4}$ is $R_c = 9134\sigma$. For $\delta\varepsilon_{sf} = 0.0$ this is to be expected, as it was previously shown in section 6.2.3 that R_c in this case separates radii of solutes for which the solvophobic behaviour is curvature dependent and independent. However, the behaviour for $\delta\varepsilon_{sf} = 0.1$ in figure 6.14(a) suggests that curvature independent behaviour should begin for smaller values of R_s, and hence it is surprising that δ_e becomes curvature independent also at R_c when $\delta\varepsilon_{sf} = 0.1$.

8.4 Discussion

Within this chapter, it has been confirmed that the mesoscopic thermodynamic relations predicted to exist between χ_μ and χ_T on the approach to the drying critical point in section 5.3 are indeed obeyed. This is true for both planar substrates, for which the relation is given in equation (5.3.8), and for curved substrates, for which the relation is given in equation

(5.3.17). This confirms that χ_μ, χ_T and by nature of equation (2.5.3) χ_*, diverge in the same way on the approach to the drying critical point. Any study of the influence of critical drying on hydrophobicity and solvophobicity is therefore free to choose any of these as the measure of density fluctuations, as knowledge of one is equivalent to knowledge of all.

Within this study, χ_μ was chosen, in part due to its ease of access within the GC ensemble. Comparing the profiles of χ_μ, χ_T and χ_* for planar and curved substrates given in figures 8.1 and 8.2, it can be seen that this choice is also justified by the larger variation χ_μ shows from its bulk value than χ_T or χ_*. However, it should be noted that the magnitude of χ_T depends heavily on the definition of the thermal de Broglie wavelength, Λ, which was discussed in section 2.2 [71]. Within the present work, and is standard for cDFT and simulation studies, this has been defined as $\Lambda = \sigma$ and $\Lambda = \sigma_{mw}$ when using cDFT and GCMC respectively, and as such χ_T shows less variation from its bulk value than χ_μ. However, if the temperature dependence of Λ is maintained, such that $\Lambda \equiv \Lambda(T)$, it has been shown by Eckert at. al. [71] that χ_T varies significantly more from its bulk value than χ_μ. Whilst both conventions are valid, the simplest and most commonly used is the one adopted within the present work, and hence the results presented within this thesis are the most relevant to the majority of studies. It should also be noted that the relationships predicted between χ_μ and χ_T are expected to be valid in either convention.

Chapter 9

Conclusions

Hydrophobicity and solvophobicity present in many ways. Around both solutes and surfaces in contact with fluids near to liquid-vapour coexistence, regions of depleted density, colloquially referred to as vapour films, have been shown both within this thesis and previous work [6, 9, 22–27] to emerge. These regions are associated with enhanced density fluctuations, and it has been the purpose of this thesis to understand the physical origin of these. Doing so requires a measure of density fluctuations which allows for their magnitude and spatial location with respect to the solute or surface to be understood. Within this thesis, the measure of choice for this was the local compressibility, $\chi_\mu(r)$, which was defined in equation (2.5.1).

It was proposed in chapter 1 that enhanced density fluctuations within hydrophobic and solvophobic systems were related to a drying surface critical point. This hypothesis has been tested in three ways. Firstly, an effective interface potential analysis was performed in chapter 5, to anticipate how systems close to this critical point should be expected to behave. To quantify this behaviour, two measures were used: the equilibrium width of the vapour film, ℓ_{eq}, and the the magnitude of the local compressibility at ℓ_{eq}, $\chi_\mu(\ell_{eq}; R_s)$. The validity of the predictions of chapter 5 were then evaluated for solvophobic systems consisting of solutes and planar surfaces in contact with a LJ fluid in chapter 6 using cDFT. Systems encompassing all parameters identified in chapter 5 as influencing behaviour near critical drying - the radius of the solute, R_s, the deviation of the chemical potential of the fluid from its value at coexistence, $\delta\mu$, and the magnitude of the attraction felt between the fluid and solute/substrate, ε_{sf} - were explored. The validity of the predictions for the behaviour of ℓ_{eq} and $\chi_\mu(\ell_{eq}; R_s)$ in hydrophobic systems were investigated in chapter 7 using GCMC of a simple water model, mW. In contrast to cDFT, GCMC is far more computationally demanding, which limited the range of parameters which could be considered.

This thesis concludes by returning to postulates in chapter 1 and assessing their validity in light of the results presented.

Postulate 1

The physical mechanism which underlies hydrophobicity is a surface critical point called drying, and it is this mechanism which relates hydrophobicity on the microscopic and macroscopic length scales.

Within chapter 7 only solutes were considered. Because of this, the present work was limited in the number of relationships identified in chapter 5 it could verify for hydrophobicity. For small hard solutes, which equated to $\delta\varepsilon_{sf} = 0$, the effective interface potential analysis predicted that $\ell_{eq} \sim \ln R_s$ and $\chi_\mu(\ell_{eq}; R_s) \sim R_s$. This was tested in figure 7.6, where excellent agreement was found. Such relationships were also predicted to remain valid for small $\delta\varepsilon_{sf}$, which was shown to be true in figure 7.7. Chapter 5 predicted that these systems should depend little on $\delta\mu$, which was confirmed in figure 7.4. All predictions of chapter 5, which could reasonably be tested using the methods utilised within this thesis, were therefore found to be obeyed by hydrophobic systems. This is clear evidence that the mechanism underlying hydrophobicity is indeed a drying surface critical point.

Although only solutes were considered here, it is possible to examine the relation between the behaviour of hydrophobicity on the microscopic (solute) and macroscopic (planar surface) length scales, due to previous work by Evans and Wilding [23]. Their study considered both density and local compressibility profiles of the SPC/E water model confined within a slit with smooth planar surfaces. For most values of surface-water attraction considered in [23], the surfaces could be considered non-interacting, and hence each thought of as a single smooth planar surface. Both the density and local compressibility profiles of Evans and Wilding's study [23] show near identical forms to those presented in figure 7.3 for solutes. Evans and Wilding's study specifically related the hydrophobic behaviour observed at planar surfaces to a critical drying transition. This is clear evidence that the both microscopic and macroscopic hydrophobicity is related to the drying critical point.

Whilst all evidence presented within this thesis, and evidence presented in previous studies [23], supports the postulate, it may be pertinent to test more of the predictions of chapter 5 before formally concluding it to be valid. For example, investigating the accuracy of the predicted behaviour specific to a planar substrate, which was presented in section 5.5.1, would definitively prove whether macroscopic hydrophobicity is related to critical drying, and would quantitatively relate hydrophobicity of solutes and surfaces. Such a study is likely to be very demanding and plagued by FS effects.

All results for hydrophobicity presented within this thesis were obtained using molecular simulation of a particular water model, and hence it is sensible to ask how well they can be expected to describe physical phenomenon. The water model used, mW, is well documented to accurately describe the structure of water at ambient conditions, and to outperform other popular water models when reproducing the liquid-vapour surface tension [132], both of which are properties expected to be important in studies of hydrophobicity. However, the majority of results presented in chapter 7 were not obtained at ambient conditions, but instead at a higher temperature. This temperature was chosen to reflect the ratio of ambient temperature to the temperature of the bulk critical point for water, $T/T_c \approx 0.46$. Figure 7.2(b) justifies

this, as it can be seen that when both the density and temperature of the liquid-vapour coexistence curves of mW and water are scaled by their bulk critical values, the coexistence curves of water and mW collapse onto one another. The results presented within this thesis were therefore gathered at a state point of mW which corresponded to the state point for water at ambient conditions. In addition, limited results for mW were obtained at ambient conditions, and compared to those obtained at higher temperatures in figure 7.5. Very similar behaviour is observed at all temperatures. Considering all of this, it is concluded that the results presented within this thesis accurately characterize the hydrophobic behaviour of mW near ambient conditions, and can be expected to reasonably describe the hydrophobic behaviour of real water under similar conditions.

Postulate 2

Hydrophobicity is simply a specific case of solvophobicity, and the mechanism underlying both is a drying critical point.

Chapter 6 tested almost all of the predictions of the effective interface potential analysis for the case of solvophobicity using cDFT, and found excellent agreement. Figures 6.7 and 6.11 showed that the predicted behaviour of ℓ_{eq} and $\chi_\mu(\ell_{eq}; R_s)$ is obeyed for a wide range of parameters, whilst contour plots in figures 6.9 and 6.14 provided a visual understanding of the role of individual parameters in solvophobicity. Specific predictions, for example that for $R_s > R_c$, where R_c is the length scale of capillary evaporation, it should not be possible to distinguish behaviour of solutes from that of a surface, were also confirmed. Chapter 6 provided a wealth of evidence that solvophobicity on both microscopic and macroscopic length scales is related to a drying critical point.

As all predictions of chapter 5 tested for hydrophobicity were also obeyed, it is highly likely that hydrophobicity and solvophobicity are both influenced by critical drying. Furthermore, the density and local compressibility profiles for hydrophobicity presented in section 7.2 and for solvophobicity in section 6.2 exhibit remarkably similar behaviour, in form and also when varying R_s and ε_{sf}. Because of this, it can be concluded that hydrophobicity is simply a specific case of solvophobicity, and hence the postulate is valid. The results presented in chapter 6 for solvophobicity then serve as further evidence in support of postulate 1.

The results presented to validate the postulates specifically refer to systems with SR ff LR sf interactions, which best represent those expected in computational studies. It was highlighted in section 2.4.5 that the range of ff and sf interactions is important for determining firstly whether the drying transition is critical, and secondly for identifying its location. Experimental systems are expected to have LR ff LR sf interactions, and whilst these systems are also expected to undergo critical drying, the conditions for the drying critical point are not the same as in the case of SR ff LR sf interactions. Because of this, all predictions of chapter 5 investigated for solvophobic systems with SR ff LR sf interactions in chapter 6 were also verified for systems with LR ff LR sf interactions. Excellent agreement was again found, and hence the conclusions drawn from the postulates within this thesis can be expected to be applicable to experimental conditions.

During the effective interface potential analysis of chapter 5, it was found that the local compressibility, χ_μ, and the local thermal susceptibility, χ_T, were related to one another in the vicinity of the drying critical point. Explicitly, equations (5.3.8) and (5.3.17) for planar and curved substrates respectively predicted that χ_μ and χ_T diverge in the same way on the approach to critical drying. Subsequent analysis within chapter 5 suggested that these relations should be obeyed by systems with both SR ff LR sf and LR ff LR sf interactions. Within chapter 8, these predictions were tested using cDFT of systems with SR ff LR sf interactions, and excellent agreement was found for systems very near to the drying critical point.

It has already been noted within this chapter that future investigations should consider testing the validity of the predictions of chapter 5 for planar hydrophobic substrates. In addition to this, there are many possible directions for future study. For example, within this thesis, evidence has been presented in chapter 7 and appendix E for a possible law of corresponding states between mW and water. It would be interesting to take this further, in order to confirm whether such a relationship exists. If one were to be found, it could provide further insight into the influence of the structure of water on its unusual characteristics. Another possible avenue for future work is to apply the spatially resolved measures of density fluctuations, shown within this work to be highly sensitive measures in microscopic hydrophobic and solvophobic systems, to more realistic situations such as proteins or hydrophobic polymers. These measures could be particularly insightful when considering substrates with both hydrophilic and hydrophobic areas. Such areas would induce different spatial forms of, for example, χ_μ, with hydrophilic fluctuations following the density profile with its peaks and troughs and hydrophobic fluctuations exhibiting a large peak. Investigating how these types of fluctuations interact with one another when in close proximity could provide further understanding into the behaviour of water near chemically heterogeneous surfaces. This could, for example, help explain why water in the vicinity of Melittin and the BphC enzyme, discussed in chapter 3, behaves in the way it does.

Finally, it is worth considering the relevance of this thesis to applications of hydrophobicity. Only smooth, chemically homogeneous solutes and surfaces have been considered within the present work, which have been taken to interact with fluids via very simple interaction potentials. The models employed here are therefore somewhat removed from the proteins and plant leaves discussed in chapter 3. Nevertheless, this thesis has provided evidence for the physical origin of enhanced density fluctuations observed in such systems, and furthermore provided a comprehensive understanding of how such fluctuations depend on changes in local conditions, such as the chemical potential. This thesis therefore contributes to understanding the fundamental physics behind hydrophobicity.

Appendix A

Partial Derivatives of the Rosenfeld Functional

The one-body direct correlation function for the hard-sphere fluid, defined in equation (4.1.32), requires knowledge of the partial derivatives of the excess free energy density with respect to the weighted densities. For the Rosenfeld functional, defined in equation (4.1.30), these are

$$\begin{aligned}
\frac{\partial \Phi_{RF}}{\partial n_0} &= -\ln(1-n_3) \\
\frac{\partial \Phi_{RF}}{\partial n_1} &= \frac{n_2}{1-n_3} \\
\frac{\partial \Phi_{RF}}{\partial \mathbf{n_1}} &= -\frac{\mathbf{n_2}}{1-n_3} \\
\frac{\partial \Phi_{RF}}{\partial n_3} &= \frac{n_0}{1-n_3} + \frac{n_1 n_2 - \mathbf{n_1}\cdot\mathbf{n_2}}{(1-n_3)^2} + \frac{n_2^3 - 3n_2\mathbf{n_2}\cdot\mathbf{n_2}}{12\pi(1-n_3)^3} \\
\frac{\partial \Phi_{RF}}{\partial n_2} &= \frac{n_1}{1-n_3} + \frac{n_2^2 - \mathbf{n_2}\cdot\mathbf{n_2}}{8\pi(1-n_3)^2} \\
\frac{\partial \Phi_{RF}}{\partial \mathbf{n_2}} &= -\frac{\mathbf{n_1}}{1-n_3}
\end{aligned} \tag{A.0.1}$$

Appendix B

Derivations for Implementation of Planar Substrates in cDFT

This appendix gives detailed derivations relevant to the implementation of a smooth planar substrate and one-component attractive fluid within cDFT.

B.1 Lennard-Jones Fluid-Fluid Interaction

The attractive part of the Lennard-Jones interaction between two particles located at $\mathbf{r}$ and $\mathbf{r}'$ respectively under the WCA splitting is

$$\phi_{att}(r' = |\mathbf{r} - \mathbf{r}'|) = \begin{cases} -\varepsilon & r' < r_{min} \\ 4\varepsilon \left[\left(\frac{\sigma}{r'}\right)^{12} - \left(\frac{\sigma}{r'}\right)^{6} \right] & r_{min} < r' < r_c \\ 0 & r' > r_c \end{cases} \tag{B.1.1}$$

where $r_{min} = 2^{1/6}\sigma$ is the location of the minimum of the potential, r_c is the cut-off radius of interaction, ε is the well-depth, and σ is the diameter of a fluid particle. If the fluid is in contact with a smooth planar substrate, then the density profile will be homogeneous parallel to the surface of the substrate. This potential can therefore be reduced to a function of the perpendicular distance from the substrate only, by analytically evaluating the interaction felt by a single particle due to a plane of particles of homogeneous density a given distance away.

Consider figure B.1 which shows a single particle, p, located at a distance z from the surface of the planar substrate. Due to the form of $\phi_{att}(r')$ given in equation (B.1.1), p will interact with planes of fluid particles of homogeneous density in one of three ways

1. If the plane of fluid particles falls within r_{min} of p, then p will interact with the plane via all parts of $\phi_{att}(r')$. This is the case for the plane at z'.

2. If the plane of fluid particles is further than a distance r_{min} but less than a distance r_c from p, then the particle will interact with the plane via only part of $\phi_{att}(r')$. This is the case for the plane at z''.

3. If the plane of fluid particles is further than a distance r_c from p, then p will not interact

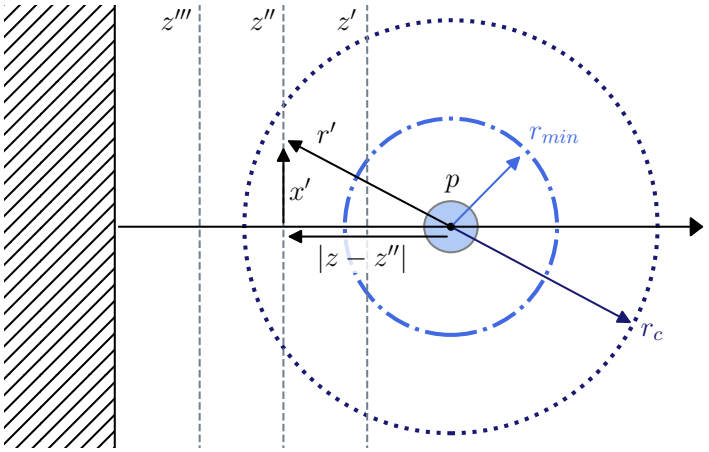

Figure B.1: Illustration of the interaction between a particle p, located a distance z from a planar substrate, and various planes of particles of homogeneous density, at distances z', z'', and z''' from the substrate. p interacts with other particles via a piece-wise potential, the components of which are indicated by the circles of radius r_{min} and r_c centred on p.

with the plane. This is the case for the plane at z'''.

The potential felt by p due to any plane of fluid particles can be expressed generally as

$$\phi_{plane}(x') = \int_0^{2\pi} \mathrm{d}\varphi' \int_0^{\infty} \mathrm{d}x' x' \phi_{att}(r') \tag{B.1.2}$$

Using Pythagoras theorem, x' can be rewritten as $x' = \sqrt{r'^2 - |z - \tilde{z}|^2}$, where $\tilde{z}$ is general distance measured from the substrate. The derivative of x' can then be written as $x'\mathrm{d}x' = r'\mathrm{d}r'$. Performing the change of variables then gives the expression

$$\phi_{plane}(r') = 2\pi \int_{|z-\tilde{z}|}^{\infty} \mathrm{d}r' r' \phi_{att}(r') \tag{B.1.3}$$

Considering the first scenario, which equates to the plane located at z' in figure B.1, the interaction at p can be found to be

$$\begin{aligned}
\phi_{plane}(|z - z'| < r_{min}) &= 2\pi \int_{|z-z'|}^{r_{min}} \mathrm{d}r' r' (-\varepsilon) + 2\pi \int_{r_{min}}^{r_c} \mathrm{d}r' r' 4\varepsilon \left[\left(\frac{\sigma}{r'}\right)^{12} - \left(\frac{\sigma}{r'}\right)^{6} \right]] \\
&= -2\pi\varepsilon \left[\frac{r'^2}{2} \right]_{|z-z'|}^{r_{min}} + 8\pi\varepsilon \left[-\frac{\sigma^{12}}{10 r'^{10}} + \frac{\sigma^6}{4 r'^4} \right]_{r_{min}}^{r_c} \\
&= \pi\varepsilon \left[|z - z'|^2 - r_{min}^2 + \frac{4}{5}\sigma^{12} \left(\frac{1}{r_{min}^{10}} - \frac{1}{r_c^{10}} \right) - 2\sigma^6 \left(\frac{1}{r_{min}^4} - \frac{1}{r_c^4} \right) \right]
\end{aligned} \tag{B.1.4}$$

The second scenario corresponds to the plane located at z'' in figure B.1. The potential felt

by p due to such a plane is then

$$\begin{aligned}\phi_{plane}(r_{min} < |z - z''| < r_c) &= 2\pi \int_{|z-z''|}^{r_c} \mathrm{d}r' r' 4\varepsilon \left[\left(\frac{\sigma}{r'}\right)^{12} - \left(\frac{\sigma}{r'}\right)^{6} \right] \\ &= \pi\varepsilon \left[\frac{4}{5}\sigma^{12} \left(\frac{1}{|z-z''|^{10}} - \frac{1}{r_c^{10}} \right) - 2\sigma^6 \left(\frac{1}{|z-z''|^4} - \frac{1}{r_c^4} \right) \right]\end{aligned} \tag{B.1.5}$$

For the third scenario, corresponding to the plane located at z''', the interaction potential will be zero everywhere. Therefore, the potential felt at a particle p located a distance z from the substrate due to a plane of fluid particles of homogeneous density at a distance $\tilde{z}$ from the substrate, can be written as

$$\phi_{att}(|z-\tilde{z}|) = \begin{cases} \pi\varepsilon \left[|z-\tilde{z}|^2 - r_{min}^2 + \frac{4}{5}\sigma^{12} \left(\frac{1}{r_{min}^{10}} - \frac{1}{r_c^{10}} \right) - 2\sigma^6 \left(\frac{1}{r_{min}^4} - \frac{1}{r_c^4} \right) \right] & |z-\tilde{z}| < r_{min} \\ \pi\varepsilon \left[\frac{4}{5}\sigma^{12} \left(\frac{1}{|z-\tilde{z}|^{10}} - \frac{1}{r_c^{10}} \right) - 2\sigma^6 \left(\frac{1}{|z-\tilde{z}|^4} - \frac{1}{r_c^4} \right) \right] & r_{min} < |z-\tilde{z}| < r_c \\ 0 & |z-\tilde{z}| > r_c \end{cases} \tag{B.1.6}$$

This can then be substituted into equation (4.1.38) to find $c^{(1)}(z)$.

B.2 Lennard-Jones Substrate-Fluid Interaction

The smooth planar substrate is imagined to be formed of planes of particles of diameter, σ_s and to be of homogeneous density, ρ_s. Each particle within the substrate is assumed to individually interact with the fluid via

$$V_{ext}(r') = \begin{cases} \infty & z < 0 \\ 4\varepsilon_s \left[\left(\frac{\sigma_s}{r'}\right)^{12} - \left(\frac{\sigma_s}{r'}\right)^{6} \right] & z > 0 \end{cases} \tag{B.2.1}$$

where ε_s is the well-depth of the interaction and r' is the distance between the interacting fluid and substrate particles.

Consider a single fluid particle, p, located at a distance z from the surface of the substrate, as shown in figure B.2. The attractive interaction felt at p due to a plane of substrate particles of homogeneous density a distance z' from the particle is given by

$$V_{plane}(r') = \int_0^{2\pi} \mathrm{d}\varphi' \int_0^{\infty} \mathrm{d}x' x' \rho_s V_{ext}(r'; z > 0) \tag{B.2.2}$$

Substituting for $V_{ext}(r'; z > 0)$ and using Pythagoras theorem to rewrite $r'^2 = x'^2 + z'^2$ gives

$$V_{plane}(x'; z > 0) = 8\pi\varepsilon_s\rho_s \int_0^{\infty} \mathrm{d}x' \left[\frac{\sigma_s^{12} x'}{(x'^2 + z'^2)^6} - \frac{\sigma_s^6 x'}{(x'^2 + z'^2)^3} \right] \tag{B.2.3}$$

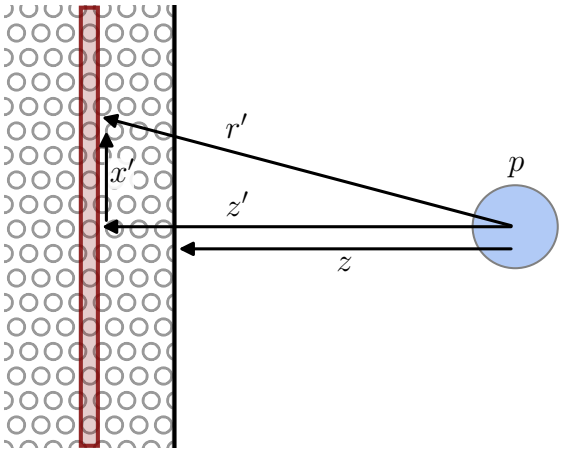

Figure B.2: Illustration of the interaction between a particle p, which is located a distance z from the surface of the planar substrate, and a plane of substrate particles of homogeneous density which is located at a distance z' from the particle.

Applying the substitution $s' = x'^2$, $\mathrm{d}s' = 2x'\mathrm{d}x'$ reduces this to

$$\begin{aligned} V_{plane}(z'; z > 0) &= 4\pi\varepsilon_s\rho_s \int_0^\infty \mathrm{d}s' \left[\frac{\sigma_s^{12}}{(s' + z'^2)^6} - \frac{\sigma_s^6}{(s' + z'^2)^3} \right] \\ &= 4\pi\varepsilon_s\rho_s \left[\frac{\sigma_s^{12}}{5z'^{10}} - \frac{\sigma_s^6}{2z'^4} \right] \end{aligned} \tag{B.2.4}$$

The potential at p due to all particles within the substrate is then found by integrating over all planes of particles within the substrate, which gives

$$\begin{aligned} V_{ext}(z; z > 0) &= \int_z^\infty \mathrm{d}z' V_{plane}(z'; z > 0) \\ &= \varepsilon_{sf} \left[\frac{2}{15} \left(\frac{\sigma_s}{z} \right)^9 - \left(\frac{\sigma_s}{z} \right)^3 \right] \end{aligned} \tag{B.2.5}$$

where $\varepsilon_{sf} = 2\pi\varepsilon_s\rho_s\sigma_s^3/3$.

At the surface of the substrate, $V_{ext}(z)$ diverges. However, due to the limits of finite number representation in computers, this divergence is capped at a large number. For the discretised systems considered within cDFT, this can lead to nonphysical behaviour in the density profile close to the surface of the planar substrate. To avoid this, $V_{ext}(z)$ is shifted such that the minimum occurs at the surface of the substrate. The location of the minimum can be found to be $z_{min} = (2/5)^{1/6}\sigma_s$, and hence the final potential used is

$$V_{ext}(z) = \begin{cases} \infty & z < 0 \\ \varepsilon_{sf} \left[\frac{2}{15} \left(\frac{\sigma_s}{z + z_{min}} \right)^9 - \left(\frac{\sigma_s}{z + z_{min}} \right)^3 \right] & z > 0 \end{cases} \tag{B.2.6}$$

B.3 Contact Sum Rule

The planar contact sum rule takes the form [42, 111, 125]

$$p = -\int_{-\infty}^{\infty} \mathrm{d}z \rho(z) \frac{\mathrm{d}V_{ext}(z)}{\mathrm{d}z} \tag{B.3.1}$$

where p is the pressure of the fluid. The derivative of $V_{ext}(z)$ can be found by first separating it into the sum of its purely repulsive and purely attractive components

$$V_{ext,rep}(z) = \begin{cases} \infty & z < 0 \\ 0 & z > 0 \end{cases} \qquad V_{ext,att}(r) = \begin{cases} 0 & z < 0 \\ \varepsilon_{sf}\left[\frac{2}{15}\left(\frac{\sigma_s}{z+z_{min}}\right)^9 - \left(\frac{\sigma_s}{z+z_{min}}\right)^3\right] & z > 0 \end{cases} \tag{B.3.2}$$

and taking the derivatives of each component individually. The derivative of $V_{ext,rep}(z)$ is poorly defined at $z = 0$. To prevent this ambiguity, the derivative is rewritten as [42]

$$\frac{\mathrm{d}V_{ext,rep}(z)}{\mathrm{d}z} = -\beta^{-1} e^{\beta V_{ext,rep}(z)} \frac{\mathrm{d}}{\mathrm{d}z} e^{-\beta V_{ext,rep}(z)} \tag{B.3.3}$$

Substituting for $V_{ext,rep}(z)$ in the second exponential gives a Heaviside function, whose derivative is the well defined Dirac-Delta function. This then gives

$$-\int_{-\infty}^{0} \mathrm{d}z \rho(z) \frac{\mathrm{d}V_{ext,rep}(z)}{\mathrm{d}z} = \beta^{-1} \int_{-\infty}^{0} \mathrm{d}z \rho(z) e^{\beta V_{ext,rep}(z)} \delta(z) = \beta^{-1} \rho(0^+) \tag{B.3.4}$$

where $\beta = (k_\mathrm{B}T)^{-1}$ and 0^+ represents the approach from the right of the substrate, where the density profile is well defined. Evaluating the attractive interaction part gives

$$-\int_{0}^{\infty} \mathrm{d}z \rho(z) \frac{\mathrm{d}V_{ext,att}(z)}{\mathrm{d}z} = -\varepsilon_{sf} \int_{0}^{\infty} \mathrm{d}z \rho(z) \left[\frac{3\sigma_s^3}{(z+z_{min})^4} - \frac{6\sigma_s^9}{5(z+z_{min})^{10}}\right] \tag{B.3.5}$$

Therefore, the contact sum rule is

$$p = \beta^{-1}\rho(0^+) - \varepsilon_{sf} \int_{0}^{\infty} \mathrm{d}z \rho(z) \left[\frac{3\sigma_s^3}{(z+z_{min})^4} - \frac{6\sigma_s^9}{5(z+z_{min})^{10}}\right] \tag{B.3.6}$$

Appendix C

Derivations for Implementation of Solutes in cDFT

This appendix gives detailed derivations for the implementation of solutes within cDFT.

C.1 Lennard-Jones Fluid-Fluid Interaction Potential

Consider a system consisting of a smooth spherical solute, of radius R_s, in contact with a fluid which interacts with itself via the potential given in equation (B.1.1). The solute acts as a spherically symmetric external potential on this fluid. As the density profile takes the symmetry of the external potential, it is also expected to be spherically symmetric.

The layout for such a system is given in figure C.1. Consider the fluid particle p located at the vector $\mathbf{r}$. Due to the spherical symmetry of the density profile, it is possible to analytically evaluate the interaction potential felt by p due to a shell of other fluid particles located on the general vector $\tilde{\mathbf{r}}$. As the system has radial symmetry, the alignment of the vectors $\mathbf{r}$ and $\tilde{\mathbf{r}}$ can be freely chosen to be

$$\begin{aligned} \mathbf{r} &= r\hat{\mathbf{k}} \\ \tilde{\mathbf{r}} &= \tilde{r}\sin\tilde{\theta}\cos\tilde{\varphi}\hat{\mathbf{i}} + \tilde{r}\sin\tilde{\theta}\sin\tilde{\varphi}\hat{\mathbf{j}} + \tilde{r}\cos\tilde{\theta}\hat{\mathbf{k}} \\ |\mathbf{r}-\tilde{\mathbf{r}}| &= r^2 + \tilde{r}^2 - 2r\tilde{r}\cos\tilde{\theta} \end{aligned} \tag{C.1.1}$$

where $\hat{\mathbf{i}}$, $\hat{\mathbf{j}}$ and $\hat{\mathbf{k}}$ represent unit vectors along the x, y and z axes respectively. The angle, $\tilde{\varphi}$ varies in the $x-y$ plane in figure C.1, between 0 and 2π. The angle, $\tilde{\theta}$ varies in the $y-z$ plane. Its limits are related to the angle of $\tilde{\mathbf{r}}$ at which the shell of constant density intersects various parts of the fluid-fluid interaction potential. Two general angles for this are defined in figure C.1: γ is the angle at which $\tilde{\mathbf{r}}$ intersects the $r < r_{min}$ part of the potential and α the angle at which $\tilde{\mathbf{r}}$ intersects the $r_{min} < r < r_c$ part.

Due to the piece-wise nature of $\phi_{att}(|\mathbf{r}-\tilde{\mathbf{r}}|)$ given in equation (B.1.1), there are several possible scenarios. Assuming first that R_s is sufficiently large, such that $\alpha < \pi$, the possible scenarios are then

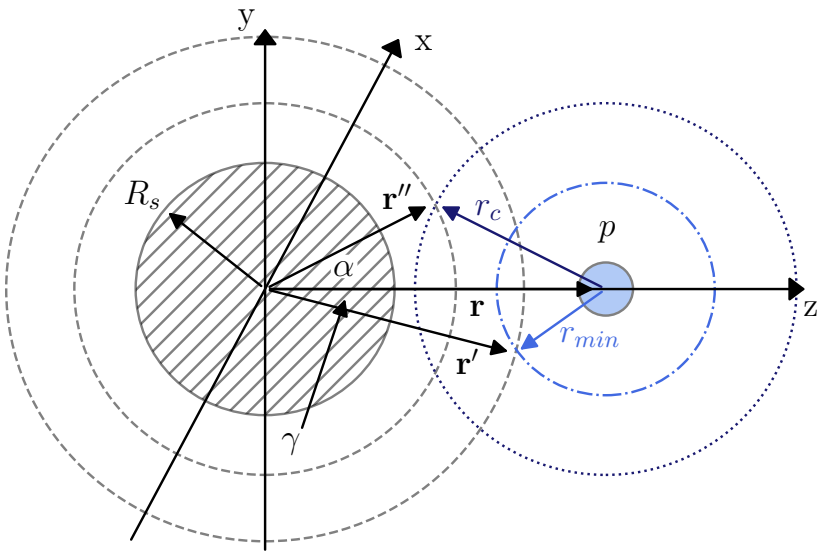

Figure C.1: Illustration of the interaction between a particle, p, located at $\mathbf{r}$, and various spherically symmetric shells of fluid particles of constant density, located at $\mathbf{r}'$ and $\mathbf{r}''$. The components of the interaction potential between p and each shell are shown by the blue circles of radius r_{min} and r_c. The angle subtended from the axis z to $\mathbf{r}''$ is denoted as α, whilst the angle subtended by the z-axis and $\mathbf{r}'$ is denoted at γ.

1. If $|\mathbf{r} - \tilde{\mathbf{r}}| < r_{min}$, as is the case for particles on the vector $\mathbf{r}'$ in figure C.1, then p will interact with these particles via all parts of $\phi_{att}(|\mathbf{r} - \tilde{\mathbf{r}}|)$.

2. If $r_{min} < |\mathbf{r} - \tilde{\mathbf{r}}| < r_c$, which is the case for the vector $\mathbf{r}''$ in figure C.1, then p will interact with these particles with only the components $\phi_{att}(|\mathbf{r} - \tilde{\mathbf{r}}| > r_{min})$.

3. If $|\mathbf{r} - \tilde{\mathbf{r}}| > r_c$, the particle p will not interact with the particles.

The potential felt at p due to one shell of particles with constant density is given by

$$\phi_{shell}(|\mathbf{r} - \tilde{\mathbf{r}}|) = \int_0^{2\pi} \mathrm{d}\tilde{\phi} \int \mathrm{d}\tilde{\theta} \phi_{att}(|\mathbf{r} - \tilde{\mathbf{r}}|) \tag{C.1.2}$$

Considering the first scenario, corresponding to $\mathbf{r}'$, the potential felt at p due to all particles on $\mathbf{r}'$ can be found to be

$$\phi_{shell}(|\mathbf{r}-\mathbf{r}'|) = \int_0^{2\pi} \mathrm{d}\varphi' \int_0^{\gamma} \mathrm{d}\theta' \sin\theta'(-\varepsilon) + \int_0^{2\pi} \mathrm{d}\varphi' \int_{\gamma}^{\alpha} \mathrm{d}\theta' \sin\theta' 4\varepsilon \left[\frac{\sigma^{12}}{|\mathbf{r} - \mathbf{r}'|^{12}} - \frac{\sigma^6}{|\mathbf{r} - \mathbf{r}'|^6} \right] \tag{C.1.3}$$

Evaluating the first integral gives

$$\int_0^{2\pi} \mathrm{d}\varphi' \int_0^{\gamma} \mathrm{d}\theta' \sin\theta'(-\varepsilon) = -2\pi\varepsilon(\cos\gamma - 1) = -2\pi\varepsilon \left[\frac{(r - r')^2 - r_{min}^2}{2rr'} \right] \tag{C.1.4}$$

where the substitution for $(\cos\gamma - 1)$ is found using the cosine rule. The second integral takes the form

$$\int_0^{2\pi} \mathrm{d}\varphi' \int_\gamma^\alpha \mathrm{d}\theta' \sin\theta' 4\varepsilon \left[\frac{\sigma^{12}}{|\mathbf{r}-\mathbf{r}'|^{12}} - \frac{\sigma^6}{|\mathbf{r}-\mathbf{r}'|^6}\right] = 8\pi\varepsilon \int_\gamma^\alpha \mathrm{d}\theta' \sin\theta' \left[\frac{\sigma^{12}}{(r^2+r'^2-2rr'\cos\theta')^6} - \frac{\sigma^6}{(r^2+r'^2-2rr'\cos\theta')^3}\right] \quad \text{(C.1.5)}$$

Using the substitutions, $A = r^2 + r'^2$, $B = 2rr'$ and $u = \cos\theta'$ such that $\mathrm{d}u = -\sin\theta'\mathrm{d}\theta'$, this integral can be simplified to

$$\begin{aligned}\int_0^{2\pi} \mathrm{d}\varphi' \int_\gamma^\alpha \mathrm{d}\theta' \sin\theta' 4\varepsilon \left[\frac{\sigma^{12}}{|\mathbf{r}-\mathbf{r}'|^{12}} - \frac{\sigma^6}{|\mathbf{r}-\mathbf{r}'|^6}\right] &= -8\pi\varepsilon \int_{\cos\gamma}^{\cos\alpha} \mathrm{d}u \left[\frac{\sigma^{12}}{(A-Bu)^6} - \frac{\sigma^6}{(A-Bu)^3}\right] \\ &= -\frac{8\pi\varepsilon}{B}\left[\frac{\sigma^{12}}{5}\left(\frac{1}{(A-B\cos\alpha)^5} - \frac{1}{(A-B\cos\gamma)^5}\right) - \frac{\sigma^6}{2}\left(\frac{1}{(A-B\cos\alpha)^2} - \frac{1}{(A-B\cos\gamma)^2}\right)\right] \quad \text{(C.1.6)}\end{aligned}$$

Substituting $A - B\cos\alpha = r_c^2$ and $A - B\cos\gamma = r_{min}^2$, the final result is

$$\phi_{shell}(|\mathbf{r}-\mathbf{r}'|) = \frac{\pi\varepsilon}{rr'}\left[(r-r')^2 - r_{min}^2 + \frac{4}{5}\sigma^{12}\left(\frac{1}{r_{min}^{10}} - \frac{1}{r_c^{10}}\right) - 2\sigma^6\left(\frac{1}{r_{min}^4} - \frac{1}{r_c^4}\right)\right] \quad \text{(C.1.7)}$$

The second scenario, given by the vector $\mathbf{r}''$ in figure C.1, gives

$$\begin{aligned}\phi_{shell}(|\mathbf{r}-\mathbf{r}''|) &= \int_0^{2\pi} \mathrm{d}\varphi' \int_0^\alpha \mathrm{d}\theta' \sin\theta' 4\varepsilon \left[\frac{\sigma^{12}}{|\mathbf{r}-\mathbf{r}''|^{12}} - \frac{\sigma^6}{|\mathbf{r}-\mathbf{r}''|^6}\right] \\ &= 8\pi\varepsilon \int_0^\alpha \mathrm{d}\theta' \sin\theta' \left[\frac{\sigma^{12}}{(r^2+r''^2-2rr''\cos\theta)^6} - \frac{\sigma^6}{(r^2+r''^2-2rr''\cos\theta')^3}\right] \quad \text{(C.1.8)}\end{aligned}$$

Using the same substitution as before, with r' replaced by r'', and noting that $A-B = (r-r'')^2$ this evaluates to

$$\phi_{shell}(|\mathbf{r}-\mathbf{r}''|) = \frac{\pi\varepsilon}{rr''}\left[\frac{4}{5}\sigma^{12}\left(\frac{1}{(r-r'')^{10}} - \frac{1}{r_c^{10}}\right) - 2\sigma^6\left(\frac{1}{(r-r'')^4} - \frac{1}{r_c^4}\right)\right] \quad \text{(C.1.9)}$$

For the third scenario, the potential will be zero everywhere. The potential felt at p due to a spherical shell of fluid particles at constant density a general radial distance $\tilde{r}$ from the origin can be written as

$$\phi_{att}(|r-\tilde{r}|) = \begin{cases} \frac{\pi\varepsilon}{r\tilde{r}}\left[(r-\tilde{r})^2 - r_{min}^2 + \frac{4}{5}\sigma^{12}\left(\frac{1}{r_{min}^{10}} - \frac{1}{r_c^{10}}\right) - 2\sigma^6\left(\frac{1}{r_{min}^4} - \frac{1}{r_c^4}\right)\right] & |r-\tilde{r}| < r_{min} \\ \frac{\pi\varepsilon}{r\tilde{r}}\left[\frac{4}{5}\sigma^{12}\left(\frac{1}{(r-\tilde{r})^{10}} - \frac{1}{r_c^{10}}\right) - 2\sigma^6\left(\frac{1}{(r-\tilde{r})^4} - \frac{1}{r_c^4}\right)\right] & r_{min} < |r-\tilde{r}| < r_c \\ 0 & |r-\tilde{r}| > r_c \end{cases} \quad \text{(C.1.10)}$$

This derivation assumes that $\alpha < \pi$, which equates to $r + \tilde{r} > r_c$. This is true providing $2R_s > r_c$. For a short-ranged fluid attraction, with $r_c = 2.5\sigma$, this interaction potential is therefore valid providing $R_s > 1.25\sigma$. For the long-ranged fluid potential, with $r_c = 200\sigma$, this is true only if $R_s > 100\sigma$.

Cases for when $\alpha < \pi$ can be evaluated in much the same way as above. Doing so gives two new cases for the interaction potential

$$\phi_{att}(|r-\tilde{r}|) = \begin{cases} \frac{\pi\varepsilon}{r\tilde{r}}\left[(r-\tilde{r})^2 - r_{min}^2 + \frac{4}{5}\sigma^{12}\left(\frac{1}{r_{min}^{10}}\frac{1}{(r+\tilde{r})^{10}}\right) - \right. & |r-\tilde{r}| < r_{min}, \\ \qquad\qquad \left. -2\sigma^6\left(\frac{1}{r_{min}^4} - \frac{1}{(r+\tilde{r})^4}\right)\right] & r+\tilde{r} < r_c \\ \frac{\pi\varepsilon}{r\tilde{r}}\left[\frac{4}{5}\sigma^{12}\left(\frac{1}{(r-\tilde{r})^{10}} - \frac{1}{(r+\tilde{r})^{10}}\right)\right. & \\ \qquad\qquad \left. -2\sigma^6\left(\frac{1}{(r-\tilde{r})^4} - \frac{1}{(r+\tilde{r})^4}\right)\right] & r_{min} < |r-\tilde{r}| < r_c, \\ & r+\tilde{r} < r_c \end{cases} \tag{C.1.11}$$

Finally, it should be noted that there is also the possibility that $\gamma = \pi$, which occurs when $2R_s < r_{min}$. As $r_{min} = 2^{1/6}\sigma$, this would require considering substrates of approximately the same size as a fluid particle. This is not considered here and hence this case is irrelevant.

C.2 Lennard-Jones Substrate-Fluid Interaction Potential

The solute is taken to be smooth and centred on the origin. It is assumed it is made of particles of constant density ρ_s and diameter σ_s, which individually interact with fluid particles according to

$$V_{ext}(r') = \begin{cases} \infty & r < R_s \\ 4\varepsilon_s\left[\left(\frac{\sigma_s}{r'}\right)^{12} - \left(\frac{\sigma_s}{r'}\right)^6\right] & r > R_s \end{cases} \tag{C.2.1}$$

where ε_s is the minimum of the potential, which occurs at $R_s + r_{min}$ and R_s is the radius of the solute. Due to the radial symmetry, the external potential felt by a particle p can be reduced to a function of the radial distance from the origin only.

Consider the particle p as given in figure C.2. As in the derivation of the fluid-fluid interaction, the radial axis is chosen to coincide with the Cartesian z-axis. The external potential felt at p due to a plane of particles within the solute a distance $r - z'$ away is

$$V_{plane}(r'; r > R_s) = \int_0^{2\pi} \mathrm{d}\varphi' \int_0^{\sqrt{R_s^2 - z'^2}} \mathrm{d}x' x' \rho_s V_{ext}(r') \tag{C.2.2}$$

where Pythagoras theorem has been used to find the maximum value of x'. Substituting for $V_{ext}(r')$, and using Pythagoras theorem to write $r'^2 = (r-z')^2 + x'^2$, $V_{plane}(x')$ can be written as

$$V_{plane}(x'; r > R_s) = 8\pi\varepsilon_s\rho_s \int_0^{\sqrt{R_s^2 - z'^2}} \mathrm{d}x' x' \left[\frac{\sigma_s^{12}}{(x'^2 + (r-z')^2)^6} - \frac{\sigma_s^6}{(x'^2 + (r-z')^2)^3}\right] \tag{C.2.3}$$

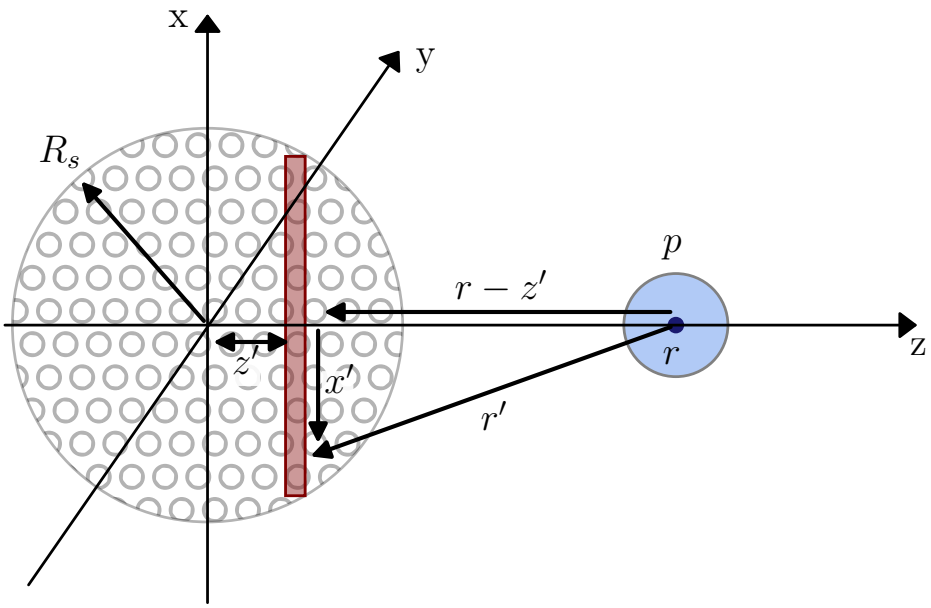

Figure C.2: Diagram of necessary components for the integration of $V_{ext}(r)$. A particle p, shown in blue, interacts with a solute of radius R_s shown in grey. The solute is assumed to be of homogeneous density. The interaction between p and the solute can therefore be found by first finding the interaction between p and a plane of particles within the solute, shown in red, and then integrating over all planes of particles. The variables needed to perform this calculation are given by the arrows.

Applying the substitution, $s = x'^2$, $\mathrm{d}s = 2x'\mathrm{d}x'$, this evaluates to

$$V_{plane}(z'; r > R_s) = 4\pi\varepsilon_s\rho_s \left[\frac{\sigma_s^{12}}{5}\left(\frac{1}{(r-z')^{10}} - \frac{1}{(R_s^2 + r^2 - 2rz')^5}\right) - \frac{\sigma_s^6}{2}\left(\frac{1}{(r-z')^4} - \frac{1}{(R_s^2 + r^2 - 2rz')^2}\right)\right] \quad \text{(C.2.4)}$$

The full external potential felt at p is then found by integrating over all planes of particles within the solute, which gives

$$\begin{aligned} V_{ext}(r; r > R_s) &= \int_{-R_s}^{R_s} \mathrm{d}z' V_{plane}(z') \\ &= \varepsilon_{sf}\left[\frac{2}{15}\sigma_s^9\left(\frac{1}{(r-R_s)^9} - \frac{1}{(r+R_s)^9}\right) + \frac{3}{20r}\sigma_s^9\left(\frac{1}{(r+R_s)^8} - \frac{1}{(r-R_s)^8}\right) + \right. \\ &\quad \left. \sigma_s^3\left(\frac{1}{(r+R_s)^3} - \frac{1}{(r-R_s)^3}\right) + \frac{3}{2r}\sigma_s^3\left(\frac{1}{(r-R_s)^2} - \frac{1}{(r+R_s)^2}\right)\right] \end{aligned} \quad \text{(C.2.5)}$$

where $\varepsilon_{sf} = 2\pi\varepsilon_s\rho_s\sigma_s^3/3$. For numerical reasons, the substrate-fluid interaction potential is then shifted such that the minimum occurs at the surface of the solute. This is equivalent to

replacing r with $r_+ = r + r_{min}$. The full piece-wise interaction is then

$$V_{ext}(r) = \begin{cases} \infty & r < R_s \\ \varepsilon_{sf}\left[\frac{2}{15}\sigma_s^9\left(\frac{1}{(r_+-R_s)^9} - \frac{1}{(r_++R_s)^9}\right) + \frac{3}{20r_+}\sigma_s^9\left(\frac{1}{(r_++R_s)^8} - \frac{1}{(r_+-R_s)^8}\right)\right. & \\ \left. +\sigma_s^3\left(\frac{1}{(r_++R_s)^3} - \frac{1}{(r_+-R_s)^3}\right) + \frac{3}{2r_+}\sigma_s^3\left(\frac{1}{(r_+-R_s)^2} - \frac{1}{(r_++R_s)^2}\right)\right] & r > R_s \end{cases} \tag{C.2.6}$$

C.3 Contact Sum Rule

The contact theorem sum rule for a curved substrate or solute is derived using [126]

$$\left(\frac{\partial\Omega}{\partial R_s}\right)_{T,\mu} = 4\pi\int \mathrm{d}r r^2\rho(r)\frac{\partial V_{ext}(r)}{\partial R_s} \tag{C.3.1}$$

Considering the form of the external potential given in equation (C.2.6), it can be seen that the external potential can be separated into the sum of its purely repulsive and attractive components as

$$V_{ext,rep}(r) = \begin{cases} \infty & r < R_s \\ 0 & r > R_s \end{cases} \tag{C.3.2}$$

$$V_{ext,att}(r) = \begin{cases} 0 & r < R_s \\ \varepsilon_{sf}\left[\frac{2}{15}\sigma_s^9\left(\frac{1}{(r_+-R_s)^9} - \frac{1}{(r_++R_s)^9}\right) + \frac{3}{20r_+}\sigma_s^9\left(\frac{1}{(r_++R_s)^8} - \frac{1}{(r_+-R_s)^8}\right)\right. & \\ \left. +\sigma_s^3\left(\frac{1}{(r_++R_s)^3} - \frac{1}{(r_+-R_s)^3}\right) + \frac{3}{2r_+}\sigma_s^3\left(\frac{1}{(r_+-R_s)^2} - \frac{1}{(r_++R_s)^2}\right)\right] & r > R_s \end{cases} \tag{C.3.3}$$

where $r_+ = r + r_{min}$ represents that the minimum of the attractive potential is shifted such that it coincides with the surface of the solute. The density is poorly defined at $r = R_s$, and hence a similar substitution as in the planar case is used

$$\frac{\mathrm{d}V_{ext,rep}(r)}{\mathrm{d}R_s} = -\beta^{-1}e^{\beta V_{ext,rep}(R_s)}\frac{\mathrm{d}}{\mathrm{d}R_s}e^{-\beta V_{ext,rep}(R_s)} \tag{C.3.4}$$

The second exponential can be recognised as expressing a Heaviside function therefore, similar to the planar case, the repulsive component evaluates to

$$4\pi\int_0^{R_s}\mathrm{d}r r^2\rho(r)\frac{\mathrm{d}V_{ext,rep}(R_s)}{\mathrm{d}R_s} = 4\pi R_s^2 k_\mathrm{B}T\rho(R_s^+) \tag{C.3.5}$$

where R_s^+ signifies that we approach from the right, where the density profile is well defined.

The attractive component can be evaluated to give

$$\begin{aligned}
&4\pi \int_{R_s}^{\infty} \mathrm{d}r r^2 \rho(r) \frac{\partial V_{ext,att}(r)}{\partial R_s} \\
&= 4\pi\varepsilon_{sf} \int_{R_s}^{\infty} \mathrm{d}r r^2 \rho(r) \left[\frac{6\sigma_s^9}{5} \left(\frac{1}{(r_+ - R_s)^{10}} + \frac{1}{(r_+ + R_s)^{10}} - \frac{1}{r_+(r_+ + R_s)^9} - \frac{1}{r_+(r_+ - R_s)^9} \right) \right. \\
&\qquad \left. + 3\sigma_s^3 \left(\frac{1}{r_+(r_+ + R_s)^3} + \frac{1}{r_+(r_+ - R_s)^3} - \frac{1}{(r_+ + R_s)^4} - \frac{1}{(r_+ - R_s)^4} \right) \right] \quad \text{(C.3.6)}
\end{aligned}$$

Finally, the grand potential can be rewritten as a function of R_s and the differential evaluated to be

$$\left(\frac{\partial \Omega}{\partial R_s} \right)_{T,\mu} = \frac{\partial}{\partial R_s} \left(-p \left(V - \frac{4}{3}\pi R_s^3 \right) + 4\pi R_s^2 \gamma(R_s) \right)_{T,\mu} = 4\pi R_s^2 \left[p + \frac{2\gamma(R_s)}{R_s} + \frac{\partial \gamma(R_s)}{\partial R_s} \right] \quad \text{(C.3.7)}$$

where p is the pressure, V the volume and γ the surface tension. Combining the individual components gives the contact sum rule for a curved substrate of

$$\begin{aligned}
&p + \frac{2\gamma(R_s)}{R_s} + \frac{\partial \gamma(R_s)}{\partial R_s} = k_\mathrm{B} T \rho(R_s^+) + \\
&\frac{\varepsilon_{sf}}{R_s^2} \int_{R_s}^{\infty} \mathrm{d}r \rho(r) r^2 \left[\frac{6\sigma_s^9}{5} \left(\frac{1}{(r_+ - R_s)^{10}} + \frac{1}{(r_+ + R_s)^{10}} - \frac{1}{r_+(r_+ + R_s)^9} - \frac{1}{r_+(r_+ - R_s)^9} \right) \right. \\
&\qquad \left. + 3\sigma_s^3 \left(\frac{1}{r_+(r_+ + R_s)^3} + \frac{1}{r_+(r_+ - R_s)^3} - \frac{1}{(r_+ + R_s)^4} - \frac{1}{(r_+ - R_s)^4} \right) \right] \quad \text{(C.3.8)}
\end{aligned}$$

Appendix D

Binding Potential Derivations

This appendix details derivations relevant to the binding potential of section 5.4.

D.1 Short-Ranged Fluid-Fluid Long-Ranged Substrate-Fluid Interactions

The sf component of the binding potential for a system consisting of a planar substrate with SR ff LR sf interactions is found using [41, 117]

$$\omega_{LR,sf}(\ell) = \Delta\rho\rho_s \int_{\ell+dw}^{\infty} \mathrm{d}z V_{ext}(z) \tag{D.1.1}$$

For the planar substrate,

$$V_{ext}(z) = \begin{cases} \infty & z < 0 \\ \frac{2\pi}{3}\varepsilon_s\sigma_s^3\left[\frac{2}{15}\left(\frac{\sigma_s}{z+z_{min}}\right)^9 - \left(\frac{\sigma_s}{z+z_{min}}\right)^3\right] & z > 0 \end{cases} \tag{D.1.2}$$

Substituting this and evaluating the integral gives

$$\begin{aligned} \omega_{LR,sf}(\ell) &= \frac{2\pi}{3}\Delta\rho\rho_s\varepsilon_s\sigma_s^3\left[-\frac{\sigma_s^9}{60(z+z_{min})^8} + \frac{\sigma_s^3}{2(z+z_{min})^2}\right]_{\ell+dw}^{\infty} \\ &= \frac{2\pi}{3}\Delta\rho\rho_s\varepsilon_s\sigma_s^3\left[\frac{\sigma_s^9}{60(\ell+(dw+z_{min}))^8} - \frac{\sigma_s^3}{2(\ell+(dw+z_{min}))^2}\right] \end{aligned} \tag{D.1.3}$$

Only leading order terms are required for the binding potential, hence the term proportional to $(\ell+(dw+z_{min}))^{-8}$ is neglected. The remaining term is Taylor expanded to give

$$\begin{aligned} \omega_{LR,sf}(\ell) &= \frac{2\pi}{3}\Delta\rho\rho_s\varepsilon_s\sigma_s^3\left[-\frac{1}{2\ell^2} + \frac{(dw+z_{min})}{\ell^3} + \mathcal{O}\left(\frac{1}{\ell^4}\right)\right] \\ &= -\frac{\pi}{3}\Delta\rho\rho_s\varepsilon_s\sigma_s^6\frac{1}{\ell^2} + \frac{2\pi}{3}\Delta\rho\rho_s\varepsilon_s\sigma_s^6\frac{(dw+z_{min})}{\ell^3} \\ &= \frac{b(T)}{\ell^2} + \frac{c(T)}{\ell^3} \end{aligned} \tag{D.1.4}$$

where

$$b(T) = b_o\rho_s\varepsilon_s\sigma_s^6 \qquad c(T) = 2(dw+z_{min})b_o\rho_s\varepsilon_s\sigma_s^6 \tag{D.1.5}$$

and $b_o = \pi\Delta\rho/3$.

D.2 Long-Ranged Fluid-Fluid Long-Ranged Substrate-Fluid Interactions

In the case of LR ff LR sf interactions, the binding potential has the form [50, 117]

$$\omega_{LR}(\ell) = \Delta\rho\left(\rho_s\int_{\ell+dw}^{\infty} V_{ext}(z)\mathrm{d}z - \rho_v\int_{\ell}^{\infty}\phi(z)\mathrm{d}z\right) \tag{D.2.1}$$

where $\Delta\rho = (\rho_l - \rho_v)$ is the difference between the coexisting liquid and vapour densities, ρ_s is the density of the substrate, V_{ext} is the external potential, ϕ is the attractive ff interaction felt by a single fluid particle due to the presence of all others, and all other measures are as given in figure 5.4. The first term was evaluated previously in appendix D.1, where V_{ext} is assumed to have the form of equation (D.1.2). The second term can be evaluated by assuming a form for $\phi(z)$.

$\phi(z)$ is the energy felt by a single particle due to a slab of fluid. It can therefore be found by evaluating

$$\phi(z) = \int_z^{\infty}\phi_{att}(z'' = |z' - \tilde{z}|)\mathrm{d}z'' \tag{D.2.2}$$

where ϕ_{att} is a purely attractive potential assumed to have the form of equation (B.1.6). As LR potentials are considered, r_c is taken to be $r_c = \infty$. In this case, $\phi_{att}(z'')$ becomes

$$\phi_{att}(z'') = \begin{cases} \pi\varepsilon(z''^2 - r_{min}^2) + 4\pi\varepsilon\left[\frac{\sigma^{12}}{5r_{min}^{10}} - \frac{\sigma^6}{2r_{min}^4}\right] & z'' < r_{min} \\ 4\pi\varepsilon\left[\frac{\sigma^{12}}{5z''^{10}} - \frac{\sigma^6}{2z''^4}\right] & z'' > r_{min} \end{cases} \tag{D.2.3}$$

Evaluating equation (D.2.2) for the first case can be done using

$$\phi(z; z < r_{min}) = \pi\varepsilon\int_z^{r_{min}}\left[z''^2 - r_{min}^2 + \frac{4\sigma^{12}}{5r_{min}^{10}} - \frac{2\sigma^6}{r_{min}^4}\right]\mathrm{d}z'' + \pi\varepsilon\int_{r_{min}}^{\infty}\left[\frac{4\sigma^{12}}{5z''^{10}} - \frac{2\sigma^6}{z''^4}\right]\mathrm{d}z'' \tag{D.2.4}$$

whilst for the second case this is done using

$$\phi(z; z > r_{min}) = 4\pi\varepsilon\int_z^{\infty}\left[\frac{\sigma^{12}}{5z''^{10}} - \frac{\sigma^6}{2z''^4}\right]\mathrm{d}z'' \tag{D.2.5}$$

Performing these integrals leads to

$$\phi(z) = \begin{cases} 4\pi\varepsilon\left[-\frac{r_{min}^3}{6} - \frac{z^3}{12} + \frac{2\sigma^{12}}{9r_{min}^9} - \frac{2\sigma^6}{3r_{min}^3} - \left(\frac{\sigma^{12}}{5r_{min}^{10}} - \frac{\sigma^6}{2r_{min}^4}\right)z + \frac{r_{min}^2 z}{4}\right] & z < r_{min} \\ 4\pi\varepsilon\left[\frac{\sigma^{12}}{45z^9} - \frac{\sigma^6}{6z^3}\right] & z > r_{min} \end{cases} \tag{D.2.6}$$

It is assumed that the vapour film is thick, and hence $\ell > r_{min}$. Because of this, the first case

for $\phi(z)$ is irrelevant, and hence the ff part of the binding potential can be evaluated to be

$$\begin{aligned}\omega_{LR,ff}(\ell) &= -\Delta\rho\rho_v \int_\ell^\infty 4\pi\varepsilon \left[\frac{\sigma^{12}}{45z^9} - \frac{\sigma^6}{6z^3}\right] \\ &= -\frac{2\pi}{3}\Delta\rho\rho_v\varepsilon \left[-\frac{\sigma^{12}}{60z^8} + \frac{\sigma^6}{2z^2}\right]_\ell^\infty \\ &= -\frac{2\pi}{3}\Delta\rho\rho_v\varepsilon \left[\frac{\sigma^{12}}{60\ell^8} - \frac{\sigma^6}{2\ell^2}\right] \end{aligned} \tag{D.2.7}$$

Substituting this and equation (D.1.4) into equation (D.2.1) then gives

$$\begin{aligned}\omega_{LR}(\ell) &= \frac{2\pi}{3}\Delta\rho \left[\rho_s\varepsilon_s\sigma_s^6 \left(-\frac{1}{2\ell^2} + \frac{2(dw + z_{min})}{\ell^3}\right) + \rho_v\varepsilon\sigma^6 \left(\frac{1}{2\ell^2}\right)\right] + \mathcal{O}\left(\frac{1}{\ell^4}\right) \\ &= \frac{b(T)}{\ell^2} + \frac{c(T)}{\ell^3} + \mathcal{O}\left(\frac{1}{\ell^4}\right) \end{aligned} \tag{D.2.8}$$

where the constants $b(T)$ and $c(T)$ are identified as

$$b(T) = b_o(\rho_v\varepsilon\sigma^6 - \rho_s\varepsilon_s\sigma_s^6) \qquad c(T) = 2b_o(dw + z_{min})\rho_s\varepsilon_s\sigma_s^6 \tag{D.2.9}$$

and $b_o = \pi\Delta\rho/3$.

Appendix E

Assessment of Suitability of mW for the Study of Hydrophobicity

Having only been proposed in 2009, mW is a relatively new model for water and has been used only in a handful of studies of hydrophobicity, for example [138–140]. Furthermore, many of its bulk properties have not yet been fully explored and are not widely reported. However, it shows great promise for use in the study of hydrophobicity for many reasons. Firstly, it is able to accurately reproduce the density and structure of water at ambient conditions [132]. Secondly, its liquid-vapour surface tension at ambient conditions is closer to that of water than many popular water models [132]. Importantly, mW models a water molecule as a single particle, and reproduces the tetrahedral structure using only SR interactions. This greatly reduces the computational resource required, and thus allows larger systems to be accessed more easily. Within this appendix, the suitability of mW as a water model for use in the study of hydrophobicity is assessed, through comparisons of mW's phase diagram and surface tension properties to those of both real water, and a leading model of water, SPC/E.

E.1 Comparison of Critical Point Properties

Whilst the critical temperature, T_c, of mW has been mentioned in previous studies [138, 141], it is unclear whether these studies took into account FS effects. In order to do so, it is necessary to follow the GCMC method outlined in section 4.2.8.1. Firstly, the critical point parameters for several simulation box sizes, quantified by the length of the cubic box, L, must be determined. This is done by comparing the distributions of the scaling variable, defined in equation (4.2.28) as $\mathcal{M} = \rho - su$, where ρ is the density, u the energy density and s a mixing parameter, to the universal Ising distribution. Figure E.1 shows these comparisons for the distributions obtained within the present study for the five box lengths considered. On average, the value of the mixing parameter was found to be $s = 0.33$. This agrees well with the value quoted by Russo et al. [141], though their value was related to a weaker value of the tetrahedrality parameter, λ, than used in mW.

Figure E.2 compares the T_c and critical density, ρ_c obtained from each box length, L, considered to the expected FS scaling relationships, given in [68]. For the case of T_c in figure

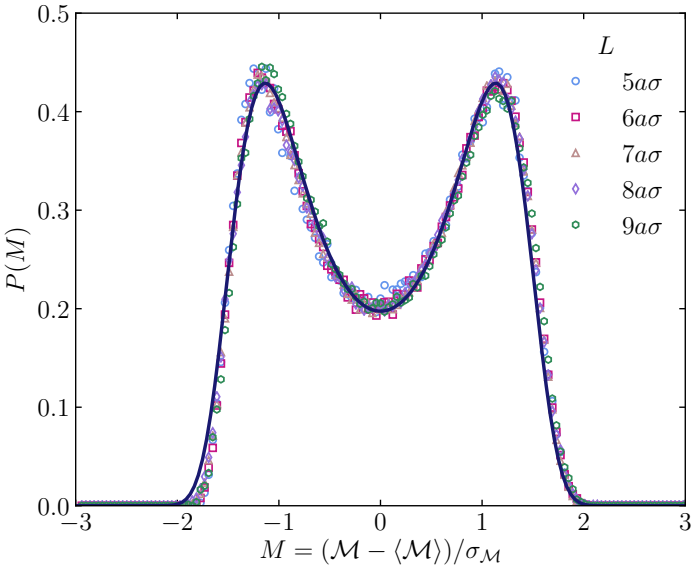

Figure E.1: Comparison of scaling variable distribution of mW (symbols) for various lengths (L) of cubic simulation box, to the Ising distribution (solid line), obtained from [142].

E.2(a), the uncertainty was taken to be 1K. Excellent agreement to a linear fit (dotted line) can be seen. Extrapolating this to infinite L gives a critical temperature of $T_c = 917.6$K. This is similar to that quoted by Xu and Molinero [138], of $T_c \approx 925$K. Figure E.2(b) compares the values of ρ_c obtained for each T_c in figure E.2(a) to the expected scaling relation. In this case, the uncertainty was found by considering the densities of the upper and lower limits of T_c from figure E.2(a). Again, excellent agreement with a linear fit is found. Extrapolation to infinite L gives a critical density of $\rho_c = 0.311\text{gcm}^{-3}$.

Table E.1 compares the critical point properties of mW obtained here to those of SPC/E, obtained from [133], and water, obtained from [149]. The critical temperature of mW is

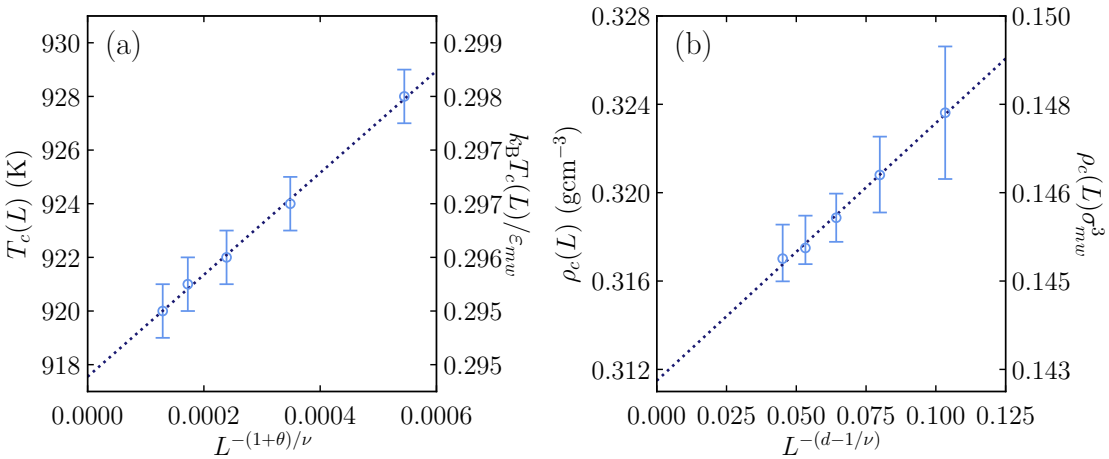

Figure E.2: Finite size scaling analysis of the critical (a) temperature and (b) density of mW, in both physical and reduced units. Uncertainties in (a) are taken to be 1K, whilst in (b), the uncertainty is taken to be the density of the upper and lower critical temperatures from (a). The exponents were taken to be those used by Wilding [68] and had the values $\theta = 0.54$, $\nu = 0.629$ and $d = 3$. σ_{mw} and ε_{mw} were as defined in section 4.2.7 and took the values $\sigma_{mw} = 2.3925$Å and $\varepsilon_{mw} = 6.189$kcal/mol.

clearly much larger than that of SPC/E or real water. mW is therefore unable to accurately reproduce this. However, the critical density of mW is in very good agreement with that of water, and is much closer than that of SPC/E.

Table E.1: Critical point properties for water, the popular water model SPC/E and mW. Properties for water were obtained from [149], whilst properties for SPC/E were obtained from [133].

Model	T_c (K)	ρ_c (gcm^{-3})
Water	647.096	0.322
SPC/E	638.6	0.273
mW	917.6	0.311

E.2 Comparison of Liquid-Vapour Phase Diagram

Sub-critical liquid-vapour coexistence state points for mW have been reported previously [132], however these studies have generally focused on properties near ambient conditions. In order to assess mW's coexistence properties, the entire liquid-vapour coexistence curve should be considered. This was found within the present work using the GCMC methods outlined in section 4.2.8.2. Figure E.3(a) shows the liquid-vapour coexistence diagram of mW, along with that of water and SPC/E, in physical units.

Due to its much larger T_c, the liquid-vapour phase diagram of mW extends over a larger range of temperatures than that of water and SPC/E. Despite this, figure E.3(a) shows that mW reproduces the coexisting liquid density of water fairly well for $T < 400$K. Below 350K, the agreement is similar to that of SPC/E, which indicates that, in terms of coexistence properties, mW is a good alternative model to SPC/E near ambient conditions. However, above 400K, mW over-predicts the density of water. This is most severe when $T > 420$K,

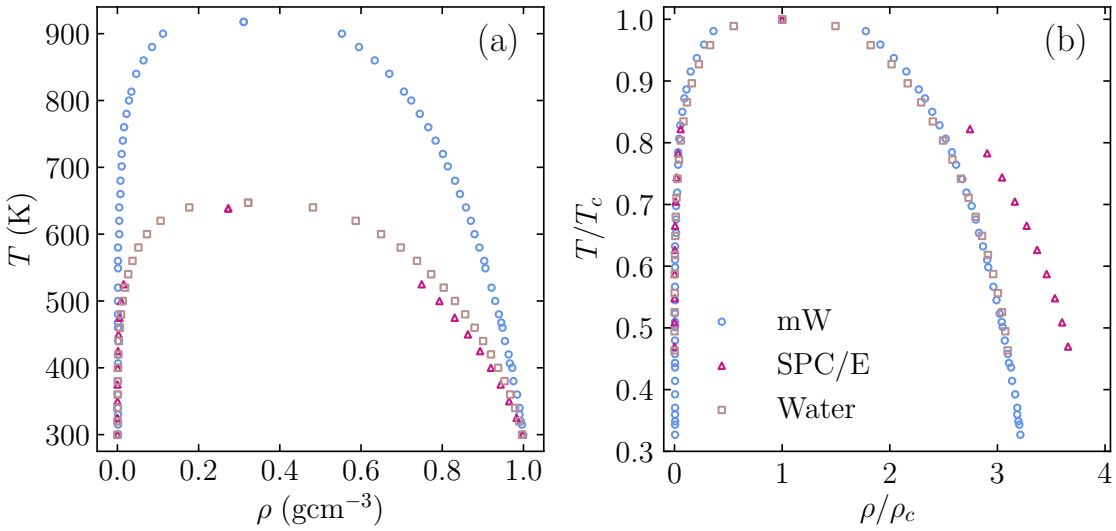

Figure E.3: Liquid-Vapour phase diagram for mW (circles), SPC/E (triangles) and water (squares) in (a) physical units and (b) scaled units. Data for SPC/E was obtained from [150] whilst for water from [149].

and suggests that away from ambient conditions, mW is a poor model of water.

The excellent agreement between the critical density of water and mW suggests that mW may better reproduce the phase diagram of water if T and ρ in both cases were scaled by their critical values. This is tested in figure E.3(b). The agreement between the phase diagrams of mW and water is remarkable, and far better than between that of water and SPC/E. Small differences in the coexistence curves of water and mW can be seen near to the bulk critical point, though these may be partially due to FS effects, and thus further study is needed to confirm whether the deviation in behaviour does occur.

E.3 Comparison of Liquid-Vapour Surface Tension

In addition to reproducing the structure of water, a good water model for the study of hydrophobicity is expected to reproduce the liquid-vapour surface tension. Molinero and Moore [132] have previously shown that mW at ambient conditions has a surface tension closer to that of water then SPC/E, and it was noted by Xu and Molinero [138] that mW almost exactly reproduces the surface tension of water at 360K. Investigation of the behaviour of the surface tension of mW over its entire temperature range is therefore of interest.

The liquid-vapour surface tension can be determined from the probability distributions of the density at each coexistence state point in figure E.3, using [1, 151, 152]

$$\gamma_{lv} = \left(\frac{1}{2\beta L^2}\right) \ln\left(\frac{P_{max}}{P_{min}}\right) \tag{E.3.1}$$

where L is the side length of a cubic simulation box, P_{max} is the maximum probability within the distribution, which will be in the vapour or liquid peaks, and P_{min} is the minimum of the density distribution, which occurs between the liquid and vapour peaks. Figure E.4 shows the surface tension values obtained from mW, along with values for SPC/E and water.

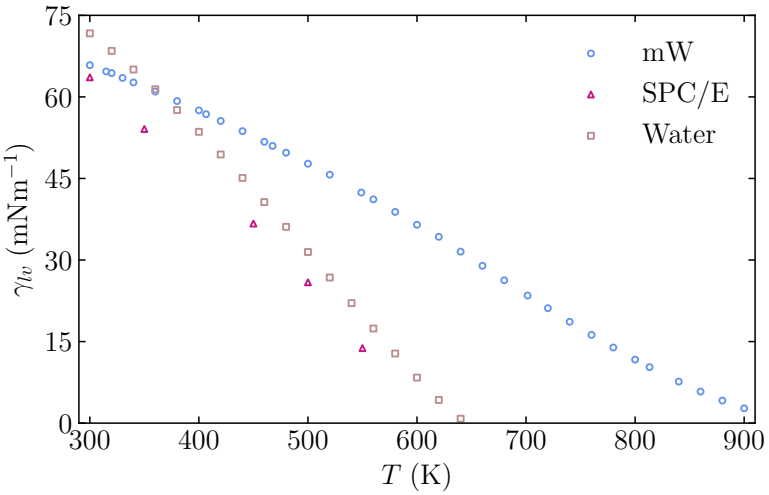

Figure E.4: Comparison of surface tension of mW (circles), SPC/E (triangles) and water (squares). Data for SPC/E was obtained from [134], whilst data for water was obtained from [149].

In agreement with the findings of Molinero and Moore [132], figure E.4 shows that the surface tension of mW is closer to that of water than SPC/E at ambient conditions. Similarly, in agreement with Xu and Molinero [138], the surface tensions of mW and water also appear near identical at 360K. Only when $T > 400$K does SPC/E appear to better reproduce the surface tension of water. mW's higher critical temperature again means that its surface tension extends over a much larger temperature range than water or SPC/E, however it is interesting to note that much like water, the surface tension of mW features a weak 'S' shape, in agreement with the behaviour expected of associating fluids.

In light of the excellent agreement between the phase diagrams of mW and water, it is interesting to ask whether mW is better able to reproduce the liquid-vapour surface tension properties of water if T and γ_{lv} are scaled appropriately. In section 2.4.5, it was mentioned that γ_{lv} is expected to vanish as $\gamma_{lv} \sim (1 - T/T_c)^{\mu}$ on the approach to the bulk critical point, where μ in this case is a critical exponent [50, 153]. Using this expected scaling, figure E.5 compares γ_{lv} for mW, SPC/E and water. The results presented in figure E.5 are interesting, and in many ways inconclusive. Comparing first SPC/E and water, it can be seen that $\beta\sigma^2\gamma_{lv}$ is very similar in each case. However the gradient for SPC/E appears to be different from water. In contrast, the values of $\beta\sigma^2\gamma_{lv}$ for mW and for water are very different, however for the range $-2 < \ln(1 - T/T_c) < -0.6$, the gradients appear as though they may correspond well. Outwith this range, there is little agreement between the gradients, though this is not unsurprising. When $\ln(1 - T/T_c) < -2$, the expected relation between γ_{lv} and $(1 - T/T_c)$ appears to break down for mW. This range corresponds to $T/T_c > 0.86$ which, from figure E.3(b) can be seen to be the range for which the agreement in the scaled phase diagrams of mW and water was poor. It was suggested that the poor agreement in figure E.3(b) for

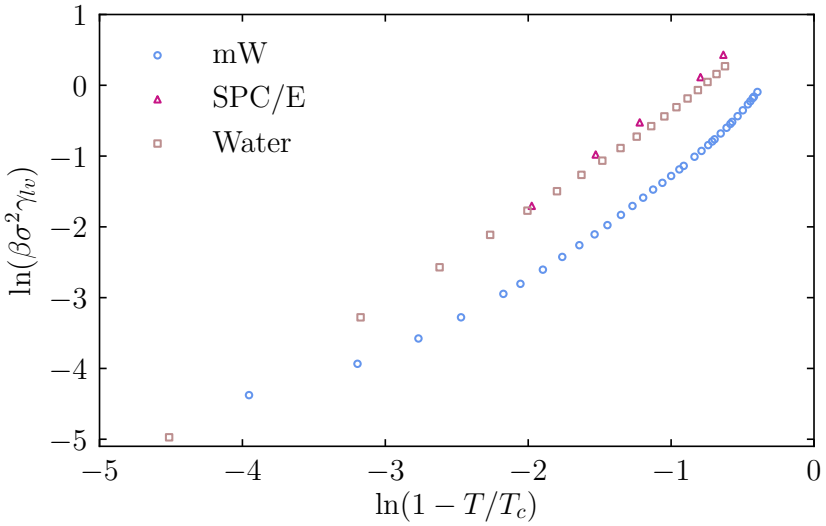

Figure E.5: Comparison of the surface tension of mW (circles), SPC/E (triangles) and water (squares) in scaled units. Data for SPC/E was obtained from [134], whilst data for water was obtained from [149]. σ represents the diameter of a fluid particle/molecule, and was taken to be $\sigma_{mw} = 2.3925$Å in the case of mW [132], $\sigma_{spc/e} = 3.1656$Å in the case of SPC/E [150] and $\sigma_w = 2.8$Å for the case of water [154].

$T/T_c > 0.86$ was due to finite size effects which were not accounted for. Such effects would also explain the change in behaviour of mW in figure E.5 when $\ln(1 - T/T_c) < -2$. There is also disagreement between the gradients of mW and water when $\ln(1 - T/T_c) > -0.6$, which would correspond to $T/T_c < 0.46$. In this range of scaled temperatures, water approaches its freezing point, hence any difference in behaviour is understandable. Figure E.5 therefore provides early evidence that the liquid-vapour surface tension of water and mW may obey similar scaling relationships, however to confirm this, a far more detailed study must be performed. Such a study is beyond the scope of this thesis.

E.4 Summary

Near ambient conditions, mW is an excellent model for the study of hydrophobicity. It performs just as well as SPC/E when reproducing the density of water in the liquid branch of the coexistence phase diagram below 350K, and outperforms SPC/E when reproducing the surface tension of water below approximately 400K. As mW utilises only short-ranged interactions, and coarse grains a water molecule into a single particle, it is also far more computationally efficient than SPC/E.

Away from ambient conditions, mW does not reproduce the properties of water as well as SPC/E. mW features a much higher critical temperature than water, and above 400K, grossly overestimates the surface tension. However, when the phase diagrams of mW, SPC/E and water are all scaled by their critical temperatures and densities, mW and water show remarkable agreement. The same is not true for SPC/E and water. Furthermore, when the appropriate scaling is applied to the liquid-vapour surface tension, mW and water appear to have similar gradients. These two observations potentially imply that mW and water obey a law of corresponding states [153]. If this were the case, it would make mW an excellent model for water at all temperatures. A firm conclusion on this is not possible within the present work, as far more properties than the bulk phase diagram and liquid-vapour surface tension would need to be considered, and finite size effects close to the critical point accounted for. Such considerations are beyond the scope of the present work. Nevertheless, this observation that mW and water may have corresponding states does not appear to have been made previously, and hence it would be very interesting to investigate further.

References

[1] R. Evans, M. C. Stewart, and N. B. Wilding, J. Chem. Phys. **147**, 044701 (2017).

[2] C. Neinhuis and W. Barthlott, Annals of Botany **79**, 667–77 (1997).

[3] Y. Zheng, X. Gao, and L. Jiang, Soft Matter **3**, 178–82 (2007).

[4] J. Qvist, M. Davidovic, D. Hamelberg, and B. Halle, PNAS **105**, 6296–301 (2008).

[5] D. Chandler, Nature **437**, 640–647 (2005).

[6] K. Lum, D. Chandler, and J. D. Weeks, J. Phys. Chem. B **103**, 4570–7 (1999).

[7] N. T. Southall and K. A. Dill, J. Phys. Chem. B **104**, 1326–31 (2000).

[8] D. M. Huang and D. Chandler, PNAS **97**, 8324–7 (2000).

[9] D. M. Huang and D. Chandler, J. Phys. Chem. B **106**, 2047–53 (2002).

[10] X. Huang, C. J. Margulis, and B. J. Berne, J. Phys. Chem. B **107**, 11742–8 (2003).

[11] U. Schnupf and J. W. Brady, Phys. Chem. Chem. Phys. **19**, 11851–63 (2017).

[12] J. Grdadolnik, F. Merzel, and F. Avbelj, PNAS **114**, 322–7 (2016).

[13] P. Buchanan, N. Aldiwan, A. K. Soper, J. L. Creek, and C. A. Koh, Chem. Phys. Lett. **415**, 89–93 (2005).

[14] Y. L. A. Rezus and H. J. Bakker, Phys. Rev. Lett. **99**, 148301 (2007).

[15] J. Grabowska, A. Kuffel, and J. Zielkiewicz, J Phys. Chem. B **125**, 1611–7 (2021).

[16] P. N. Perera, K. R. Fega, C. Lawrence, E. J. Sundstrom, J. Tomlinson-Phillips, and D. Ben-Amotz, PNAS **106**, 12230–4 (2009).

[17] J. B. Boreyko, C. H. Baker, C. R. Poley, and C. Chen, Langmuir **27**, 7502–9 (2011).

[18] A. Marmur, Langmuir **20**, 3517–9 (2004).

[19] S. Parvate, P. Dixit, and S. Chattopadhyay, J. Phys. Chem. B **124**, 1323–60 (2020).

[20] Q. Du, E. Freysz, and Y. R. Shen, Science **264**, 826–8 (1994).

[21] L. F. Scatena, M. G. Brown, and G. L. Richmond, Science **292**, 908–12 (2001).

[22] S. I. Mamatkulov and P. K. Khabibullaev, Langmuir **20**, 4756–63 (2004).

[23] R. Evans and N. B. Wilding, Phys. Rev. Lett. **115**, 016103 (2015).

[24] T. R. Jensen, M. Ø. Jensen, N. Reitzel, K. Balashev, G. H. Peters, K. Kjaer, and T. Bjørnholm, Phys. Rev. Lett. **90**, 086101 (2003).

[25] M. Mezger, F. Sedlmeier, D. Horinek, H. Reichert, D. Pontoni, and H. Dosch, J. Am. Chem. Soc. **132**, 6735–41 (2010).

[26] M. Mezger, H. Reichert, B. M. Ocko, J. Daillant, and H. Dosch, Phys. Rev. Lett. **107**, 249801 (2011).

[27] S. Chattopadhyay, A. Uysal, B. Stripe, Y. Ha, T. J. Marks, E. A. Karapetrova, and P. Dutta, Phys. Rev. Lett. **105**, 037803 (2010).

[28] A. J. Patel, P. Varilly, and D. Chandler, J. Phys. Chem. B **114**, 1632–7 (2010).

[29] H. Acharya, S. Vembanur, S. N. Jamadagni, and S. Garde, Faraday Discuss. **146**, 353–65 (2010).

[30] P. R. ten Wolde and D. Chandler, PNAS **99**, 6539–43 (2002).

[31] A. J. Patel, P. Varilly, S. N. Jamadagni, M. F. Hagan, D. Chandler, and S. Garde, J. Phys. Chem. B **116**, 2498–503 (2012).

[32] R. Evans, M. C. Stewart, and N. B. Wilding, Phys. Rev. Lett. **117**, 176102 (2016).

[33] M. C. Stewart and R. Evans, J. Phys.: Condens. Matter **17**, S3499–505 (2005).

[34] M. C. Stewart and R. Evans, Phys. Rev. E **71**, 011602 (2005).

[35] J. R. Dowdle, S. V. Buldyrev, H. E. Stanley, P. G. Debenedetti, and P. J. Rossky, J. Chem. Phys. **138**, 064506 (2013).

[36] E. Wu and S. Garde, J. Phys. Chem. B **119**, 9287–94 (2014).

[37] R. Evans and M. C. Stewart, J. Phys.:Condens. Matter **27**, 194111 (2015).

[38] R. Evans, M. C. Stewart, and N. B. Wilding, PNAS **116**, 23901–8 (2019).

[39] M. Plischke and B. Bergersen, *Equilibrium Statistical Physics*, 3rd ed. (Singapore, 2006).

[40] R. Evans, "Microscopic Theories of Simple Fluids and their Interfaces", in *Les Houches 1988 Session XLVIII Liquids at Interfaces*, edited by J. Charvolin, J. F. Joanny, and J. Zinn-Justin (North-Holland, 1990).

[41] M. Schick, "Introduction to Wetting Phenomena", in *Les Houches 1988 Session XLVIII Liquids at Interfaces*, edited by J. Charvolin, J. F. Joanny, and J. Zinn-Justin (North-Holland, 1990).

[42] J. Hansen and I. R. McDonald, *Theory of Simple Liquids*, 4th ed. (Academic Press, Oxford, 2013).

[43] M. P. Allen and D. J. Tildesley, *Computer Simulation of Liquids*, 2nd ed. (Oxford University Press, Oxford, 2017).

[44] D. Frenkel and B. Smit, *Understanding Molecular Simulation, From Algorithms to Applications*, 2nd ed. (Academic Press, London, 2002).

[45] R. Evans, "Density Functionals in the Theory of Nonuniform Fluids", in *Fundamentals of Inhomogeneous Fluids*, edited by D. Henderson (Marcel Dekker Inc., 1992), pp. 85–175.

[46] R. Evans, Advances in Physics **28**, 143–200 (1979).

[47] J. M. Yeomans, *Statistical Mechanics of Phase Transitions* (Oxford University Press, 1992).

[48] B. Widom, J. Chem. Phys. **43**, 3898–905 (1965).

[49] D. E. Sullivan and M. M. T. da Gama, "Wetting Transitions and Multilayer Adsorption at Fluid Interfaces", in *Fluid Interfacial Phenomena*, edited by C. A. Croxton (John Wiley & Sons, 1986).

[50] S. Dietrich, "Wetting Phenomena", in *Phase Transitions and Critical Phenomena*, Vol. 12, edited by C. Domb and J. L. Lebowitz (Academic Press, 1988).

[51] J. W. Cahn, J. Chem. Phys. **66**, 3667–72 (1977).

[52] C. Ebner and W. F. Saam, Phys. Rev. Lett. **38**, 1486–9 (1977).

[53] J. E. Lane, T. H. Spurling, B. C. Freasier, J. W. Perram, and E. R. Smith, Phys. Rev. A **20**, 2147–53 (1979).

[54] R. M. Nieminen and N. W. Ashcroft, Phys. Rev. A **24**, 560–71 (1981).

[55] R. Evans and P. Tarazona, Phys. Rev. A **28**, 1864–8 (1983).

[56] C. Ebner, Phys. Rev. A **23**, 1935–30 (1981).

[57] C. Ebner, Phys. Rev. B **28**, 2890–2 (1983).

[58] D. E. Sullivan, Phys. Rev. B **20**, 3991–4000 (1979).

[59] P. Tarazona and R. Evans, Molecular Physics **48**, 799–831 (1983).

[60] E. H. Hauge and M. Schick, Phys. Rev. B **27**, 4288–301 (1983).

[61] R. Pandit, M. Schick, and M. Wortis, Phys. Rev. B **26**, 5112–40 (1982).

[62] D. E. Sullivan, Faraday Symp. Chem. Soc. **16**, 191–204 (1981).

[63] K. Ragil, J. Meunier, D. Broseta, J. O. Indekeu, and D. Bonn, Phys. Rev. Lett. **77**, 1532–5 (1996).

[64] D. Bonn, H. Kellay, and G. H. Wegdam, Phys. Rev. Lett. **69**, 1975–8 (1992).

[65] D. Ross, D. Bonn, and J. Meunier, J. Chem. Phys. **114**, 2784–92 (2001).

[66] S. Rafaï, D. Bonn, E. Betrand, and J. Meunier, Phys. Rev. Lett. **92**, 245701 (2004).

[67] E. Bertrand, H. Dobbs, D. Broseta, J. Indekeu, D. Bonn, and J. Meunier, Phys. Rev. Lett. **85**, 1282–5 (2000).

[68] N. B. Wilding, Phys. Rev. E **52**, 602–11 (1995).

[69] D. M. Kroll and G. Gompper, Phys. Rev. B **39**, 433–45 (1989).

[70] A. Parola and L. Reatto, Phys. Rev. A **31**, 3309–22 (1985).

[71] T. Eckert, N. C. X. Stuhlmüller, F. Sammüller, and M. Schmidt, Phys. Rev. Lett. **125**, 268004 (2020).

[72] Y. Levy and J. N. Onuchic, Annu. Rev. Biophys. Biomol. Struct. **35**, 389–415 (2006).

[73] S. N. Jamadagni, R. Godawat, and S. Garde, Annu. Rev. Chem. Biomol. Eng. **2**, 147–71 (2011).

[74] J. Genzer and K. Efimenko, Biofouling **22**, 339–60 (2006).

[75] M. Callies and D. Quéré, Soft Matter **1**, 55–61 (2005).

[76] N. T. Southall, K. A. Dill, and A. D. J. Haymet, J. Phys. Chem. B **106**, 521–33 (2002).

[77] S. Rajamani, T. M. Truskett, and S. Garde, PNAS **102**, 9475–80 (2005).

[78] X. Wu, W. Lu, L. M. Streacker, H. A. Ashbaugh, and D. Ben-Amotz, J. Phys. Chem. Lett. **9**, 1012–7 (2018).

[79] S. Sarurpria and S. Garde, Phys. Rev. Lett. **103**, 037803 (2009).

[80] N. Giovambattista, C. F. Lopez, P. J. Rossky, and P. G. Debenedetti, PNAS **105**, 2274–9 (2008).

[81] D. M. Huang and D. Chandler, Phys. Rev. E **61**, 1501–6 (2000).

[82] A. Giacomello, L. Schimmele, S. Dietrich, and M. Tasinkevych, Soft Matter **12**, 8927–34 (2016).

[83] D. M. Huang, P. L. Geissler, and D. Chandler, J. Phys. Chem. B **105**, 6704–9 (2001).

[84] J. Monroe, M. Barry, A. Destefano, P. A. Gokturk, S. Jiao, D. Robinson-Brown, T. Webber, E. J. Crumlin, S. Han, and M. S. Shell, Annu. Rev. Chem. Biomol. Eng. **11**, 523–57 (2020).

[85] D. Laage, G. Stirnemann, and J. T. Hynes, J. Phys. Chem. B **113**, 2428–35 (2009).

[86] B. J. Berne, J. D. Weeks, and R. Zhou, Annu. Rev. Phys. Chem. **60**, 85–103 (2009).

[87] F. H. Stillinger, J. Solution Chem. **2**, 141–58 (1973).

[88] J. W. G. Tyrrell and P. Attard, Phys. Rev. Lett. **87**, 176104 (2001).

[89] J. Israelachvili, *Intermolecular and Surface Forces*, 2nd ed. (Academic Press, London, 1991).

[90] H. S. Frank and M. W. Evans, J. Chem. Phys. **13**, 507–532 (1945).

[91] J. Qvist and B. Halle, J. Am. Chem. Soc. **130**, 10345–53 (2008).

[92] S. Garde, G. Hummer, A. E. García, M. E. Paulaitis, and L. R. Pratt, Phys. Rev. Lett. **77**, 4966–8 (1996).

[93] G. Hummer, S. Garde, A. E. Garía, A. Pohorille, and L. R. Pratt, PNAS **93**, 8951–5 (1996).

[94] C. Vega, J. L. F. Abascal, and I. Nezbeda, J. Chem. Phys. **125**, 034503 (2006).

[95] J. Mittal and G. Hummer, PNAS **105**, 20130–5 (2008).

[96] C. A. Cerdeiriña, P. G. Debenedetti, P. J. Rossky, and N. Giovambattista, J. Phys. Chem. Lett. **2**, 1000–3 (2011).

[97] R. C. Remsing and A. J. Patel, J. Chem. Phys. **142**, 024502 (2015).

[98] M. V. Athawale, G. Goel, T. Ghosh, T. M. Truskett, and S. Garde, PNAS **104**, 733–8 (2007).

[99] R. Zhou, X. Huang, C. J. Margulis, and B. J. Berne, Science **305**, 1605–9 (2004).

[100] P. Liu, X. Huang, R. Zhou, and B. J. Berne, Nature **437**, 159–62 (2005).

[101] M. Mezger, H. Reichert, S. Schöder, J. Okasinki, H. Schröder, H. Dosch, D. Palms, J. Ralston, and V. Honkimäki, PNAS **103**, 18401–4 (2006).

[102] A. P. Willard and D. Chandler, J. Chem. Phys. **141**, 18C519 (2014).

[103] R. Steitz, T. Gutberlet, T. Hauss, B. Klösgen, R. Krastev, S. Schemmel, A. C. Simonsen, and G. H. Findenegg, Langmuir **19**, 2409–18 (2003).

[104] S. Chattopadhyay, A. Uysal, B. Stripe, Y. Ha, T. J. Marks, E. A. Karapetrova, and P. Dutta, Phys. Rev. Lett. **107**, 249802 (2011).

[105] N. Giovambattista, P. G. Debenedetti, and P. J. Rossky, J. Phys. Chem. B **111**, 9581–7 (2007).

[106] A. A. Ganesh, H. K. Raut, A. S. Nair, and S. Ramakrishna, J. Mater. Chem. **21**, 16304–22 (2011).

[107] F. Geyer, M. D'Acunzi, A. Sharifi-Aghili, A. Saal, N. Gao, A. Kaltbeitzel, T. Sloot, R. Berger, H. Butt, and D. Vollmer, Sci. Adv. **6**, eaaw9727 (2020).

[108] M. P. Moody and P. Attard, J. Chem. Phys. **115**, 8967–77 (2001).

[109] N. Choudhury and B. M. Pettitt, J. Am. Chem. Soc. **129**, 4847–52 (2007).

[110] R. C. Remsing, E. Xi, S. Vembanur, S. Sharma, P. G. Debenedetti, S. Garde, and A. Patel, PNAS **112**, 8181–6 (2015).

[111] R. Roth, J. Phys.:Condens. Matter **22**, 0631102 (2010).

[112] A. P. Hughes, U. Thiele, and A. J. Archer, J. Chem. Phys. **142**, 074702 (2015).

[113] B. Chacko, R. Evans, and A. J. Archer, J. Chem. Phys. **146**, 124703 (2017).

[114] Y. Rosenfeld, Phys. Rev. Lett. **63**, 980–3 (1989).

[115] N. D. Mermin, Phys. Rev. **137**, A1441 (1965).

[116] R. Roth, "Introduction to Density Functional Theory of Classical Systems: Theory and Applications", Lecture Notes for the Front Researcher Development Program of Kyushu University, Nov. 2006.

[117] M. C. Stewart, "Effect of Substrate Geometry on Interfacial Phase Transitions", PhD thesis (University of Bristol, 2006).

[118] J. Hughes, E. J. Krebs, and D. Roundy, J. Chem. Phys. **138**, 024509 (2013).

[119] F. Grußmann, S. Dietrich, and R. Roth, Phys. Rev. E **102**, 062112 (2020).

[120] H. Hansen-Goos and R. Roth, J. Phys.: Condens. Matter **18**, 8413–25 (2006).

[121] E. Kierlik and M. L. Rosinberg, Phys. Rev. A **42**, 3382–7 (1990).

[122] J. de Gussem, "A Study of Pair Correlation Functions Using Classical DFT", M.Sc. (Delft University of Technology, 2012).

[123] R. Roth, R. Evans, A. Lang, and G. Kahl, J. Phys.: Condens. Matter **14**, 12063–78 (2002).

[124] K. Ng, J. Chem. Phys. **61**, 2680–9 (1974).

[125] F. van Swol and J. R. Henderson, Phys. Rev, A **40**, 2567–78 (1989).

[126] P. Bryk, R. Roth, K. R. Mecke, and S. Dietrich, Phys. Rev. E **68**, 031602 (2003).

[127] G. R. Smith and A. D. Bruce, J. Phys. A: Math Gen. **28**, 6623–43 (1995).

[128] G. C. McNeil-Watson and N. B. Wilding, J. Chem. Phys. **124**, 064504 (2006).

[129] D. J. Ashton and N. B. Wilding, Molecular Physics **109**, 999–1007 (2010).

[130] A. H. Ferrenberg and R. H. Swendsen, Phys. Rev. Lett. **61**, 2635–8 (1988).

[131] A. H. Ferrenberg and R. H. Swendsen, Computers in Physics **3**, 101–4 (1989).

[132] V. Molinero and E. B. Moore, J. Phys. Chem. B **113**, 4008–16 (2009).

[133] C. Vega and J. L. F. Abascal, Phys. Chem. Chem. Phys. **13**, 19663–88 (2011).

[134] C. Vega and E. de Miguel, J. Chem. Phys. **126**, 154707 (2007).

[135] J. Lam and J. F. Lutsko, J. Chem. Phys. **149**, 134703 (2018).

[136] L. Maibaum and D. Chandler, J. Phys. Chem. B **111**, 9025–30 (2007).

[137] V. Kumar and J. R. Errington, J. Phys. Chem. C **117**, 23017–26 (2013).

[138] L. Xu and V. Molinero, J. Phys. Chem. B. **114**, 7320–8 (2010).

[139] B. Song and V. Molinero, J. Chem. Phys. **139**, 054511 (2013).

[140] N. Islam, M. Flint, and S. W. Rick, J. Chem. Phys. **150**, 014502 (2019).

[141] J. Russo, K. Akahane, and H. Tanaka, PNAS **115**, E3333–E3341 (2018).

[142] M. M. Tsypin and H. W. J. Blöte, Phys. Rev. E **62**, 73–6 (2000).

[143] S. Dietrich and M. Schick, Phys. Rev. B **33**, 4952–68 (1986).

[144] S. Dietrich and M. Napiórkowski, Phys. Rev. A **43**, 1861–85 (1991).

[145] T. Bieker and S. Dietrich, Physica A **252**, 85–137 (1998).

[146] R. Evans, J. R. Henderson, and R. Roth, J. Chem. Phys. **121**, 12074–84 (2004).

[147] E. Brézin, B. I. Halperin, and S. Leibler, Journal de Physique **44**, 775–83 (1983).

[148] N. B. Wilding, unpublished, Program to calculate liquid-vapour phase diagram., 2018.

[149] E. W. Lemmon, M. O. McLinden, and D. G. Friend, "Thermophysical Properties of Fluid Systems", in *NIST Chemistry WebBook, NIST Standard Reference Database Number 69*, edited by P. J. Linstrom and W. G. Mallard, Accessed 29 June 2021 (National Institute of Standards and Technology Gaithersburg MD, 20899).

[150] "NIST Standard Reference Simulation Website", in *NIST Standard Reference Database Number 173*, edited by V. K. Shen, D. W. Siderius, W. P. Krekelberg, and H. W. Hatch, Accessed 29 June 2021 (National Institute of Standards and Technology, Gaithersburg MD, 20899).

[151] K. Binder, Phys. Rev. A **25**, 1699–1709 (1982).

[152] J. R. Errington, Phys. Rev. E **67**, 012102 (2003).

[153] E. A. Guggenheim, J. Chem. Phys **13**, 253–61 (1945).

[154] J. S. D'Arrigo, American Journal of Physiology - Cell Physiology **235**, C109–17 (1978).